

# Diffraction Focusing of Sound Field in an Underwater Sound Channel

D. I. Abrosimov and Yu. V. Petukhov

*Institute of Applied Physics, Russian Academy of Sciences,  
ul. Ul'yanova 46, Nizhni Novgorod, 603600 Russia*

*e-mail: petukhov@hydro.appl.sci-nnov.ru*

Received September 2, 1998

**Abstract**—For the simplest underwater sound channel modeled by a bilinear depth dependence of the squared refractive index, the main features of the spatial domains of the sound field diffraction focusing are determined in the framework of the WKB approximation. The optimum conditions for the observation of the diffraction focusing of mode beams in natural ocean waveguides are formulated. A numerical simulation of the spatial diffraction focusing of sound field in a sound channel with the canonic sound speed profile is performed. The results of the numerical simulation agree well with those of the approximate analysis. © 2000 MAIK “Nauka/Interperiodica”.

It is well known [1–5] that the spatial interference structure of the sound field periodically varies along the ocean waveguide. These variations are characterized by the minimum and maximum periods,  $R_{\min}$  and  $R_{\max}$ , and manifest themselves in a partial repetition of the features of the spatial intensity distribution observed at  $0 \leq r < R_{\min}$ . The repetition leads to the diffraction focusing of the sound field at certain ranges [3, 4]:

$$mR_{\min} \leq r \leq mR_{\max} \quad (m = 1, 2, \dots), \quad (1)$$

where

$$\begin{aligned} R_{\min} &= \min[R_g(l, l+1; l+1, l+2)], \\ R_{\max} &= \max[R_g(l, l+1; l+1, l+2)]. \end{aligned} \quad (2)$$

Here the term

$$\begin{aligned} R_g(l, l+1; l+1, l+2) \\ = R_{l, l+1} R_{l+1, l+2} / |R_{l, l+1} - R_{l+1, l+2}| \end{aligned} \quad (3)$$

corresponds to the period of the rearrangement of the interference structure of the sound field formed by a pair of adjacent modes with the characteristic interference periods

$$\begin{aligned} R_{l, l+1} &= 2\pi/(k_l - k_{l+1}), \\ R_{l+1, l+2} &= 2\pi/(k_{l+1} - k_{l+2}). \end{aligned} \quad (4)$$

The frequency dependence of the horizontal wave number  $k_l$  of the  $l$ th mode is determined by the dispersion relation corresponding to the specific waveguide.

Note that, as in our earlier works [3, 4], by analogy with the diffraction imaging of periodic structures in optics [6], the diffraction focusing of a guided sound field means the formation of zones of enhanced insonification. In ordinary refraction focusing [7], the spatial

period only weakly depends on the wavelength through a small diffraction correction to the ray approximation [8–11]. In contrast, a significant dependence of the period on the wavelength is characteristic of the diffraction focusing [3, 4].

In ocean waveguides, under some conditions, the spatial (in depth  $z$  and horizontal range  $r$ ) distribution of the sound field intensity  $J(r, z)$  exhibits a beam-like structure that is most pronounced in the presence of the underwater sound channel [5]. Hence, according to the results of our theoretical study [4], the diffraction focusing of the beams should occur within the spatial domains (1).

The objective of this paper is the quantitative description of the diffraction focusing of the sound field and the associated diffraction focusing of the mode beams in a deep-water ocean waveguide with the underwater sound channel that is open to the surface and has an acoustically transparent bottom.

To solve the problem, namely, to pre-estimate the boundaries of the domains (1), it is advantageous to obtain explicit dependences of  $R_{\min}$  and  $R_{\max}$  (2) (even approximate ones) on the parameters governing the phenomenon under study. To begin with, we consider a model deep-water waveguide with a bilinear dependence of the squared refractive index  $n^2(z)$  on the depth within the water layer ( $0 \leq z \leq H$ ) and with an acoustically transparent bottom ( $z \geq H$ ):

$$n^2(z) = \begin{cases} 1 + a_1(z - z_0), & 0 \leq z \leq z_0 \\ 1 - a_2(z - z_0), & z_0 \leq z \leq H \\ 1 - a_2(H - z_0), & z \geq H. \end{cases} \quad (5)$$

Here  $a_1 > 0$  and  $a_2 > 0$  are the parameters determining the gradients of the quantity  $n^2(z)$  above and below the channel axis, respectively;  $z_0$  is the channel axis depth;  $H$  is the thickness of the water layer; and  $a_1 z_0 < a_2(H - z_0)$ .

We assume that the multi-mode propagation of the sound waves takes place (the diffraction focusing being most pronounced in this case [4]), and the WKB approximation is valid. Then, we use the expressions derived in [4] to determine the quantities  $R_{\min}$  and  $R_{\max}$ :

$$R_{\min} = \frac{k}{2\pi} \min \left[ D_l^3 / \left| \frac{dD_l}{d\beta_l} \right| \right], \quad (6)$$

$$R_{\max} = \begin{cases} \frac{k}{2\pi} \max \left[ D_l^3 / \left| \frac{dD_l}{d\beta_l} \right| \right], & \frac{dD_l}{d\beta_l} \neq 0 \\ \left( \frac{k}{2\pi} \right)^2 \left[ D_l^4 / \left| \frac{d^2 D_l}{d\beta_l^2} \right| \right]_{\beta_l = \beta_c}, & \frac{dD_l}{d\beta_l} \Big|_{\beta_l = \beta_c} = 0. \end{cases} \quad (7)$$

Here,

$$D_l = 2\beta_l \int_{z_{lL}}^{z'_l} \frac{dz}{\sqrt{n^2(z) - \beta_l^2}} \quad (8)$$

is the cycle length for the associated Brillouin ray having the grazing angle  $\chi_l$  and the ray parameter  $\beta_l = \cos \chi_l$

at the channel axis;  $z'_l = \begin{cases} 0 \\ z_{lU} \end{cases}$ , where  $z_{lU}$ , and  $z_{lL}$  are the

upper and lower turning horizons of this ray;  $\beta_l = \beta_c$  corresponds to the extremum of the function  $D_l(\beta_l)$ ; and  $k = \omega/c_0$ , where  $c_0 = \min[c(z)] = c(z_0)$  is the minimum sound speed,  $c(z) = c_0/n(z)$ ,  $\omega = 2\pi f$ , and  $f$  is the frequency of the transmitted cw signal. The values of  $\beta_l$  are determined by the dispersion equation of the WKB approximation [7]:

$$k \int_{z_{lL}}^{z'_l} \sqrt{n^2(z) - \beta_l^2} dz = \pi(l - \nu), \quad (9)$$

where

$$\nu = \begin{cases} 1/2, & z'_l = z_{lU} \\ 1/4, & z'_l = 0. \end{cases} \quad (10)$$

With this model of the underwater sound channel (5), in view of (8) and (9), we derive the following relations for the cycle length and the ray parameter of the refracted rays ( $1 \leq l \leq L_r$ ) and the rays interacting with the ocean surface ( $1 + L_r \leq l \leq L$ ):

$$D_l(\beta_l) = \frac{6\pi}{k_a} \beta_l \sqrt{1 - \beta_l^2} \quad (\beta_r \leq \beta_l \leq 1), \quad (11)$$

$$\beta_l = \sqrt{1 - \left[ \frac{k_a}{k} \left( l - \frac{1}{2} \right) \right]^{2/3}} \quad (1 \leq l \leq L_r), \quad (12)$$

$$D_l(\beta_l) = \frac{6\pi}{k_a} \beta_l \left( \sqrt{1 - \beta_l^2} - \frac{a_2}{a_1 + a_2} \sqrt{1 - a_1 z_0 - \beta_l^2} \right) \quad (13)$$

$$(\beta_s \leq \beta_l < \beta_r),$$

$$(1 - \beta_l^2)^{3/2} - \frac{a_2}{a_1 + a_2} (1 - a_1 z_0 - \beta_l^2)^{3/2} = \frac{k_a}{k} \left( l - \frac{1}{4} \right) \quad (14)$$

$$(1 + L_r \leq l \leq L).$$

Here,

$$k_a = \frac{3\pi a_2}{2(1 + a_2/a_1)}, \quad \beta_r = \sqrt{1 - a_1 z_0}, \quad (15)$$

$$\beta_s = \sqrt{1 - a_2(H - z_0)},$$

and the numbers  $L_r$  and  $L$  of the modes are determined by expressions that follow from (12) at  $\beta_l = \beta_r$  and (14) at  $\beta_l = \beta_s$ :

$$L_r = \frac{1}{2} + \frac{k}{k_a} (a_1 z_0)^{3/2}, \quad (16)$$

$$L = \frac{1}{4} + \frac{k}{k_a}$$

$$\times \left\{ [a_2(H - z_0)]^{3/2} - \frac{a_2}{a_1 + a_2} [a_2(H - z_0) - a_1 z_0]^{3/2} \right\}. \quad (17)$$

Because the function  $D_l(\beta_l)$  (11) has no extrema within the allowable range of the ray parameter, expressions (6) and (7) take the following forms for the refracted modes:

$$R_{\min} = R_{r\min} = 18\pi \frac{k}{k_a^2} F(\beta_l), \quad (18)$$

$$R_{\max} = R_{r\max} = 18\pi \frac{k}{k_a^2} F(\beta_r), \quad (19)$$

where

$$F(\beta_l) = \frac{\beta_l^3 (1 - \beta_l^2)^2}{2\beta_l^2 - 1}. \quad (20)$$

By substituting (12) and (15) into (18)–(20), we find the approximate expressions for the characteristic periods of the diffraction-focused refracted modes of the sound field:

$$R_{r\min} \approx 9 \frac{\pi}{k_a} (k_a/2k)^{1/3}, \quad (21)$$

$$R_{r\max} \approx \frac{8}{\pi} k H_r^2, \quad (22)$$

where

$$H_r = z_0(1 + a_1/a_2) \quad (23)$$

is the characteristic thickness of the underwater sound channel (5). The values of this thickness are the solutions of the equation  $n(0) = n(H_r)$ .

According to (21) and (22),  $R_{r\min}$  decreases and  $R_{r\max}$  increases as  $k$  increases. Then, the length of each spatial domain of the diffraction focusing of the acoustic field formed solely by the refracted modes can be expressed as

$$\Delta r_m = m\Delta R_g, \quad (24)$$

where

$$\Delta R_g = R_{\max} - R_{\min}, \quad (25)$$

and this length sharply increases as the emitted frequency grows.

However, the situation is most interesting when the source is located at the depth  $z_s$  that is far away from both the free surface and the channel axis,  $2\pi/k < z_s \ll z_0$ . In this case, the beam-like structure of the guided sound field is most pronounced [5]. Under such conditions, for the refracted Brillouin rays, the range of variations of the ray parameter has the lower bound

$$\beta_l = \beta_p = n(z_s) = \sqrt{1 - a_1(z_0 - z_s)}. \quad (26)$$

Here we use the fact that modes of numbers  $l < l_p$ ,

$$l_p = \frac{1}{2} + \frac{k}{k_a} [a_1(z_0 - z_s)]^{3/2}, \quad (27)$$

whose turning horizons are deeper than the source horizon ( $z_s < z_{lU}$ ) are virtually not excited. The latter means that the actual dependence  $R_{\min} = \bar{R}_{r\min}$  will have the form similar to (22):

$$\bar{R}_{r\min} \approx 18\pi \frac{k}{k_a} F(\beta_p) \approx \frac{8}{\pi} k H_p^2, \quad (28)$$

where

$$H_p = (z_0 - z_s)(1 + a_1/a_2) \quad (29)$$

is the depth "conjugated" to that of the source. Its value (29) is obtained as the solution of the equation  $n(z_s) = n(H_p)$ .

By using expressions (22) and (28), we find the dependence

$$\Delta R_g \approx \frac{8}{\pi} k H_r^2 \frac{z_s}{z_0} \left(2 - \frac{z_s}{z_0}\right), \quad (30)$$

which leads to a conclusion that, in the case at hand, the length of each spatial domain of the diffraction focusing of the sound field, which is formed solely by the refracted modes, will decrease as the source depth and the emitted frequency decrease. In view of the fact that the domains (1) become closer to the source as the emitted frequency decreases (see (22) and (28)),

expression (30) means that the diffraction focusing of sound beams formed by the refracted modes is best observed when the emitted frequency is relatively low and the source is located near the ocean surface ( $z_s/z_0 \ll 1$ ). Note that, in the case of multi-mode propagation ( $kH_r \gg 1$ ), the values of  $z_s$  and  $\omega$  are related to each other by the expression that follows from the condition of the efficient excitation of a large number of refracted modes:

$$L_r - l_p \gg 1. \quad (31)$$

The latter condition is that of the formation of a pronounced beam-like structure of the sound field by the refracted modes. Actually, in view of (16) and (27), at  $z_s/z_0 \ll 1$ , we obtain from (31):

$$kz_s \gg \pi / [(1 + a_1/a_2)\sqrt{a_1 z_0}], \quad (32)$$

which is the lower bound for the frequency range.

In the allowable range of the ray parameter, the dependence  $D_l(\beta_l)$  (13) that corresponds to the modes interacting with the ocean surface has a minimum at some  $\beta_l = \beta_c$  [12]. Let us introduce a quantity  $\alpha_l^2 = 1 - \beta_l^2 = \sin^2 \chi_l$ . To determine the corresponding value of  $\alpha_c^2 = 1 - \beta_c^2$ , we use the condition

$$\left(\frac{dD_l}{d\beta_l}\right)\Big|_{\beta_l=\beta_c} = 0 \quad (33)$$

and expression (13) to obtain the equation

$$\alpha_c^2 \left[1 - \left(\frac{a_2}{a_1 + a_2}\right)^2 \left(\frac{1 + \alpha_r^2 - 2\alpha_c^2}{1 - 2\alpha_c^2}\right)^2\right] = \alpha_r^2. \quad (34)$$

At low grazing angles  $\chi_l \ll 1$  ( $\alpha_c^2 \ll 1$ ), this equation has the following approximate solution:

$$\alpha_c^2 \approx \alpha_r^2 / \left[1 - \left(\frac{a_2}{a_1 + a_2}\right)^2 (1 + \alpha_r^2)^2\right], \quad (35)$$

where  $\alpha_r = \sqrt{a_1 z_0}$ .

In view of the mentioned extremum (33) in the dependence  $D_l(\beta_l)$  (13), for the surface-interacting modes, we reduce expressions (6) and (7) to the form

$$R_{\min} = R_{s\min} = \frac{18\pi k}{k_a^2} |\Phi(\alpha_g)|, \quad (36)$$

$$R_{\max} = R_{s\max} = \frac{54\pi k^2}{k_a^3} |\Psi(\alpha_c)|, \quad (37)$$

where

$$\Phi(\alpha_l) = \frac{\alpha_l^4 \left( 1 - \frac{a_2}{a_1 + a_2} \sqrt{1 - \frac{\alpha_r^2}{\alpha_l^2}} \right)^3 \sqrt{1 - \frac{\alpha_r^2}{\alpha_l^2}}}{(1 - 2\alpha_l^2) \left[ \sqrt{1 - \frac{\alpha_r^2}{\alpha_l^2}} - \frac{a_2}{a_1 + a_2} \left( 1 + \frac{\alpha_r^2}{1 - 2\alpha_l^2} \right) \right]}, \quad (38)$$

$$\Psi(\alpha_l) = \frac{\alpha_l^7 (1 - \alpha_l^2)^{3/2} \left( 1 - \frac{a_2}{a_1 + a_2} \sqrt{1 - \frac{\alpha_r^2}{\alpha_l^2}} \right)^4}{\left[ \frac{a_2}{a_1 + a_2} (1 - \alpha_r^2/\alpha_l^2)^{3/2} - 1 - 2\alpha_l^2 \right]}. \quad (39)$$

Here, the value  $\alpha_l = \alpha_g$  corresponds to the minimum of the function  $\Phi(\alpha_l)$  (38) for the allowable range of this quantity:  $\alpha_r < \alpha_l \leq \alpha_s = \sqrt{a_2(H - z_0)}$ . According to (38),  $\alpha_g$  must differ from  $\alpha_r$  by the limiting allowable small value

$$\sigma = \frac{\alpha_g}{\alpha_r} - 1. \quad (40)$$

To determine this value, we use (14) at  $l = l_s = L_r + 1$  ( $\alpha_{l_s} = \alpha_g$ ) to obtain the following equation:

$$(1 + \sigma)^3 - \frac{a_2}{a_1 + a_2} [\sigma(\sigma + 2)]^{3/2} = 1 + \frac{k_a}{4k\alpha_r^3}. \quad (41)$$

Because  $k_a/4k\alpha_r^3 \ll 1$  in the situation at hand, the first approximation of (41) yields the following solution:

$$\sigma \approx k_a/12k\alpha_r^3. \quad (42)$$

Then, with the use of (36)–(39) in view of (35) and (42), simple approximate expressions are obtained for the characteristic spatial periods:

$$R_{s\min} \approx \frac{18\pi(1 + a_1/a_2)\alpha_r^{5/2} \sqrt{k}}{\sqrt{6}k_a}, \quad (43)$$

$$R_{s\max} \approx \frac{16}{\pi^2} k^2 H_r^3 \sqrt{\frac{a_2 H_r}{(1 + a_1/a_2)^3 (2 + a_1/a_2)}}. \quad (44)$$

According to (43) and (44), the length of each spatial domain of the focused sound field (24) formed solely by the surface-interacting modes increases with increasing emitted frequency much more rapidly than the corresponding quantity (24) for the refracted modes. In this case, the evident relation  $R_{r\max}/R_{s\max} \ll 1$  is valid.

However, one should keep in mind that the aforementioned features of the dependence  $D_l(\beta_l)$  (13) manifest themselves in the corresponding dependence  $R_{l,l+1}(l)$  only at relatively high emitted frequencies

when a sufficiently large number of surface-interacting modes are excited,  $L - L_r \gg 1$  [5, 12]. With the use of (16) and (17), one can determine the frequency band that corresponds to the latter condition:

$$k \gg \frac{5}{4} k_a / \left[ \alpha_s^3 - \alpha_r^3 - \frac{a_2}{a_1 + a_2} (\alpha_s^2 - \alpha_r^2)^{3/2} \right]. \quad (45)$$

Within this band, expressions (43) and (44) are valid along with their corollaries.

The following points should be mentioned. First, the quantity  $R_{s\max}$  (44) significantly predominates over  $R_{r\max}$  (22), because, when condition (45) is met, the weakly divergent acoustic beams formed by the surface-interacting modes can be excited [5]. These beams exhibit a minimum geometrical spread of the wavefront and noticeably shift the outer boundary of each spatial diffraction-focusing domain of the sound field (1) in the direction away from the source. At certain emitted frequencies and source depths, these beams can form the narrowest far convergence zones [12] in deep-water waveguides with sound channels that are open to the surface. Second, in contrast to an erroneous conclusion of Caruthers *et al.* [13], a weakly divergent beam is also excited in the model sound channel (5), this beam being formed by the refracted modes in the vicinity of the singular (caustic) geometric-acoustic ray which leaves the source in the horizontal direction [14–16]. Because the condition similar to (33) at  $k \rightarrow \infty$  is violated for this ray (see [14, 15]), condition (33) itself is also not valid for the beam-forming refracted Brillouin rays at  $\beta_l \rightarrow \beta_p$  (26). The latter means that the outer boundary of each diffraction-focusing domain of the corresponding modes (1) is governed by the maximum period  $R_{r\max}$  (22) of the rearrangement of the spatial interference structure of an ordinary beam of modes.

Thus, for the model underwater sound channel (5), the approximate analysis of the dependences  $R_{\min}$  (6) and  $R_{\max}$  (7) leads to the following conclusion. For the observation of the diffraction focusing of the acoustic field in the sound channel similar to the model one (5), it is preferable to use the emitted frequencies and the source depths at which the refracted modes are predominantly excited. To obtain the most pronounced diffraction focusing of the beams at ranges that are allowable for deep-water ocean waveguides, one should select the aforementioned parameters in such a way that a single mode beam is excited, and this beam is not a weakly divergent one.

In view of the above conclusions, let us proceed with a precise quantitative description of the diffraction-focusing of the sound field in the ocean waveguide with an acoustically transparent bottom at  $z \geq H$  and with the canonic underwater sound channel [17] that is open to the surface:

$$c(z) = c_0 [1 + \varepsilon(e^\eta - \eta - 1)], \quad 0 \leq z \leq H, \quad (46)$$

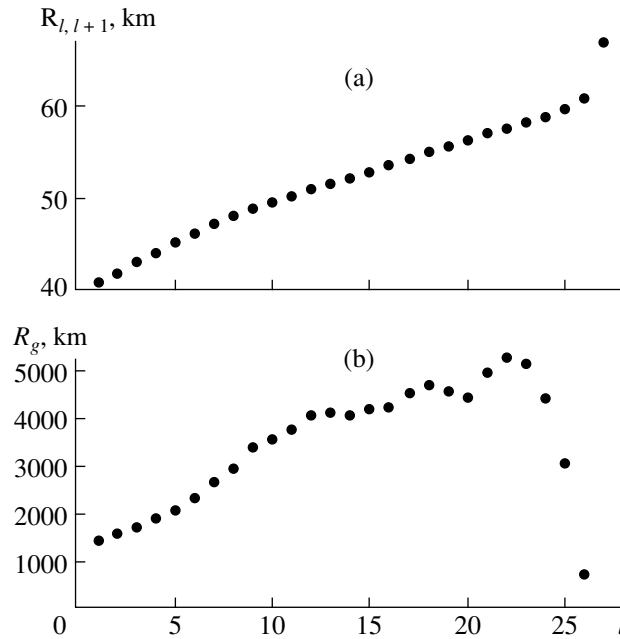


**Fig. 1.** Spatial periods of (a) the interference of adjacent modes,  $R_{l,l+1}$ , and (b) the rearrangement of the interference structure of the sound field formed by adjacent mode pairs,  $R_g(l, l + 1; l + 1, l + 2)$ , versus the mode number  $l$  at  $f = 20$  Hz.

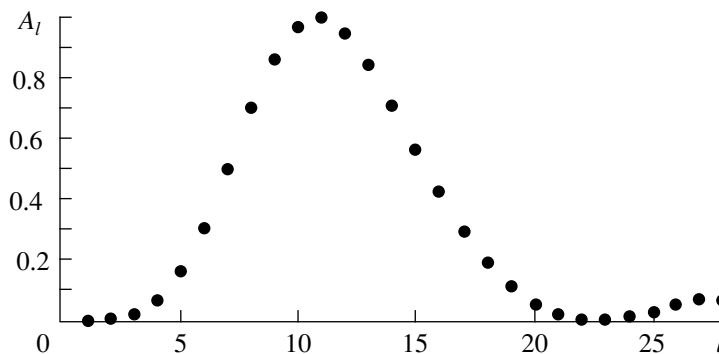


**Fig. 2.** Normalized product of the amplitudes of adjacent modes  $A_l = B_{l,l+1}/\max [B_{l,l+1}]$  versus the mode number  $l$  for the source depth  $z = z_s = 200$  m at  $f = 20$  Hz.

where

$$\eta = 2(z_0 - z)/H_g, \quad \varepsilon = \gamma H_g/2. \quad (47)$$

The parameters of expressions (46) and (47) are specified as follows:  $c_0 = 1.48$  km/s,  $z_0 = 0.9$  km,  $H_g = 0.8$  km,  $\gamma = 1.14 \times 10^{-2}$  km<sup>-1</sup>, and the thickness of the water layer  $H = 5$  km. These parameters are chosen to coincide with those used in our previous paper [5].

To obtain the spatial distribution of the acoustic intensity  $J(r, z)$  over the horizontal distance and in the depth of the water layer, we use the rigorous mode theory [18]. In numerical computations, we choose the emitted frequency  $f = 20$  Hz at which no extremum occurs in the dependence of  $R_{l,l+1}$  (4) on  $l$  (Fig. 1a). Then, we obtain adequate values for the quantity

$R_g(l, l + 1; l + 1, l + 2)$  (3) (Fig. 1b). In addition, we specify the source depth  $z_s = 200$  m in order to satisfy the condition of the excitation of a single mode beam that is not a weakly divergent one. If the product of the amplitudes of adjacent modes  $B_{l,l+1}$  is plotted versus their number  $l$  for this beam, there appears a pronounced maximum at  $z = z_s$  (Fig. 2).

From the numerical calculations illustrated by Figs. 1b and 2, the following preliminary conclusions can be drawn. First, for the mode beam that is formed by the refracted and surface-interacting modes ( $1 \leq l \leq 22$ ) and predominates in its intensity, one can expect the most pronounced diffraction focusing with the values of the spatial period within a relatively narrow interval:

$$4 \times 10^3 \leq R_g(l, l + 1; l + 1, l + 2) < 4.2 \times 10^3 \text{ km.}$$

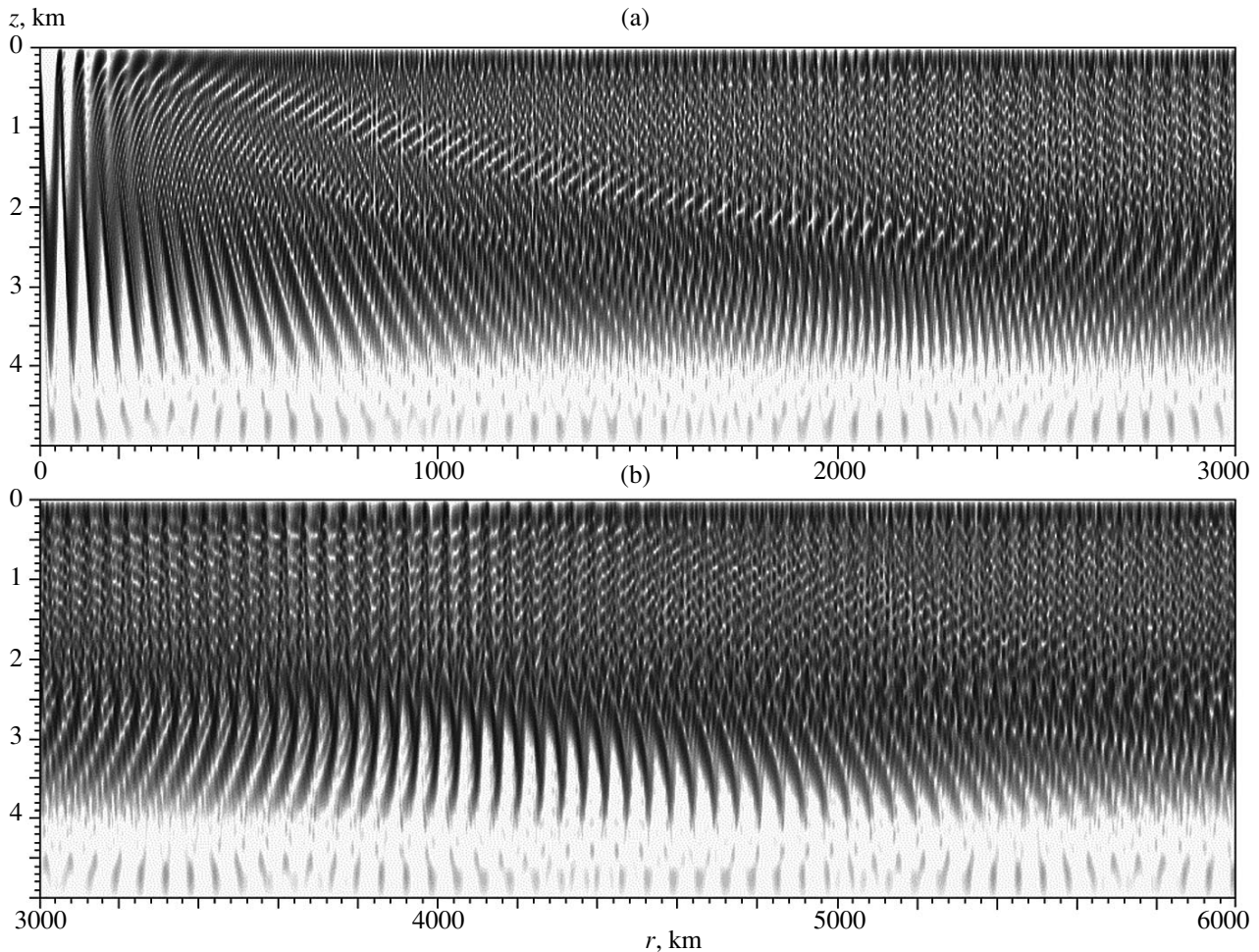


**Fig. 3.** Spatial distribution of the normalized sound field intensity  $J_0(r, z)$  in the horizontal distance  $r$  and depth  $z$ . Density-type record with the dynamic range 26 dB. Spatial domains: (a)  $0 \leq r \leq 3 \times 10^3$  km, (b)  $3 \times 10^3 \leq r \leq 6 \times 10^3$  km, (c)  $6 \times 10^3 \leq r \leq 9 \times 10^3$  km, and (d)  $9 \times 10^3 \leq r \leq 12 \times 10^3$  km;  $z_s = 200$  m;  $f = 20$  Hz.

These values correspond to pairs of the adjacent modes with the numbers  $12 \leq l \leq 16$ . Second, for the mode beam formed by the surface-interacting modes ( $23 \leq l \leq 28$ ), the diffraction focusing should be most pronounced with the spatial period  $R_g(l, l+1; l+1, l+2) \approx 620$  km that corresponds to the adjacent pairs of modes with  $l = 27$ .

The above considerations are confirmed by Fig. 3 that presents the numerically computed spatial distributions of the sound field intensity  $J_0(r, z) = rJ(r, z)$  normalized to the cylindrical spread of the wave front. According to the figure, the diffraction focusing of the intensity-predominant mode beam gives rise to zones of acoustic shadow at the distances  $r \approx (4-4.2) \times 10^3$  km in the first domain ( $m = 1$ ) and  $r \approx (8-8.4) \times 10^3$  km in the second one ( $m = 2$ ). These zones are rather narrow ( $\Delta r \approx 5$  km) near the surface ( $0 \leq z \leq z_s$ ) and relatively wide ( $\Delta r \approx 20$  km) at the depths  $3 \text{ km} < z < 4$  km. Naturally, the width  $\Delta r$  of the shadow zones decreases as the number  $m$  of the focusing domain increases, and

they become nearly undetectable already starting from  $m = 2$ .

To conclude, we formulate the main results of this study; these results seem to be important for modeling the super-long-range sound transmission in the ocean [19, 21].

1. For the simplest model of a deep-water oceanic waveguide with the underwater sound channel that is open to the surface, has an acoustically transparent bottom, and is approximated by a bilinear depth dependence of the squared refractive index, the WKB approximation is used to determine the main features of the spatial domains of the sound field focusing. On this basis, the optimum conditions for the observation of the diffraction focusing of the mode beams are formulated.

2. In view of the conclusions drawn from the approximate analysis, by using the exact mode theory, the numerical simulation is carried out for the process of the formation of the spatial distribution of the sound field intensity in both the depth and the horizontal dis-

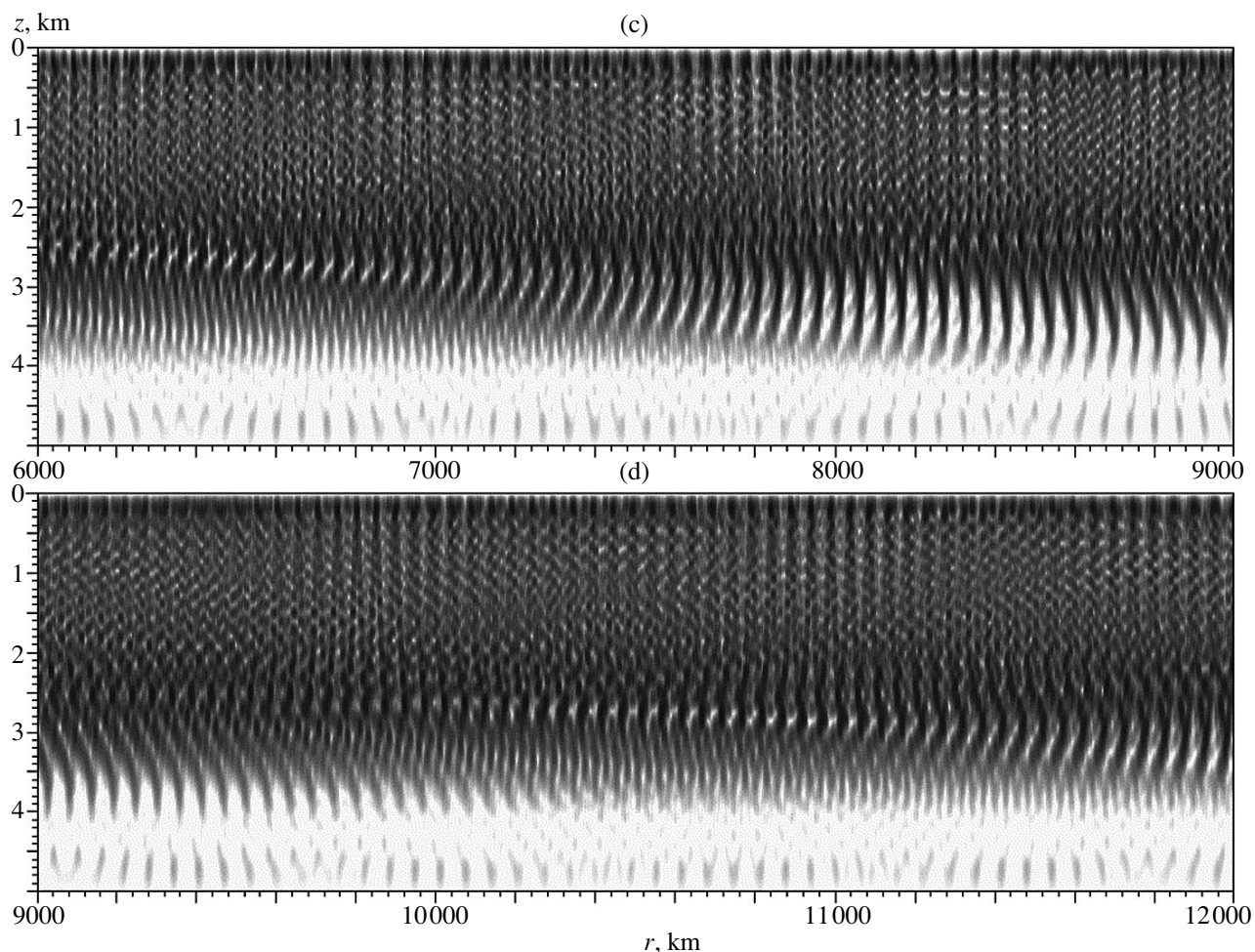


Fig. 3. (Contd.)

tance within a deep-ocean waveguide with the canonic sound speed profile. In an illustrative form, it is shown that the periodic rearrangement of the interference structure of the sound field along the path leads to a periodic diffraction focusing of the mode beams at certain distances.

#### ACKNOWLEDGMENTS

This work was supported by the Russian Foundation for Basic Research (project nos. 96-02-16116a and 98-02-16402) and by the Competition Center for Basic Natural Sciences (project no. 97-8.2-78).

#### REFERENCES

1. Yu. V. Petukhov, *Akust. Zh.* **37**, 585 (1991) [*Sov. Phys. Acoust.* **37**, 305 (1991)].
2. Yu. V. Petukhov, *Akust. Zh.* **38**, 917 (1992) [*Sov. Phys. Acoust.* **38**, 499 (1992)].
3. Yu. V. Petukhov, *Akust. Zh.* **42**, 688 (1996) [*Acoust. Phys.* **42**, 606 (1996)].
4. Yu. V. Petukhov, Preprint No. 443, NIRFI (Research Radiophysical Inst., Nizhni Novgorod, 1998); *Akust. Zh.* (in press) [*Acoust. Phys.* (in press)].
5. D. I. Abrosimov and Yu. V. Petukhov, *Akust. Zh.* **43**, 437 (1997) [*Acoust. Phys.* **43**, 373 (1997)].
6. R. F. Edgar, *Optica Acta* **16**, 281 (1969).
7. L. M. Brekhovskikh and Yu. P. Lysanov, *Fundamentals of Ocean Acoustics* (Gidrometeoizdat, Leningrad, 1982; Springer, Berlin, 1982).
8. N. C. Nicholas and H. Uberall, *J. Acoust. Soc. Am.* **44**, 1259 (1968).
9. N. C. Nicholas and H. Uberall, *J. Acoust. Soc. Am.* **48**, 745 (1970).
10. White DeWayne, *J. Acoust. Soc. Am.* **46**, 1318 (1969).
11. A. T. Semenov, *Akust. Zh.* **27**, 315 (1981) [*Sov. Phys. Acoust.* **27**, 174 (1981)].
12. Yu. V. Petukhov, *Akust. Zh.* **42**, 401 (1996) [*Acoust. Phys.* **42**, 352 (1996)].
13. J. W. Caruthers, A. I. Khil'ko, and I. P. Smirnov, in *The Formation of Acoustical Fields in Oceanic Waveguides. Coherence Phenomena*, Ed. by V. A. Zverev (Inst. of Applied Physics, Russian Academy of Sciences, Nizni Novgorod, 1997), pp. 71–113.

14. Yu. V. Petukhov, *Akust. Zh.* **41**, 807 (1995) [*Acoust. Phys.* **41**, 712 (1995)].
15. Yu. V. Petukhov, *Akust. Zh.* **40**, 111 (1994) [*Acoust. Phys.* **40**, 97 (1994)].
16. V. V. Goncharov and V. M. Kurtepov, *Akust. Zh.* **40**, 773 (1994) [*Acoust. Phys.* **40**, 685 (1994)].
17. W. H. Munk, *J. Acoust. Soc. Am.* **55**, 220 (1974).
18. A. V. Vagin and N. E. Mal'tsev, *Vopr. Sudostr., Ser. Akust.*, No. 9, 61 (1977).
19. K. Prada, J. L. Spiesberger, and E. Terray, *J. Acoust. Soc. Am.* **95**, 3654 (1994).
20. D. E. Norris, D. W. Merdes, and J. L. Spiesberger, *J. Acoust. Soc. Am.* **103**, 182 (1998).
21. K. D. Heaney and W. A. Kuperman, *J. Acoust. Soc. Am.* **104**, 2149 (1998).

*Translated by E.A. Kopyl*

# Study of the Spectral Inharmonicity of Musical Sound by the Algorithms of Pitch Extraction

A. Askenfelt\* and A. S. Galembo\*\*

\* *Department of Speech, Music and Hearing, Royal Institute of Technology, Stockholm, Sweden*

\*\* *Sechenov Institute of Evolution Physiology and Biochemistry, St. Petersburg, Russia*

*e-mail: galembo@comset.net*

Received February 15, 1999

**Abstract**—The algorithms of pitch extraction are widely used in the studies of signals and, specifically, speech signals for the determination of the fundamental frequency. From the previous studies performed by Galembo and the calculations and experiments described in this paper, it follows that these methods can be adapted for the analysis and evaluation of the factors which form the sound property called “pitch strength,” “pitch salience,” or “intonation clarity.” Although this property plays an important role in music, it is quite poorly investigated. One of the aforementioned factors is represented by the distributed spectral inharmonicity which is typical of sounds produced, e.g., by strings. This paper presents a method of visualization, evaluation, and measurement of the inharmonicity of the spectrum of a musical sound with the help of the well-known algorithms of pitch extraction, namely, the cepstrum and the harmonic product spectrum. © 2000 MAIK “*Nauka/Interperiodica*”.

## TERMS AND NOTIONS

### *Intonation Clarity and Spectral Inharmonicity*

The pitch of sound is of great importance in the perception and discrimination of acoustic signals and images. In speech, the main distinction of vowels from consonants is their periodicity and pitch. An ordered pitch variation forms the basis of music.

The interpretation of the phenomenon of pitch—acoustical, psychological, physiological, and even esthetical—is the subject of many scientific papers and books.

Much less attention is paid to the fact that real sounds can be classified not only into those with definite pitch and those without pitch; there are also many intermediate sound categories with the pitch feature being to one or another extent depressed by the presence of noise, inharmonic relations in the line spectrum, or transient processes that hinder the perception of pitch. Different authors characterize these sounds by “pitchiness” [1], “pitch strength” [2], “pitch salience,” “pitch prominence” [3], “intonation clarity,” or “pitch definiteness” [4].

By the standards of acoustics, the corresponding sound feature should be attributed to timbre; on the other hand, it is directly related to the perception of pitch. This sound feature has not been adequately studied, described, and terminologically defined in the literature; even less progress is observed in the development of methods for its evaluation and measurement.

However, the intonation clarity of sound plays an important role in music. Volodin [4] even proposed

some kind of an “indeterminacy principle” in the perception of music; he argued that almost every enhancement in the character of a musical sound is achieved at the expense of a reduction in its pitch definiteness.

An insufficient intonation clarity of sound produced by a musical instrument may lead to such defects of sound as “metal” bass tones of “glass” treble tones of a piano.

The latter instrument designed for universal musical applications always “tended” to cover the maximum possible pitch range. An obstacle for its extension was the deficiency of the intonation clarity in the extreme registers. The technical history of the piano—from five octaves at the time of Mozart to the modern eight octaves—was the history of overcoming this deficiency. This was possible, on the one hand, at the expense of the improvements in the materials and the instrument design and, on the other hand, at the expense of the development of music and its perception. The process continues to this day: for example, in the Imperial concert pianos produced by the Bösendorfer company, the bass register is extended by nine notes as compared to the conventional version. However, the obvious deficiency of the pitch feature in the additional sounds makes this novelty to be more a commercial success than a musical one.

Today, when we buy a piano, the intonation clarity of sounds in its extreme registers is one of the main criteria used to decide upon the quality of sound produced by the instrument.

Being a subjective parameter, the intonation clarity of sound depends on the characteristics of hearing and

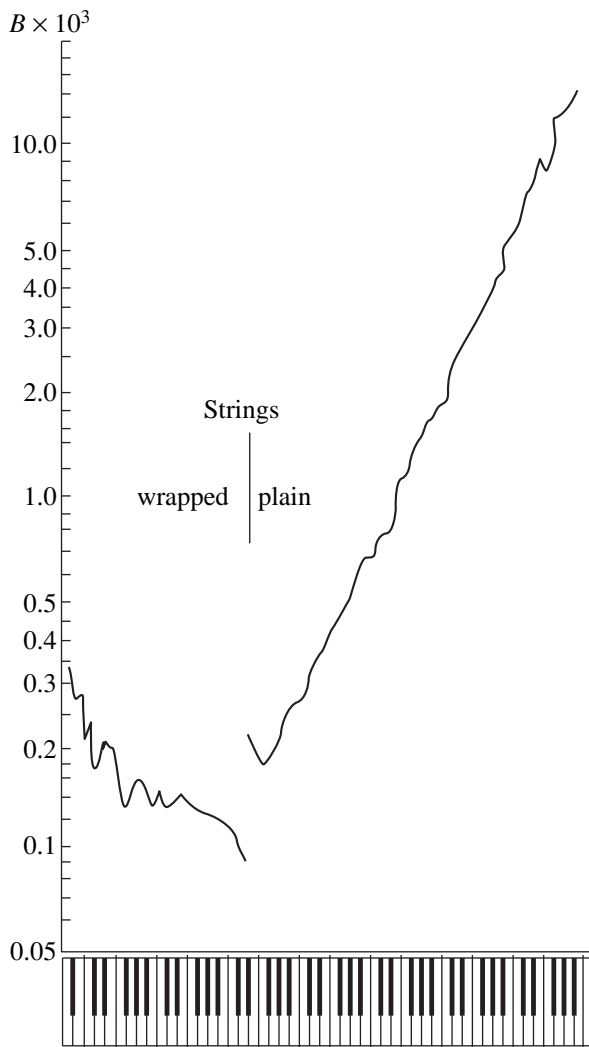


Fig. 1. Measured values of the inharmonicity coefficient for the strings of a Noktyurn upright piano [28].

the conditions of perception; at the same time, it is also determined by objective parameters of the sound signal. For example, in the treble sounds of a piano, the main factor causing the reduction in the intonation clarity is the accompanying noise, while, in the bass sounds whose spectrum may contain up to hundred and more overtones, the corresponding factor is their spectral inharmonicity.

The inharmonicity of the overtones of the strings of musical instruments has been much studied by physicists. The mechanism of this phenomenon is as follows: the presence of the flexural rigidity, which determines the difference between a real string and an ideal one, leads to a dispersion; as a result, transverse waves of different length propagate along the string with different velocities. Therefore, the overtones of higher orders have frequencies which progressively exceed those of a harmonic series.

The theory describing the inharmonicity of piano strings was developed by a number of authors [5–10]. The corresponding experimental measurements revealed the important role of spectral inharmonicity in the tuning of musical intervals [11, 12].

In several studies considering the inharmonicity of the sound spectrum from the viewpoint of the timbre perception [13–16], it was found that the inharmonicity not only affects the perception of the pseudostationary (attenuating) part of sound but also gives rise to the “slip of frequency” in the perception of its attack. The spectral inharmonicity is not an *a priori* detrimental feature of a piano sound; to an optimum degree, it is necessary, because it makes the sound variable and lively [13]. However, a too high inharmonicity unfavorably affects the bass sounds of a musical instrument.

Therefore, in the modern manuals describing the calculation of the string scales of a piano, it is recommended to take into account and optimize the spectral inharmonicity of strings [17].

According to the results of the aforementioned studies (both theoretical and experimental ones), the distributed spectral inharmonicity (subsequently referred to as inharmonicity) of string vibrations is adequately described by the formula

$$f_n = n f_0 (1 + n^2 B)^{0.5}. \quad (1)$$

Here,  $f_n$  is the frequency of the  $n$ th mode of natural vibrations,  $f_0$  is the fundamental frequency of an ideally flexible string, and  $B$  is the inharmonicity coefficient. For a plain string, the latter quantity depends on the parameters of the string wire:  $B = \pi^3 Y r^3 / 64 T L^2$ , where  $Y$  is Young’s modulus of the wire material,  $r$  is the radius of its cross-section,  $T$  is the string tension, and  $L$  is the string length.

The minimum value of the inharmonicity coefficient characterizing the vibration spectrum of a piano string falls in the middle of the piano scale, and the inharmonicity increases toward the scale ends (Fig. 1). The maximum value of the inharmonicity coefficient occurs in the treble (shortest) strings. However, the inharmonicity plays no significant role in the treble sounds, because the spectra of these sounds are poor in overtones. The maximum effect of inharmonicity on the timbre is observed in the bass sounds.

Although the sounds with harmonic and inharmonic spectra can be clearly distinguished by ear, the inharmonicity that occurs within the limits characteristic of real strings of musical instruments cannot be revealed and estimated by a spectrogram or oscillogram of a real sound of a musical instrument: the inharmonicity is a hidden parameter. In real musical sounds, the inharmonicity is usually detected and measured by a complicated procedure that includes a manual study of the spectrum, namely, the intuitive detection of overtones among the partial tones of other origin; the measurement and comparison of frequencies in several pairs of overtones; the calculation of the inharmonicity coeffi-

cient in each pair by formula (1); and the averaging of the results [18].

Despite the important role of inharmonicity in the formation of the timbres of musical sounds (the inharmonicity of spectra is characteristic of not only string instruments but also other types of instruments) and the frequent use of this parameter by researchers, the procedure of the detection and measurement of the inharmonicity of spectra remained for years at the same level as it was at the beginning of the studies of this phenomenon.

#### *Pitch Extraction: Cepstrum and Harmonic Product Spectrum*

A considerable part of algorithms developed in the last few decades for digital processing of sound signals is represented by the algorithms of pitch extraction, i.e., the algorithms for the determination of the fundamental frequency and the dynamics of its variation. Today, these algorithms are improved and adapted by researchers for different specific applications: they are widely used in echo sounding, technical diagnostics of machines, and analysis of speech signals, i.e., in all cases that require an automatic selection of a periodic signal from the sound flow and the determination of its fundamental frequency. Digital methods are most extensively used in the analysis of speech signals. The exact determination of the fundamental frequency is important for such purposes as speech synthesis, speech discrimination, and speaker identification [19].

The methods of pitch extraction from nonstationary signals are based on the analysis of the temporal or spectral functions of short-time signal segments. To make the solution of the problem more efficient, special operations of signal transformation are introduced in the algorithms. These transformations, e.g., frequency or amplitude limitations or scale transformations, make the signal periodicity more pronounced.

Earlier, the methods of pitch extraction were not used for studying and evaluating musical sounds. Primitive methods of the determination of the sound position in the musical scale can be found only in the publications on automatic music notation [20, 21].

In this paper, we use the modifications of two well-known algorithms of pitch extraction. The physical foundations of these algorithms are briefly described below.

Cepstrum is one of the most popular algorithms of pitch extraction based on the analysis of the periodicity of the sound spectrum envelope. The cepstral analysis developed in the 1960s for echo sounding has found a wide utility in the analysis of speech signals. The cepstrum is determined as the power spectrum of the logarithm of the power spectrum. Its mathematical formulation is as follows:

$$C(\tau) = |F[\log|F(\omega)|^2]|^2,$$

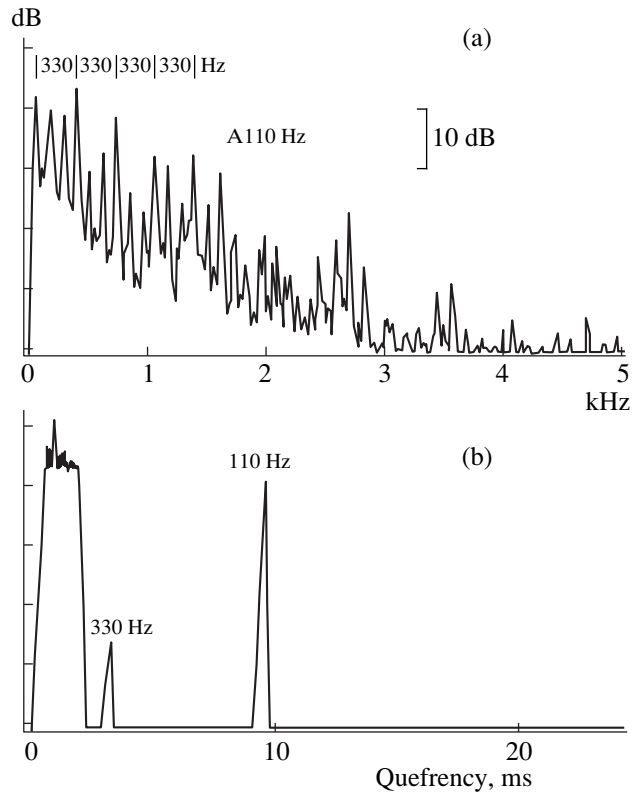


**Fig. 2.** (a) Spectrum envelope and (b) cepstrum of the sound **A** of a piano [28].

where  $F$  is the Fourier transform.

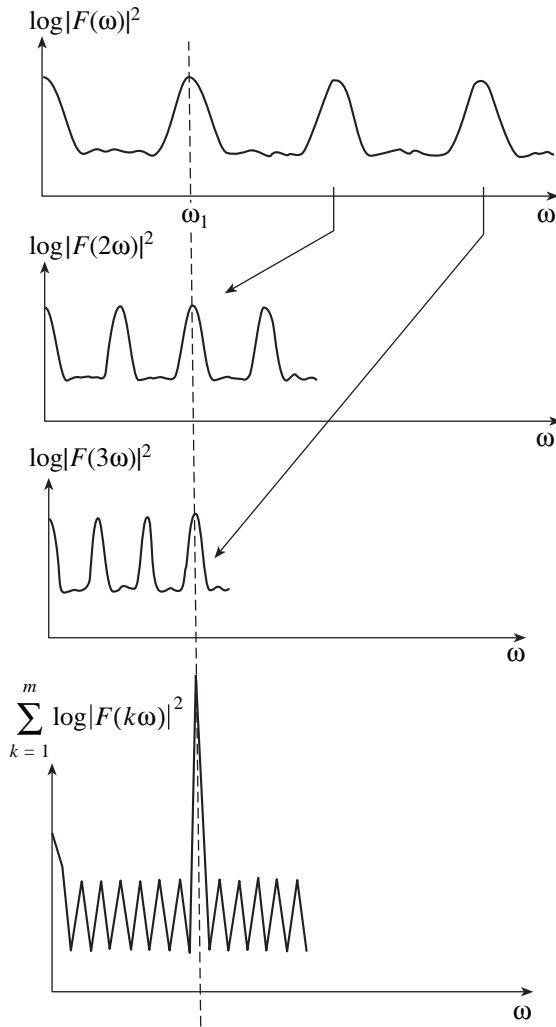
The term *cepstrum* is formed by a free inversion of the word *spectrum*. Similarly, the periodicity of the spectral envelope in the frequency domain is characterized by a “repiod,” and small repiods correspond to large “quefrequencies” (the quefrequency is the independent variable of the cepstrum, and this variable is measured in time units) [22].

Figure 2 illustrates the foregoing definitions; it schematically depicts the spectrum and the cepstrum of the sound **A** of a piano (to denote the sounds, we use the European notation). Both characteristics were obtained by a Bruel & Kjer 3348 spectrum analyzer.

The algorithm named “the harmonic product spectrum” (HPS) was developed in the 1960s on the basis of the ideas put forward by Miller [23], Schroeder [24], and Noll [25]. However, judging from the literature, it was not used for the pitch extraction.

The idea underlying the HPS algorithm is based on the fact that, since the frequencies of the harmonics of a periodic signal are multiples of its fundamental frequency, the information on the fundamental frequency can be amplified by compressing the sound spectrum along the frequency axis by a factor of 1, 2, 3, 4, ...,  $m$  and then combining the obtained versions as shown in Fig. 3 (in a simplified form). The resulting function will contain an increased (compared with the component

JUSTIFICATION OF THE METHOD



**Fig. 3.** Schematic diagram of the formation of the harmonic product spectrum after A.M. Noll [25].

versions) peak at the fundamental frequency of sound. Mathematically, this kind of signal processing is described by the formula

$$\log \pi(\omega) = \sum_{k=1}^m \log |F(k\omega)|^2. \quad (2)$$

Taking an antilogarithm of this formula, we obtain the expression that explains why this transformation was called the harmonic product spectrum:

$$\pi_{\text{HPS}} = \prod_{\ddot{v}=1}^{\ddot{v}} |F(k\omega)|^2.$$

The quantity  $m$  is called the order of the HPS, and it is equal to the number of the spectrum compressions or, which is the same, the number of harmonics involved in the formation of the pitch peak of the HPS.

The method of analyzing the spectral inharmonicity of sound is developed on the basis of the general idea of applying the algorithms of pitch extraction to the studies of the intonation clarity of musical instruments. This idea was experimentally justified by Galembo in analyzing the intonation clarity of treble sounds of a piano in the late 1970s [26–28]. The idea originates from the assumption that, because the algorithms of pitch extraction are directed at the elimination of the objective noise suppressing the pitch feature, the results of pitch extraction must contain the information on the eliminated noise, and, hence, they can be adapted for the evaluation of the factors affecting the intonation clarity of sound.

This explains why in this paper we use the term *pitch extraction* instead of the term commonly used in the Russian scientific literature, “selection of the fundamental tone.” The inharmonicity is a spectrum parameter determining the timbre; hence, the evaluation of the inharmonicity is a more general problem than the determination of the fundamental tone, and therefore it requires a more general term.<sup>1</sup>

Let us show that the cepstrum and the harmonic product spectrum of a musical sound must contain the information on the degree of its spectral inharmonicity.

Since the envelope of the spectrum of a complex periodic sound is also periodic, the theoretical result of the cepstral analysis of a periodic (harmonic) sound is a delta-function whose coordinate on the quefrequency axis is equal to the period of the fundamental tone of this sound.

Thus, the cepstral analysis allows one to classify the sounds into periodic ones (e.g., vowels) forming such a delta-function and aperiodic ones (e.g., consonants) forming no delta-function.

According to formula (1), an inharmonic spectrum of sound is characterized by a progressive increase in the frequency shift between the neighboring overtones. In the cepstral analysis of periodic signals, this shift is called the repoid (it is convenient to retain this term also for an inharmonic sound, although in this case the repoid is no more a constant value: it varies in some range of values). The increase in the repoid occurs from its minimum value at the beginning of the spectrum

$$f_L = f_1 = f_0(1 + B)^{0.5} \quad (4)$$

<sup>1</sup> An interesting way to this idea, almost at the level of a play on words, can be found from the well-known scientific definition according to which the timbre of sound includes all sound characteristics unrelated to its loudness, duration, and pitch. This means that if the pitch is extracted from two sounds of equal loudness and duration, these sounds will differ only by their timbres.

to its maximum value attained between the last two partial tones

$$f_H = f_n - f_{n-1} = f_0 \{ n(1 + n^2 B)^{0.5} - (n-1)[1 + (n-1)^2 B]^{0.5} \}. \quad (5)$$

Then, the relative (normalized to the fundamental frequency  $f_0$  of an ideal string) range of this quantity is expressed as

$$\frac{f_L - f_H}{f_0} = n(1 + n^2 B)^{0.5} - (n-1)[1 + (n-1)^2 B]^{0.5} - (1 + B)^{0.5}. \quad (6)$$

This result suggests that the degree of periodicity of the spectrum of such a sound will be represented in the cepstrum by a broad peak or a set of peaks rather than by a delta-function, and these peaks will occupy the pitch region from the lower quefrequency  $\tau_L = 1/f_H$  to the higher one  $\tau_H = 1/f_L$ .

The relative (normalized to the period of an ideal string,  $\tau_0 = 1/f_0$ ) width of this region should have the form

$$\frac{\tau_H - \tau_L}{\tau_0} = \frac{f_0(f_H - f_L)}{f_L f_H} = \frac{n(1 + n^2 B)^{0.5} - (n-1)[1 + (n-1)^2 B]^{0.5} - (1 + B)^{0.5}}{(1 + B)^{0.5} \{ n(1 + n^2 B)^{0.5} - (n-1)[1 + (n-1)^2 B]^{0.5} \}}.$$

We note that this width depends on both the inharmonicity coefficient and the number of tone components of the spectrum subjected to the cepstral analysis. One of the curves in Fig. 4 shows this calculated width as a function of the inharmonicity coefficient for a thirty-component sound. The curve demonstrates that the width of the pitch peak-region of the cepstrum increases steadily with increasing inharmonicity coefficient.

The intuitive idea to use the HPS for the evaluation of the degree of inharmonicity of a musical sound is based on the logical conclusion that the incoherence of the overtones in the combined compressed spectrum versions must lead to the formation of a pitch peak-region of the HPS, and the width of this region will be uniquely related to the inharmonicity coefficient of sound: the greater the inharmonicity coefficient  $B$  and the number  $m$  of the spectrum tone components involved in the calculation of the HPS, the greater the width of the pitch peak-region. If we proceed from formulas (1) and (2), the lower ( $f_L$ ) and higher ( $f_H$ ) boundaries of the pitch peak-region of the HPS will be calculated as follows:

$$f_L = f_1 = f_0(1 + B)^{0.5}, \quad (7)$$

$$f_H = f_0(1 + m^2 B)^{0.5}. \quad (8)$$

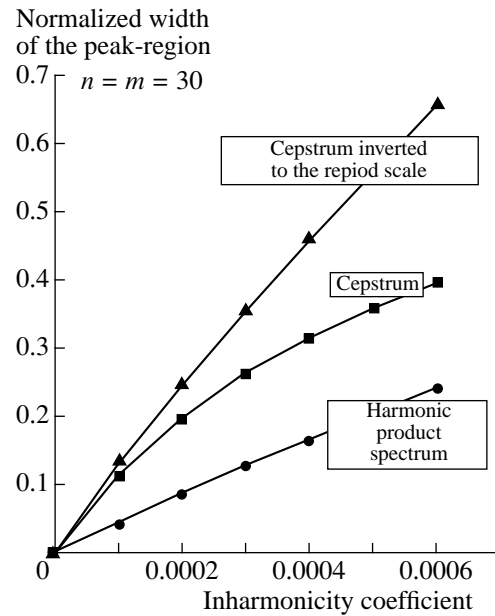


Fig. 4. Dependence of the relative width of the pitch peak-region on the inharmonicity coefficient for a thirty-component musical sound.

Thus, the width ( $W_{HPS}$ ) of the pitch peak in terms of the fractions of the fundamental frequency of sound should depend on  $B$  and  $m$  according to the formula:

$$W_{HPS} = (1 + m^2 B)^{0.5} - (1 + B)^{0.5}. \quad (9)$$

This dependence for  $m = 30$  is also presented in Fig. 4.

### SOUND MATERIAL

We studied the bass sounds  $A_2$ ,  $E_1$ ,  $A_1$ ,  $E$ , and  $A$  (we use the European notation where  $a_1$  corresponds to 440 Hz) of five pianos of different structure and, hence, with different degrees of inharmonicity of overtones. The pianos were a Steinway D concert piano of length 274 cm, a Steinway C salon piano of length 229 cm, two modern Nordiska upright pianos of height 110 cm, and one Straud upright piano of height 130 cm made in the early twentieth century.

The inharmonicity of all listed sounds was preliminarily measured by the following procedure based on the conventional principles:

—The sound under study was represented by its digital record on a professional Sony DAT TCD D10 tape recorder.

—We studied the power spectrum of the sound by means of an HP 356-2A dynamical signal analyzer.

—The spectral components representing the overtones of the fundamental tone of transverse string vibrations were subjectively identified by the distance between the spectral components on the linear frequency scale.

**Table 1.** Sound parameters measured by the conventional procedure for different pianos

Fundamental frequency (Hz)					
Note	Stein. D	Stein. C	Nord. 1	Nord. 2	Straud
A <sub>2</sub>	27.25	26.92	26.99	27.4	26.54
E <sub>1</sub>	40.97	40.65	41	41.1	40.54
A <sub>1</sub>	54.75	54.14	54.67	55.02	54.16
E	82.31	81.55	82.2	82.39	81.41
A	109.55	108.52	109.83	110.27	108.8
Inharmonicity coefficient					
Note	Stein. D	Stein. C	Nord. 1	Nord. 2	Straud
A <sub>2</sub>	0.00016	0.00019	0.000345	0.000346	0.000568
E <sub>1</sub>	0.0000654	0.0000906	0.000207	0.000202	0.000263
A <sub>1</sub>	0.0000568	0.0000923	0.00016	0.000153	0.000214
E	0.0000684	0.0001144	0.000142	0.000133	0.000235
A	0.0000849	0.0001306	0.000154	0.000141	0.000202

**Table 2.** Notation and parameters of synthesized musical sounds

No. of sound	File name	$f_0$ (Hz)	$B$	No. of sound	File name	$f_0$ (Hz)	$B$
1	b00f27	27	0	21	b22f54	54.5	0.00022
2	b10f27	27	0.0001	22	b30f54	54.5	0.0003
3	b16f27	27	0.00016	23	b40f54	54.5	0.0004
4	b20f27	27	0.0002	24	b50f54	54.5	0.0005
5	b30f27	27	0.0003	25	b00f82	82.2	0
6	b40f27	27	0.0004	26	b07f82	82.2	0.00007
7	b50f27	27	0.0005	27	b10f82	82.2	0.0001
8	b58f27	27	0.00058	28	b20f82	82.2	0.0002
9	b00f41	41	0	29	b22f82	82.2	0.00022
10	b07f41	41	0.000067	30	b30f82	82.2	0.0003
11	b10f41	41	0.0001	31	b40f82	82.2	0.0004
12	b20f41	41	0.0002	32	b50f82	82.2	0.0005
13	b26f41	41	0.00026	33	b00f110	110	0
14	b30f41	41	0.0003	34	b05f110	110	0.00005
15	b40f41	41	0.0004	35	b08f109	109.6	0.000085
16	b50f41	41	0.0005	36	b10f110	110	0.0001
17	b00f54	54.5	0	37	b15f110	110	0.00015
18	b06f54	54.5	0.000059	38	b20f110	110	0.0002
19	b10f54	54.5	0.0001	39	b22f108	108.6	0.00022
20	b20f54	54.5	0.0002				

—We measured the frequencies  $\varphi_n$  of the spectral components visually determined as the fundamental tone of the sound and its overtones.

—Using formula (1), we determined the approximate value of the inharmonicity coefficient

$$B_{\text{approx}} = [(\varphi_n/\varphi_1 n^2) - 1]/n^2.$$

—We calculated the sum of the square deviations of all measured values of  $\varphi_n$  from the corre-

sponding values of  $f_n$  obtained by formula (1) at  $f_0 \equiv \varphi_1$  and  $B \equiv B_{\text{approx}}$ :

$$\Phi = \sum [nf_0(1 + n^2 B)^{0.5} - \varphi_n]^2.$$

Varying the parameters  $f_0$  and  $B$ , we determined their values minimizing the function  $\Phi$ . These values were considered as the result of the measurements; they are presented in Table 1.

We decided that these results obtained for real sounds with spectral compositions depending on many neglected factors are too rough to serve as a basis for estimating the accuracy of the new methods of measurement.

Therefore, we synthesized musical sounds with the spectra exactly corresponding to formula (1) with different pitch and inharmonicity.

These sounds were composed of thirty frequency components of equal amplitude, and their fundamental frequencies and inharmonicity coefficients were selected so as to uniformly cover the range characteristic of the piano bass register (Table 2).

### CEPSTRAL ANALYSIS OF MUSICAL SOUNDS

The preliminary series of experiments showed that some parameters of the algorithm of the cepstral transformation should be optimized in order to increase the efficiency of the cepstrum as a graphic representation of inharmonicity.

First, to obtain maximum amplitudes and well-defined boundaries of the pitch peak-region of the cepstrum, it is necessary to achieve the maximum possible resolution in frequency for the spectrum. Second, the width of the spectrum involved in the second Fourier transform should be not too large in order to restrict (as far as possible) the effect of the specific features of the spectral envelope (especially, its decline at high frequencies) on the formation of the contour of the pitch peak-region of the cepstrum.

Figure 5 displays the result of the cepstral analysis of synthesized thirty-component sounds  $A_2$  with different degrees of inharmonicity. The dashed vertical lines show the calculated positions of the boundaries of the pitch peak-region according to formulas (4) and (5).

The cepstra of real bass sounds  $A_2$  of five aforementioned pianos are shown in Fig. 6. The shaded regions in the upper parts of the graphs, near the line of the calculated upper quefrequency, indicate the limits within which the fundamental frequency of the sound under study was subjectively identified by experienced tuners relative to the harmonic sound produced by a signal generator. We note that, for each sound with a distributed spectral inharmonicity, the pitch was subjectively attributed to a frequency band. The illustrations presented above show that the cepstral representation of a sound signal contains the information on the degree of the spectral inharmonicity of sound. The information is contained in the value of the width of the pitch peak-region, and this value is in a quantitative agreement with the theoretical calculations.

### HARMONIC PRODUCT SPECTRUM

The incoherence of the combined compressed spectrum versions provides the basis for the theoretical estimate of the inharmonicity through the HPS; on the

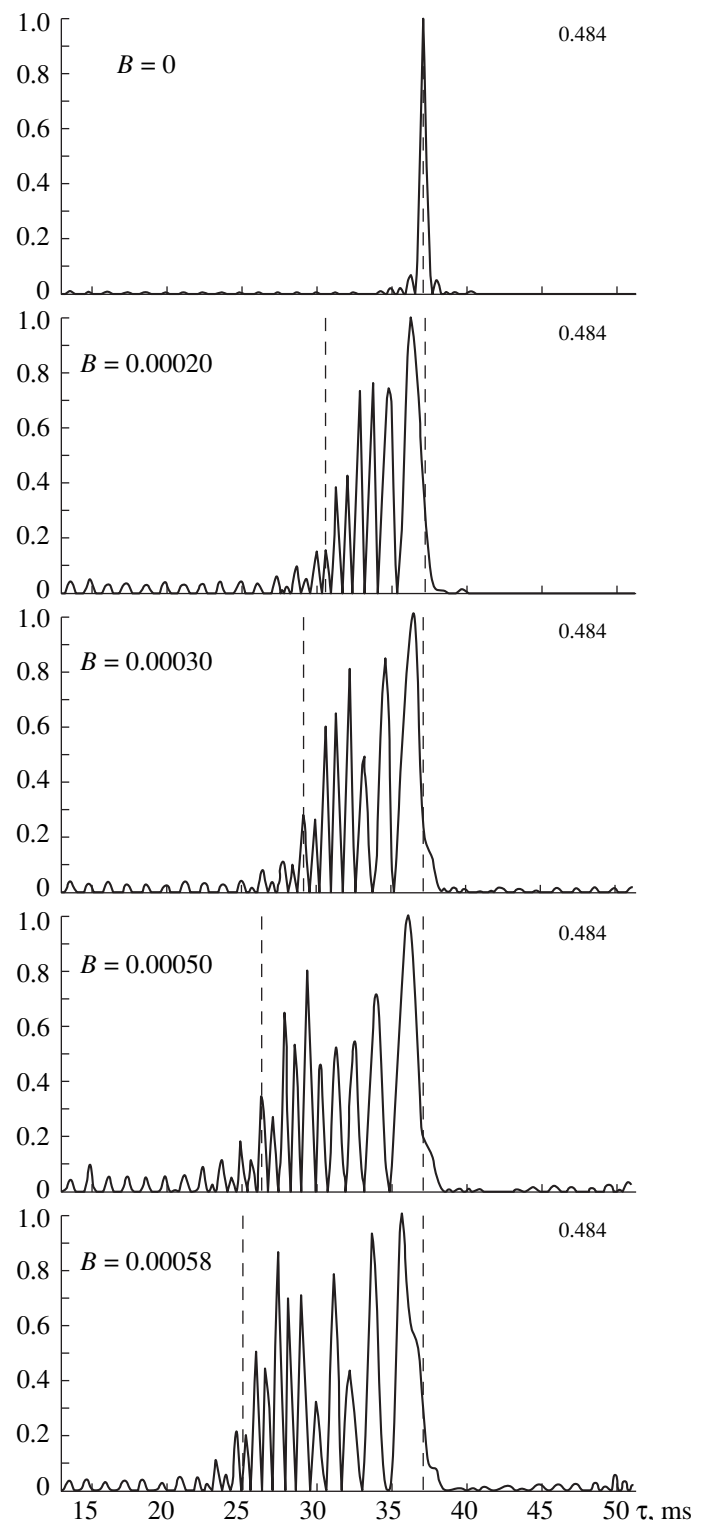
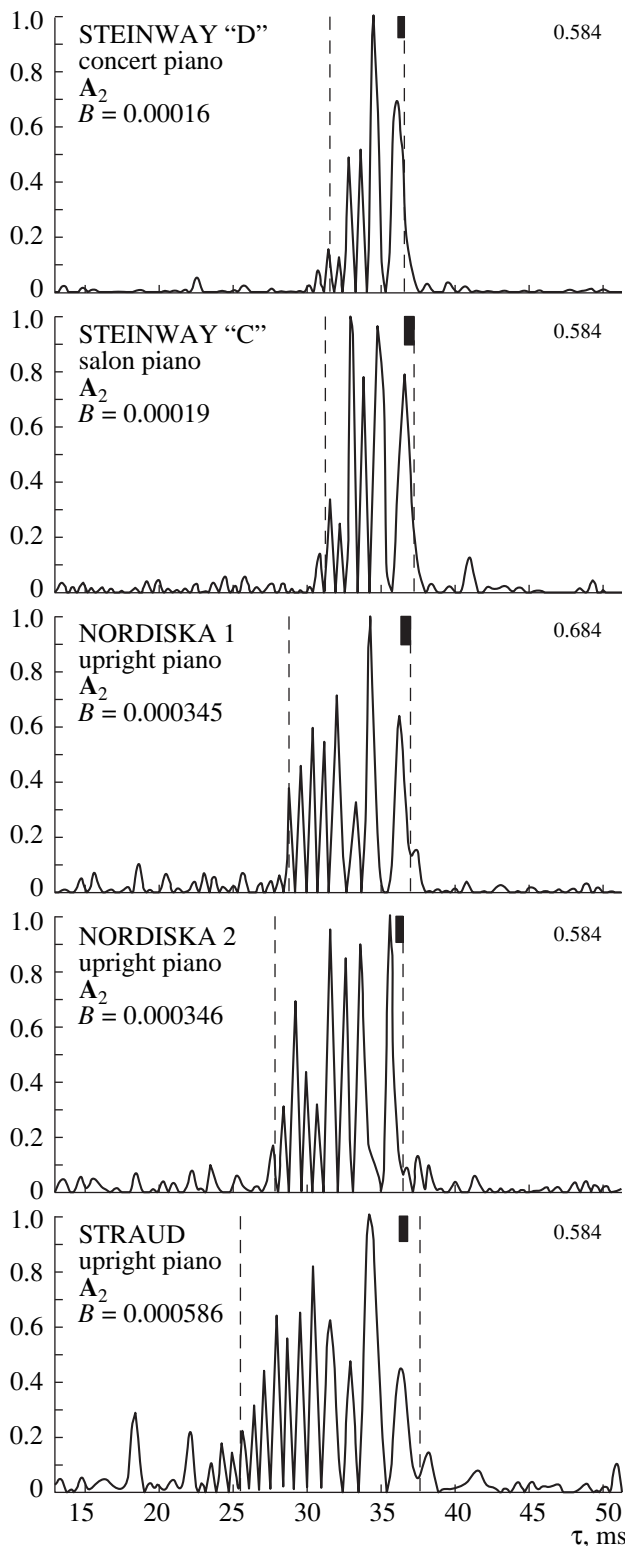


Fig. 5. Cepstra of synthesized sounds  $A_2$  ( $f_0 = 27.5$  Hz) of different inharmonicity.

other hand, it contributes to the suppression of the sought-for information in the resulting spectrum. This effect is illustrated by Fig. 7 showing the theoretical frequency filling of the pitch peak-region of the HPS



**Fig. 6.** Cepstra of sounds  $A_2$  ( $f_0 \approx 27.5$  Hz) of different pianos.

for sounds with zero, low, and high spectral inharmonicities.

Each plot shows the values of the relative (normalized to  $f_0$ ) central frequencies of overtones in the com-

pressed spectrum versions for different values of the spectrum compression coefficient  $k$ . In the HPS of order  $m$ , components of all frequencies below the ordinate  $k = m$  will be present. The frequency band of the pitch peak-region is enclosed in a rectangle. The plot also shows the effect of the total number  $n$  of pitch components (the fundamental tone and the overtones) of the signal under study up to the value  $n = 30$  on the "prominence" of the pitch peak-region.

First, with increasing inharmonicity of the signal, the peak-regions of the HPS expand, their boundaries approach those of other regions, and finally the peak-regions overlap. This behavior is illustrated by Figs. 7b and 7c corresponding to sounds with different degrees of inharmonicity. The overlapping can be eliminated by restricting the number of combined versions that form the HPS. For example, from Fig. 7c, one can see that, for the given inharmonicity coefficient, the pitch peak-region does not overlap with the neighboring ones at  $m = 15$ – $20$ . However, the value of  $m$  should not be too small, because at small  $m$  the inharmonicity will be represented with a low resolution.

Second, the incoherence of the combined versions of inharmonic spectra reduces the efficiency of the summation of the spectral densities. Theoretically, ideal inharmonic line spectra are unsuitable for the evaluation of the fundamental frequency and the inharmonicity from the HPS. In reality, such estimates are possible, because the fundamental tone and the overtones are represented as spectral bands of finite width rather than ideal lines. Hence, in this case, a reasonable reduction of the resolution in frequency may be appropriate in the spectral analysis of sound.

An example of the application of the HPS algorithm to synthesized bass sounds of different inharmonicity with  $m = 18$  is shown in Fig. 8.

For comparison, Fig. 9 presents the HPS of the sound **A** produced by the Steinway concert piano ( $B = 0.0001$ ) and the Straud upright piano ( $B = 0.00016$ ).

The boundaries of the pitch peak-region of the HPS were calculated for each sound by formulas (7) and (8). These boundaries are shown by vertical lines at the top of the graph.

The results presented above testify that the HPS carries the information on the inharmonicity of a musical sound; this information is contained in the width of the pitch peak-region, and the value of this width well agrees with the theoretical calculations.

#### COMPARISON OF THE METHODS AND THE PROSPECTS FOR THEIR IMPROVEMENT

The analysis of the results of our measurements allows us to make the following conclusions concerning the comparison of the two proposed methods for the evaluation of the inharmonicity of a musical sound:

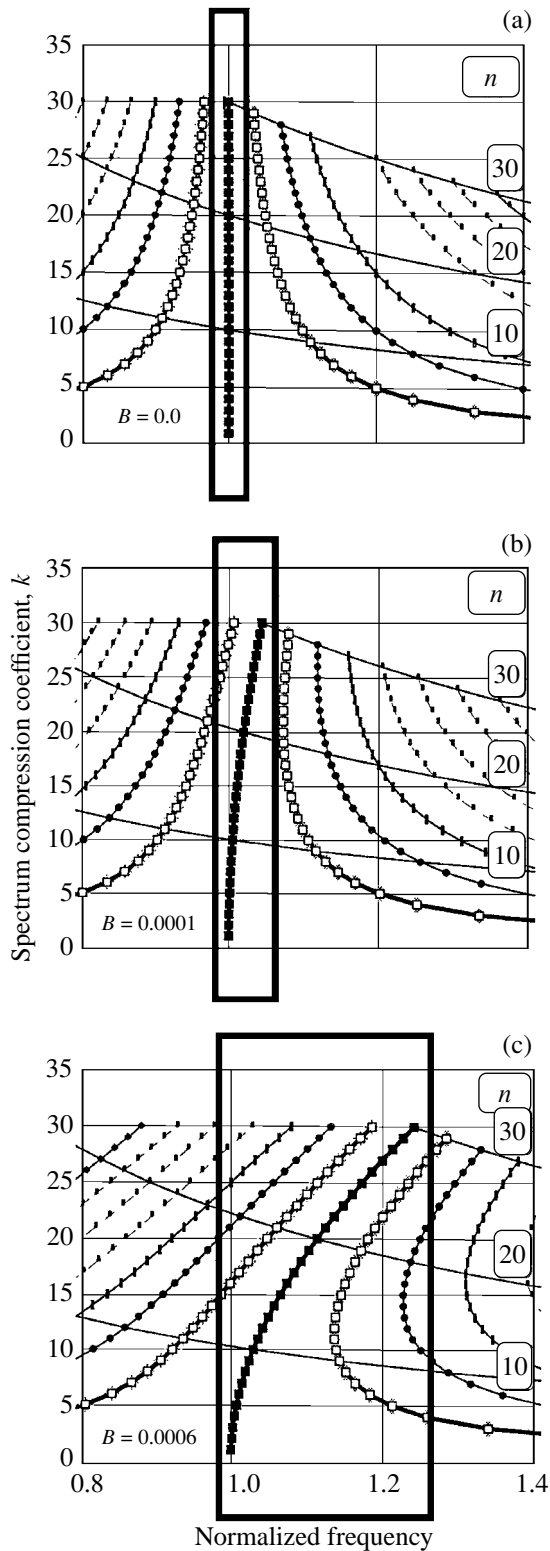


**Fig. 7.** Limitation of the possibility of selecting the pitch peak-region of the HPS for signals with (a) a harmonic spectrum ( $B = 0$ ), (b) a low inharmonicity ( $B = 0.0001$ ), and (c) a high inharmonicity ( $B = 0.0006$ ).

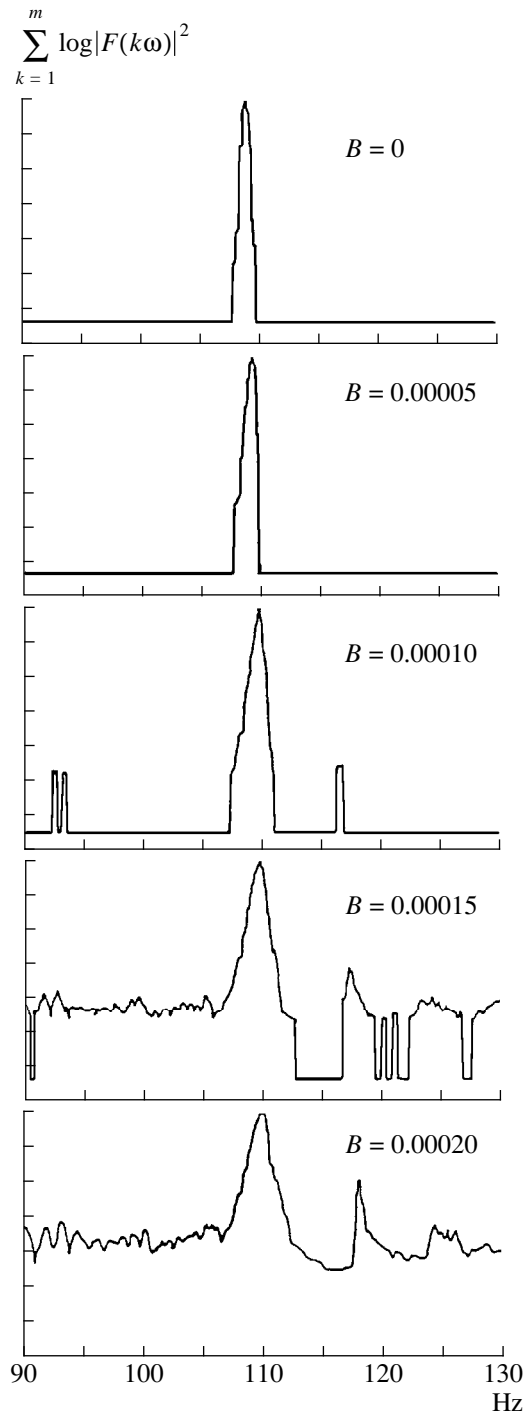


**Fig. 8.** Harmonic product spectrum of synthesized sounds A ( $f_0 = 110$  Hz) of different inharmonicity.

(1) From the viewpoint of the resolution in the inharmonicity coefficient, the most promising method is the representation of the inharmonicity by a cepstrum inverted into the repiod scale. In this representation, the dependence of the width of the pitch peak-region on the inharmonicity coefficient is close to a linear one (see Fig. 4).

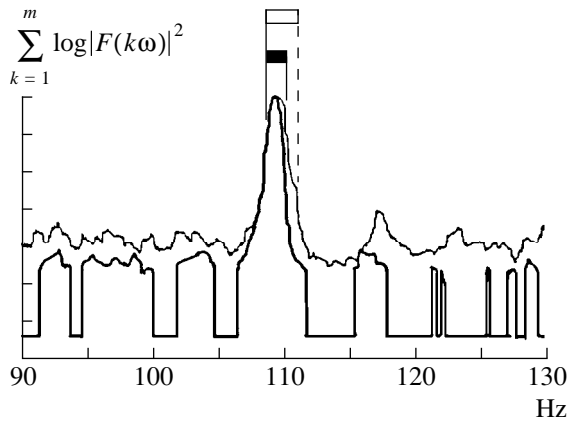


**Fig. 9.** Harmonic product spectrum of sounds A ( $f_0 = 110$  Hz) of the concert piano (thick line) and the Straud upright piano (thin line). The horizontal bars at the top correspond to the calculations by formula (6).

(2) An obstacle to a successful application of the cepstral analysis of inharmonicity, as well as to the analysis based on the HPS, is the effect of the envelope of the signal spectrum on the envelope of the pitch peak-region. Since the envelope of the spectrum of a real musical sound may vary in wide limits, the relief of the lower boundary of the pitch quefrequency zone of the cepstrum, as well as the relief of the upper boundary of the pitch peak-region of the HPS, may be quite unpredictable. This fact hinders the determination of the exact position of the corresponding boundary and, hence, reduces the accuracy of the inharmonicity estimate. The effect of this disadvantage can be reduced by introducing a special normalization or a limitation of the amplitudes of spectral components in the algorithm of sound signal processing. In this case, the application of a modified cepstrum—a clipstrum—seems to be promising.

(3) The disadvantage of the cepstral analysis of inharmonicity lies in the fact that equal widths of the spectra involved in the measurement of the cepstra of sounds of different inharmonicity do not automatically mean the presence of equal numbers of overtones. Therefore, although this difference usually does not exceed two overtones, the discrimination between large values of inharmonicity coefficients may be inaccurate. The HPS algorithm is free of this disadvantage. In this algorithm, the number of the combined spectrum versions is automatically equal to the number of spectral components participating in the formation of the pitch peak-region; this fact provides a fundamental possibility to directly transform the frequency scale of the HPS to the inharmonicity coefficient scale.

#### INHARMONICITY MEASUREMENTS USING THE CEPSTRUM AND THE HPS

We have shown that the cepstrum and the HPS are convenient means for the illustration and comparative

visual evaluation of the inharmonicity of musical sounds.

Since the width of the pitch zone of both the cepstrum and the HPS fits well into the calculated boundaries of this zone, the most simple method of measurement should consist of measuring this width and calculating the quantity  $B$  by using formulas (6) and (9). However, with the aforementioned limitations of the methods and the complexity of the spectral envelopes of real musical sounds, it is difficult to achieve a high degree of accuracy in measuring the inharmonicity coefficient, especially, in the region of its large values, by applying such a simple method.

Therefore, we developed an algorithm of digital signal processing which allowed us to directly calculate the inharmonicity coefficient through the cepstrum or the HPS by using the method of the search for the extremum of a function by the parameter variation.

In our case, the method consists of the search for the maximum of the level of the pitch peak-region of the cepstrum or the HPS by varying the inharmonicity of the signal. In this procedure, we use the fact that the maximum height of the pitch peak-region of both the cepstrum and the HPS is maximal when the signal spectrum is a harmonic one.

The signal processing based on this method can be interpreted as the transformation of the frequency scale of the signal spectrum by the introduced inharmonicity, which modifies formula (3) as follows:

$$\pi_{\text{IPS}}(\omega) = \prod |F[k\omega(1 + k^2b)^{0.5}]|^2. \quad (10)$$

Unlike formula (3), the algorithm corresponding to expression (10) is called the inharmonic product spectrum (IPS). According to its content, the procedure of signal processing for the HPS (i.e., the procedure described by Noll [25]) is modified and supplemented; namely, the signal spectrum is compressed along the frequency axis not by a factor of  $k = 1, 2, \dots, m$  but by a factor of  $k(1 + bk^2)^{0.5}$ , where  $k = 1, 2, \dots, m$  and  $b$  is the introduced inharmonicity coefficient subjected to variation. As the equality  $b = B$  is achieved, the quantity  $\pi(\omega)$  reaches its maximum; i.e., the pitch peak-region is transformed to a narrow peak of maximum height.

Thus, in the three-dimensional space where the IPS is realized (frequency-introduced inharmonicity coefficient-level of the pitch peak-region), the maximum level of the pitch peak-region will occur at the point with the coordinates equal to the fundamental frequency  $f_0$  of the signal under study and the coefficient  $B$  of its spectral inharmonicity.

A similar approach to the cepstrum yields

$$C(\omega) = |F\{\log|F[(1 + k^2b)^{0.5}\omega]|\}^2|. \quad (11)$$

However, while the formula for the IPS contains no additional parameters as compared to the formula for the HPS, the cepstrum variation requires the knowledge of the quantity  $k$ . Let us explain this statement.

As it was mentioned above, the proposed method of a direct measurement of the inharmonicity coefficient is virtually analogous to a controlled change of the scale of the original inharmonic spectrum with the aim to convert it to a harmonic one. In this procedure, the frequency coordinate of each overtone is corrected depending on the deviation of this frequency from the harmonic series. According to formula (1), the aforementioned deviation depends on two parameters, namely, the inharmonicity coefficient and the number of the overtone.

The procedure of changing the scale of the IPS is performed automatically without specifying the number of the overtone under transformation, because, according to the algorithm, each overtone is automatically involved in the pitch peak-region only with the compression coefficient (which characterizes the compression of the original spectrum) corresponding to its number. Thus, the change in the scale of the spectrum fits conveniently into the procedure of the IPS calculation.

In the case of the cepstrum, such a convenience is absent, and it is necessary to change the scale of the signal spectrum before calculating the cepstrum. For this purpose, it is necessary to know or determine the number of every overtone in the sound spectrum.

This problem has no algorithm for an instrumental solution (here, it should be remembered that it is the identification of overtones that is performed subjectively in the conventional procedure and, hence, may cause considerable errors).

A simple algorithm can be proposed for this purpose. If the fundamental frequency of the sound under study is  $f_0$  and the frequency of some component of its spectrum is  $f$ , the number  $n$  of the harmonic relative to which this overtone is shifted in frequency may be calculated according to formula (1) by the relation

$$n = \text{floor}(f/f_0). \quad (12)$$

This formula<sup>2</sup> is valid only for the overtones with numbers not high enough for the error to reach unity, i.e., to yield  $n = k + 1$  where the true number is  $n = k$ .

Therefore, the maximum value of  $n$  below which formula (12) can be considered as valid is calculated as follows:

$$\begin{aligned} n &= \text{floor}(u) \text{ at } n \neq u, \\ n &= [\text{floor}(u) - 1] \text{ at } n = u, \end{aligned}$$

where  $u$  is determined from the equation

$$u(1 + u^2 B)^{0.5} = u + 1.$$

This dependence is plotted in Fig. 10. The spectrum region where formula (12) is applicable lies below the limiting curve shown in the plot. Since the inharmonicity coefficient characterizing the spectral inharmonicity

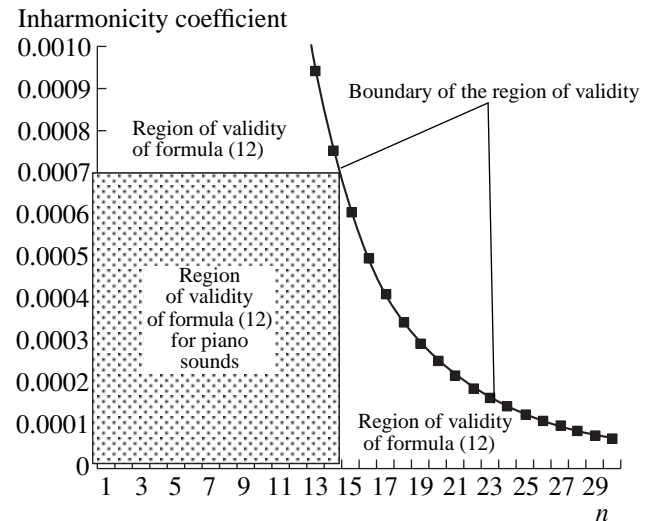


Fig. 10. Region of validity of formula (12).

of sounds of the bass and intermediate registers of a piano (in these registers and, especially, in the bass one, the inharmonicity plays the crucial role in the formation of the quality of sound) does not usually exceed the value 0.0007, we can conclude from Fig. 10 that formula (12) is valid up to  $n = 14$ . Such a number of overtones is sufficient for the determination of the spectral inharmonicity coefficient of a musical sound by the cepstral analysis.

In addition to the frequencies of transverse vibrations of strings, the spectra of real musical sounds contain spectral components of other origin. These components will be erroneously estimated by formula (12) as overtones of the fundamental frequency of transverse vibrations. However, being not "supported" by a considerable overtone series, they will have no significant effect on the formation of the cepstral pitch peak-region.

Evidently, the spectral inharmonicity coefficient of a musical sound cannot be determined independently of its fundamental frequency (or some other quantity proportional to it). Hence, the practical problems of measuring the inharmonicity coefficient can be subdivided into those with the known fundamental frequency (which can be, e.g., previously measured or determined by the position of the note on the piano scale) and more complicated problems that require the measurements of both parameters.

Thus, we can conclude that, if the fundamental frequency of a sound is known, the inharmonicity of its spectrum can be easily measured by varying the introduced inharmonicity with the use of either the cepstral transformation or the IPS.

If the fundamental frequency of the signal under study is unknown, this frequency and the inharmonicity coefficient are more conveniently measured by varying the inharmonicity introduced in the IPS algorithm.

<sup>2</sup> The operation  $Y = \text{floor}(X)$  means the determination of the nearest integer less than or equal to  $X$  [29, 30].

## SUMMARY

The experiments confirm the assumption that the cepstrum and the harmonic product spectrum yield an informative graphic representation of the degree of inharmonicity of musical sounds. Hence, these algorithms can be used for the illustration, evaluation, and comparison of the inharmonicity of sounds in the course of their analysis. Applying the procedure of the search for the maximum of the pitch peak by varying the introduced inharmonicity, these methods of pitch extraction can be adapted for a direct measurement of the fundamental frequency and the inharmonicity coefficient of a musical sound. The algorithm that is most convenient for this purpose is the inharmonic product spectrum.

The results of our studies once again confirm that the principles of pitch extraction can be efficiently used for analyzing the objective factors of the intonation clarity of sounds.

## ACKNOWLEDGMENTS

The work was performed at the Leningrad Musical Instrument Production Association (Russia) and at the Department of Speech, Music and Hearing, Royal Institute of Technology, Stockholm (Sweden).

We are grateful to Dr. J. Liljencrants (Swedish Royal Polytechnical Institute, Stockholm) for consultations and assistance in programming, Prof. A. Rakowski (Chopin Academy of Music, Warsaw) for useful discussions on the problems of the pitch definiteness of sound, and the piano technicians H. Norén, R. Ohlsson (Swedish Radio Company), and C. Carlsson (Royal Swedish Academy of Music) for participating in the experiments.

This work being started in St. Petersburg and continued at the Royal Institute of Technology in Stockholm was possible owing to the grant received by Galembo from the Royal Institute of Technology.

## REFERENCES

1. A. Rakowski, *Catgut Acoust. Soc. News-letter* **27**, 9 (1977).
2. H. Fastl and G. Stoll, *Hearing Research* **7**, 293 (1979).
3. A. Houtsma, *Music Perception* **1**, 296 (1984).

4. A. A. Volodin, *Doctoral Dissertation in Psychology*, Moscow (1969).
5. R. Shankland and J. Coltman, *J. Acoust. Soc. Am.* **10**, 161 (1939).
6. O. Schuck and R. Young, *J. Acoust. Soc. Am.* **15**, 11 (1943).
7. R. Young, *J. Acoust. Soc. Am.* **24**, 267 (1952).
8. R. Young, *Acustica* **4**, 259 (1954).
9. H. Fletcher, *J. Acoust. Soc. Am.* **36**, 203 (1964).
10. M. Podlesak and A. Lee, *J. Acoust. Soc. Am.* **83**, 305 (1988).
11. K. Fenner, *Das Musikinstrument*, No. 1, 9 (1960).
12. S. Cordier, *Das Musikinstrument* **32**, 679 (1983).
13. H. Fletcher, E. Blackham, and R. Stratton, *J. Acoust. Soc. Am.* **34**, 749 (1962).
14. T. Kohen, *Music Perception*, No. 1, 323 (1984).
15. F. Slaymaker, *J. Acoust. Soc. Am.* **47**, 1569 (1970).
16. M. Podlesak and A. Lee, *Acustica* **68**, 61 (1989).
17. P. Tholey, *Practice-Oriented String Scale Calculations with a Computer* (Bochinsky, Frankfurt am Main, 1991).
18. J. Lattard, *J. Acoust. Soc. Am.* **94**, 46 (1993).
19. W. Hess, *Pitch Determination of Speech Signals* (Springer, Berlin, 1983).
20. M. Piszczalski and B. Galler, *Computer Music J.* (Nov. 1977).
21. C. Chafe, D. Jaffe, K. Kashima, *et al.*, in *Proceedings ICVC'85* (1985), p. 399.
22. A. Noll, *J. Acoust. Soc. Am.* **41**, 296 (1967).
23. R. Miller, US Patent No. 2,627,541 (February 1953).
24. M. R. Schroeder, *J. Acoust. Soc. Am.* **43**, 829 (1968).
25. A. Noll, in *Proceedings of Symposium on Computer Processing in Communication* (Polytechn. Inst. of Brooklyn, 1969), p. 779.
26. A. S. Galembo, USSR Inventor's Certificate No. 88215, Cl. G 10 L 1/02 (priority of 9 November 1978; published 7 May 1981).
27. A. S. Galembo, in *Proceedings of 18 Acoustical Conference* (Český Krumlov, Czechoslovakia, 1979).
28. A. Galembo, *Piano: Quality of Sound* (Legprombytizdat, Moscow, 1986).
29. *MATLAB—Reference Guide* (Math Works, 1992).
30. H. Deitel and P. Deitel, *"C" How to Program* (Prentice Hall, 1992).

*Translated by E.M. Golyamina*

## Anisotropy of Amplitude and Phase Fluctuations of a Tone Signal Received in a Coastal Wedge

S. V. Bogunets, O. P. Galkin, R. Yu. Popov,  
Yu. V. Semenov, and E. V. Simakina

*Andreev Acoustics Institute, Russian Academy of Sciences,  
ul. Shvernika 4, Moscow, 117036 Russia*

*e-mail: bvp@akin.ru*

Received December 24, 1998

**Abstract**—Experimental data on the amplitude variation coefficient and the rms value of phase fluctuations of a tone signal are presented in the form of dependences on the vertical arrival angle of the signal. The data are obtained for a tone signal of frequency 800 Hz propagating along a 210-km track and received by a vertical array located in a coastal wedge. The values of the amplitude and phase fluctuations reach their minimum at the arrival angles close to  $0^\circ$  and increase with an increasing angle. However, even at grazing angles of  $\pm 15^\circ$ , the amplitude ratio of the coherent and incoherent components of the arriving signal is  $\sim 1.6$ . The roles of the rough sea surface, internal waves, and drift and rolling of the transmitting ship in the formation of fluctuations are estimated. © 2000 MAIK “Nauka/Interperiodica”.

The solution of many problems of fundamental hydroacoustics (for example, acoustic tomography of large areas) and applied hydroacoustics (for example, sea economic zone protection or estimation of the tsunamigenic potential of underwater earthquakes) is associated with the necessity of detecting weak signals against the ambient sea noise. To do this, one needs arrays with rather large apertures and high concentration coefficients. The efficiency of such arrays is determined by the intervals of the spatial and temporal correlation of sound fields at the site of the array location. The sound field coherence is subjected to the influence of many factors, and the key factor is the multipath sound propagation in an oceanic waveguide. The receiving arrays are often located in shelf zones of the ocean. Because of this, the sound field structure is complicated by the bottom–surface bounces, which are specific for the most of signals entering into a coastal wedge, and by the high spatial-temporal variability of hydrological conditions near the coastline. From some publications (see, e.g., [1]), it follows that for a significant increase in the array efficiency, it is necessary to achieve the maximum possible spatial resolution of separate rays or mode groups arriving at close angles. To this end, the arrays extended in depth with a fan of directional patterns in the vertical plane are used. In this case, the spatial correlation radii of signals significantly increase in the separate patterns. This allows one to considerably increase the horizontal dimensions and enhance the efficiency of planar arrays. In this case, a combined correlation processing of information from the arrays separated by large distances is possible,

which allows a more reliable determination of coordinates of the sound sources and their identification.

However, the multipath propagation is not a single reason of the violation of the sound field coherence. The amplitude and phase fluctuations of signals propagating along separate rays play a certain role in this process.

This paper is devoted to studying the amplitude variation coefficients and the rms values of phase fluctuations of a tone signal in various partial lobes of the vertical fan of directional patterns and to revealing the relative roles of processes leading to such fluctuations.

The experiment was carried out on a 210-km track near the Pacific coast of the Kamchatka peninsula. Figure 1a shows the operation region and the disposition of the test track, whereas Fig. 1b presents the bottom profile obtained by echo sounding. Figure 2 exhibits the sound velocity profiles measured at the point of reception and at distances of 40 and 210 km from this point. The receiving ship was secured to an anchorage buoy at the site with a sea depth of 210 m. From the board of the ship, a 24-m vertical array was lowered, which allowed one to form the fan of main lobes of the directional patterns in the range of angles  $\pm 15^\circ$  (the plus sign denotes the upward direction). The width of each partial pattern at the radiation frequency (800 Hz) was  $\sim 4^\circ$ . The phase center of the array was located at a depth of 100 m, i.e., near the sound channel axis. The bottom slope near the point of reception was no more than  $0.5^\circ$ ; at a range of 25 km, the continental slope began with the bottom inclination up to  $\sim 5^\circ$ .

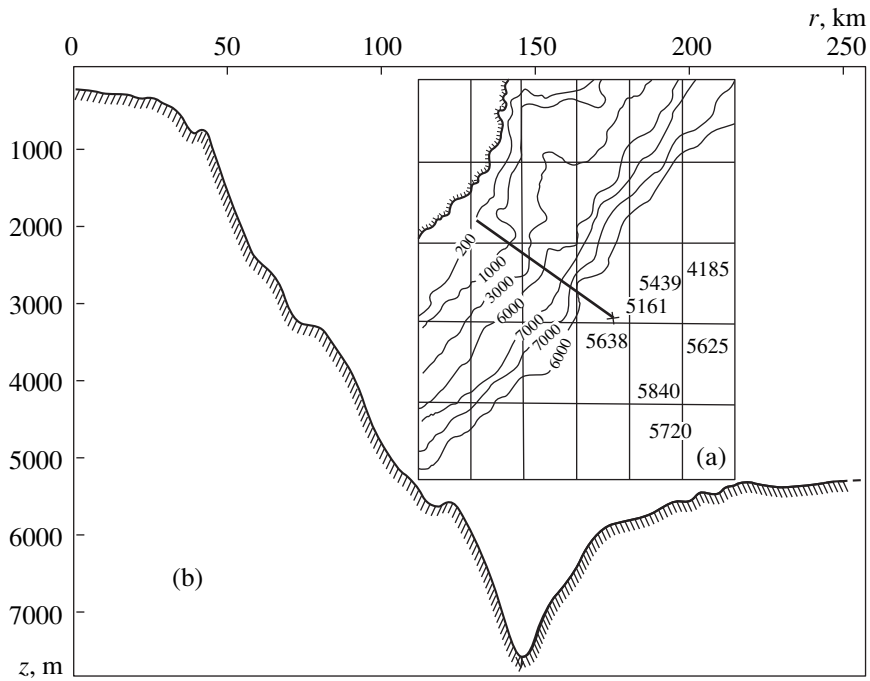


**Fig. 1.** (a) Track of the propagation of a tone signal; (b) bottom profile along the track.

A tone signal of frequency 800 Hz was radiated continuously during 70 min from a ship drifting in the deep ocean. The transmitter was also lowered to a depth of

100 m. The drift speed along the test track was determined by a satellite navigation system and was no more than 0.25 m/s. During the measurements, the wind speed was about 7–8 m/s (wind-generated waves were Beaufort 3–4).

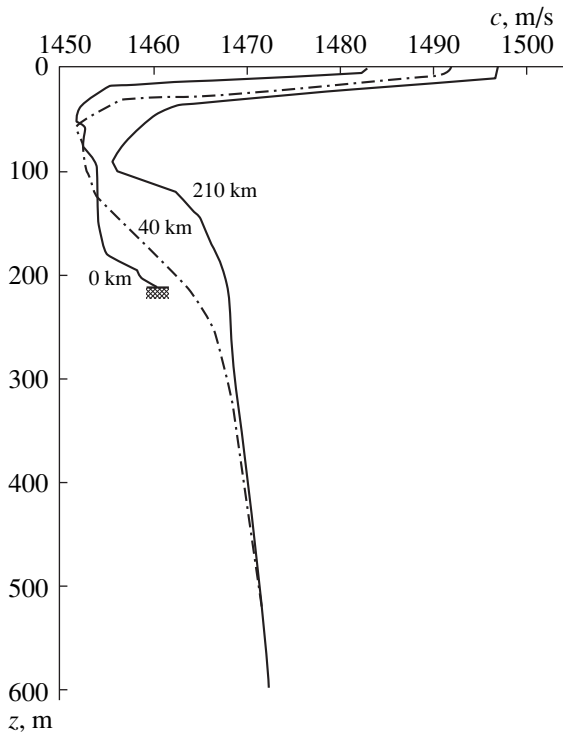


**Fig. 2.** Sound velocity  $c$  versus the depth  $z$  at the points of reception and at distances of 40 and 210 km from the array.

In general, to carry out correct measurements of amplitude-phase fluctuations, a stationary track is necessary. However, using a drifting transmitting ship, it is also possible to obtain a number of useful estimates [2].

Calculations (in the ray approximation) of sound propagation along the track were performed, and they showed that rays with small grazing angles (with the launch angles  $\alpha$  at the radiator no greater than  $\pm 5.5^\circ$ ) arrive into the coastal wedge to the site of the receiving array without any boundary reflections. The rays with angles  $\alpha$  in the range from  $\pm 5.5^\circ$  to  $\pm 11.5^\circ$  arrive at the point of reception with bottom reflections, whereas the rays with angles  $\alpha > \pm 11.5^\circ$  undergo both bottom and surface reflections. Thus, one should expect that the water layer boundaries will differently influence the signals received by different patterns of the fan.

From the output of the partial patterns, the signals were sent to a computer for processing. Figure 3 presents a specific segment of the record of a received fluctuating signal. It is easy to distinguish two noticeably different periods of fluctuations (“fast” and “slow” ones), which was observed previously many times (see, e.g., [3]).

Figure 4 shows the dependence of the amplitude variation coefficient  $\eta$  of signals on the vertical angle  $\varphi$  at which individual main lobes of the fan are located

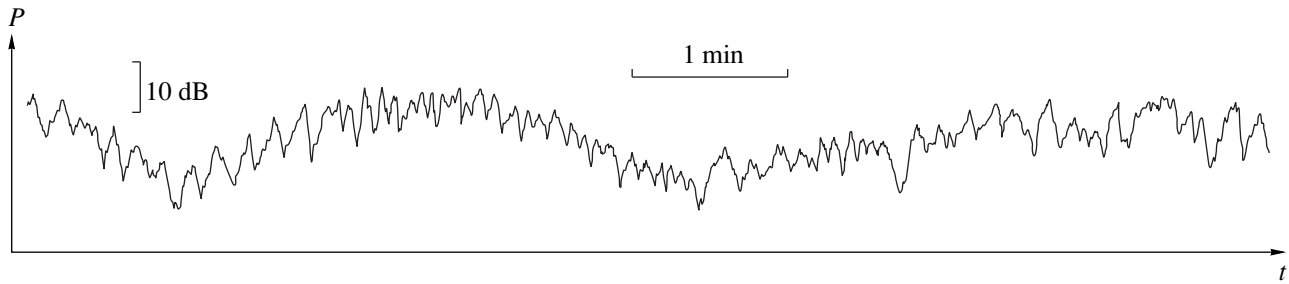


Fig. 3. Typical segment of the record of a fluctuating signal.

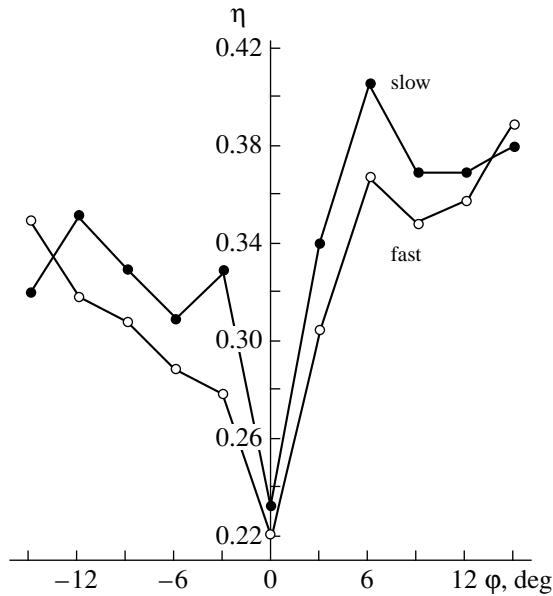


Fig. 4. Dependence of the amplitude variation coefficient  $\eta$  on the vertical angle  $\varphi$  of the tone signal arrival: fast fluctuations (empty circles) and slow fluctuations (full circles).

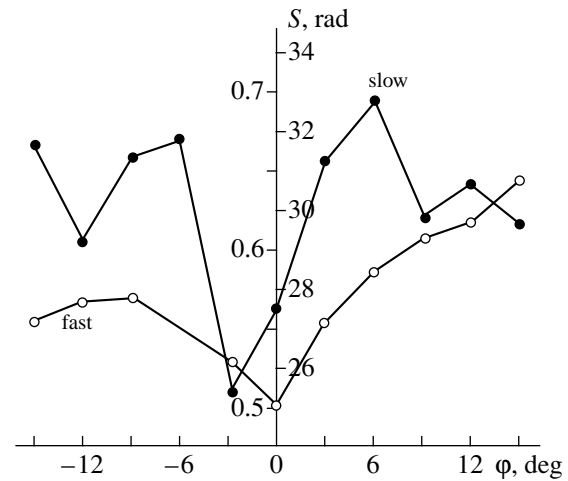


Fig. 5. Dependence of the rms value of the phase fluctuations  $S$  on the arrival angle  $\varphi$  for a tone signal: fast fluctuations (empty circles) and slow fluctuations (full circles). Two scales are used on the ordinate axis: for slow fluctuations (at the right of the axis) and for fast fluctuations (at the left).

(the positive values of  $\varphi$  refer to the patterns directed toward the sea surface, and the negative values refer to the patterns directed to the bottom):

$$\eta = \frac{[\bar{A}^2 - (\bar{A})^2]^{1/2}}{\bar{A}}$$

where  $A$  is the received signal amplitude and the over bar means time averaging. The data for fast and slow fluctuations are shown by empty and full circles, respectively.

Figure 5 shows the variation of the rms values of the phase fluctuations  $S = |\sqrt{\sigma^2}|$  with the angle  $\varphi$ , where  $\sigma$  is the rms deviation of the phase. It should be noted that the scales on the ordinate axis for fast (the left scale) and slow (the right scale) fluctuations differ by approximately one and a half orders of magnitude.

Consider now the behavior of fast fluctuations. It is easy to note that for the main lobes of the directional

patterns, which are close to the horizontal direction, both parameters  $\eta$  and  $S$  are minimum. Such small values of these parameters  $\eta = 0.22-0.23$  and  $S = 0.5$  rad can be caused by the influence of inhomogeneities of the sea medium. In fact, for a tone signal that covered the distance  $r$  in a statistically inhomogeneous medium, the upper bound of the rms values of its phase fluctuations is given by a known expression [4]

$$S = |\sqrt{\sigma^2}| = [(\pi^{1/2}/2)\bar{a}\langle\mu^2\rangle k^2 r]^{1/2},$$

where  $\bar{a}$  is the mean size of random inhomogeneities,  $\langle\mu^2\rangle$  is the mean square of fluctuations of the refractive index, and  $k$  is the wave number of sound.

Because of the vertical refraction, signals usually propagate in both upper and deep ocean layers on their path from the radiator to the receiving system. Therefore, the size of inhomogeneities which are encountered in this path can vary from 1 to 100 m. However, in the considered case, the rays with angles  $\alpha \sim \pm 5.5^\circ$

penetrate no deeper than 200 m and, therefore, the dimensions of inhomogeneities do not exceed 30–40 m. Hence, we can deem that the mean size of inhomogeneities of an equivalent stratified medium is  $\bar{a} \approx 20$  m [5]. Setting  $\langle \mu^2 \rangle \approx 5 \times 10^{-9}$  [6],  $r = 210$  km, and  $k = 3.35$ , we obtain  $S = 0.46$  rad, which is close to the value observed for  $\alpha = 0^\circ$ .

As the slope angle  $\varphi$  increases, the values of  $\eta$  and  $S$  also increase (somewhat more rapidly with a deviation from the horizontal plane toward the surface) reaching the values 0.39 and 0.65 rad, respectively, at  $\varphi = +15^\circ$ . Such a behavior of the signal parameters can be related to the fact that signals propagating over such rays undergo bottom–surface reflections, and the rough boundaries make a progressively increasing contribution to fast fluctuations. Furthermore, the receiving ship's motion, which changes the depth of the receiving array, as well as the transmitting ship drift along the acoustic track, can play a certain role. Consider now these factors in more detail.

For the phase difference of signals arriving over rays within any directional pattern of the fan to be changed by  $\pi$  because of the ship's rolling, the vertical displacements of the array transducers must reach  $\sim 10$  m. Because real displacements of hydrophones did not exceed several meters, the rolling almost did not affect the results.

The situation with the influence of the transmitting ship drift is much more complicated. The point is that the major part of the test track lies in the coastal wedge whose slope angle noticeably varies with distance (see Fig. 1b). For this reason, the change in distance to the receiver leads to changes in the conditions of the multi-ray signal entrance into the shallow-water part of the track and to nonmonotone changes in the angular structure of the sound field with distance. Detailed calculations of the temporal structure of the arriving signals (with a step of 25 m in distance) showed that for signals propagating over almost horizontal rays without reflections from the waveguide boundaries, a drift-induced change in the phase by  $\pi$  can take place within 30–40 min. For steeper rays and, therefore, main lobes of the fan of the directional patterns with large angles  $\varphi$ , the arriving signals undergo bottom reflections (or bottom–surface reflections) whose number can change with distance. The change in the number of reflections leads to jump-like changes in the temporal structure and the phase of the received signals. Therefore, as the inclination angle  $\varphi$  of the directional patterns increases, the influence of the drift on the maximum phase difference of the received signals is also enhanced. For  $\varphi = \pm 15^\circ$ , the phase difference can change by  $\pi$  only within 3–5 min at certain distances.

The origin of the fast fluctuations of the signals is related to their reflection from the waveguide boundaries and, first of all, from the rough sea surface. Many publications (see, e.g., [7–9]) are devoted to the investigation of the influence of the rough surface on the

parameters of reflected and scattered signals. Starting from these results, one can relate the fluctuation characteristics of the surface-reflected signals to the rms height  $\sigma_\delta$  of the surface. The rough surface effect on the signal characteristics is described by the Rayleigh parameter  $P = 2k\sigma_\delta \sin \chi$ , where  $k$  is the wave number and  $\chi$  is the grazing angle of a ray relative to the flat ocean surface. It is known that for small values of the Rayleigh parameter squared ( $P^2 \ll 1$ ), one can deem that [10]

$$\eta \approx P/\sqrt{2}. \quad (1)$$

From Fig. 4, it follows that the maximum value of the quantity  $\eta$  is approximately equal to 0.39 and corresponds to the angle  $\varphi = +15^\circ$ . From expression (1), we find  $P \approx 0.55$ . Although  $P^2 \approx 0.3$  and, therefore, this value does not satisfy, in general, the condition  $P^2 \ll 1$ , we may compare the calculated value of  $P$  with the experimental value of the Rayleigh parameter for the wind speed (7–8 m/s) measured during the experiment. To this end, we calculated the propagation paths of signals that travelled over the 210-km distance from the source and arrived at the point of reception at the angles  $+15^\circ \pm 2^\circ$ . It was found that the rays launched from the source at the angles  $\sim \pm(7^\circ\text{--}9^\circ)$  are not reflected from the water layer boundaries as long as they enter the coastal wedge. On entering into the wedge, they suffer the bottom–surface reflections, and each bottom reflection increases the bottom grazing angle  $\chi_b$  by the double angle of the bottom slope. After four reflections from the surface at angles  $\chi$  sequentially equal to  $1.8^\circ$ ,  $6.5^\circ$ ,  $9.4^\circ$ , and  $11.8^\circ$ , the signals arrive at the array. In spite of the fact that the Rayleigh parameter varies with every surface reflection, one can estimate the efficient Rayleigh parameter

$$P_{\text{eff}} = 2k\sigma_\delta(\sin^2 \chi_1 + \sin^2 \chi_2 + \sin^2 \chi_3 + \sin^2 \chi_4)^{1/2},$$

where  $\sigma_\delta$  is the rms displacement of the rough surface, which is determined from the expression  $\sigma_\delta = 0.53 \times 10^{-2} v^2$  ( $v$  is the wind speed in m/s);  $\chi_i$  ( $i = 1\text{--}4$ ) is the grazing angle near the surface at the first, second, third, and fourth reflection, respectively. For the mean wind speed, 7.5 m/s,  $\sigma_\delta = 0.30$ , whence it follows that  $P_{\text{eff}} \approx 0.58$ , which almost coincides with the experimental value of the Rayleigh parameter. This fact confirms our assumption about the key role of the rough surface in the angular variability of fast fluctuation parameters of the received signals.

In the case under study, the surface reflection coefficient  $V$  is close to unity ( $V = 0.92$ ) even for the maximum angle  $\chi = 11.8^\circ$ . Therefore, the intensity of the coherent component of the reflected signal can be written as  $\exp[-P_{\text{eff}}^2]$ . The ratio of the coherent and incoherent intensities of the signal equals  $\exp(P_{\text{eff}}^2) - 1$ .

Using the foregoing estimates of  $P_{\text{eff}}$ , we obtain the value of this ratio  $\sim 0.4$ . Thus, in any pattern of the fan

even with a main lobe directed at the maximum angle  $\varphi = \pm 15^\circ$ , the coherent intensity is 2.5 times as large as the incoherent intensity with allowance for only fast fluctuations. In most virtually important cases, the duration of the received signal realization does not exceed several tens of seconds. Therefore, the fast fluctuations of signal parameters, which have a close temporal scale, will play the key role in the processing. Based on this fact, we emphasize the importance of the feasibility to predict the characteristics of the fast fluctuations of a tone signal received in the shelf from the known parameters of the wind waves in this region. Choosing a place for setting up the array in natural conditions (for studying the fast fluctuations), we need to carry out the comparative analysis of the influence of the rough sea surface for the cases of a sloping wedge with a large number of reflections and a steep wedge with a small number of reflections. It should be remembered that the results of such a comparison depend on the distance to the source and its depth. Note that in the conditions of the experiment described, the influence of the rough sea surface was insignificant.

Consider now the slow signal fluctuations. Figures 4 and 5 exhibit the data obtained from a 70-min realization. In general terms, the fast and slow fluctuations have similar dependences on the vertical angle of the signal arrivals. However, if the measured values of the coefficient  $\eta$  for the fast and slow fluctuations are close each other, then the scales of the phase fluctuations of  $S$  differ by more than an order of magnitude. The curves  $\eta(\varphi)$  and  $S(\varphi)$  are fairly smooth for the fast fluctuations but have a more complicated form for the slow fluctuations. The curves representing the function  $\eta(\varphi)$  are irregular, while the function  $S(\varphi)$  exhibits well-defined local maxima for the partial patterns with  $\varphi = \pm 6^\circ$ .

The interpretation of the obtained data is a complicated problem mainly because of many factors which can affect the characteristics of fluctuations with the temporal scales of several minutes and tens of minutes. Such fluctuations can be produced by the drift of the transmitting ship, internal waves, motion of mesoscale inhomogeneities, etc. As mentioned above, the radiator drift changes the conditions of the signal entry into the coastal wedge and thus changes the bottom sites from which sound is reflected. These sites can differ by acoustic and geological characteristics. As a result, the interference pattern of the sound field changes in every directional pattern of the fan, and the amplitude and phase of the received signal fluctuate. In measuring the received signal phase, the drift effect can be appreciably reduced (assuming that the drift speed is constant, we can filter out the constant component of the phase derivative). However, to take into account the contribution of the drift to the amplitude variations presents difficulties.

Estimate now the possible influence of internal waves. In recent years, this problem received much

consideration (see, e.g., [11–13]). As is shown in the book [14], the characteristics of sound signal fluctuations in a medium with internal waves are related to environmental parameters: the diffraction parameter  $\Lambda$  connecting the spatial scale of the sound velocity fluctuations to diffraction effects and the parameter of the medium inhomogeneity  $\Phi$ . In the region of geometric approximation validity where  $\Lambda \ll 1$ , the parameter  $\Phi$  characterizes the rms value of phase fluctuations at the point of reception. Rough estimates of the internal wave influence can be obtained for the Garrett–Munk spectrum, the canonical sound velocity profile, and the so-called approximation of the upper turning point of rays [14] (it is assumed that the main contribution to fluctuations is made by the vicinity of the upper turning point of rays). For steep rays, the parameters  $\Lambda$  and  $\Phi$  can be calculated from the following expressions [14]:

$$\Lambda \approx 0.023 \frac{r}{[6kR_v^2(z_a)]^{1/2}},$$

$$\Phi \approx [C(\chi_0) \langle \Delta c_s^2 \rangle R_{sp}(0) k^2 r]^{1/2}.$$

Here,  $r$  is the track length;  $k$  is the wave number of sound;  $R_v$  and  $R_{sp}$  are the vertical and spatial (along a ray) correlation intervals of signal fluctuations, which were obtained by the numerical integration in [14];  $\langle \Delta c_s^2 \rangle = 2.5 \times 10^7$  is the mean square of sound velocity fluctuations near the ocean surface;  $C(\chi_0)$  is the coefficient depending on the angle  $\chi_0$  at which a ray crosses the channel axis in the deep ocean; and  $z_a$  is the depth of the upper turning point.

Because for our case  $r = 210$  km,  $k = 3.35$  1/m,  $R_v \approx 0.1$  km,  $R_{sp} \approx 12.7$  km,  $C(\chi_0) = 0.025$  (for a ray which crosses the channel axis at an angle of  $\sim 8^\circ$  and arrives at the point of reception at an angle of  $15^\circ$ ), and  $z_a \sim 15$  m, we obtain  $\Lambda = 0.02$  and  $\Phi = 14$ . Thus, the condition  $\Lambda \ll 1$  is satisfied, the diffraction effects are weak, and, therefore, we can deem that the rms value of the phase fluctuation  $S = \Phi = 14$  rad. According to [14], the value  $\Phi = 14$  rad is close to the limiting value. The local peaks in Figs. 4 and 5 for the slow fluctuations may be related to the fact that the upper turning points of rays arriving at the point of reception at the angles  $\varphi = \pm 6^\circ$  are located at a depth of the layer with a sharp sound velocity gradient where the influence of internal waves is maximum. Thus, although the noticeable contribution of internal waves to the slow fluctuations of a tone signal is beyond question, the measured values of  $S$  are twice as large as those predicted by calculation. Therefore, the role of other factors, in particular, the interference pattern variations caused by the transmitting ship drift is substantial.

In summarizing the results of the experiments carried out in a coastal region with the use of a tone source (800 Hz) on a 210-km track, we make the following conclusions:

(a) Fluctuations of the received signals are characterized by noticeably different periods: from several seconds (“fast”) to several minutes (“slow”), not only for omnidirectional reception [3] but even for the reception by a vertical array with relatively narrow directional patterns.

(b) The parameters of the amplitude and phase fluctuations of the signal depend on the vertical angle of the ray arrivals at the point of reception in a similar way for both fast and slow fluctuations: they are minimum for the angles close to zero and increase with the arrival angle.

(c) The ratio of intensities of the coherent and incoherent components of a signal reflected from the rough ocean surface is maximum, with allowance for only the fast fluctuations, for the partial patterns of the fan, which are close to the horizontal direction; even for the extreme directional patterns of the fan with  $\varphi = \pm 15^\circ$ , this ratio equals 2.5.

(d) In choosing a site for setting up the vertical array in a coastal wedge (for achieving the maximum ratio of the coherent component to the incoherent one) with allowance for only fast fluctuations, one should rely on the comparative analysis of the effect of the number of reflections—a large number in the case of a sloping bottom and a small number in the case of a steep bottom—on the amplitude and phase variation coefficients.

#### ACKNOWLEDGMENTS

This work was supported by the Russian Foundation for Basic Research, project no. 96-02-19021.

#### REFERENCES

1. O. P. Galkin, A. V. Mikryukov, O. E. Popov, *et al.*, *Akust. Zh.* **43**, 616 (1997) [*Acoust. Phys.* **43**, 529 (1997)].
2. O. P. Galkin, R. Yu. Popov, and E. V. Simakina, in *Acoustic Measurements. Methods and Means. IV Session of the Russian Acoustical Society* (Moscow, Russia, 1995), p. 103.
3. S. V. Bogunets, R. Yu. Popov, and Yu. V. Semenov, *Vopr. Sudostr., Ser. Akust.*, No. 18, 56 (1984).
4. N. G. Kuznetsova and L. A. Chernov, *Vopr. Sudostr., Ser. Akust.*, No. 15, 5 (1982).
5. N. G. Kuznetsova, *Vopr. Sudostr., Ser. Akust.*, No. 11, 89 (1978).
6. R. F. Shvachko, in *Ocean Acoustics*, Ed. by L. M. Brekhovskikh (Nauka, Moscow, 1974), p. 72.
7. Yu. P. Lysanov, in *Ocean Acoustics*, Ed. by L. M. Brekhovskikh (Nauka, Moscow, 1974), pp. 233–327.
8. E. A. Kopyl, in *Problems of Ocean Acoustics*, Ed. by L. M. Brekhovskikh (Nauka, Moscow, 1983), pp. 143–153.
9. S. L. Broschat and E. I. Thorsos, *J. Acoust. Soc. Am.* **101**, 2615 (1997).
10. S. D. Chuprov, in *Ocean Acoustics*, Ed. by L. M. Brekhovskikh (Nauka, Moscow, 1974), p. 337.
11. J. A. Colosi, S. M. Flatté, and C. Bracher, *J. Acoust. Soc. Am.* **96**, 452 (1994).
12. J. Lynch, Y. Jin, R. Pawlovicz, *et al.*, *J. Acoust. Soc. Am.* **99**, 803 (1996).
13. D. Tielbürger, S. Finette, and S. Wolf, *J. Acoust. Soc. Am.* **101**, 789 (1997).
14. *Sound Transmission through a Fluctuating Ocean*, Ed. by S. M. Flatté (Cambridge Univ. Press, Cambridge, 1979).

*Translated by Yu.P. Lysanov*

# The Work of a Source Maintaining a Uniform Motion of a Load along an Elastically Supported Membrane

A. V. Vostrukhov\* and A. V. Metrikin\*\*

\* Nizhni Novgorod State University, pr. Gagarina 23, korp. 4, Nizhni Novgorod, 603022 Russia

\*\* Blagonravov Institute of Machine Science, Russian Academy of Sciences,  
Nizhni Novgorod Branch, ul. Belinskogo 85, Nizhni Novgorod, 603024 Russia

e-mail: wvs@dynamo.nnov.ru

Received January 19, 1999

**Abstract**—Analytical expressions for the transverse displacement of a membrane mounted on an elastic base and subjected to a uniformly moving load are derived. Two cases are considered: a subcritical motion when the load velocity  $V$  is less than the wave propagation velocity in the membrane  $c$  and a supercritical motion when  $V > c$ . A general expression for the work provided by a source maintaining the uniform motion of a concentrated load along the membrane is obtained. In the absence of the energy loss in the membrane, this work is equal to zero for the subcritical motion and tends to infinity for the supercritical motion. The latter result is a consequence of the discontinuity of the solution obtained for the membrane displacement. With the introduction of the internal friction in the membrane, it is possible to eliminate this discontinuity. On the basis of the numerical solution to the problem with internal friction, the dependence of the work of the external source on the load velocity is analyzed. © 2000 MAIK “Nauka/Interperiodica”.

With all the progress that has been made in the high-speed surface electric transport, it has become necessary to take into account the wave processes taking place in a railroad track and in the ground under the track. In papers [1–3] it is shown that a railroad track is mainly affected by surface waves whose velocity in a soft ground (peat) may be of the order of 200 km/h. Since the velocity of today’s high-speed trains may exceed 200 km/h, it is clear that the study of the surface elastic waves generated by a moving load is urgent.

In this paper we investigate one aspect of this problem, namely, we analyze the work of a source providing the motion of a load with constant velocity. Since in the mechanics of elastic systems this problem is practically ignored, we consider one of the simplest models with a two-dimensional wave field represented by a membrane mounted on an elastic base. The load is modeled by a point object moving along the membrane uniformly and linearly.

Based on the law of change of energy, we derived a relationship for the work of a source maintaining a uniform motion of the load. Neglecting the energy loss, we have shown that, for the load velocity  $V$  not exceeding the velocity of transverse waves  $c$  in the membrane, this work is equal to zero, and, in the opposite case ( $V > c$ ), it is infinite. The latter result is a consequence of a jump discontinuity, which occurs in the membrane displacement at the boundary of the two-dimensional analog of the Mach cone formed in the membrane at  $V > c$ .

The effect of the internal friction in the membrane (according to the Voigt rheological model [4]) on the load-generated field and the work of the source maintaining the uniform motion of the load had been studied. It was found that the internal friction eliminates all singularities of the field generated by the load. With an increase in friction, the source work grows at  $V < c$  and drops at  $V > c$ .

We consider the oscillations of a membrane mounted on an elastic base and excited by a point object moving uniformly and linearly along the membrane. We assume that the friction in the contact is absent, and the vertical component of the object’s reaction to the membrane is constant and equal to  $P$  (Fig. 1). In this case, the equation for small vertical oscillations of the membrane has the form

$$\rho u_{tt} - N(u_{xx} + u_{yy}) + ku = -P\delta(x - Vt)\delta(y). \quad (1)$$

Here,  $u$  is the vertical displacement of the membrane,  $\rho$  and  $N$  are its surface density and tension,  $k$  is the modulus of elasticity of the base underlying the membrane, and  $V$  is the velocity of the object.

We determine the work per unit time of the force  $\mathbf{F}$  with which the object acts on the membrane, i.e., the power transferred from the object to the membrane. This power determines the work of the source maintaining the uniform motion of the load. To do this, we multiply both sides of equation (1) by  $u_t$ , which yields

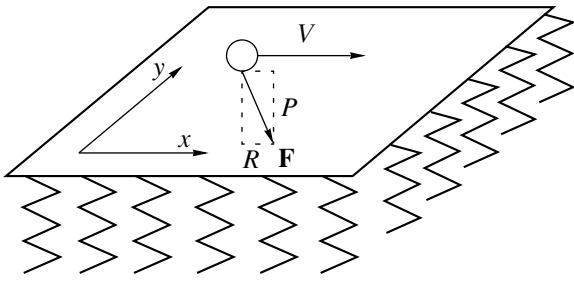


**Fig. 1.** Membrane on an elastic base with a constant load moving along it.

the law of change of the generalized energy of a membrane element

$$\frac{\partial h}{\partial t} + \text{div } \mathbf{S} = -Pu_t \delta(x - Vt) \delta(y), \quad (2)$$

where  $h = \frac{1}{2}(\rho u_t^2 + N(u_x^2 + u_y^2) + ku^2)$  is the energy

density (the Hamiltonian of a distributed system),  $\mathbf{S} = -Nu_t \nabla u$  is the energy flux (the analog of the Poynting vector), and  $-Pu_t \delta(x - Vt) \delta(y)$  is the surface power density of the external source of the force  $\mathbf{F}$  acting on the membrane.

Integrating (2) with respect to  $x$  and  $y$  gives a global law of change of energy of a membrane on an elastic base. The right-hand side of the expression obtained after the integration describes the power transferred to the membrane from the object

$$Q = P \int_{-\infty}^{\infty} \int_{-\infty}^{\infty} u_t \delta(x - Vt) \delta(y) dx dy. \quad (3)$$

We note that in a steady state, the point of contact moves strictly horizontally, and, therefore, the work is done only by the horizontal component  $R$  of the force  $\mathbf{F}$ ,  $R = Q/V$ .

For calculating the quantity  $Q$ , we need to know the membrane displacement  $u(x, y, t)$ . In a steady state, the field of the membrane displacement is stationary in the coordinate system  $\xi = x - Vt$  moving with the load. In this coordinate system, we have  $u_x = u_\xi$  and  $u_t = -Vu_\xi$ , and equation (1) has the form

$$(V^2 - c^2)u_{\xi\xi} - c^2 u_{yy} + hu = -\frac{P}{\rho} \delta(\xi) \delta(y). \quad (4)$$

Here,  $c = \sqrt{N/\rho}$  is the velocity of the wave propagation in the membrane and  $h = \sqrt{k/\rho}$  is the cut-off frequency. We apply an integral Fourier transform to (4)

with respect to coordinates  $\xi$  and  $y$ :

$$W(k_1, k_2) = \int_{-\infty}^{\infty} u(\xi, y) e^{i(k_1 \xi + k_2 y)} d\xi dy. \quad (5)$$

In the form of transforms, we obtain

$$W = -\frac{P}{\rho(c^2 k_2^2 - \beta^2 k_1^2 + h^2)}, \quad (6)$$

where  $\beta^2 = V^2 - c^2$ . Making an inverse transformation of (6), we obtain the expression for  $u(\xi, y)$ :

$$u(\xi, y) = -\frac{P}{4\pi^2 \rho} \int_{-\infty}^{\infty} \int_{-\infty}^{\infty} \frac{\exp[-i(k_1 \xi + k_2 y)] dk_1 dk_2}{c^2 k_2^2 - \beta^2 k_1^2 + h^2}. \quad (7)$$

For its computation, we first consider the integral

$$I = -\frac{1}{2\pi} \int_{-\infty}^{\infty} \frac{\exp(-k_1 \xi) dk_1}{\beta k_1^2 - c^2 k_2^2 - h^2}, \quad (8)$$

which can be calculated by the contour integration. According to the Jordan lemma, for  $\xi > 0$  the contour of integration should be closed in the lower half-plane of the complex variable  $k_1$ , and for  $\xi < 0$  it should be closed in the upper half-plane.

When the load velocity is less than the wave velocity in the membrane, i.e.,  $\beta^2 < 0$ , the integrand function has two simple poles located on the imaginary axis symmetrically about the real axis. Calculating (8) by using the residue theorem and substituting the result of integration into expression (7), we obtain

$$u = -\frac{P}{2\pi \rho c \sqrt{c^2 - V^2}} \int_{-\infty}^{\infty} \frac{\cos(k_2 y)}{\sqrt{k_2^2 + (h/c)^2}} \times \exp\left(-\frac{c|\xi|}{\sqrt{c^2 - V^2}} \sqrt{k_2^2 + (h/c)^2}\right) dk_2. \quad (9)$$

The integral in (9) is a tabular one [5]:

$$\int_0^{\infty} \exp(-b\sqrt{v^2 + x^2}) \frac{\cos(ax) dx}{\sqrt{v^2 + x^2}} = K_0(v\sqrt{a^2 + b^2}), \quad (10)$$

where  $\text{Re } b > 0$ ,  $\text{Re } v > 0$ , and  $K_0$  is the modified Bessel function of the second kind. Consequently, the displacement of the membrane at  $V < c$  is described by the expression

$$u = -\frac{P}{2\pi \rho c \sqrt{c^2 - V^2}} K_0 \times \left( \frac{h}{\sqrt{c^2 - V^2}} \sqrt{\xi^2 + y^2 (c^2 - V^2)/c^2} \right). \quad (11)$$

When the load velocity exceeds the wave velocity in the membrane, the poles of the integrand function in (8)

lie on the integration path, i.e., on the real axis. In this case, for a correct integration, it is necessary to choose the appropriate path of bypassing the poles. For this purpose, we introduce a low loss in the equation describing the membrane dynamics, for example, a loss due to the viscosity of the elastic base. Then, the term  $2\delta u$ , where  $0 < \delta \ll 1$ , appears in the left-hand side of equation (1), and integral (8) takes the form

$$I = -\frac{1}{2\pi} \int_{-\infty}^{\infty} \frac{\exp(-k_1 \xi) dk_1}{\beta^2 k_1^2 - 2i\delta V k_1 - c^2 k_2^2 - h^2}. \quad (12)$$

The poles of the integrand in formula (12) lie in the upper half-plane symmetrically about the imaginary axis. Hence, the value of the integral (12) is nonzero only at  $\xi < 0$ . Performing the contour integration, passing to the limit  $\delta \rightarrow 0$  in the expression obtained for  $I$ , and substituting the result into (7), we arrive at the expression

$$u = -\frac{P}{\pi \rho \beta c} H(-\xi) \int_0^{\infty} \frac{\cos(k_2 y)}{\sqrt{k_2^2 + (h/c)^2}} \times \sin\left(\frac{\xi c}{\beta} \sqrt{k_2^2 + (h/c)^2}\right) dk_2, \quad (13)$$

where  $H$  is Heaviside function. The integral in equation (13) is a tabular one [5]:

$$\int_0^{\infty} \frac{\sin(p\sqrt{x^2+a^2})}{\sqrt{x^2+a^2}} \cos(bx) dx = \begin{cases} \frac{\pi}{2} J_0(a\sqrt{p^2-b}), & (p > b > 0) \\ 0, & (b > p > 0), \end{cases} \quad (14)$$

where  $J_0$  is the Bessel function of the first kind. Finally, we have

$$u = -\frac{P}{2\rho\beta c} H\left(-\xi - \frac{\beta}{c}|y|\right) J_0\left(\frac{h}{\beta} \sqrt{\xi^2 - (\beta/c)^2 y^2}\right). \quad (15)$$

From the obtained solutions (11) and (15) it follows that, for  $V < c$ , the transverse displacement of the membrane is localized near the point of the load application and tends to infinity at the very point of contact. At  $V > c$ , the transverse displacement of the membrane is concentrated within the angle  $|y| < |\xi|(c/\beta)$ , ( $\xi < 0$ ), which is analogous to the Mach cone formed in the course of a supersonic motion of an object in atmosphere. At the sides of this angle, the membrane displacement has a discontinuity equal to  $P/2\rho\beta c$ .

Thus, we have determined the membrane displacement. Now, we return to the calculation of the power

given to the membrane by the load. For calculating integral (3), we represent the  $\delta$ -functions as the limit

$$\delta(x) = \lim_{\gamma \rightarrow 0} \left( \frac{\gamma}{\pi} \right) \left( \frac{1}{x^2 + \gamma^2} \right). \quad (16)$$

Then, the expression for  $Q$  at  $V < c$  can be written as

$$Q = \frac{PhV}{2\pi^3 \rho \beta^2 c \gamma \rightarrow 0} \lim_{\gamma \rightarrow 0} \int_{-\infty}^{\infty} \int_{-\infty}^{\infty} K_1 \left( \frac{h}{c^2 - V^2} \sqrt{\xi^2 - y^2} \frac{\beta^2}{c^2} \right) \times \frac{\gamma^2 \xi d\xi dy}{(\xi^2 + \gamma^2)(y^2 + \gamma^2) \sqrt{\xi^2 - y^2} \frac{\beta^2}{c^2}}. \quad (17)$$

The integrand in (17) is an odd function of the variable  $\xi$ ; hence, the integral taken with respect to  $\xi$  within symmetric limits is equal to zero. Therefore, the work required for maintaining a uniform motion of a constant load along a membrane on an elastic base also equals zero in the subcritical case ( $V < c$ ).

For the supercritical case ( $V > c$ ), taking into account that  $J_0(0) = 1$  and  $J_0'(0) = J_1(0) = 0$ , we obtain

$$Q = \frac{P^2 V}{2\pi^3 \rho \beta c}$$

$$\times \lim_{\gamma \rightarrow 0} \gamma^3 \int_{-\infty}^{\infty} \int_{-\infty}^{\infty} \left( \frac{1}{\xi^2 + \gamma^2} + \frac{1}{(-\xi - (\beta/c)y)^2 + \gamma^2} \right) \times \frac{d\xi dy}{(\xi^2 + \gamma^2)(y^2 + \gamma^2)}. \quad (18)$$

As is seen from (18), the relation for  $Q$  consists of two terms. We designate the first term by  $Q_1$  and calculate it:

$$Q_1 = \frac{P^2 V}{2\pi^3 \rho \beta c \gamma \rightarrow 0} \lim_{\gamma \rightarrow 0} \gamma^3 \int_{-\infty}^{\infty} \int_{-\infty}^{\infty} \frac{d\xi dy}{(\xi^2 + \gamma^2)^2 (y^2 + \gamma^2)} = \frac{P^2 V}{2\pi^3 \rho \beta c \gamma \rightarrow 0} \lim_{\gamma \rightarrow 0} \gamma^3 \frac{\pi}{2\gamma^3 \gamma} = \infty. \quad (19)$$

The second term in (18), like the first one, is nonnegative; consequently, it cannot change the judgment regarding the convergence of (18). This allows us to conclude that  $Q$  equals infinity. Hence, an infinite power is needed for maintaining the uniform motion of a load in the supercritical case.

This result is a consequence of the physically unrealizable discontinuity of the membrane displacement at the sides of the "Mach angle." This discontinuity, as well as the infinite displacement of the membrane under the load in the subcritical case, may be eliminated by introducing an internal friction in the mem-

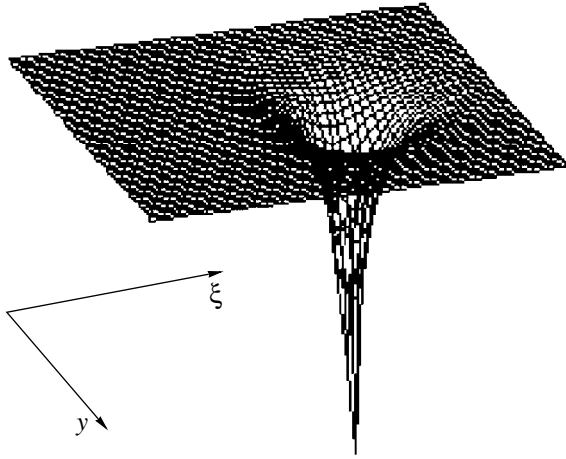


**Fig. 2.** Characteristic profile of the transverse displacements of the membrane for  $V < c$ .

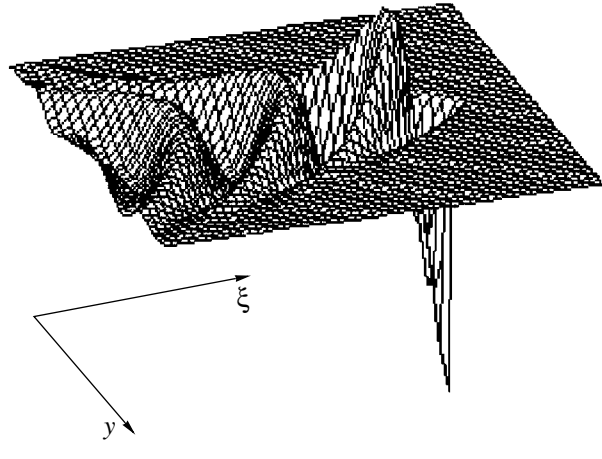


**Fig. 3.** Smoothed “Mach angle” formed in the membrane at  $V > c$ .

brane. To prove it, we introduce an internal friction according to the Voigt rheological model by adding to the left-hand side of (1) the term  $N_1 \frac{\partial}{\partial t} (u_{xx} + u_{yy})$ :

$$\rho u_{tt} - \left( N + N_1 \frac{\partial}{\partial t} \right) (u_{xx} + u_{yy}) + ku = -P\delta(x - Vt)\delta(y). \quad (20)$$

Here,  $N_1$  is the coefficient characterizing the internal friction in the membrane. Introducing the dimensionless variables  $\tau = ht$  and  $\{x_n, y_n\} = \{x, y\}(h/c)$  and passing to the “current” coordinate  $\xi = x_n - \alpha\tau$ , where  $a =$

$(V/c)$ , we obtain from (20):

$$\alpha^2 u_{\xi\xi} - \left( 1 - \frac{N_1 h \alpha}{\rho c^2} \frac{\partial}{\partial \xi} \right) (u_{\xi\xi} + u_{y_n y_n}) + u = -\frac{P}{\rho c^2} \delta(\xi) \delta(y_n). \quad (21)$$

Applying an integral Fourier transform (5) to equation (21), finding the solution in the space of transforms, and then making an inverse transformation with respect to  $k_2$  by using the contour integration, we obtain the following expression for  $u$ :

$$u = -\frac{iP}{4\pi\rho c^2} \int_{-\infty}^{\infty} \frac{\exp(-ik_1\xi + i|y_n| \sqrt{\{k_1^2(\alpha^2 - 1 - iAk_1) - 1\} / \{1 + iAk_1\}}) dk_1}{\sqrt{(1 + iAk_1)(k_1^2(\alpha^2 - 1 - iAk_1) - 1)}}, \quad (22)$$

where  $A = (N_1 h \alpha / N)$ . The results of the numerical integration of equation (21) are presented in Figs. 2 and 3 displaying the characteristic profiles of the transverse displacement of the membrane under the load. For the subcritical case, as is seen from Fig. 2, the membrane displacement is localized near the load, as before. But the displacement at the point of contact is limited. Figure 3 shows that, with allowance for the internal friction, the field of the membrane displacement remains localized within the “Mach angle.” The behavior of the displacement changes qualitatively only at the sides of the angle where the membrane displacement becomes

a continuous function tending smoothly to zero outside this angle.

The work of the external source can be found numerically from relation (3) that remains valid with allowance for the internal friction. Figure 4 displays the dependence of the work normalized to  $(P^2 V h / 4\pi\rho c^3)$  on the load velocity normalized to  $c$  for two values of the internal friction in the membrane. As is seen from the figure, with a decrease in friction, the power required for maintaining the uniform motion of the load decreases in the subcritical case and increases in the supercritical case. The maximum work shifts toward

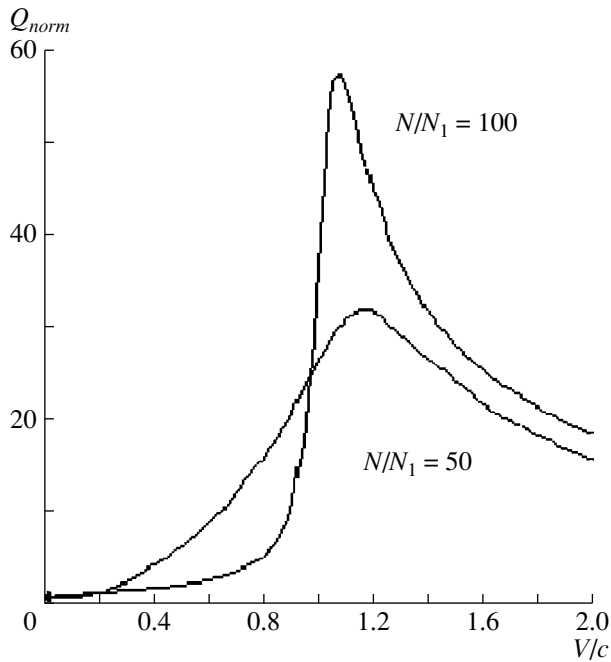


**Fig. 4.** Dependence of the work normalized to  $P^2Vh/4\pi c^3$  on the load velocity.

the load velocity  $V = c$ , i.e., the velocity of transverse waves in the membrane.

### CONCLUSIONS

The discussed problem of the work provided by a moving source of disturbances and associated with the wave generation may be of great practical importance. This is connected with the fact that modern high-speed trains may move at velocities close to the velocity of surface waves propagating in the ground underlying the railroad track. Obviously, the part of the power of loco-

motive's engine that is spent for the wave generation may be quite substantial. For evaluating the order of the radiation loss, it is necessary to consider realistic models of a railroad track. However, before analyzing complex models, one must evaluate the difficulties that may be encountered in this study. One of these, connected with the discontinuity of the displacement field generated by a moving point object, is discussed in this paper. It is shown that one of the ways of eliminating the discontinuity of the displacement field may be the introduction of internal friction in the elastic system model, which makes it possible to obtain smooth solutions while remaining in the framework of a linear model. It seems that in this way it will be possible to correctly analyze the loss connected with the motion of a load in a half-space where the problem of discontinuity of the solution is even more acute. As is shown in [6], the field of displacements of a half-space surface excited by a point load moving at a speed exceeding the Rayleigh wave velocity has a discontinuity of the second kind at the sides of the angle within which the surface waves are radiated.

### REFERENCES

1. J. J. Labra, *Acta Mech.* **22**, 113 (1975).
2. H. A. Dieterman and A. V. Metrikine, *Eur. J. Mech. Solids* **15**, 67 (1996).
3. H. A. Dieterman and A. V. Metrikine, *Eur. J. Mech. Solids* **16**, 295 (1997).
4. *Vibration in Industrial Engineering*, Ed. by V. V. Bolotin (Mashinostroenie, Moscow, 1978), Vol. 4.
5. I. S. Gradshteyn and I. M. Ryzhik, *Tables of Integrals, Sums, Series, and Products* (Fizmatgiz, Moscow, 1963).
6. D. L. Lansing, NASA Technical Report TR R-238 (1966).

*Translated by A. V. Svechnikov*

# Design and Experimental Evaluation of an Endocavitary Linear Phased Array for Ultrasound Surgery of Prostate

L. R. Gavrilov\* and J. W. Hand\*\*

\* *Andreev Acoustics Institute, Russian Academy of Sciences,  
ul. Shvernika 4, Moscow, 117036 Russia  
e-mail: bvp@akin.ru*

\*\* *Radiological Sciences Unit, Hammersmith Hospital, London W12 OHS, UK  
Received February 16, 1999*

**Abstract**—The design and the results of the experimental evaluation of a 70-element linear phased ultrasonic array intended for endocavitary (transrectal) surgical treatment of chronic prostatic disease are presented. The array consists of elements of width 1 mm and length 15 mm, and its operating frequency is 1 MHz. The array performs electronic scanning of the focus within 30–60 mm along the acoustic axis and  $\pm 20$  mm in the perpendicular direction (which corresponds to the maximum prostate dimensions). In the course of the scanning, an acceptable level of secondary intensity peaks is maintained, and the acoustic power generated by the array is no less than 200 W. The results suggest that the array can be useful for prostate surgery. However, a widespread clinical application of this ultrasound method depends on the development of combined systems providing both the ultrasound ablation of prostate tissue and the control over the location of the focal region in the prostate before ablation. © 2000 MAIK “Nauka/Interperiodica”.

Chronic prostatitis, i.e., prostate gland inflammation, is one of the most widely spread diseases among men. According to statistics [1, 2], in the USA every year 800000 men undergo surgery associated with benign prostate diseases and 200000 men have malignant prostate tumors. The death rate caused by prostate cancer (38000 men annually) makes this type of cancer the second deadliest type of men’s cancer in the USA. So there is an interest in minimum-damaging prostate surgery methods, which in future could compete with routine surgery. In the recent years, a number of laboratories launched research projects aimed at studying the possibility of using focused ultrasound for this purpose. This approach is based on the fact that the values of the main physical parameters characterizing the propagation of ultrasound in soft tissues (wavelength, attenuation, and absorption) in the frequency range from fractions to units of MHz are highly favorable for performing local ablations of specified dimensions in deep tissues. The wavelength of ultrasound in soft tissue (1.5 mm at 1 MHz) is sufficiently small to ensure effective focusing of the ultrasonic energy at a distance of several centimeters and, thus, to realize an endocavitary, transrectal, focused ultrasonic system. It should be noted that the range of distances from the rectum wall to the ablation zone is no greater than 2–5 cm, and the transverse dimension of prostate usually does not exceed 4 cm. Besides, the attenuation coefficient of ultrasound in soft tissue (usually  $5\text{--}10 \text{ Np m}^{-1} \text{ MHz}^{-1}$  [3]) is not too great, and the absorption coefficient (of the same order of magnitude) is not too small, so there

is a possibility of making thermal ablations of specified dimensions at the mentioned distances.

The objective of this paper is the development and experimental investigation of a focused ultrasonic system for endocavitary prostate surgery. At present, there are two approaches to designing such systems. The first is based on the use of a transrectal single focused transducer having the form of a part of a sphere with continuous distribution of the normal particle velocity and being moved mechanically along the rectum wall. Another approach uses an endocavitary linear phased array that electronically scans in two perpendicular directions. The first approach was realized in the Sonablate instrument (Focal Surgery Inc., Milpitas, Calif., USA) [4, 5] intended for ablating prostate tissue with several interchangeable single transducers with the operating frequency 4 MHz and various focal lengths (30, 35, and 40 mm); the transducers can be moved within a distance of 45 mm. The prostate imaging is provided by the same transducer having a maximum dimension of 30 mm. Another instrument is the Ablatherm (TechnoMed, France) [6] with a single focused radiator having the diameter 35 mm, the focal length 35 mm, and the operating frequency 2.25 MHz. In this case, for visualizing the prostate, a separate built-in transducer with the operating frequency 7.5 MHz is used. The second approach, based on the use of an endocavitary linear phased array with electronic scanning in perpendicular directions, was first discussed in a theoretical paper [7] and later realized independently by different researchers [1, 2, 8–10].

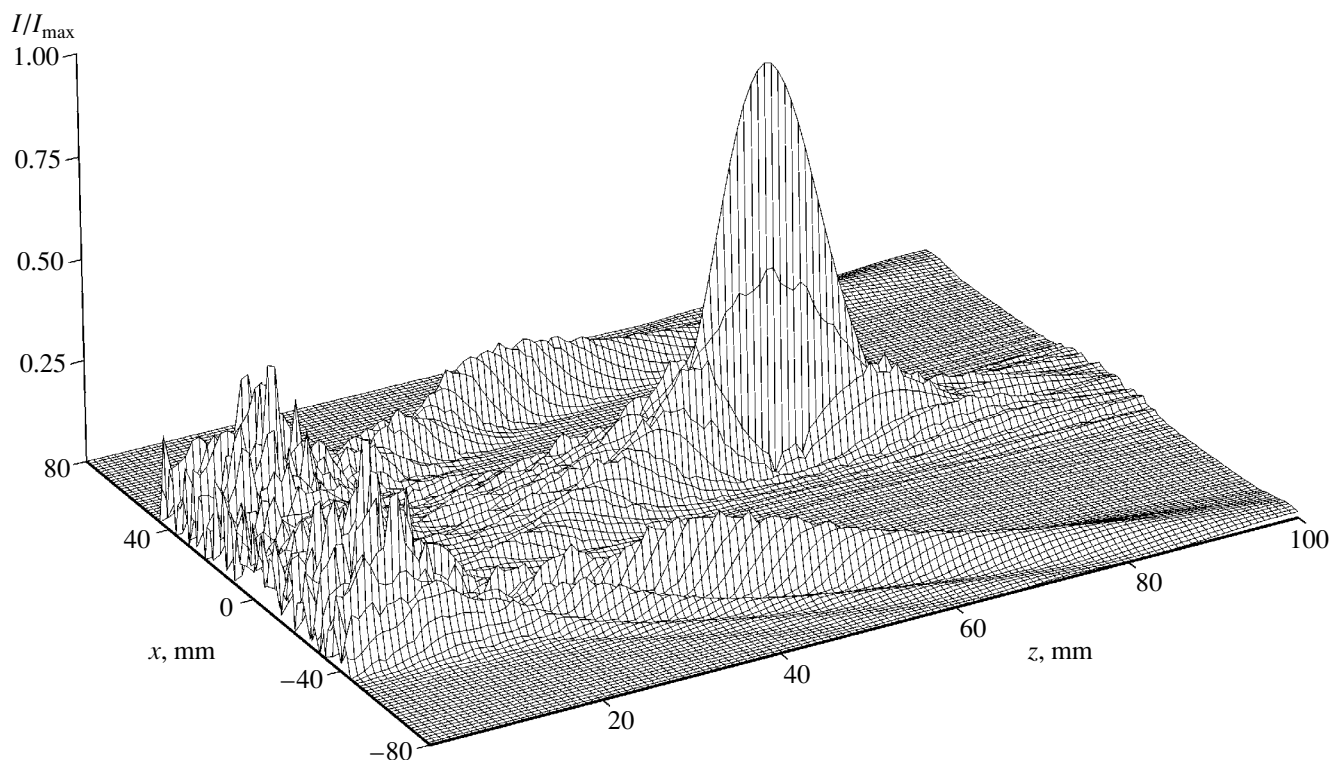


**Fig. 1.** Calculated distribution of the relative intensity of ultrasound in the field of a linear array operating at the frequency 585 kHz and consisting of 35 elements of width 2 mm, length 16 mm, and with the distance between the centers of the elements 2.5 mm; focusing on the point (0, 0, 60 mm);  $x$  is the coordinate along the array aperture and  $z$  is the coordinate along the acoustic axis.

Both aforementioned approaches to the design of focused ultrasonic systems for intracavitary prostate surgery have advantages and shortcomings. The instruments based on the use of single focused radiators are relatively simple and inexpensive, but their fundamental shortcoming is their fixed focal length. When it is necessary to change the depth of action upon the tissue, the radiator has to be changed for the one with another focal length, and this fact imposes certain limitations on the use of these systems. The advantage of phased arrays lies in the possibility of scanning over the prostate with a high speed, as well as of synthesizing, if necessary, several focuses. The disadvantages of arrays with the distances between elements greater than a half-wavelength are the relative complexity and the higher cost of the instrument, as well as the possibility of the appearance of the secondary intensity peaks located in the tissue at considerable distances from the focus.

Figure 1 illustrates the possible role of these secondary peaks of ultrasound intensity. Here, we present the results of the calculation of the acoustic field of a 35-element linear phased array with the operating frequency 585 kHz and the distance between the centers of elements 2.5 mm ( $\approx 1\lambda$ , where  $\lambda$  is the wavelength). The focusing is performed along the acoustic axis of the array at a depth of 60 mm (0, 0, 60 mm). The calculation is based on the methods described in [11, 12] for

the case of the propagation of ultrasound in a biological tissue with the sound velocity  $1500 \text{ m s}^{-1}$ , the tissue density  $1000 \text{ kg m}^{-3}$ , and the attenuation coefficient  $10 \text{ Np m}^{-1} \text{ MHz}^{-1}$  [3], which approximately corresponds to the acoustic parameters of prostate tissue. (The technique of such calculations is described in detail in [9].) The intensity was normalized to the maximum intensity at the center of focal region. It is seen that, along with the main intensity peak, there is a secondary peak of intensity whose amplitude at a distance of 40–50 mm from the array surface may be up to 20% of the intensity at the focus. The physical nature of these secondary intensity peaks is related to the presence of discrete elements in the array. Below, by the term “a secondary intensity peak” we imply the peaks of this physical nature, not the local intensity peaks that exist in the field of a single focused transducer. The comparison of the theoretical and experimental distributions of intensity produced by arrays shows that, in practice, the level of the secondary intensity peaks exceeds the calculated one, in particular, due to the acoustic interaction between the array elements [9]. Thus, the reduction in the level of secondary intensity peaks in the array field is of prime importance for safety in the ultrasound surgery of prostate.

The known methods of reducing the level of side lobes of the array radiation pattern, which are based on the reduction of the oscillation amplitude from the cen-

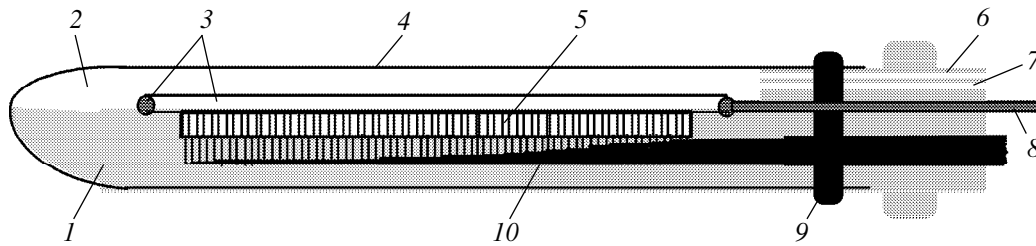


**Fig. 2.** Schematic sketch of a linear array operating at the frequency 1 MHz and consisting of 70 elements of dimensions  $1 \times 15$  mm: (1) case of array, (2) space filled with degassed cold water, (3) coil of the receiving NMR antenna, (4) membrane made of thin rubber, (5) 70-element array, (6) hole for feeding water, (7) hole for draining water, (8) cable connected to the receiving coil, (9) seal, and (10) cable for feeding the array elements.

tral part of the array to its periphery [13–15], are practically unacceptable in our case because of the requirements imposed on the level of the acoustic power of the array. Another method of decreasing the influence of secondary intensity peaks is based on the use of arrays with unequal distances between their elements [13, 14]. This method was evaluated by Hutchinson *et al.* [1, 2]. They described a linear phased array for prostate surgery that operated at 0.83 MHz and consisted of 57 elements of equal length (15 mm) and different widths (1.6 and 1.2 mm). The elements were randomly arranged and spaced at intervals of 0.13 mm. (Thus, the distance between the centers of the elements changed from 0.74 to  $0.96\lambda$ .) The calculations performed by the authors showed that the expected reduction in the level of the secondary intensity peaks due to the aperiodicity of the elements may be up to 30–45% [1].

For a considerable decrease in the level of side lobes of the array radiation pattern, the distance between the array elements should be less than  $\lambda/2$  [13–15], i.e., for example, less than 0.75 mm at 1 MHz. However, to cre-

ate an array with such small elements and a sufficiently large aperture and, in addition, to provide the required acoustic power (for instance, 200 W), it is necessary to use a considerable number of elements and electronic channels, which complicates the system and increases its cost. Besides, the “dead zone” formed by the spaces between the elements grows. However, the transverse dimensions of the array should not exceed the physiological limits (the maximum transverse dimension of the array case should not exceed 25–28 mm). Thus, the choice of the parameters and characteristics of real arrays intended for prostate surgery is a compromise between a number of contradictory requirements.

The designed linear array for transrectal surgery of prostate is shown schematically in Fig. 2. The array consists of 70 elements of 1 mm wide, 15 mm long, and with a thickness corresponding to the operating frequency of 1 MHz (1.72 mm). Out of 70 elements, only 62 were simultaneously active. For electrical and acoustic insulation of the elements, we used a tape of thickness about 0.1 mm covered by adhesive substance on both sides. The length of the array 5 was 77 mm, and the distance between the centers of the elements corresponded to  $0.73\lambda$  (i.e., it was considerably less than in the aforementioned array, Fig. 1). The array was housed in a case 1 made of plastic; the maximum dimension in the widest part of the case did not exceed 26 mm, and the minimum transverse dimension was 14–16 mm. The case was enclosed in a rubber membrane 4, the distance between the array surface and membrane being about 10 mm. The acoustic contact between the array and the biological tissue was provided through degassed cold (for cooling both the array and the adjacent tissue) water fed into the space 2 between the case and the membrane through the hole 6 and drained through the hole 7. The leads of a multiple-conductor shielded cable 10 serving for feeding the elements of the array were soldered to the elements.

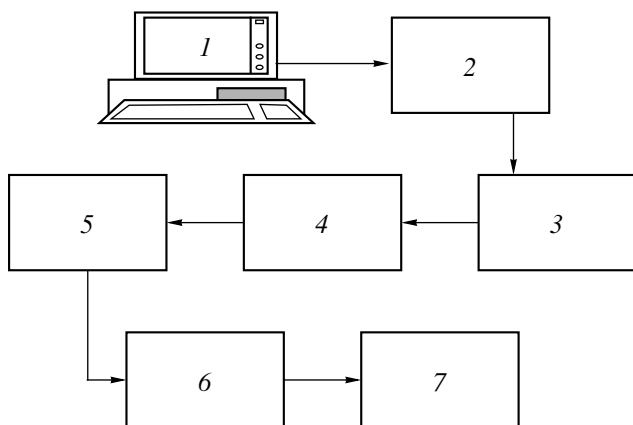


**Fig. 3.** Block diagram of a device for feeding the elements of the array: (1) PC, (2) interface, (3) buffer, (4) digital circuit controlling the frequency, amplitudes, and phases of the signals fed to the array elements, (5) 64-channel power amplifier with a short-circuit protection, (6) circuit for matching the impedances of the power amplifiers and elements, and (7) phased array.

A block diagram of an electronic device for controlling the array is shown in Fig. 3. The device operation is controlled by a computer 1 with the appropriate software; the computer is connected to the device through the interface 2 and a buffer 3. The frequency, amplitude, and phase of the signals at the elements of the

**Table 1.** Influence of the number of active elements of the array on the level of the main and secondary intensity peaks; focusing on the point (0, 0, 30 mm)

Order numbers of active elements/Total number of active elements	1–62/62	6–57/52	11–52/42	16–47/32
Maximum relative intensity at the focus	1.0	1.0	0.98	0.9
Maximum relative intensity of the secondary peaks in the focal plane	0.06	0.03	0.02	0.01
Maximum relative intensity of the highest secondary peak at a distance of 10 mm from the array	0.11	0.11	0.11	0.12
Length of the active part of the array (mm)	62	52	42	32
Reduction in the radiated ultrasonic energy (%)	0	16	32	48

array were controlled by a 8-bit digital circuit 4. The unit 5 is a 64-channel power amplifier with short-circuit protection. The output power of each amplifier in unit 5 is 10 W in the frequency range 0.1–1.5 MHz. The circuits 2–5 were developed at University of Michigan (USA). The impedance matching of the power amplifiers and the elements of the array 7 is carried out by the circuit 6. Each channel of this circuit contains an inductance coil and a matching transformer.

The acoustic field generated by the array was measured in a water-filled tank with sound-absorbing walls. For measuring the spatial distribution of acoustic pressure, we used a piezoceramic hydrophone, which was 0.6 mm in diameter and had a uniform angular sensitivity within 1 dB in the range of at least  $\pm 30^\circ$ , and a wide-band amplifier. The hydrophone was mounted on a positioner that made it possible to change and monitor the position of the hydrophone relative to the array in three mutually perpendicular directions. The measurements of acoustic pressure were carried out at 1-mm intervals in planes parallel to the array surface and at 5-mm intervals in planes perpendicular to the array.

In the development and subsequent use of the array, attention was given to the reduction in the secondary intensity peaks of the generated acoustic field. In the previous attempts of developing such arrays [9, 10], we employed a simple but efficient method based on the use of not all array elements for the ultrasound radiation but a certain part of them, which was determined by the required conditions of focusing. This approach is based on the fact that an inevitable acoustic interaction between the elements. The extent of this interaction depends on the dimensions of the elements, the way of their acoustic insulation, and other parameters and design features of the array. One of the consequences of the acoustic interaction between the elements is that the “effective” width of the elements may be considerably greater than their real geometric dimensions (e.g., 1.5 times greater for the array described in [9]). The real radiation pattern of each element correspondingly gets narrower. If the distance from the array to the focus is relatively small, the contribution of the elements located at the periphery of the array may become insignificant or become reduced to zero, and the energy radiated by these elements may be not only useless but even harmful from the point of view of safety of the

method. In the previous studies [9], it was found that the aperture of the active part of the array and the focal length should be related to each other in a certain way. If the real aperture is greater than needed, the “excess” elements should be switched off. If the focus is shifted relative to the acoustic axis, it turns out to be useful to switch off some elements on the side of the array opposite to the direction of the focus shift, so that the total length of the switched-off elements be equal to the value of the focus shift. The advantage of this approach lies in the fact that switching off the elements practically does not lead to a reduction in intensity at the focus but considerably reduces the level of secondary intensity peaks and the part of acoustic energy unnecessarily introduced in the tissues by the elements located at the array periphery.

Another approach is based on the introduction of certain irregularity (randomization) in the array operation. Since the physical nature of the discussed side lobes is connected with the regular structure of the array, one can expect that this method should result in a reduction in the level of the side lobes at the expense of some broadening of the main diffraction peak. It is clear that, in a laboratory-made array, its surface cannot be made ideally flat, and there is some difference in the element’s height, and, consequently, some phase shift. Naturally, the mentioned error in the determination of the phase values at each element may be compensated by measuring the phase shifts with a hydrophone placed at the focus and by introducing appropriate corrections. We deliberately did not use this method, which had been employed in [1], because the resulting “natural” randomization of the phase determination is more likely to lead to positive rather than negative consequences.

Both mentioned approaches were used for exciting the elements of the array described in this paper. The amplitude of signals at all active elements was constant to meet the requirements on the acoustic power of the array. Table 1 characterizes the dependence of the relative intensity measured at the focus and at secondary intensity peaks in the focal plane and nearby the array (at a distance of 10 mm from its surface) on the number of active elements when the array was focused at a distance of 30 mm along its acoustic axis (0, 0, 30 mm), which corresponds to the depth of focus in tissues 20 mm. The table also gives the length of the active part of the

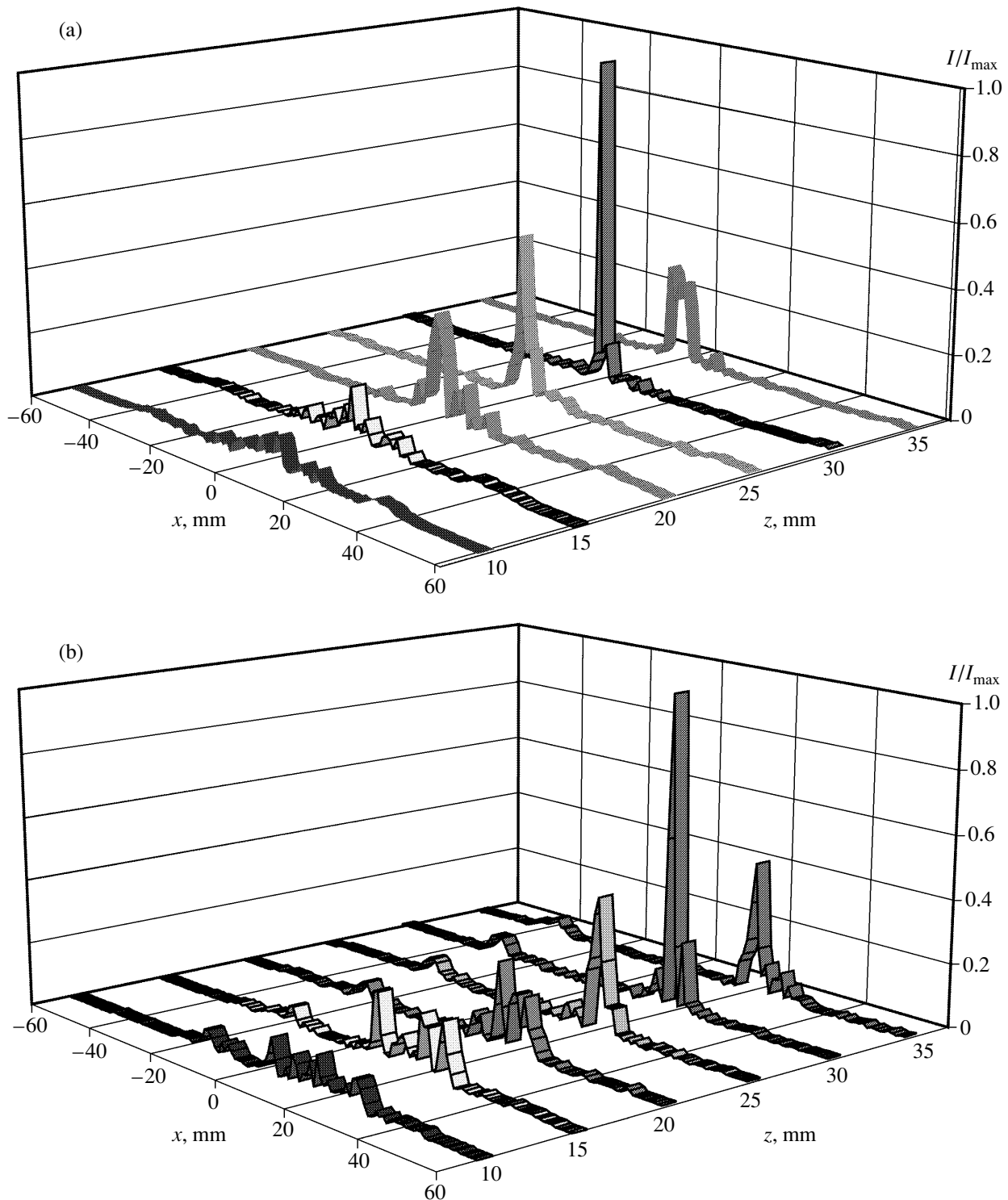


**Fig. 4.** Experimental spatial distribution of the relative intensity of the array field: (a) for focusing on the point (0, 0, 30 mm) with the use of 42 active elements out of 62 and with 10 elements at each end of the array being switched off; (b) for focusing on the point (20, 0, 30 mm) with the use of 42 active elements and with 20 elements on the side of the array opposite to the direction of the focus shift being switched off;  $x$  is the coordinate along the array aperture and  $z$  is the coordinate along the acoustic axis.

array and the extent of the reduction in the radiated ultrasonic energy.

Figure 4a shows the experimentally obtained distribution of intensity for the mentioned location of focus,

for the case of using 42 active elements out of 62. From Table 1 and Fig. 4a, it follows that the reduction in the number of active elements resulted in an acceptable distribution of intensity, with a decrease in the maxi-

**Table 2.** Influence of the number of active elements of the array on the level of the main and secondary intensity peaks; focusing on the point (20, 0, 30 mm)

Order numbers of active elements/Total number of active elements	1–62/62	21–62/42
Maximum relative intensity at the focus	1.0	1.0
Maximum relative intensity of the secondary peak in the focal plane	0.19	0.07
Maximum relative intensity of the highest secondary peak at a distance of 10 mm from the array	0.12	0.12
Reduction in the radiated ultrasonic energy (%)	0	32

imum intensity at the focus by only 2%. Simultaneously, the total radiated power was reduced by 32%, and the level of the secondary peaks in the focal plane dropped by a factor of 3 (down to 2% of the maximum intensity at the focus). The level of the maximum intensity of the highest secondary peak observed at a distance of 10 mm from the array remained the same. Under these conditions of focusing, the ratio between the length of the active part of the array (42 mm) and the focal length (30 mm) was 1.4.

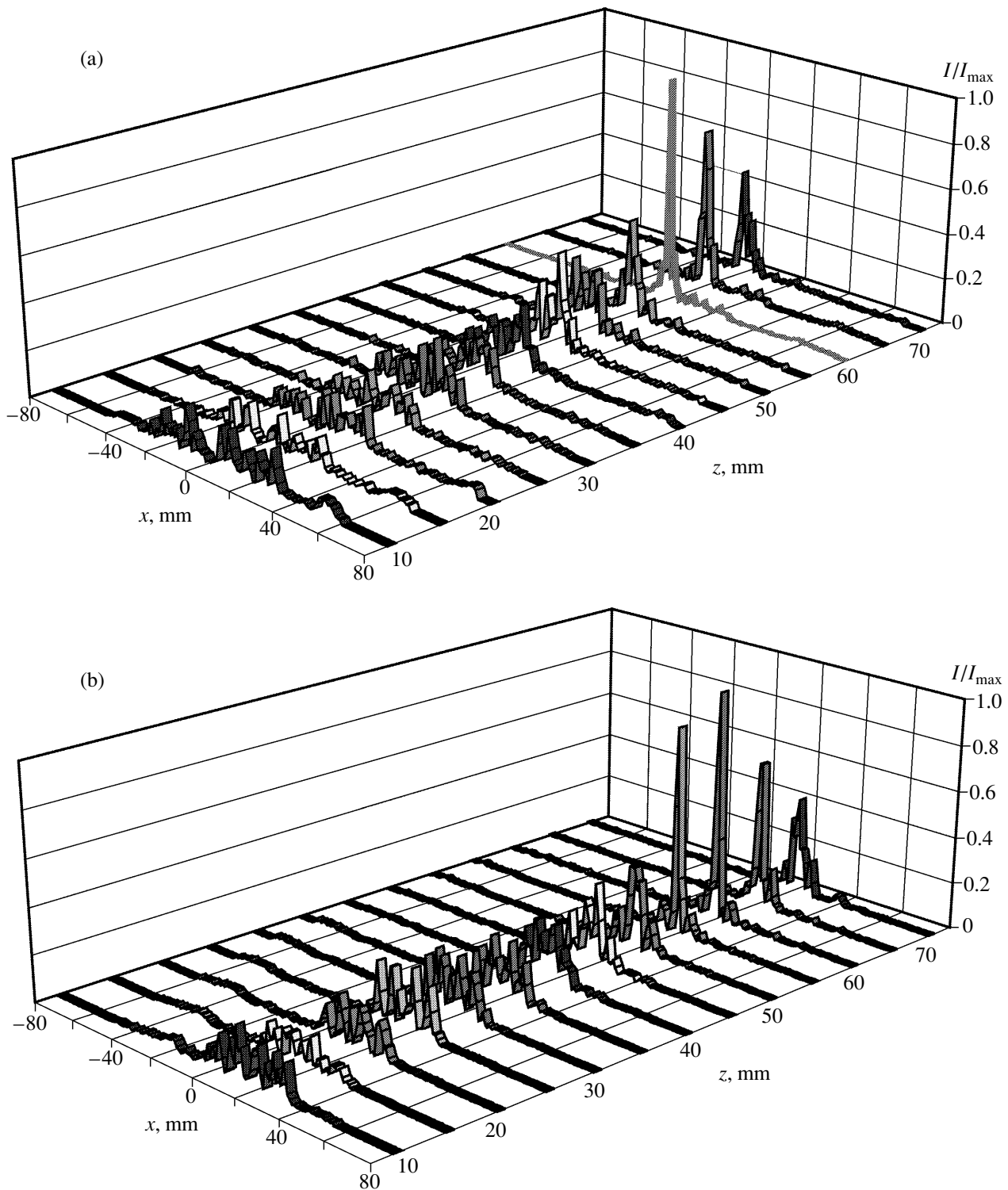
Similar data for the case of the array being focused at the same distance, but with a shift of 20 mm from acoustic axis (20, 0, 30 mm), are presented in Table 2.

Figure 4b illustrates the intensity distribution obtained in the experiment for the mentioned location of the focus when 20 elements of the array on the side opposite to the direction of the focus shift were switched off. From Table 2 and Fig. 4b, it follows that the reduction in the number of active elements from 62 to 42 resulted in an acceptable distribution of intensity without a decrease in the maximum intensity at the focus. The total radiated power was reduced by 32%, and the level of the secondary peak in focal plane dropped from 19% of the maximum intensity at the focus to 7% of this value. The level of the maximum intensity of the highest secondary peak located at a distance of 10 mm from the array remained invariable. However, when the focus was shifted by 30 mm from the acoustic axis (the spatial distribution of intensity for this case is not presented), then, for the number of active elements being equal to 62, 42, and 32, the maximum intensity at the focus practically did not change; the maximum relative intensity of the secondary peak in the focal plane was 0.7, 0.3, and 0.1, respectively; and the maximum relative intensity of the highest secondary peak at a distance of 10 mm from the array was 0.65, 0.5, and 0.45. It is clear that such a high level of secondary peaks observed for this focus shift is unacceptable from the point of view of safety.

Similar field measurements were performed for focusing at a distance of 60 mm from the array (which corresponds to the focus depth in tissue 50 mm), both without a shift of the focus relative to the acoustic axis of the array (0, 0, 60 mm) and with a shift of 20 mm from the axis (20, 0, 60 mm). In the first case for the

number of active elements 62, 56, 52, and 42, the maximum relative intensities at the focus were 1, 0.97, 0.94, and 0.76, respectively, which means that in this specific case it is better to use all 62 elements. Figure 5a displays the measured spatial distribution of intensity for this case. The ratio of the active part of the array aperture to the focal length for these conditions of focusing was 1.03. Figure 5b shows a similar distribution with the focus shifted by 20 mm from the acoustic axis (20, 0, 60 mm). In this case, the use of 42 active elements (20 elements on the side opposite to the direction of the focus shift were switched off) resulted in a reduction of the maximum intensity at the focus by only 2.5%, whereas the radiated acoustic power decreased by 32%, and the maximum relative intensity of the highest secondary peak in the focal plane dropped to 2% of the maximum intensity at the focus, compared to 5% for 62 active elements. However, when the focus was shifted by 30 mm from the acoustic axis (the spatial distribution of intensity is not presented), the maximum relative intensity at the focus for the number of active elements 62, 52, and 42 was 1.0, 0.97, and 0.72, respectively; the maximum relative intensity of the secondary peak in the focal plane was 0.15, 0.08, and 0.06; and the maximum relative intensity of the highest secondary peak at a distance of 10 mm from the array was 0.35, 0.2, and 0.2. These data are much better than for the similar focus shift in the case of the 30-mm focal length (see above), but the level of the secondary peaks for this shift is also excessively high.

The measurements of the acoustic power radiated by the array were performed with the use of a specially made 18-element array with the same elements and design as the 70-element array. The aperture of this array was about 20 mm (instead of the 77-mm aperture of the main array). The power was determined by measuring the radiation force with a target in the form of an absorber of sufficiently large dimensions (90 × 180 mm) to span the whole ultrasonic beam. The basic error of measurement was about ±10%. The acoustic power of the array was 55 W in a continuous mode of operation within 5 s; the limiting near-destructive operation mode of the array was not investigated because of the risk of damaging the circuits feeding the array. Another reason for not exceeding the mentioned power level was that,



**Fig. 5.** Experimental spatial distribution of the relative intensity of the array field: (a) for focusing on the point (0, 0, 60 mm) with the use of 62 active elements; (b) for focusing on the point (20, 0, 60 mm) with the use of 42 active elements and with 20 elements on the side of the array opposite to the direction of the focus shift being switched off. Coordinates are the same as in Fig. 4.

according to [1], the acoustic power of about 28 W per cm of linear array is more than sufficient for thermotherapy and thermosurgery of prostate tissue. Arrays with such level of power, on evidence of [2], as well as

According to the literature data [2] and to our experiments, arrays with such a power level can easily cause local thermal ablations in specimens of biological tissues (liver, beef). The results of the measurements with

the additional array allowed us to conclude that the maximum acoustic power of the main array was no less than 200 W.

Evidently, the wide clinical use of the ultrasonic method of prostate ablation depends on the development of means for monitoring the location of the focal region in prostate both before and after the ablation. The use of conventional ultrasonic diagnostic equipment intended for imaging the prostate tissue does not allow one to reliably monitor the location of the focus, since even a slight error in the rotation of the array about its axis may result in a considerable departure of the focus location from the required zone of ablation. The known ultrasonic diagnostic transducers mounted on the instruments for prostate surgery with single focused radiators [4–6] were intended for imaging the prostate tissue subjected to ablation but not for monitoring the location of the focus before ablation. The ultrasonic methods proposed recently for solving this problem [16, 17] are at the initial stage of development and make it possible to take measurements only in stationary specimens of tissue or in phantoms with predetermined properties. At the same time, a number of papers (e.g., [18–20]) point to the possibility of imaging not only the ablations at the focus but also minor, leading to no irreversible destruction of tissue, temperature increments by using methods based on the phenomenon of the nuclear magnetic resonance (NMR).

The development of an NMR imaging system of under- and overthreshold ultrasonic destruction of tissues was not the objective of this study. However, the design of our array was made compatible with the systems of NMR imaging of tissues. Moreover, in the array case 1 (Fig. 2), we mounted a removable receiving antenna 3 for NMR imaging, which was similar to the antenna described in [21] and consisting of a rectangular coil of dimensions  $86.5 \times 24$  mm. Such an NMR antenna has been used at the Hammersmith Hospital (London) for imaging the temperature increments of nonultrasonic nature. The measurements of the main parameters of this antenna (the Q-factor, the frequency shift, etc.) showed that the magnitudes of the parameters changed only slightly when the ultrasound array was brought near the antenna. All the above, as well as the encouraging literature data [18–20], allows us to anticipate the possibility of the NMR imaging of under- and overthreshold ultrasonic destruction produced in the prostate tissue by the designed (or similar) array.

Thus, the results of the laboratory evaluation of the ultrasonic part of the developed instrument show that the use of a linear array with the parameters specified above makes it possible to scan the focus within 30–60 mm in the axial direction and  $\pm 20$  mm in the perpendicular direction (which corresponds to the dimensions of prostate) with a practically acceptable level of secondary intensity peaks in the focal plane (considerably less than 10% of the maximum intensity at the focus) and

near the surface of the array (no greater than 10%). The measurements of the acoustic power radiated by the array show that it is quite sufficient for the thermal ablation of prostate tissue. The spatial distributions of intensity created by the array are not only much better than those obtained with other arrays developed earlier by us [9], but also no worse than the distributions obtained with the arrays developed in other laboratories [1, 2]. The designed array is a promising instrument for prostate surgery; however, the possibility of extensive clinical use of the ultrasound method depends on the subsequent development of combined systems that allow one to produce ultrasonic ablation and to monitor the location of the focal region in prostate before the ablation.

#### ACKNOWLEDGMENTS

This work was supported by the Health Department, UK, contract no. 121/3092. The authors are grateful to the Head of the Bioengineering Program at the University of Michigan, Prof. C. Cain, for his assistance in the development of the array control system, and to Dr. D. Gilderdale (Hammersmith Hospital, London) for manufacturing and preliminary testing the NMR receiving antenna for prostate imaging.

#### REFERENCES

1. E. B. Hutchinson, M. T. Buchanan, and K. Hynynen, *Med. Phys.* **23**, 767 (1996).
2. E. B. Hutchinson and K. Hynynen, *IEEE Trans. Ultrason. Ferroelec. Freq. Contr.* **43**, 1032 (1996).
3. F. Duck, *Physical Properties of Tissue* (Academic, London, 1990).
4. R. S. Foster, R. Bihrlé, N. T. Sanghvi, *et al.*, *Eur. Urol.* **23**, 29 (1993).
5. S. Madersbacher, C. Kratzik, N. Szabo, *et al.*, *Eur. Urol.* **23**, 39 (1993).
6. A. Gelet, J. Y. Chapelon, J. Margomari, *et al.*, *Eur. Urol.* **23**, 44 (1993).
7. J. W. Hand, E. Ebbini, D. O'Keefe, D., *et al.*, *Proc. IEEE Ultrason. Symp.* (1993), pp. 1225–1228.
8. L. R. Gavrilov, J. W. Hand, and P. Abel, in *Hyperthermic Oncology 1996*, Ed. by C. Franconi, G. Arcangeli, and R. Cavaliere (Tor Vergata University, Rome, 1996), Vol. 2, pp. 399–401.
9. L. R. Gavrilov, J. W. Hand, P. Abel, *et al.*, *IEEE Trans. Ultrason. Ferroelec. Freq. Contr.* **44**, 1010 (1997).
10. L. R. Gavrilov and J. W. Hand, *Ultrasonics Sonochemistry* **4**, 173 (1997).
11. K. Ocheltree and L. Frizzell, *IEEE Trans. Ultrason. Ferroelec. Freq. Contr.* **36**, 242 (1989).
12. E. Ebbini and C. A. Cain, *IEEE Trans. Ultrason. Ferroelec. Freq. Contr.* **36**, 540 (1989).

13. M.I. Skolnik, *Introduction to Radar Systems* (McGraw-Hill, New York, 1962; Mir, Moscow, 1965).
14. *Radar Handbook*, Ed. by M. I. Skolnik (McGraw-Hill, New York, 1970; Sovetskoe Radio, Moscow, 1977), Vol. 2.
15. G. M. Sverdlin, *Hydroacoustic Transducers and Arrays* (Sudostroenie, Leningrad, 1988).
16. S. Seip and E. S. Ebbini, *IEEE Trans. Biomed. Eng.* **42**, 828 (1995).
17. N. L. Bush, I. Rivens, G. R. ter-Haar, *et al.*, *Ultrasound Med. Biol.* **19**, 789 (1993).
18. H. E. Cline, K. Hynynen, R. D. Watkins, *et al.*, *Radiology* **194**, 731 (1995).
19. H. E. Cline, K. Hynynen, C. J. Hardy, *et al.*, *Magn. Reson. Med.* **31**, 628 (1994).
20. K. Hynynen, A. Chung, T. Fjield, *et al.*, *IEEE Trans. Ultrason. Ferroelec. Freq. Contr.* **43**, 1043 (1996).
21. N. M. de Souza, D. J. Gilderdale, R. Puni, *et al.*, *J. Magn. Reson. Imaging* **6**, 801 (1996).

*Translated by A.V. Svechnikov*

# Experimental Determination of the Mode Composition of the Acoustic Field Generated by a Parametric Radiator in a Waveguide

S. N. Gurbatov, S. A. Egorychev, V. V. Kurin,  
L. M. Kustov, and N. V. Pronchatov-Rubtsov

Lobachevskii State University, Nizhni Novgorod, pr. Gagarina 23, Nizhni Novgorod, 603600 Russia

e-mail: nikvas@rf.unn.runnet.ru

Received January 20, 1999

**Abstract**—A new method is proposed for recording the complex amplitude (i.e., the amplitude and phase) of signals generated by a nonlinear sound radiator in a low-mode oceanic waveguide. Results of model experimental studies of acoustic fields in Pekeris shallow-water waveguides are presented. Using the Fourier analysis of the complex amplitude of the acoustic signal detected by a receiver uniformly moving along the sound propagation track, specific features of the mode composition of the low-frequency field formed in a laboratory waveguide are revealed. The feasibility of the selective excitation of modes by varying the orientation angle of the parametric radiator in the vertical plane is demonstrated experimentally. © 2000 MAIK “Nauka/Interperiodica”.

The unique abilities of the parametric radiators (PR) of relatively small dimensions to generate highly directional low-frequency radiation allow their efficient application for the remote diagnostics of bounded and inhomogeneous media [1], as well as for the investigation of sound scattering by discrete inhomogeneities in water in a wide frequency band [2]. These properties of the PR, as well as the virtual absence of side lobes in their directional patterns, make them indispensable, in particular, for the acoustic waveguide excitation at given modes without using expensive and cumbersome phased arrays [3]. This fact extends the possibilities of such remote investigations as the long-range low-frequency acoustic diagnostics of discrete and smooth inhomogeneities located both in the water column and in the surface layers of the ocean bottom, the determination of statistical characteristics of wind waves on the sea surface, and the studies of the sea sediment parameters for [4]. The use of PR carried by ships offers considerable promise for acoustic ocean tomography [5].

The formation of the PR fields in shallow sea has been much studied theoretically (see, e.g., [6–8]). The experimental investigations carried out in this area of research are mainly limited to studying the amplitude-time characteristics of acoustic signals [1, 9], which restricts the variety of data available to the researchers. By using composite signals, e.g., frequency modulated ones, as well as more complicated techniques for recording and processing the received signals, it is possible to obtain new results, which makes the experimental data more valuable. Applying the correlation processing of a received pulsed PR signal by its convolution with the radiated reference signal, Donskoĭ *et al.*

[10] managed to single out a number of short pulses corresponding to signal arrivals over different rays or groups of modes.

The determination of the modal composition of an acoustic field from its horizontal structure recorded by a receiver uniformly moving along the sound propagation track is widely used in experiments [11–14]. In this case, not only the amplitude of the signal transmitted through a medium is continuously recorded, but its phase as well.

In this paper, a similar method was used for recording and processing the complex amplitude of a received signal in laboratory experimental investigations of the modal composition of a low-frequency field generated by a nonlinear source in a shallow-water acoustic waveguide. The fields of a difference-frequency wave were experimentally studied in the region of the intense interaction of high-frequency pump waves under various conditions of the mode excitation. The spatial spectra of signals were compared for various orientation angles of the pump wave radiator in the vertical plane. A comparative analysis of the horizontal interference structures of acoustic waveguide fields was also performed when the waveguide was excited by both parametric and omnidirectional sound sources operating in a nonlinear regime at a frequency of  $\omega_0$ .

Discuss now this signal processing method in more detail [12]. Assume that sound propagates in a homogeneous water layer overlying a homogeneous liquid halfspace (the simplest ocean model with an absorbing bottom, i.e., the so-called the Pekeris model). The layer of thickness  $h$  is bounded by the free water surface from

above and by a plane horizontal bottom from below. The velocity of longitudinal waves in the layer is  $c$ , the medium density is  $\rho$ , and the corresponding bottom parameters are  $c_1$  and  $\rho_1$ .

Consider the sound pressure field  $P$  of a point source located at a point  $r = 0$ ,  $z = z_0$  with the singularity  $P \propto \frac{1}{r}$  at  $r \rightarrow 0$ . Such a field is described by the Helmholtz equation

$$\frac{\partial^2 P}{\partial r^2} + \frac{1}{r} \frac{\partial P}{\partial r} + \frac{\partial^2 P}{\partial z^2} + k^2 P = -\frac{2}{r} \delta(z - z_0) \delta(r) \quad (1)$$

with the boundary conditions

$$P(r, 0) = 0, \quad [P]|_{z=h} = [V_z]|_{z=h} = 0, \quad (2)$$

where  $k^2 = \frac{\omega^2}{c^2}$ ,  $[P]$  and  $[V_z]$  denote the jumps of  $P$  and

$V_z$  at the boundary  $z = h$ , and  $\delta(r)$  and  $\delta(z - z_0)$  are the delta functions of the respective arguments.

The solution to inhomogeneous equation (1) is represented as a sum of normal waves [15]

$$P(r, z) = \pi i \sum_m \psi_m(z_0) \psi_m(z) H_0^{(1)}(\xi_m r), \quad (3)$$

where  $H_0^{(1)}(\xi_m r)$  is the zero-order Hankel function of the first kind,  $\psi_m(z)$  satisfies the equation

$$\frac{d^2 \psi_m}{dz^2} + [k^2 - \xi_m^2] \psi_m = 0, \quad (4)$$

and  $\xi_m$  is the horizontal wave number of the  $m$ th mode, the imaginary part of this number being nonzero because of the sound absorption in the bottom.

The sound absorption is taken into account by introducing the imaginary part of the wave number:  $k = \tilde{k} (1 + i\alpha)$ , where  $\tilde{k} = \frac{\omega}{c}$ . Using the asymptotic expression for the Hankel function for large values of the argument and representing  $\xi_m$  as  $\xi_m = \xi_m' + i\beta_m$ , where  $\beta_m$  is the attenuation coefficient of the respective mode, expression (3) can be written as

$$P(r, z) = \frac{i}{\rho} \left( \frac{2\pi}{r} \right)^{\frac{1}{2}} \sum_m \frac{1}{\sqrt{\xi_m}} \varphi_m(z_0) \varphi_m(z) \times \exp[-\beta_m r] \exp \left[ i \left( \xi_m' r - \frac{\pi}{4} \right) \right]. \quad (5)$$

Denoting  $\frac{i}{\rho} \sqrt{\frac{2\pi}{\xi_m}} \varphi_m(z_0) \varphi_m(z) = Q_m(z_0, z)$  and restoring the temporal factor previously omitted, we obtain the

following expression for the complex amplitude of the field excited by a harmonic point source operating at the frequency  $f_0$ :

$$P(r, z_0, z, t) = \frac{1}{\sqrt{r}} \sum_m Q_m(z_0, z) \quad (6)$$

$$\times \exp[-\beta_m r] \exp \left[ i \left( \xi_m' r - \omega_0 t - \frac{\pi}{4} \right) \right],$$

where  $\omega_0 = 2\pi f_0$ . In the experiment, the recorded signal coincides with the real component of expression (6) and, therefore, can be written as

$$P(r, z_0, z, t) = \frac{C}{\sqrt{r}} \sum_m Q_m(z_0, z) \quad (7)$$

$$\times \exp[-\beta_m r] \cos(\xi_m' r - \omega_0 t),$$

where the constant  $C$  depends on the radiator power. Note that the product  $Q_m(z_0, z) \exp[-\beta_m r]$  specifies the amplitude of the  $m$ th mode at the point of reception  $(r, z)$ .

In order to single out the complex envelope of the recorded signal, the latter is multiplied by reference harmonic signals of frequency  $\omega_0$  shifted in phase by  $\pi/2$  relative to each other; then, the signal is subjected to low-frequency filtering. According to (7), the quadrature components obtained as a result of the described operations are expressed as follows:

$$P_1(z_0, z, r) = \frac{a_1}{\sqrt{r}} \sum_m Q_m(z_0, z) \exp[-\beta_m r] \cos(\xi_m' r), \quad (8)$$

$$P_2(z_0, z, r) = \frac{a_2}{\sqrt{r}} \sum_m Q_m(z_0, z) \exp[-\beta_m r] \sin(\xi_m' r), \quad (9)$$

where  $a_1$  and  $a_2$  are the constants determined by the amplification coefficient of the recording equipment (in the experiments, by varying the amplification coefficient, we achieved the equality of these constants).

Assume that the receiving hydrophone moves away from the radiator with a constant speed  $v$  starting from a point with the coordinates  $(R_0, z)$ . In this case, the dependence of the quadrature components on time will be determined by expressions (8) and (9), where  $r$  is replaced by  $R_0 + vt$ .

The resulting quadrature components are used to form the complex envelope of the recorded signal, and then its Fourier transform is calculated. The latter presents the spatial spectrum of the horizontal section of

the sound field along the line  $z = \text{const}$ , where  $z$  is the vertical coordinate of the receiver

$$G(\xi, R_0) = \left| \frac{1}{L} \int_{R_0}^{R_0+L} P(z_0, z, r) \exp[-i\xi(r - R_0)] dr \right|. \quad (10)$$

Here,  $L$  denotes the length of the path covered by the receiver. This quantity determines the resolution in the spatial frequency  $\xi$ .

For a small variation of the quantity  $\frac{1}{\sqrt{r}} \exp[-\beta_m r]$  on the interval  $L$ , we have

$$G(\xi, R_0) = \left| \frac{\text{const}}{\sqrt{R^*}} \sum_m Q_m \exp[-\beta_m R^* + i\xi_m R_0] \frac{\sin(\xi - \xi_m) \frac{L}{2}}{(\xi - \xi_m) \frac{L}{2}} \right|, \quad (11)$$

where  $R^*$  is the distance from the source to the middle of the waveguide part through which the receiver travels in the process of recording.

If the conditions of the resolution of individual normal waves are satisfied [11]

$$L \gg \frac{2\pi}{\min|\xi_m - \xi_n|}, \quad m \neq n, \quad (12)$$

the maximum spectral components will be those for which  $\xi$  coincides with the longitudinal wave number  $\xi_m$  of some mode. In this case, the amplitude of the spectral component (correct to a constant factor common for all modes) coincides with the amplitude of the corresponding mode (clearly, if condition (12) is met). Thus, the difference in the horizontal wave numbers allows one to select the modes of the spectrum  $G(\xi, R_0)$ .

The proposed algorithm for analyzing the received signal in investigating the field of a PR provides the information not only on the amplitude, but on the phase of the received signal as well, which allows one to study the specific features of the modal composition of the low-frequency sound field in a model acoustic waveguide.

It should be noted that the use of the described method in the parametric excitation of waveguides requires highly stable sources of harmonic signals, with a relative frequency stability no worse than  $10^{-9}$ .

The concept of the method of recording the complex amplitude of the PR field is as follows. The received low-frequency signal of the difference-frequency wave (DFW), which is formed as the result of the nonlinear interaction of two primary pump waves of frequencies  $\omega_1$  and  $\omega_2$ , has the frequency  $\omega_0 = \omega_1 - \omega_2$ . The phase of the difference-frequency electric signal obtained by multiplying two oscillations with frequencies  $\omega_1$  and  $\omega_2$  of the same generators that are used in the radiation channel is obviously related to the phase of the radiated

signal. This fact allows one to use this electric signal as a reference one. In this case, the phase difference between this signal and the received signal transmitted through the waveguide under study is uniquely determined by the radiator–receiver distance. Such a phase dependence of these signals considerably loosens the requirements on the stability of the oscillators generating the primary pump waves of the PR, since only their short-time stability is important during the wave propagation from the source to the receiver.

The application of this method allowed us to perform the selection of the modes forming the PR field in a waveguide, to determine the phase and group velocities and the sound pressure distribution in depth for individual normal waves.

The experimental investigations of the modal composition of the field generated by the PR were carried out in a model hydroacoustic waveguide in a laboratory tank (500 cm in length, 65 cm in width, and 55 cm in depth). The tank had a suspended bottom with a rubber coating. With the use of screws, the upper boundary of the rubber layer (4 cm thick) could be fixed relatively to the water surface with the accuracy of  $\Delta h = 2$  mm in depth. The rubber layer thickness variations were of the order of  $\delta h_{\text{max}} = 0.5$  mm. The waveguide was modeled by a plane homogeneous water layer of thickness  $h = 38 \pm 1$  mm with the sound velocity  $c = 1468$  m/s. The water layer overlaid a thick rubber layer with the density  $\rho_1 = 1.13$  g/cm<sup>3</sup>, the longitudinal wave velocity  $c_1 = 1778$  m/s, and the loss tangent  $\alpha = 0.28$ . The comparison of the previous experimental results obtained using the same setup (see, e.g., [12, 16]) with numerical calculations shows that our two-layer waveguide is adequately described in the framework of the Pekeris model. In mathematical modeling, the layered rubber bottom is replaced by an effective liquid halfspace where the sound velocity equals the longitudinal sound velocity in rubber, and the presence of shear waves in rubber is taken into account by introducing an addition to the attenuation coefficient.

Figure 1 shows a simplified schematic diagram of the setup operating in the parametric regime and the relative positions of the radiator and receiver during the experiment.

A piezoceramic pump transducer ( $S$ ) represented a circular piston radiator of the diameter  $2a = 1.8$  cm. The center of its aperture was located in the waveguide at a depth  $z_0$ . The radiator was mounted on a cross-bar which allowed us to change the radiator depth (with an error no more than 1 mm) and orient the axis of the PR radiation in the vertical plane (the angle  $\theta$  in Fig. 1) with an accuracy no worse than  $1^\circ$ .

Biharmonic signals with the frequencies  $f_1 = 3.2$  and  $f_2 = 3.0$  MHz, where  $f_i = \frac{\omega_i}{2\pi}$ ,  $i = 1, 2$ , were fed to the radiator. For determining the regime of the pump transducer operation, some preliminary experiments were

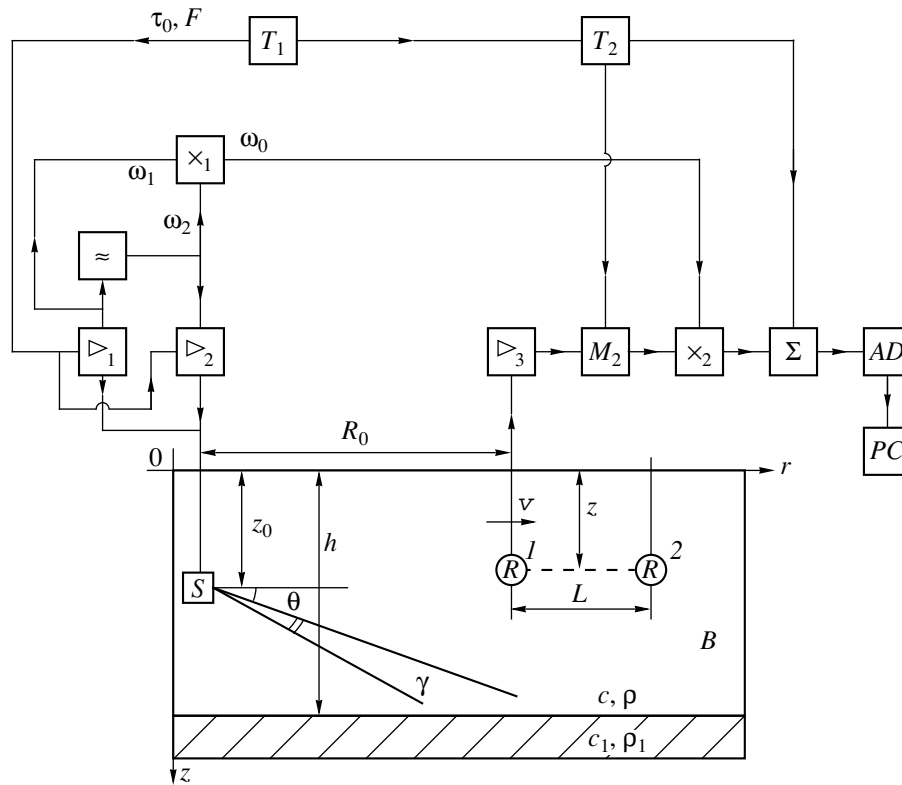


Fig. 1. Schematic diagram of the experimental setup.

carried out in an unbounded space. The attenuation length experimentally found was equal to  $l_0 = 1.47$  m. As is known [1], the PR operation regime is determined by the parameter  $\eta = \frac{l_0}{R_f} \left( \frac{\omega_0}{\omega_1} \right)$ , where  $R_f$  is the length of the diffraction divergence at the high frequency (the near zone). For conditions of our experiment, this parameter equals  $\eta = 0.135$ , i.e., the regime of the PR operation was close to the Westervelt regime.

For generating high-frequency oscillations, we used two powerful amplifiers ( $\triangleright_1$  and  $\triangleright_2$ ). To their inputs, two continuous sinusoidal signals of frequencies  $\omega_1$  and  $\omega_2$  were supplied from a block of reference frequencies ( $\approx$ ). For reducing the level of the reverberation noise associated with the finite size of the object tested, the impulse regime of radiation was used. The duration of the radiated pulses  $\tau_0$  satisfied the condition  $\omega_0 \tau_0 \gg 2\pi$ , and thus a quasimonochromatic regime of the radiation was provided.

As a generator of modulation pulses ( $T_1$ ), we used a generator of video pulses of a rectangular form with the controlled duration  $\tau_0$  and the repetition frequency  $F = 64$  Hz. These pulses arrived at the modulation inputs of the amplifiers ( $\triangleright_1$  and  $\triangleright_2$ ) where radio pulses were formed and amplified. The signal thus formed arrived at the pump wave transducer ( $S$ ).

For synchronizing the operation of the total setup, we used a synchro pulse produced by the pulse generator ( $T_1$ ).

Having passed through the medium under study, the signal arrived at an omnidirectional piezoceramic receiver ( $R$ ), which was mounted on a rod capable of uniformly moving along the laboratory tank ( $B$ ) at a fixed depth  $z$ . In all experiments, the speed of the receiver motion along the hydroacoustic tank was  $v = 1.8$  cm/s. The uncontrollable speed fluctuations did not exceed  $\pm 0.005$  cm/s. After a two-stage amplification and filtering performed in an amplifier ( $\triangleright_3$ ), the received pulsed signal arrived to a strobe-bloc ( $M_2$ ) controlled by an impulse strobe generator ( $T_2$ ). This generator produced pulses of duration  $\tau_1$  with a controlled time delay relative to the radiated pulse onset. These pulses allow one, first, to suppress pulsed reverberation noise and, second, to record the amplitude at any point within the signal. The strobe signal arrived at one of the multiplier ( $\times_2$ ) inputs. The other input of this multiplier was fed with a continuous reference signal obtained by multiplying the signals of frequencies  $\omega_1$  and  $\omega_2$  in the multiplier ( $\times_1$ ). As a result, at the multiplier output ( $\times_2$ ), video pulses were formed with the duration  $\tau_1$  and amplitude depending on both the received signal amplitude and the difference in phase between the reference and received signals. The transformed signal proceeded to an integrator ( $\Sigma$ ), which was controlled by the impulse of the strobe generator

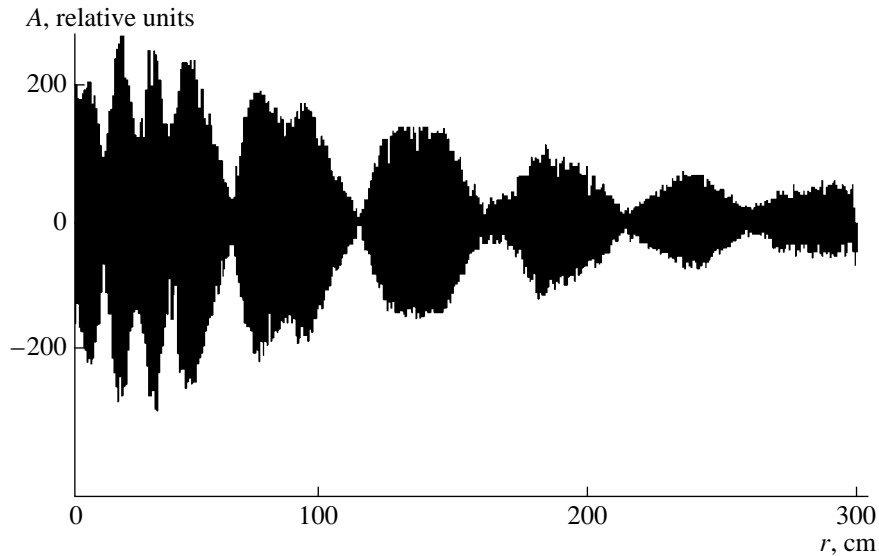


Fig. 2. Horizontal interference structure of the PR field in the waveguide ( $z = 10$  mm,  $\theta = 10^\circ$ ).

( $T_2$ ). After the integrator, the constant voltage whose level was proportional to the pulsed signal amplitude at the input of the integrator, proceeded to the input of the ten-bit analog-to-digital converter (AD) and was stored in the computer memory (PC) for further processing. In all experiments, the quantization frequency in analog-to-digital conversions was 50 Hz.

The second quadrature component of the complex amplitude of the sound field (see (9)) is obtained in a similar way, but, as a reference signal, we used the signal from the multiplier ( $\times_1$ ), which was out of phase by  $\frac{\pi}{2}$  relative to the first signal.

The normal waves were separated from the spatial spectra using the fast Fourier transform. The spectral component amplitudes characterize the mode amplitudes averaged over the analysis window  $L$  for a fixed depth of reception. If we record the complex amplitude of the acoustic field at different reception depths and perform the spectral processing, we will be able to restore experimentally the vertical structure of the sound pressure in each of the modes forming the field at the given distance from the radiator.

Figure 2 exhibits the horizontal interference structure of the acoustic field of the PR in the waveguide at a depth of  $z = 10$  mm. In this and all subsequent experiments, the center of the radiator aperture was at a depth of  $z_0 = 19$  mm, i.e., in the middle of the water layer. The axis of the directional pattern of the radiator was directed toward the bottom at the angle  $\theta = 10^\circ$ . This angle coincides with the angle  $\beta_2 = 10.5^\circ$  of the Brillouin wave of the second mode of this waveguide. For the first, third, and fourth modes, these angles were  $\beta_1 = 5.3^\circ$ ,  $\beta_3 = 16^\circ$ , and  $\beta_4 = 21.5^\circ$ , respectively. Because the directional pattern width  $\gamma$  is about  $8^\circ$ , it is evident that,

for such a geometry of radiation, the first and second modes of the waveguide are excited in the best way, which can be seen in Fig. 2. The contribution of the third mode to the total field is significant only at distances of about 60 cm from the radiator. For this case, the modal spectrum is presented in Fig. 3. The abscissa axis represents the horizontal wave numbers, and the ordinate axis represents the amplitudes of the spectral components (in relative units). The vertical lines mark the calculated values of the horizontal wave numbers of the first four propagating modes. As seen in Fig. 3, the experimental values of the wave numbers agree well

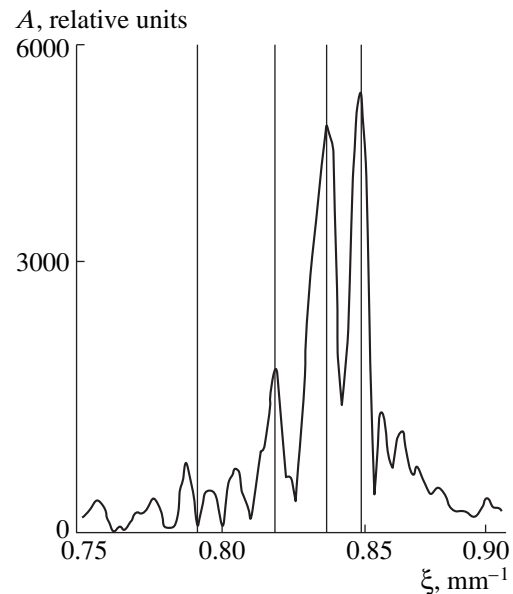
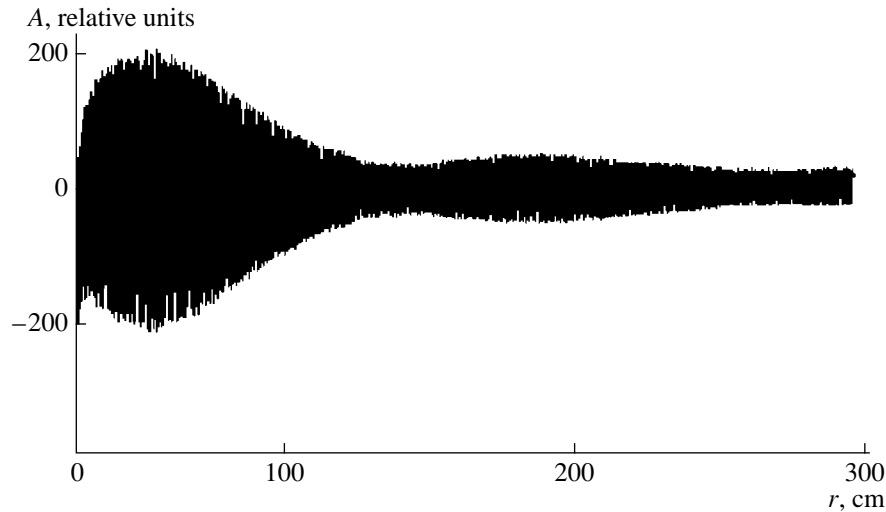


Fig. 3. Spatial spectrum of the received signal of the difference-frequency wave ( $z = 10$  mm,  $\theta = 10^\circ$ ).



**Fig. 4.** Horizontal interference structure of the PR field in the waveguide ( $z = 20$  mm,  $\theta = 0^\circ$ ).

with the calculated ones for the first three modes. In all experiments, the initial distance between the source and the receiver was not varied and was equal to  $R_0 = 5$  cm. The spectral analysis was performed with the algorithm of fast Fourier transform over the aperture  $L = 300$  cm. To reduce the levels of the side outliers in the received signal spectrum, we used the Blackman temporal weight window.

As the orientation angle  $\theta$  of the axis of the PR directional pattern varies, the mode composition of the sound field significantly changes. Figure 4 presents the horizontal interference structure of the field of the difference-frequency wave at a depth of  $z = 20$  mm for the horizontal orientation of the radiator  $\theta = 0^\circ$ . The spatial

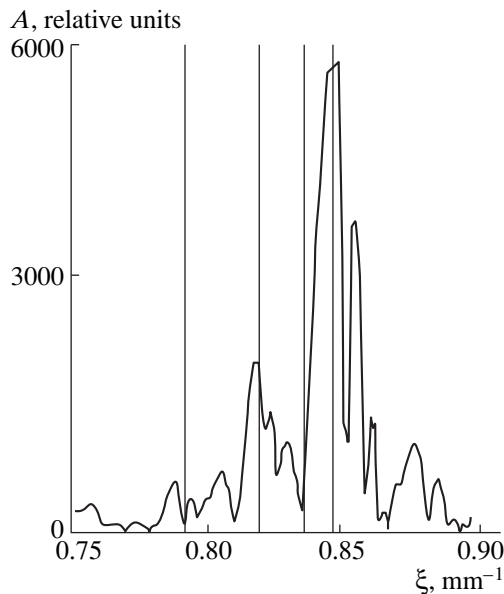


**Fig. 5.** Spatial spectrum of the received signal of the difference-frequency wave ( $z = 20$  mm,  $\theta = 0^\circ$ ).

spectrum of this realization is shown in Fig. 5. In this case, the analysis shows that, along with the spectral components corresponding to the first and third propagating modes of this waveguide ( $\xi_1 = 0.85$  mm $^{-1}$  and  $\xi_3 = 0.82$  mm $^{-1}$ ), the spectrum of the received signals has a maximum whose horizontal wave number is equal to  $\xi_0 = 0.86$  mm $^{-1}$ . Because the sound velocity in

the water layer is  $c = 1468$  m/s, we obtain that  $k = \frac{\omega_0}{c}$

equals  $0.856$  mm $^{-1}$ , which almost coincides with  $\xi_0$ . The presence of the spectral component corresponding to signal propagation in the free space is related to the fact that the interaction of the low-frequency wave with the waveguide boundaries begins at some distance from the radiator. Near the parametric transducer, the pump wave propagates as an almost nondivergent beam (the

diffraction length is  $R_f = \frac{4a^2}{\lambda_1} = 65$  cm, where  $a$  is the

radius of the radiator aperture and  $\lambda_1$  is the wavelength at the pump frequency). As a result, the difference-frequency wave propagates without any significant interaction with the boundaries, i.e., almost in the same manner as in free space. The analysis of the interference structures and modal spectra of the waveguide fields excited by an omnidirectional linear source shows that such a component is absent in the received signal. In this case, the interaction of the radiated wave with the waveguide boundaries begins in the immediate vicinity of the source. For comparison, Fig. 6 presents the horizontal interference structure of the complex amplitude of the field at a frequency of 200 kHz when the waveguide is excited by a linear point source. The source and the receiver were located in the middle of the water layer ( $z_0 = z = 20$  mm). The sound field at this depth is mainly formed by the first and third modes, while the contribution of the second mode is insignificant.

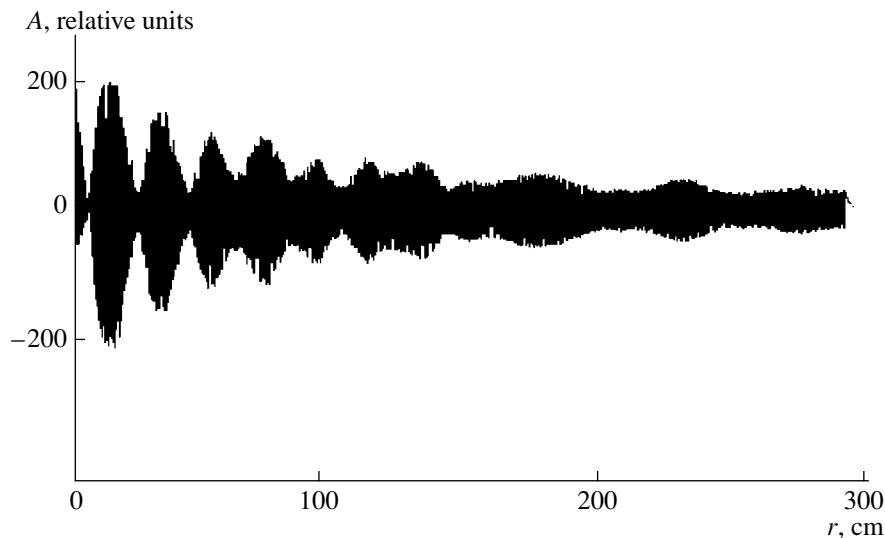


Fig. 6. Horizontal interference structure of a point source operating in the linear regime in the waveguide ( $z = 20$  mm).

With the variation of the angle of the axis of the PR radiation in the vertical plane, the excitation of the waveguide modes occurs mainly for such angles of the Brillouin waves, which are close to  $\theta$ , the number of the excited waves being determined by the low-frequency directional pattern width [8–10]. In particular, the variation in the spectrum of the received modes with varying excitation conditions can be seen from the comparison of Figs. 3 and 5.

Thus, the model experiments aimed at studying the acoustic fields of the difference-frequency waves in the shallow-water Pekeris waveguides with the use of the new method of the determination of the modal composition allowed us to determine the phase and group velocities and the sound pressure distributions in the waveguide depth for individual normal waves, as well as to reveal a component specific for the free space in the received signal spectrum. The analysis of the interference structures and modal spectra of the waveguide fields generated by an omnidirectional linear sound source shows that such a component is absent in the received signal. A possibility of the selective mode excitation by varying the orientation angle of the parametric radiator in the vertical plane was experimentally demonstrated.

#### ACKNOWLEDGMENTS

This work was supported by the Russian Foundation for Basic Research (project nos. 98-02-16402 and 99-02-18354) and the INTAS grant no. 97-11134.

#### REFERENCES

1. B. K. Novikov and V. I. Timoshenko, *Parametric Arrays in Underwater Detection and Ranging* (Sudostroenie, Leningrad, 1989).
2. P. A. Chinnery, V. F. Humphrey, and J. Zhang, *J. Acoust. Soc. Am.* **101**, 2571 (1997).
3. D. F. Gingras, *J. Acoust. Soc. Am.* **103**, 195 (1998).
4. T. G. Muir, in *Physics of Sound in Marine Sediments*, Ed. by L. Hampton (Plenum, New York, 1974; Mir, Moscow, 1977).
5. V. V. Goncharov, V. Yu. Zaitsev, V. M. Kurteпов, *et al.*, *Acoustic Ocean Tomography* (Inst. of Applied Physics, Nizhni Novgorod, 1997).
6. S. N. Gurbatov, V. Yu. Zaitsev, A. G. Kosterin, *et al.*, in *Acoustics in the Ocean* (Nauka, Moscow, 1992), pp. 208–227.
7. N. E. Karabutova and B. K. Novikov, *Akust. Zh.* **32**, 65 (1986) [*Sov. Phys. Acoust.* **32**, 38 (1986)].
8. V. Yu. Zaitsev, L. A. Ostrovskii, and A. M. Sutin, *Akust. Zh.* **33**, 37 (1987) [*Sov. Phys. Acoust.* **33**, 21 (1987)].
9. V. Yu. Zaitsev, V. V. Kurin, and A. M. Sutin, *Akust. Zh.* **35**, 266 (1989) [*Sov. Phys. Acoust.* **35**, 160 (1989)].
10. D. M. Donskoï, V. Yu. Zaitsev, K. A. Naugol'nykh, *et al.*, *Akust. Zh.* **39**, 266 (1993) [*Acoust. Phys.* **39**, 141 (1993)].
11. N. V. Gorskaya, G. N. Nikolaev, T. A. Rychova, *et al.*, *Akust. Zh.* **27**, 202 (1981) [*Sov. Phys. Acoust.* **27**, 110 (1981)].
12. A. L. Virovlyansky, V. V. Kurin, N. V. Pronchatov-Rubtsov, *et al.*, *J. Acoust. Soc. Am.* **101**, 163 (1997).
13. V. V. Tyutekin, D. V. Stepanov, S. P. Klimov, *et al.*, USSR Inventor's Certificate no. 661 326 (1979).
14. V. V. Tyutekin and V. N. Merkulov, *Akust. Zh.* **30**, 405 (1984) [*Sov. Phys. Acoust.* **30**, 242 (1984)].
15. L. M. Brekhovskikh and Yu. P. Lysanov, *Fundamentals of Ocean Acoustics* (Gidrometeoizdat, Leningrad, 1982; Springer, Berlin, 1982).
16. V. V. Kurin, O. V. Lebedev, and N. V. Pronchatov-Rubtsov, *Akust. Zh.* **40**, 464 (1994) [*Acoust. Phys.* **40**, 435 (1994)].

Translated by Yu.P. Lysanov

# Sound Scattering by Small Compact Inhomogeneities in a Sea Waveguide

A. D. Zakharenko

*Pacific Institute of Oceanology, Far East Division, Russian Academy of Sciences,  
ul. Baltiĭskaya 43, Vladivostok, 690041 Russia*

*e-mail: root%dan86@poi/marine/su*

Received June 24, 1998

**Abstract**—The scattering of sound by small compact inhomogeneities of density, sound velocity, and internal boundaries in the sea bottom is considered from the viewpoint of the redistribution of the acoustic energy between waveguide modes. Formulas are derived for the coefficients of intermode interaction; these formulas generalize the previous ones presented in the literature and are convenient for solving direct and inverse problems. The results are illustrated by the corresponding calculations. © 2000 MAIK “Nauka/Interperiodica”.

An approach to the problem of sound scattering by small compact inhomogeneities of the density, the sound velocity, and the internal boundaries of the sea bottom from the viewpoint of the redistribution of the acoustic energy between waveguide modes was successfully used in a number of works as a fairly convenient method for handling three-dimensional problems. We note only some of them: Ingenito [1] considered the scattering from a closed body, Wetton and Fawcett [2] studied the scattering by inhomogeneities of the sea bottom, and Fawcett [3] considered the scattering by a cylindrical centrally symmetric inhomogeneity of the density and the sound velocity. The results of paper [2] were used in [4] for setting and solving some direct and inverse problems.

In this paper, we derive new formulas for the coefficients of the intermode scattering of sound generated by a point source from small compact inhomogeneities; these formulas generalize the previous results obtained in [2, 3]. The use of the Fourier series expansion of inhomogeneities in the angular variable and the Fourier–Bessel series expansion in the radial variable allowed us to obtain simple formulas that are convenient for computation. The assumption that the source is far from the scatterer is not used in these formulas, which is important for some applications.

We consider a stationary sound field in the region defined by the condition  $-H \leq z \leq 0$ ,  $H = \text{const}$ , where the field is described by the Helmholtz equation and the boundary conditions

$$\begin{aligned} \rho \operatorname{div} \left( \frac{1}{\rho} \operatorname{grad} u \right) + \frac{\omega^2}{c^2} u &= f, \\ u|_{z=0} &= 0, \quad \frac{\partial u}{\partial z} \Big|_{z=-H} = 0. \end{aligned} \quad (1)$$

Here,  $u$  is the complex sound pressure,  $\rho$  is the density,  $c$  is the sound velocity,  $\omega$  is the circular frequency, and  $f$  is the source function.

We assume that the density and the sound velocity are piecewise continuous functions with discontinuities at the surfaces  $z = h^{(l)}(x, y)$ ,  $l = 1, \dots, N$ . In this case, problem (1) has piecewise smooth solutions with the conventional conditions of continuity for the sound pressure and the normal velocities at  $z = h^{(l)}(x, y)$ ,  $l = 1, \dots, N$  (section 1.1 in [5]).

In a plane-layered medium, separate modes propagate independently of one another. We will study the mode conversion caused by small perturbations of the internal boundaries, density, and sound velocity on the background of the plane-layered medium. We introduce a small parameter  $\epsilon$  and assume that the sound velocity, the density, and the internal boundaries can be represented as  $c = c_0(z) + \epsilon c_1(x, y, z) + \dots$ ,  $\rho = \rho_0(z) + \epsilon \rho_1(x, y, z) + \dots$ , and  $h^{(l)}(x, y) = h_0^{(l)} + \epsilon h_1^{(l)}(x, y) + \dots$  ( $l = 1, \dots, N$ ), respectively, where  $h_0^{(l)}$  are constants and  $\rho_1$ ,  $c_1$ , and  $h_1^{(l)}$  equal zero everywhere outside some bounded region  $\Omega$ . In this paper, we will restrict our consideration of this problem to the approximation of a single scattering (the Born approximation) and assume that the sound field is represented as  $u = u_0 + \epsilon u_1 + \dots$ , where  $u_0$  is the source field or the incident field and  $u_1$  is the principal term of the scattering field.

Substituting these expansions in equation (1) and separating the terms multiplying different powers of  $\epsilon$ , we obtain a sequence of boundary problems. In the order  $O(1)$ , we obtain problem (1) with  $u$ ,  $\rho$ , and  $c$  being replaced by  $u_0$ ,  $\rho_0$ , and  $c_0$ , respectively. It is known [5] that the solution to this problem with a point source represented as  $f = \delta(z - z_0)\delta(x - x_0)\delta(y - y_0)$  has the form

$u_0(x, y, z) = \sum_n H_0^{(1)}(k_n \xi) \phi_n(z) \phi_n(z_0)$ , where  $\xi = \sqrt{(x-x_0)^2 + (y-y_0)^2}$  and  $\phi_n$  is the mode with the spectral parameter (the wave number)  $k_n$ . The latter mode is the solution to the ordinary spectral problem for a layered medium with the conditions of continuity for  $\phi_n$  and  $(1/\rho_0)d\phi_n/dz$  at  $z = h_0^{(l)}$ ; the function  $\phi_n$  with the weighting function  $1/\rho_0$  is normalized within the segment  $[-H, 0]$ . Because our concern is only with the interrelation of the modal composition of incident and scattered fields, we will assume that the incident field consists only of the  $j$ th mode,  $u_0 = H_0^{(1)}(k_j \xi) \phi_j(z)$ .

In the order  $O(\epsilon)$ , we obtain

$$\begin{aligned} & \rho_0 \operatorname{div} \left( \frac{1}{\rho_0} \operatorname{grad} u_1 \right) + \frac{\omega^2}{c_0^2} u_1 \\ &= \frac{1}{\rho_0} \frac{\partial \rho_1}{\partial x} \frac{\partial u_0}{\partial x} + \frac{1}{\rho_0} \frac{\partial \rho_1}{\partial y} \frac{\partial u_0}{\partial y} \\ &+ \frac{\partial}{\partial z} \left( \frac{\rho_1}{\rho_0} \right) \frac{\partial u_0}{\partial z} + 2 \frac{\omega^2 c_1}{c_0^2 c_0} u_0 \end{aligned} \quad (2)$$

with the conditions at  $z = h^{(l)}(x, y)$  ( $l = 1, \dots, N$ )

$$\begin{aligned} & \left( \frac{1}{\rho_0} \frac{\partial u_1}{\partial z} \right)_+ - \left( \frac{1}{\rho_0} \frac{\partial u_1}{\partial z} \right)_- \\ &= h_1^{(l)} \omega^2 u_0 \left( \frac{1}{c_{0+} \rho_{0+}} - \frac{1}{c_{0-} \rho_{0-}} \right) \\ &+ \frac{\partial h_1^{(l)}}{\partial x} \frac{\partial u_0}{\partial x} \left( \frac{1}{\rho_{0+}} - \frac{1}{\rho_{0-}} \right) + \frac{\partial h_1^{(l)}}{\partial y} \frac{\partial u_0}{\partial y} \left( \frac{1}{\rho_{0+}} - \frac{1}{\rho_{0-}} \right), \\ &u_{1+} - u_{1-} = h_1^{(l)} \left[ \left( \frac{\partial u_0}{\partial z} \right)_- - \left( \frac{\partial u_0}{\partial z} \right)_+ \right], \end{aligned} \quad (3)$$

where the plus sign marks the limits of the variables at the point under study  $z = z_0$  from above, i.e., at  $z > z_0$ , and the minus sign marks the corresponding limits from below. We will seek the scattered field in the form  $u_1 = \sum_n C_{jn}(x, y) \phi_n$  and call the functions  $C_{jn}(x, y)$  the scattering coefficients from the  $j$ th mode into the  $n$ th mode. Substitute now expressions for  $u_0$  and  $u_1$  in (2), multiply both parts of this equation by  $\phi_n/\rho_0$ , and integrate this expression with respect to  $z$  from  $-H$  to  $0$ . Using the conditions of the mode normalization and conditions (3), we obtain the equation for the coefficients  $C_{jn}$

$$\begin{aligned} & \frac{\partial^2 C_{jn}}{\partial x^2} + \frac{\partial^2 C_{jn}}{\partial y^2} + k_n^2 C_{jn} \\ &= F_0 H_0^{(1)}(k_j \xi) + F_1 H_1^{(1)}(k_j \xi), \end{aligned} \quad (4)$$

where

$$\begin{aligned} F_0 &= \int_{-H}^0 \left( \frac{\partial}{\partial z} \left( \frac{\rho_1}{\rho_0} \right) \frac{\phi_n}{\rho_0} \frac{\partial \phi_j}{\partial z} + 2 \frac{\omega^2 c_1}{c_0^2 c_0} \frac{\phi_n \phi_j}{\rho_0} \right) dz \\ &+ \sum_{l=1}^N h_1^{(l)} \left\{ \phi_n \phi_j \left[ k_j^2 \left( \frac{1}{\rho_{0+}} - \frac{1}{\rho_{0-}} \right) \right. \right. \\ &\left. \left. - \omega^2 \left( \frac{1}{\rho_{0+} c_{0+}^2} - \frac{1}{\rho_{0-} c_{0-}^2} \right) \right] + \frac{\partial \phi_n}{\partial z} \frac{\partial \phi_j}{\partial z} \frac{(\rho_{0-} - \rho_{0+})}{\rho_{0+}^2} \right\} \Bigg|_{z=h_0^{(l)}}, \\ F_1 &= \int_{-H}^0 \left( - \frac{\partial \rho_1}{\partial x} \frac{k_j (x-x_0)}{\xi} - \frac{\partial \rho_1}{\partial y} \frac{k_j (y-y_0)}{\xi} \right) \frac{\phi_n \phi_j}{\rho_0^2} dz \\ &+ \sum_{l=1}^N \phi_n \phi_j \left( \frac{1}{\rho_{0+}} - \frac{1}{\rho_{0-}} \right) \\ &\times \left( \frac{k_j (x-x_0)}{\xi} \frac{\partial h_1^{(l)}}{\partial x} + \frac{k_j (y-y_0)}{\xi} \frac{\partial h_1^{(l)}}{\partial y} \right) \Bigg|_{z=h_0^{(l)}}. \end{aligned}$$

The solution to equation (4) is written as the convolution of the fundamental solution  $-(i/4)H_0^{(1)}(k_n \sqrt{x^2 + y^2})$  of the Helmholtz operator with a right-hand member [6]. Introduce now a polar system of coordinates  $x = r \cos \alpha$ ,  $y = r \sin \alpha$  and denote the coordinates of the point of reception and the source by  $(r_r, \alpha_r)$  and  $(r_0, \alpha_0)$ , respectively. Using the addition theorem for the Bessel functions [7], we express the functions  $H_i^{(1)}(k_j \xi)$  and  $H_i^{(1)}(k_n \sqrt{r_r^2 + r^2 - 2rr_r \cos(\alpha - \alpha_r)})$  ( $i = 0, 1$ ) in terms of the Hankel functions  $H_\mu^{(1)}(k_j r_0)$  and  $H_\mu^{(1)}(k_n r_r)$  ( $\mu = -\infty, \dots, +\infty$ ). Assuming that the distance  $r_r$  from the inhomogeneous area to the point of reception is rather long, we replace the Hankel functions  $H_\mu^{(1)}(k_n r_r)$  by the principal terms of their asymptotics at  $r_r \rightarrow \infty$ . Expand  $\rho_1(r, \alpha)$ ,  $c_1(r, \alpha)$ , and  $h_1^{(l)}(r, \alpha)$  ( $l = 1, \dots, N$ ) as functions of  $\alpha$  in Fourier series and expand the corresponding radial Fourier coefficients  $\rho_{1m}(r)$ ,  $c_{1m}(r)$ , and  $h_{1m}^{(l)}(r)$  within the segment  $[0, L]$  where they do not vanish in the Fourier-Bessel series in the functions  $J_m(r\gamma_p/L)$  (see, [7],  $\gamma_p$  are the positive roots of the equation  $J_m(r) = 0$ ). Denoting the expansion

coefficients by  $\tilde{\rho}_{1mp}$ ,  $\tilde{c}_{1mp}$ , and  $\tilde{h}_{1mp}^{(l)}$ , respectively, we finally obtain

$$\begin{aligned}
C_{jn} &= -\frac{i\sqrt{2\pi}\exp(ik_n r_r - i\pi/4)}{2\pi\sqrt{k_n r_r}} \\
&\times \sum_{\nu=-\infty}^{\infty} e^{i\nu(\alpha_0 - \pi/2)} \sum_{m=-\infty}^{\infty} (i)^m e^{-i(m+\nu)\alpha_r} \\
&\times \sum_{p=1}^{\infty} (F_{mp}^0 H_{\nu}^{(1)}(k_j r_0) \\
&+ ik_j k_n F_{mp}^1 H_{\nu+1}^{(1)}(k_j r_0) \cos(\alpha_0 - \alpha_r)) I_{m\nu}^p,
\end{aligned} \tag{5}$$

where

$$\begin{aligned}
F_{mp}^0 &= \int_{-H}^0 \left[ \frac{\tilde{\rho}_{1mp}}{\rho_0^2} \left( \frac{\omega^2}{c_0^2} \phi_n \phi_j - \frac{\partial \phi_n}{\partial z} \frac{\partial \phi_j}{\partial z} \right) + 2 \frac{\omega^2 \tilde{c}_{1mp}}{c_0^2} \frac{\phi_n \phi_j}{\rho_0} \right] dz \\
&+ \sum_{l=1}^N \tilde{h}_{1mp}^{(l)} \left( \frac{\partial \phi_n}{\partial z} \frac{\partial \phi_j}{\partial z} \frac{(\rho_{0-} - \rho_{0+})}{\rho_{0+}^2} \right. \\
&\left. + \omega^2 \left( \frac{1}{\rho_{0+} c_{0+}^2} - \frac{1}{\rho_{0-} c_{0-}^2} \right) \phi_n \phi_j \right) \Big|_{z=h_0^{(l)}}, \\
F_{mp}^1 &= \int_{-H}^0 \frac{\tilde{\rho}_{1mp}}{\rho_0} \frac{\phi_n \phi_j}{\rho_0} dz + \sum_{l=1}^N \tilde{h}_{1mp}^{(l)} \phi_n \phi_j \left( \frac{1}{\rho_{0+}} - \frac{1}{\rho_{0-}} \right) \Big|_{z=h_0^{(l)}}, \\
I_{m\nu}^p &= \int_0^L J_m \left( \frac{\gamma_p}{L} r \right) J_{\nu}(k_j r) J_{m-\nu}(k_n r) r dr.
\end{aligned}$$

This formula allows a further reduction when the source is far from the inhomogeneous area and the Hankel functions  $H_{\nu}(k_j r_0)$  and  $H_{\nu+1}(k_j r_0)$  can be replaced by their asymptotics. Introducing the sum over  $\nu$  under the integral sign and transforming the integrand with the use of the addition theorem for the Bessel functions, we obtain

$$\begin{aligned}
C_{jn} &= \frac{-1}{2\pi\sqrt{k_j k_n}} \frac{e^{i(k_j r_0 + k_n r_r)}}{\sqrt{r_0 r_r}} \sum_{m=-\infty}^{\infty} e^{im(\alpha_r - \pi/2)} e^{im\psi_2} \\
&\times \sum_{p=1}^{\infty} (F_{mp}^0 + k_j k_n F_{mp}^1 \cos(\alpha_0 - \alpha_r)) \\
&\times \frac{\gamma_p L^2}{\gamma_p^2 - L^2 \kappa^2} J_{m+1}(\gamma_p) J_m(\kappa L).
\end{aligned} \tag{6}$$

Here,  $\kappa = \sqrt{k_j^2 + k_n^2 - 2k_j k_n \cos(\alpha_0 - \alpha_r)}$  and  $e^{-i\psi_2} = (k_j - k_n e^{i(\alpha_0 - \alpha_r)})/\kappa$ . The formula obtained in [2] is derived from (6) at  $\tilde{\rho}_{1mp} = \tilde{c}_{1mp} = 0$  and  $N = 1$ .

When the dimensions of the inhomogeneous area are much less than the sound wavelength, the numerical estimate of the integrals  $I_{m\nu}^p$  in (5) can be obtained with the use of the asymptotic expansions of the Bessel function in the vicinity of zero without any limitations for the distance between the source and the scatterer. Below, we present the results of the model calculations illustrating this case.

The calculations were performed for a two-layer medium (water and bottom) with the sound velocities and densities being constant within each of the two layers and equal to 1470 m/s and 1000 kg/m<sup>3</sup>, respectively, in water, and 2000 m/s and  $\rho = 1150$  kg/m<sup>3</sup> in the sea bottom. The thickness of the water layer was 200 m, and the thickness of the bottom layer was 1000 m. All functions describing the inhomogeneities, except those that describe the bottom relief,  $h_1^{(l)}$ , were assumed to be zero; following [2], we assumed that  $h_1^{(l)} = \exp(-r^2/(2\sigma^2))$ , where  $\sigma$  is a parameter. Such a choice of the inhomogeneity function allows one to perform an analytical summation of the Fourier–Bessel series (the Fourier series in the angular variable contain only the zero harmonic) and to use the resulting expression for testing formula (5). Note that now seven terms of the Fourier–Bessel series well agree with the analytical sum. In calculations, we assumed that  $\sigma = 2$  m and, in this case, the effective radius of the inhomogeneous area (the radius was used in expanding in the Fourier–Bessel series) was equal to 10 m. The sound frequency was 10 Hz.

The results of calculations by formula (5) and by the Wetton and Fawcett formula from [2] are presented in Figure 1, which exhibits the angular dependence of the modulus of the scattering coefficient  $|C_{11}(r_r, \alpha_r)|$  of the first mode to the first mode on  $\alpha_r$  for  $r_r = 5000$  m and different distances of the source from the center of the inhomogeneity. The origin of coordinates coincides with the center of the inhomogeneity, and the angular coordinate of the source is 180°. These results show that the Wetton and Fawcett formula from [2] does not describe even qualitatively the specific features of the scattered field when the source is located close to the inhomogeneity.

In conclusion, we note that the formulas obtained using the Fourier series expansions of the inhomogeneities in the angular variable and the Fourier–Bessel series expansions in the radial variable provide a good basis for setting and solving the inverse problems.

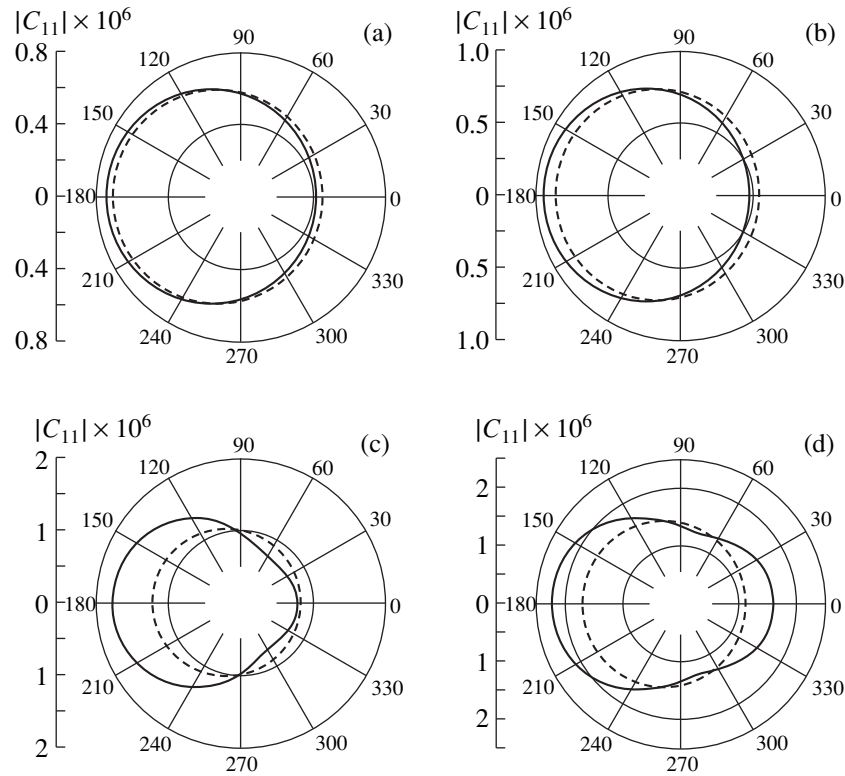


**Fig. 1.** Angular dependence of the modulus of the intermode scattering coefficient: calculations by formula (5) (solid curves) and by formula taken from [2] (dotted curves) for the distances from the source to the center of the inhomogeneous area (a) 150, (b) 100, (c) 50, and (d) 25 m.

These problems will be discussed in the following publications.

#### REFERENCES

1. F. Ingenito, *J. Acoust. Soc. Am.* **82**, 2051 (1987).
2. B. T. R. Wetton and J. A. Fawcett, *J. Acoust. Soc. Am.* **85**, 1482 (1989).
3. J. A. Fawcett, *J. Acoust. Soc. Am.* **102**, 3387 (1997).
4. J. A. Fawcett, *Inverse Problems* **6**, 185 (1990).
5. L. M. Brekhovskikh and O. A. Godin, *Acoustics of Layered Media* (Nauka, Moscow, 1989; Springer, Berlin, 1990).
6. V. S. Vladimirov, *Equations of Mathematical Physics* (Nauka, Moscow, 1988).
7. A. Erdelyi and H. Bateman, *Higher Transcendental Functions* (McGraw-Hill, New York, 1953; Nauka, Moscow, 1966).

*Translated by Yu.P. Lysanov*

# Ways to Improve Acoustooptic Transducers Using Liquid Crystals

O. A. Kapustina

Andreev Acoustics Institute, ul. Shvernika 4, Moscow, 117036 Russia

e-mail: [bvp@akin.ru](mailto:bvp@akin.ru)

Received March 25, 1998

**Abstract**—The results of the investigation of an acoustooptic transducer using a nematic liquid crystal and operating under the conditions of two-wave acoustic effect on its sensitive element are presented. © 2000 MAIK “Nauka/Interperiodica”.

An integral part of all systems of acoustic visualization is an image detector. The first reports on designing image detectors in the form of thin layers of liquid crystals capable of direct transformation of acoustic images into optical ones appeared in the 1970s [1–3]. Two types of liquid crystals that may be used for this purpose are known. These are cholesteric and nematic liquid crystals [4]. The first of them changes its color due to the change in the medium temperature in the process of absorption of ultrasound, while the second type of liquid crystals has the property of changing the polarization of light transmitted through its thin layer or the polarization of light scattered due to the change in the orientation of molecules under the impact of ultrasound [5]. The major part of the studies was devoted to designing image detectors of the polarization type. These studies were initiated by Greguss [1] and Kapustina and Lupanov [2]. The analysis of the latest data on the operational characteristics of such acoustooptic transducers with the sensitive element in the form of a homeotropic layer of a nematic liquid crystal and the mechanism of the ultrasonic effect on its macrostructure is given in the *Handbook of Liquid Crystals* [6]. It turned out that the potential capabilities of these devices are limited because of the properties inherent in the orientation transition induced in nematic liquid crystals by ultrasound. First of all, the optical response of a nematic liquid crystal to an ultrasonic impact is connected with its intensity  $J$  by the dependence of the type  $J^n$  with the power index  $n = 4$ . Therefore, the dynamical range of the transducer is not wide ( $\sim 5$ – $6$  dB). The fact that the optical pattern corresponding to the acoustic image has an inhomogeneous structure is also important. This limits the transducer resolution. Finally, the device has a low sensitivity (several milliwatts or several tens of milliwatts per square centimeter).

The search for ways to overcome these natural disadvantages of polarization acoustooptic transducers [6–11] has led to the idea [11] of additionally introducing coherent acoustic radiation into a nematic liquid

crystal and create the conditions for a more intense generation of steady-state flows due to the interference of oscillatory processes. According to modern concepts [5], these flows determine the mechanism of the effect of ultrasound on the orientation of a liquid crystal. This idea was tested successfully in the case of visualization of surface acoustic waves (SAW) [11]. A coherent viscous wave was introduced into a nematic liquid crystal with the help of an external source (a shear-wave source). This wave amplified the tangential component of one of the normal modes of the layer (the second fast-attenuating and slower mode).<sup>1</sup> The cross-interaction of the normal component  $v_{1z}$  of the first mode of the layer with the amplified tangential component  $v_{2x}$  of the second mode produced an inhomogeneous acoustic flow in the layer with higher velocities, which led to an increase in the deviation angle of molecules and provided an opportunity to observe the optical effect at those parts of the layer where it had been impossible in the absence of additional excitation. This idea was also discussed in the application of the control over the mode of generation of acoustic flows in a layer of a nematic liquid crystal under the conditions of interaction of bulk waves. It was established that interference of coherent ultrasonic waves with mutually perpendicular polarizations also leads to an amplification of the expected optical effect [6, 12].

<sup>1</sup> The number of natural modes excited by SAW in a liquid layer confined between two solid halfspaces depends on its thickness and the wavelengths (of surface and bulk waves). If these wavelengths are considerably greater than the layer thickness, we can assume that the wave field within the layer is the superposition of two modes with the tangential and normal components of the particle velocities  $v_{1x}$  and  $v_{1z}$  (the fast mode) and  $v_{2x}$  and  $v_{2z}$  (the slow mode). According to the general scheme of the formation of an inhomogeneous flow [5], these modes cross-interact:  $v_{1x}$  with  $v_{2z}$  and  $v_{1z}$  with  $v_{2x}$ , the optical effect in the case of interference of  $v_{1x}$  and  $v_{2z}$ , being an order of magnitude less than in the case of the interaction of  $v_{1z}$  and  $v_{2x}$ . It is essential that the interactions of  $v_{1x}$  with  $v_{1z}$  and  $v_{2x}$  with  $v_{2z}$  cause a weak homogeneous flow of the nematic liquid, which does not influence the orientation of molecules.

This paper presents the results of the first tests of a polarization acoustooptic transducer that is designed by taking into account the published data [6, 11, 12] and can operate both in the conventional mode of a single-wave impact [1–3] and under the conditions of a simultaneous effect of a longitudinal (signal) and shear (reference) waves on the nematic liquid crystal. The particular features of the optical response of the transducer in the two-wave mode are studied, and the main characteristics of the transducer are determined and compared to those obtained in the conventional mode.

In the course of these tests, the transducer operated within the system of acoustic visualization, which had been designed according to the scheme given in Fig. 1a. This scheme shows the next basic devices: an acoustooptic transducer (1) incorporating a source of shear (reference) waves (2), which is located at the end of a dish (3) filled with water; a source of longitudinal (signal) waves (4) is located in the same dish. The distance between the source of longitudinal waves and the acoustooptic transducer can be varied within the range 2–20 cm.

The design of the cell with a nematic liquid crystal in the acoustooptic transducer corresponds to the new mode of its operation: one of the support plates of the cell is made of quartz (Y-cut) and the other is a polymer film coated with a thin aluminum layer deposited by evaporation. An eutectic liquid-crystal mixture of MBBA (4-methoxybenziledene-4'-butylaniline) and EBBA (4-ethoxybenziledene-4'-butylaniline) (type H 8) fills this cell in such way that two opposite edges (5) of the layer are open. Two spacers (6) are introduced into the cell in order to set the layer thickness. Positioning of the spacers in the layer plane is pictured schematically in Fig. 1b (view from above). The arrow indicates the direction (7) of shear vibrations produced by the reference source (2).

In order to provide the coherence of waves radiated by the sources (2) and (4), which is necessary for a stationary interference pattern, they were excited by a single oscillator (8) through an amplifier (9) with two outputs. This allowed us to control the intensities  $J_1$  and  $J_s$  of longitudinal and shear waves in the course of the experiment. The intensity of the signal longitudinal wave incident on the layer was measured by an acoustic radiometer. The values of intensity in the shear wave were estimated according to the effective electric voltage fed to the source (2) using a well-known technique developed for multi-layer oscillating systems (see [12]). The system of the dish temperature stabilization provided an opportunity to maintain a constant temperature of water in the dish (25°C) with the precision up to  $\pm 0.5^\circ\text{C}$ .

The monitoring of the orientation state of the liquid-crystal layer in the cell of the acoustooptic transducer and the detection of its optical response was performed in polarized reflected light according to the scheme with the basic elements shown in Fig. 1a. A collimated

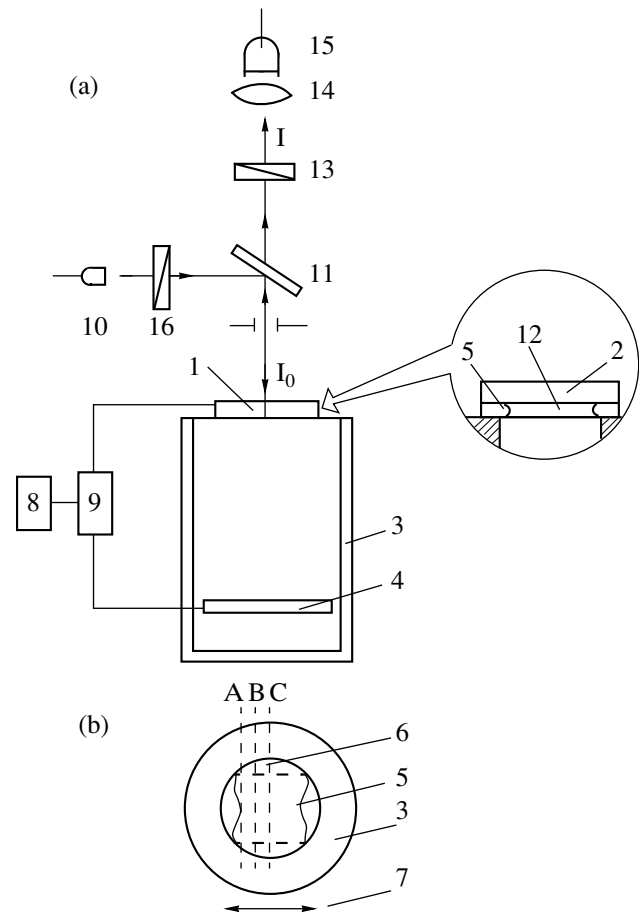


**Fig. 1.** Schematic diagram of the experiment and the geometry of the cell with a nematic liquid crystal. (a): (1) An acoustooptic transducer, (2) a source of reference waves, (3) a dish, (4) a source of signal waves, (5) open edges of the layer, (6) spacers, (7) the direction of shear oscillations, (8) an oscillator, (9) an amplifier, (10) a light source, (11) a beam splitter, (12) a layer of a nematic liquid crystal, (13) a polarizer-analyzer, (14) the eye-piece of a microscope, (15) a photomultiplier tube, and (16) a polarizer. (b) The view on the cell from above and positions of the spacers in it.

beam of polarized light with the intensity  $I_0$  incident from the source (10) through a beam splitter (11) on the layer (12) in the cell is reflected from a flat mirror to the surface of the polymer film (a thin layer of aluminum). After that, it is again transmitted through the beam splitter, and, after the analyzer (13), it arrives at the eye-piece of a microscope (14) and a photomultiplier tube (15).

Two series of experiments were conducted at a frequency of  $\sim 15$  MHz.<sup>2</sup> In one of them the reference radiator (2) was not excited, and the acoustooptic transducer operated in the mode of the conventional single-wave action. In the other series, two radiators operated simultaneously. In this case, the ratio of the intensities  $J_1$  and  $J_s$  was varied. The intensity of the light flux  $I$

<sup>2</sup> The radiator of signal waves was excited at the fifth harmonic, and the radiator of shear waves was excited at the main resonance frequency.

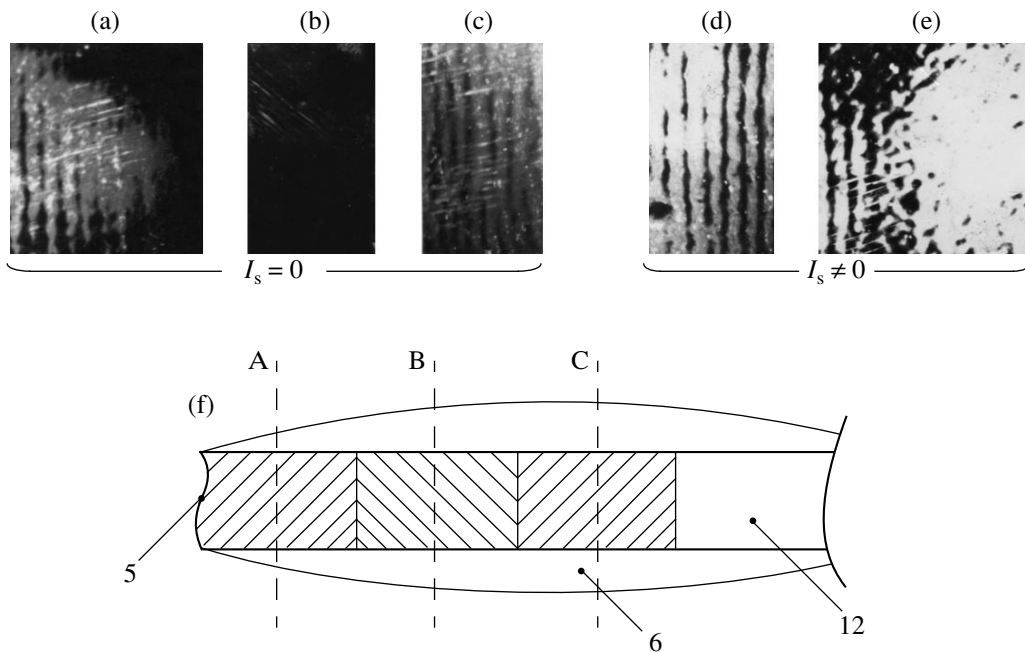


**Fig. 2.** Clarification patterns in a layer of a nematic liquid crystal observed in parallel beams of light in the zones A, B, and C (cell view from above): single-wave action ( $J_s = 0$ ) for  $d = 10 \mu\text{m}$ , in (a) zone A and (b) zone C, and for (c)  $d = 100 \mu\text{m}$  in zone B; two-wave action ( $J_s \neq 0$ ) for  $d = 10 \mu\text{m}$  in (d) zone A and (e) zone C. (f) The layer geometry.

transmitted through the nematic liquid crystal–analyzer system was recorded in the process of measurements under the conditions when the polarizers were crossed and the angle between the polarization plane of light incident upon the nematic layer and the plane where the rotation of molecules occurred under the effect of ultrasound was  $\pi/4$ . The thickness of the nematic layer was varied within the interval 10–100  $\mu\text{m}$ . The orientation of molecules of the nematic liquid crystal in the cell was homeotropic. The inner surfaces of the cell were preliminarily cleaned and then treated with lecithin in order to produce such an orientation [4].

It is known that, in the case of the homeotropic alignment of molecules of nematic liquid crystals in a plane capillary, the mesophase layer is similar from the point of view of crystal optics to a plate of a uniaxial crystal cut perpendicularly to the optical axis. Such a layer looks dark in distortion-free light in the case of crossed polarizers. The change of molecule orientation under the effect of ultrasound leads to the layer clarification. According to the known data [6], the character of the clarification is determined by the experiment geometry and the frequency, intensity, and type of the wave.

The observations conducted in the first series of experiments (the conventional mode of operation of the acoustooptic transducer) demonstrated that under these conditions the pattern of clarification of the homeotropic layer of a nematic liquid crystal depends on its thickness and the observation zone (zones A–C in Fig. 1b). In thin layers (10 and 40  $\mu\text{m}$ ), the clarification pattern near the

open edge of the layer (zone A) has the form of a system of light and dark stripes parallel to it. The brightness of these stripes decreases with distance from this edge (Fig. 2a;  $d = 10 \mu\text{m}$ ), and the viewing field in the central part of the layer plane (zone C) stays dark (Fig. 2b;  $d = 10 \mu\text{m}$ ). In the thick layer (100  $\mu\text{m}$ ), the stripes are visible over the whole plane, their brightness being slightly varied in the area of transition from the zone A to the zone C. The micrograph of the clarification pattern of the layer in the zone B (the intermediate zone between the zones A and C) is given in Fig. 2c as an example. It is found that the spatial period of the stripes is  $\Lambda \sim \lambda/2$ , where  $\lambda$  is the longitudinal wavelength in the nematic liquid crystal, and does not depend on the layer thickness. The mechanism of the formation of this system of stripes is as follows: the periodic motion of the open edges of the layer, which is caused by its compression in the longitudinal wave incident on the layer, generates liquid oscillations along the layer, i.e., the secondary longitudinal waves propagating from the open edges to the layer center. Nonlinear stresses arising because of the considerable (with respect to thickness) gradient of the motion velocity in the tangential direction lead to the formation of a steady-state flow of nematic liquid. The scale of the flow is determined by the ultrasonic wavelength in the nematic liquid crystal. The velocity gradients in this flow across the layer thickness cause the rotation of the molecules of the nematic liquid crystal. According to Gus'kov and Kozhevnikov [13], the distribution of the rotation angle along the layer of a nematic liquid crystal within the ultrasonic beam depends on the attenuation

coefficient  $\beta = k\delta/d$  of the secondary longitudinal waves. Here,  $\delta$  is the thickness of the viscous boundary layer and  $k$  is the wave number of the ultrasonic wave in the nematic liquid crystal. If the layer thickness is increased from 10 to 100  $\mu\text{m}$ , the value of the coefficient  $\beta$  decreases by an order of magnitude. The attenuation of these waves in the thin layer can be so strong that they attenuate before arriving at the cell center. On the contrary, in the thick layer, the longitudinal waves propagating from its edges attenuate weakly. Therefore, the optical effect can manifest itself over the whole layer plane or its major part. Just these patterns caused by the influence of the open edges of the layer were observed in the experiments. The results are given in Figs. 2a–2c. Thus, in this series of experiments with the acoustooptic transducer operating in the conventional mode, the spatially-inhomogeneous optical response of a homeotropic layer of a nematic liquid crystal to a longitudinal signal wave reflects the influence of the edge effects. The response is determined by the interaction of the longitudinal signal wave incident on the layer with the secondary longitudinal waves propagating from its open edges.

In the second series of experiments, the acoustooptic transducer operated under the conditions of the combined action of the signal and reference waves on the nematic liquid crystal. Observations showed that in such situations, the character of the orientation distortion of the layer macrostructure varied to some extent: the system of stripes described above and created by the interaction of the signal and secondary longitudinal waves was still visible in thin layers near the open edge, while a clarification homogeneous over the sample plane occurred close to the center of the layer. This effect manifests itself most clearly in the layer of thickness 10  $\mu\text{m}$  (Figs. 2d, 2e). It is essential that the brightness of the zone of homogeneous clarification of the layer, as well as the brightness of the stripes, depends on the intensity of not only the signal wave, but the reference wave as well. By increasing the intensity of the reference wave, it is possible to obtain the same optical response to the combined action but at a lower value of intensity of the signal wave.

The most interesting property of the homeotropic structure of nonlinear liquid crystals, which manifests itself under the conditions of two-wave action, is its ability to demonstrate a spatially-homogeneous response to this action in certain situations (thin layers and weak edge effects). The intensity  $I$  of the light flux transmitted through the layer in the zone of homogeneous clarification under the combined action of the signal and reference waves was measured in order to describe this effect. Plots 1–6 in Fig. 3 present the dependence of the optical response  $I/I_0$  on the intensity  $J_1$  in the longitudinal signal wave for the following values of the intensity  $J_s$  in the reference wave: 0.07, 0.16, 0.3, 0.7, 0.9, and 1.3  $\text{W}/\text{cm}^2$ . The layer thickness was 40  $\mu\text{m}$  and the frequency was  $\sim 15$  MHz. This depen-

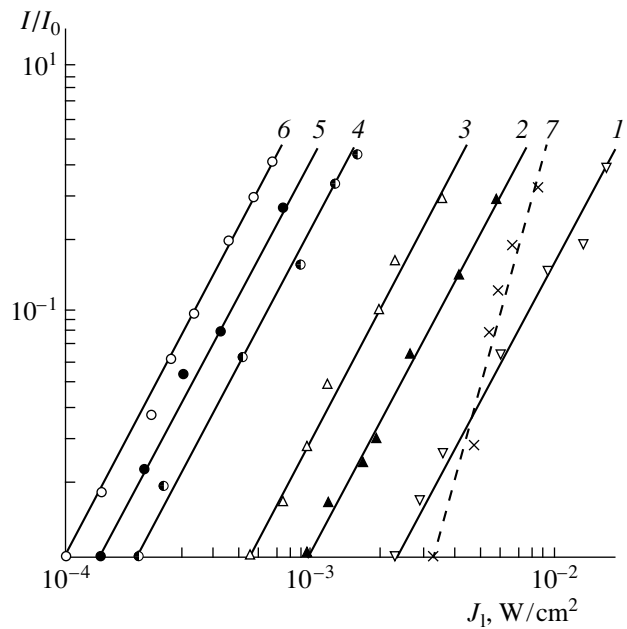


**Fig. 3.** Optical response of an acoustooptic transducer to the action of the signal wave ( $J_s = 0$ , plot 7) and the combined action of the signal and reference waves for the following values of the intensity of the reference wave:  $J_s = (1)$  0.08, (2) 0.16, (3) 0.3, (4) 0.7, (5) 0.9, and (6) 1.3  $\text{W}/\text{cm}^2$ ; the layer thickness is 40  $\mu\text{m}$  and the frequency  $\sim 15$  MHz.

dence is described by the exponential function of the form  $I/I_0 \sim J_1^2$ . The values of the minimum intensity  $J_1^{\min}$  corresponding to the level of clarification  $I/I_0 = 0.01$ , which is usually considered as a conditional threshold in the observation of the effect with a polarization-optical technique, are 2.4, 0.9, 0.55, 0.2, 0.17, and 0.1  $\text{mW}/\text{cm}^2$ , respectively. Plot 7 is given in Fig. 3 for comparison. This plot presents the dependence of the optical response of a nematic liquid crystal to the action of signal waves on their intensity  $J_1$  at  $J_s = 0$ . This dependence is described by the function of the form  $I/I_0 \sim J_s^n$ , where  $n = 3.8$ . The value of the minimum intensity  $J_1^{\min}$  in this situation is 3  $\text{mW}/\text{cm}^2$ .<sup>3</sup>

The relation of the optical signal  $I/I_0$  to the intensity  $J_s$  in the reference wave at a fixed value of intensity in the signal wave is illustrated by the plot given in Fig. 4a. It follows from these data that  $I/I_0 \sim J_s^n$ , where  $n = 1.8$ . The plot in Fig. 4b demonstrates the experimental values of the minimum intensity in the signal wave  $J_1^{\min}$  for a nematic layer of thickness 40  $\mu\text{m}$  at different val-

<sup>3</sup> Plot 7 approximates the values of  $I/I_0$  pertaining to the central part of the first light stripes at the open edge of the layer. The brightness of this part is not yet affected by the attenuation of secondary longitudinal waves.

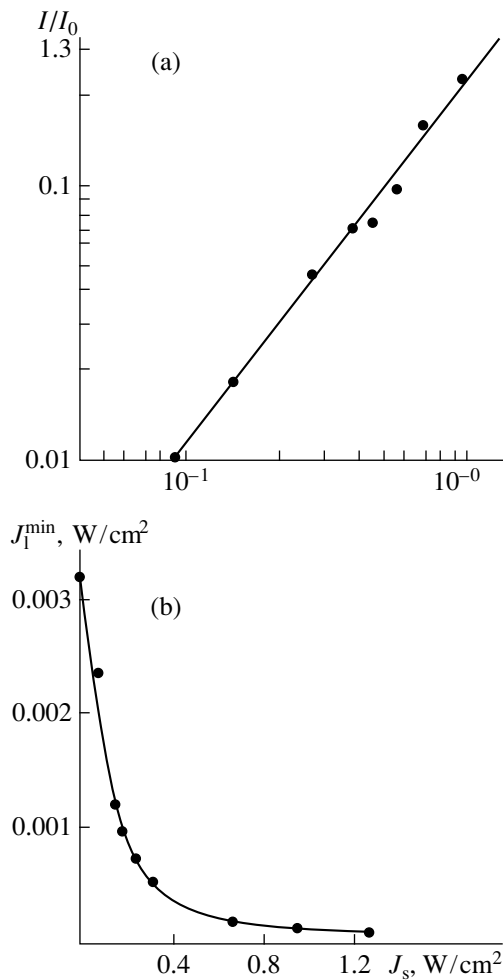


**Fig. 4.** Main features of an acoustooptic transducer in the two-wave mode. (a) Relation between the optical response of an acoustooptic transducer and the intensity  $J_s$  of the reference wave at  $J_1 = \text{const}$  and (b) the relation between the minimum intensity of the signal wave and the intensity in the reference wave.

ues of intensity in the reference wave. This dependence is described by the function of the form  $J_1^{\min} \sim 1/J_s$ .

It is *a priori* clear that, in the conditions of two-wave effect on a nematic liquid crystal, the effect of the “flow” mechanism of the orientation distortion of the homeotropic structure of a nematic in an ultrasonic field, which had been discussed earlier (see [5, 6, 11–13]), is retained independently of the type of the interacting waves. In the geometry of experiments, which is given in Fig. 1, oscillations in the viscous wave generated in a nematic liquid by a shear wave occur in the same direction as the oscillatory motion of the liquid in the layer plane due to the presence of the open ends of the layer and causes an amplification of this motion. The interaction of the amplified tangential component of the motion with the normal component (the signal wave) increases the efficiency of the flow generation. If

we accept such an interpretation of the phenomenon, we can quantitatively estimate the expected optical response by using the results by Anikeev, Bocharov, and Vuzva [11] who analyzed the interaction of a viscous wave with the normal component of one of the layer modes excited by SAW. According to these researchers [11], we have  $I/I_0 \sim \xi_{01}^4 \xi_{0s}^4$ , and this ratio corresponds to the experimental data given in Fig. 3. Here,  $\xi_{01}$  and  $\xi_{0s}$  are the amplitudes of longitudinal and shear oscillations. The formation of a spatially-homogeneous pattern of clarification at the center of a thin layer of a nematic liquid crystal is apparently related to the fact that secondary longitudinal waves do not reach this part of the layer because of the high attenuation, and the viscous wave interacts here with a single elastic wave, i.e., the longitudinal signal wave from the source (4). The normal components of the oscillatory motion in this wave are homogeneous over the section of the ultrasonic beam (correct to the homogeneity of the radiation field of the source (4)). The analysis of the interference processes in the nematic liquid crystal at the open edges of the layer where the viscous wave interacts with two elastic waves, as well as their connection with the orientation state of the layer, lies beyond the scope of this paper. Some data on this aspect of the problem can be found in the handbook [6] and a paper by Kini [14].

The above consideration of the operation of an acoustooptic transducer using a nematic liquid crystal in the mode of two-wave action provides an opportunity to formulate the following main conclusions about its properties:

(a) An optical response of a nematic liquid crystal to a two-wave action  $(I/I_0)_s$  is determined by the combination of the intensities of interacting waves, i.e.,  $(I/I_0)_s \sim J_1^2 J_s^2$ . In the case of the conventional mode of operation of the acoustooptic transducer, we have  $(I/I_0)_1 \sim J_1^4$ .

(b) The exponent in the function describing the relation between the optical response of the acoustooptic transducer and the intensity of the signal wave decreases from 4 to 2, which means an expansion of its dynamical range. It follows from the data given in Fig. 3 that, in the conditions of these experiments, the dynamical range increases by approximately a factor of two.

(c) In the case of a two-wave action on a nematic liquid crystal, it is possible to reduce the intensity of the signal wave by increasing the intensity of the reference wave up to the values providing an opportunity to observe the image. This fact can be essential for designing the systems of acoustic visualization intended for medical diagnostics.

(d) In the conditions of two-wave action, it is necessary to select a certain relationship between the intensities of the interacting waves. On the one hand, the clarification effect produced in a nematic liquid crystal by

each source ( $(I/I_0)_1$  and  $(I/I_0)_s$ ) must not mask the results of their combined action  $(I/I_0)_{1s}$ . In order to satisfy this condition, it is necessary to limit the intensities of the signal and reference waves by the values close to the conditional thresholds of clarification  $J_1^{\min}$  and  $J_s^{\min}$  when the levels of clarification  $(I/I_0)_1$  and  $(I/I_0)_s$  are lower than 0.01. On the other hand, the interaction of the signal and reference waves must be sufficiently effective for the optical response of a nematic liquid crystal to exceed the level 0.01.

(e) The minimum intensity of the signal wave  $J_1^{\min}$  corresponding to the clarification level  $(I/I_0)_{1s} = 0.01$  under two-wave action decreases with respect to its value providing the same clarification level in the case of the action of only the signal wave. From the data given above, it follows that, at the frequency  $\sim 15$  MHz and the thickness of the layer of a nematic liquid crystal in the cell of the acoustooptic transducer equal to  $40 \mu\text{m}$ , the conditional levels of clarification are equal to  $3 \text{ mW/cm}^2$  (at  $J_s = 0$ ) and  $0.17 \text{ mW/cm}^2$  (at  $J_s = 0.9 \text{ mW/cm}^2$ ); i.e., the sensitivity of the acoustooptic transducer increases by more than one order of magnitude.

(f) An acoustooptic transducer operating according to the two-wave scheme opens some additional opportunities relating to the spatial structure of the image.

Based on these conclusions, we can assume that the use of an acoustooptic transducer capable of operating in the two-wave mode opens up an opportunity to design a system of acoustic visualization with a wider dynamical range and a new quality of the spatial characteristics of the optical response to ultrasonic action. This could not be achieved using conventional acoustooptic transducers [2, 3, 8–10]. An attractive feature of such a system is also its higher (by one order of magnitude) sensitivity and the possibility of controlling it by varying the intensity in the reference wave.

These new operational features provide an opportunity to expand the field of application of acoustooptic transducers using nematic liquid crystals and proceed from the regular problems of nondestructive testing to the problems of medical diagnostics [15]. High power ultrasound is not permissible in this field. Evidently, the problems of technology and design are also essential while developing such systems. In particular, such problems are the utilization of modern electronics and promising techniques applied now to designing liquid crystal displays [16] and the selection of multi-component liquid-crystal mixtures [17] with a desired set of

physical-chemical parameters (viscosity, elasticity, birefringence, and temperature of phase transitions) that determine the corresponding characteristics of a specific acoustooptical device.

#### ACKNOWLEDGMENTS

I am grateful to S. Garin for his assistance in the fabrication of an acoustooptic transducer using a nematic liquid crystal.

#### REFERENCES

1. P. Greguss, *Acustica* **29**, 52 (1973).
2. O. A. Kapustina and V. N. Lupanov, *Akust. Zh.* **23**, 390 (1977) [*Sov. Phys. Acoust.* **23**, 218 (1977)].
3. O. A. Kapustina, V. N. Lupanov, and G. S. Chilaya, *Akust. Zh.* **24**, 136 (1978) [*Sov. Phys. Acoust.* **24**, 76 (1978)].
4. P. De Gennes, *The Physics of Liquid Crystals* (Clarendon, Oxford, 1974; Mir, Moscow, 1977).
5. A. P. Kapustin and O. A. Kapustina, *Acoustics of Liquid Crystals* (Nauka, Moscow, 1985).
6. *Handbook of Liquid Crystals*, Ed. by D. Demus, J. Goodby, G. W. Gray, *et al.* (Wiley, 1998), Chap. VII, pp. 549–568.
7. R. S. Akopyan, B. Ya. Zel'dovich, and N. V. Tabiryan, *Akust. Zh.* **34**, 583 (1988) [*Sov. Phys. Acoust.* **34**, 337 (1988)].
8. J. N. Perbet, M. Hareng, and S. Le Berre, *Rev. Phys. Appl.* **14**, 569 (1979).
9. Y. Kagawa, T. Hatakeyama, and Y. Tanaka, *J. Sound Vibr.* **36**, 407 (1974).
10. A. Strigazzi and G. Berbero, *Mol. Cryst. Liquid Cryst.* **103**, 193 (1983).
11. D. Anikeev, Yu. V. Bocharov, and A. D. Vuzhva, *Liquid Cryst.* **6**, 593 (1989).
12. Yu. V. Bocharov and O. A. Kapustina, *Akust. Zh.* **44**, 166 (1998) [*Acoust. Phys.* **44**, 128 (1998)].
13. N. K. Gus'kov and E. N. Kozhevnikov, *Akust. Zh.* **29**, 38 (1983) [*Sov. Phys. Acoust.* **29**, 21 (1983)].
14. U. D. Kini, *Mol. Cryst. Liquid Cryst. Comm.* **1** (2), 1 (1997).
15. D. De Rossi and P. Dario, in *Proceedings of I Scuola Nazionale del GNCL* (Rende, Italy, 1996), p. 807.
16. Lin Chern-Sheng *et al.*, *Optik* **109**, 133 (1998).
17. V. Bezborodov and R. Dabrowski, *Mol. Cryst. Liquid Cryst. Comm.* **1** (2), 7 (1997).

*Translated by M. L. Lyamshev*

# Nonlinear Distortion and Attenuation of Intense Acoustic Waves in Lossy Media Obeying a Frequency Power Law

S. S. Kashcheeva\*, O. A. Sapozhnikov\*, V. A. Khokhlova\*,  
M. A. Averkiou\*\*, and L. A. Crum\*\*\*

\* Moscow State University, Vorob'evy gory, Moscow, 119899 Russia  
e-mail: oleg@acs366b.phys.msu.su

\*\* ATL Ultrasound, 22100 Bothell Everett Hwy, P.O.Box 3003, Bothell, WA 98041-3003, USA

\*\*\* Applied Physics Laboratory, 1013 NE 40th Street, University of Washington, Seattle, WA 98105, USA

Received February 15, 1999

**Abstract**—Nonlinear propagation of a periodic wave and a single pulse with a shock front through a lossy medium is studied theoretically. The medium is characterized by the frequency dependence of the attenuation coefficient obeying a power law and by a corresponding dispersion law. The numerical modeling of the problem is performed on the basis of the modified spectral approach. It is found that the exponent of the aforementioned power law essentially affects the efficiency of nonlinear interactions, the distortion of the wave profile, and the absorption of acoustic energy in the nonlinear mode. The stability of the discontinuous structure of a shock front is investigated for different power laws close to a linear one. The possibility of pulsed diagnostics of the parameters of the frequency power law governing the attenuation in the medium by the shape of a single pulse with a shock front after its passage through the medium is considered. © 2000 MAIK “Nauka/Interperiodica”.

The nonlinear effects that accompany the propagation of intense acoustic waves in lossy media have been studied in detail for the case of a classical fluid with a square-law frequency dependence of the attenuation coefficient and for a medium with a single relaxation time [1, 2]. However, in many acoustic media, e.g., biological tissues [3] or sea sediments [4], the frequency dependence of the attenuation coefficient deviates from a square-law one. The theoretical description of nonlinear interactions in such media requires the solution of fairly complicated integro-differential equations, and, therefore, the problems related to this phenomenon have been little investigated. However, these problems are important for many practical applications of intense ultrasound and, specifically, for medical acoustics including hyperthermia, acoustical surgery [3, 5], and extracorporeal lithotripsy [6]. The fundamental aspect of the problem is also of interest, especially, in relation to the study of severely distorted nonlinear disturbances containing steep segments, i.e., shock fronts.

This paper presents a theoretical study of the specific features of the nonlinear propagation of periodic and pulsed disturbances in such media; namely, the effect of the parameters of the power law, which governs the attenuation in the medium, on the evolution of the wave profile, the structure of the shock front, and the wave attenuation. The mathematical model developed below allows for the nonlinear effects, the attenuation, and the sound velocity dispersion. The numerical calculations are based on the modified spectral approach [7, 8] that allows one to describe severely dis-

torted waves containing discontinuities by a small number of harmonics. We select the characteristic parameters of the medium and the initial signals to be close to those used in ultrasound therapy. We also discuss the possibility of a pulsed diagnostics of the parameters of the power law, which governs the frequency dependence of attenuation, by single intense pulses with shock fronts.

To describe the propagation of an acoustic wave of finite amplitude in a medium with an arbitrary attenuation law and an arbitrary dispersion, we use a Burgers-type equation

$$\frac{\partial p}{\partial x} - \frac{\varepsilon}{c_0^3 \rho_0} p \frac{\partial p}{\partial \tau} = L(p). \quad (1)$$

Here,  $p$  is the acoustic pressure,  $x$  is the coordinate of the propagating wave,  $\tau = t - x/c_0$  is the time in the moving coordinate system,  $c_0$  is the phase velocity of sound at the characteristic frequency  $\omega_0$ ,  $\varepsilon$  is the coefficient characterizing the acoustic nonlinearity of the medium, and  $L(p)$  is the linear operator responsible for the attenuation and dispersion.

We assume that the frequency dependence of the attenuation coefficient is described by the power law

$$\alpha(\omega) = \alpha_0(\omega/\omega_0)^\eta. \quad (2)$$

In this case, it is impossible to rearrange the right-hand member  $L(p)$  of equation (1) in a unique way with the causality principle being met. The reason is that the power law (2) cannot be obeyed in the entire infinite

frequency range; in particular, at high frequencies, the dependence  $\alpha(\omega)$  tends to saturation [9]. The ambiguity of the selection of the operator  $L(p)$ , which should correspond to attenuation law (2) and meet the causality principle, is related to the possibility of using different models of attenuation at high frequencies. Several different integral forms of  $L(p)$  can be found in the literature [4, 10–13]. The solution of the aforementioned integro-differential equations describing the propagation of severely distorted nonlinear waves presents an extremely complicated problem. Even in numerical modeling, the integral form of equations makes it necessary to perform a convolution at every step of the computational scheme, which considerably complicates and slows down the calculations [14]. Approximate analytical solutions can only be obtained for some particular cases [13].

In our study, for describing nonlinear waves in media where the frequency dependence of attenuation is governed by a power law, we use the spectral approach. We consider a system of coupled equations for an infinite number of harmonics; for each harmonic, the corresponding attenuation and dispersion are taken into account.

We assume that, in a broad frequency band, the attenuation obeys the power law (2). According to the causality principle, we can write the Kramers–Kronig-type integral dispersion relations between the attenuation law and the sound velocity dispersion [9, 15]. In the case of a smooth frequency dependence of the attenuation coefficient, we can determine the approximate relationship between the attenuation and dispersion by using the so-called local dispersion relations [15]. From the given attenuation law and the dependences obtained for the sound velocity, we can calculate the characteristics of the nonlinear propagation of waves without any rearrangement of the evolution equation (1).

Now, in equation (1), we pass to dimensionless variables:

$$\frac{\partial V}{\partial z} - NV \frac{\partial V}{\partial \theta} = L'(V), \quad (3)$$

where  $V = p/p_0$  is the acoustic pressure normalized to the characteristic amplitude value  $p_0$ ;  $\theta = \omega_0 \tau$  is time in the moving coordinate system;  $z = x/x_{at}$  is the wave propagation coordinate normalized to the attenuation length  $x_{at} = 1/\alpha_0$ ;  $\alpha_0$  is the attenuation coefficient at the frequency  $\omega_0$ ;  $\omega_0$  is the characteristic frequency of the acoustic signal, where, for a pulse disturbance of duration  $t_0$ , the frequency is  $\omega_0 = 1/t_0$ ;  $x_{nl} = c_0^3 \rho_0 / \epsilon p_0 \omega_0$  is the length of the discontinuity formation for a harmonic wave in the absence of attenuation;  $N = x_{at}/x_{nl}$  is the dimensionless parameter of nonlinearity; and the oper-

ator  $L'(V)$  corresponds to the initial operator  $L(p)$  expressed through the new variables.

We represent the solution to equation (3) in the form of a Fourier series expansion

$$V(z, \theta) = C_0 + \sum_{\substack{n = -\infty \\ n \neq 0}}^{\infty} C_n(z) \exp(-in\theta). \quad (4)$$

Then, substituting solution (4) into equation (3), we obtain a system of an infinite number of coupled equations for the Fourier components:

$$\begin{aligned} \frac{dC_n}{dz} = & -\frac{in}{2}N \\ & \times \left( 2C_0C_n + \sum_{k=1}^{n-1} C_kC_{n-k} + 2 \sum_{k=n+1}^{\infty} C_kC_{k-n}^* \right) \\ & + iK'(n)C_n - K''(n)C_n. \end{aligned} \quad (5)$$

Here,  $K'$  and  $K''$  are the real and imaginary parts of the dimensionless wave number  $K(n) = K' + iK''$ . They describe the dispersion ( $K'$ ) and the attenuation ( $K''$ ) of sound, and, in the moving coordinate system, they have the form:

$$K''(n) = \alpha(n\omega_0)/\alpha_0, \quad (6)$$

$$K'(n) = n\omega_0(1/(c(n\omega_0) - 1/c_0)/\alpha_0.$$

The frequency dependence of the attenuation coefficient  $K''$  was selected according to the experimental data for biological tissues [3, 16], and the sound velocity dispersion  $K'$  was calculated using the local dispersion relations [15]

$$\alpha(\omega) = \frac{\pi\omega^2}{2c_0^2} \frac{dc(\omega)}{d\omega}, \quad (7)$$

$$\Delta c = c(\omega) - c_0 = \frac{2c_0^2}{\pi} \int_{\omega_0}^{\omega} \frac{\alpha(\omega')}{(\omega')^2} d\omega'. \quad (8)$$

For the attenuation obeying the power law (2), the sound velocity dispersion calculated by formula (8) has the form

$$\begin{aligned} \frac{\Delta c}{c_0} = & \frac{c(\omega) - c_0}{c_0} \\ = & \frac{2c_0\alpha_0}{\pi(\eta - 1)\omega_0} \begin{cases} ((\omega/\omega_0)^{\eta-1} - 1), & \eta \neq 1 \\ \ln(\omega/\omega_0), & \eta = 1. \end{cases} \end{aligned} \quad (9)$$

We select the parameters of the power law (2) to be close to the parameters of biological media or the biological tissue phantom 1.3 butanediol [16]. Figure 1a shows the frequency dependences of the attenuation coefficient normalized to its value  $\alpha_0$  at 1 MHz. The curves presented in the figure refer to blood ( $\eta = 1.42$ ,

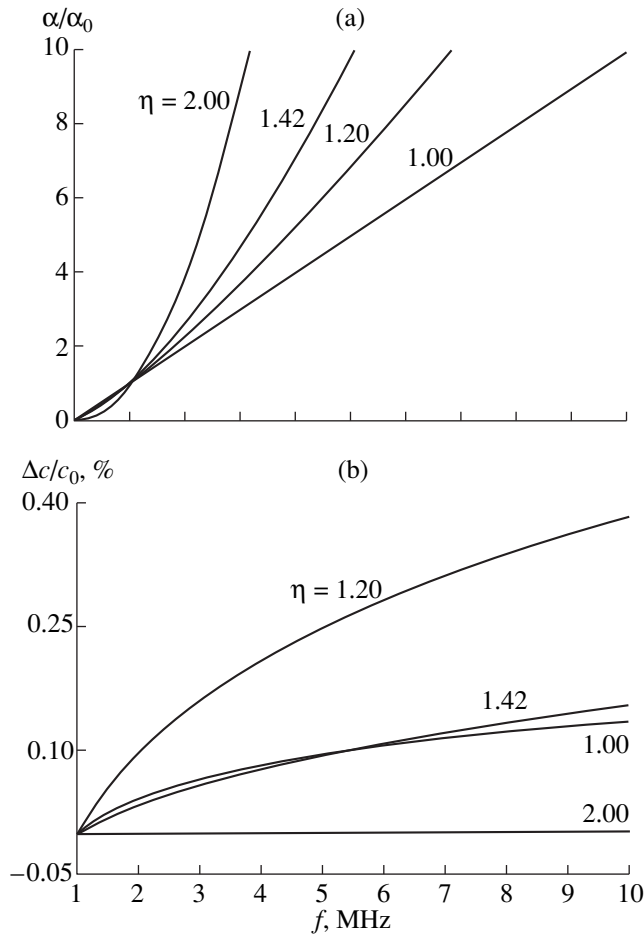


**Fig. 1.** Frequency dependences of (a) the attenuation coefficient and (b) the sound velocity dispersion for different exponents of the frequency power law governing the attenuation in the medium:  $\eta = 2$  (water), 1.42 (blood), 1.2 (liver), and 1 (butanediol).

$\alpha_0 = 0.025 \text{ cm}^{-1}$ , and  $c_0 = 1570 \text{ m/s}$ ), liver ( $\eta = 1.2$ ,  $\alpha_0 = 0.082 \text{ cm}^{-1}$ , and  $c_0 = 1600 \text{ m/s}$ ) [3], water ( $\eta = 2$ ,  $\alpha_0 = 0.0003 \text{ cm}^{-1}$ , and  $c_0 = 1500 \text{ m/s}$ ), and butanediol ( $\eta = 1$ ,  $\alpha_0 = 0.038 \text{ cm}^{-1}$ , and  $c_0 = 1546 \text{ m/s}$ ). The sound velocity calculated by formula (9) with these data is shown in Fig. 1b. From this figure, one can see that the dispersion characteristics of butanediol and blood are close to each other. The theoretical dispersion curves shown in the figure agree well with the experimental data [3], which testify that the values of the sound velocity dispersion in biological tissues do not exceed 1% in the frequency range 1–10 MHz.

To perform a numerical integration of the system of equations (5), we use a modified spectral approach based on the *a priori* data on the high-frequency asymptotics of the shock-wave spectrum. The main idea of the approach developed in our previous publication [7] lies in the replacement of the exact system of an infinite number of equations (5) by an approximate sys-

tem of equations for the amplitudes of the first  $N_{\max}$  harmonics:

$$\begin{aligned} \frac{dC_n}{dz} = & -inN \left\{ C_0 C_n + \frac{1}{2} \sum_{k=1}^{n-1} C_k C_{n-k} \right. \\ & + \sum_{k=n+1}^{N_{\max}} C_k C_{k-n}^* + \sum_{k=N_{\max}+1}^{N_{\max}-n} \tilde{C}_k C_{k-n}^* \\ & \left. + \left( \frac{A_s}{2\pi} \right)^2 \frac{\exp(in\theta_s)}{n} \sum_{k=N_{\max}+1}^{N_{\max}+n} \frac{1}{k} \right\} + iK'(n)C_n - K''(n)C_n. \end{aligned} \quad (10)$$

On the right-hand side of equations (10), the amplitudes of harmonics with the numbers  $n > N_{\max}$  are approximated by their asymptotic values

$$\tilde{C}_n = iA_s \exp(in\theta_s) / 2\pi n, \quad (11)$$

which correspond to the spectrum of a sawtooth wave with the amplitude  $A_s$  and the discontinuity at the point  $\theta_s$ . Such a replacement allows one to analytically calculate the infinite sums on the right-hand side of equations (5). The quantities  $A_s$  and  $\theta_s$  are determined from the values of the two last spectral components of the system,  $C_{N_{\max}-1}$  and  $C_{N_{\max}}$ , on the assumption that, at  $n \approx N_{\max}$ , the form of the spectrum differs little from its high-frequency asymptotics

$$A_s = 2\pi N_{\max} |C_{N_{\max}}|, \quad \theta_s = \arg(C_{N_{\max}} / C_{N_{\max}-1}). \quad (12)$$

The proposed method allows a fairly accurate modeling of the propagation of waves with narrow shock fronts by using a limited number of harmonics  $N_{\max} = 30\text{--}50$ .

Equations (10) were numerically integrated by the Runge-Kutta scheme with a fourth-order precision at  $N_{\max} = 50$ . For each subsequent step of calculation in  $z$ , the values of  $A_s(z)$  and  $\theta_s(z)$  were reconstructed by formulas (12) from the values of the coefficients  $C_{N_{\max}-1}$  and  $C_{N_{\max}}$  calculated at the preceding step.

The important characteristics that determine the thermal or cavitation effect on the tissue are the temporal wave profile, the behavior of the wave intensity in the medium, and the structure and width of the shock front. The wave profile can be reconstructed as a sum of the smooth and sawtooth components from the numerically calculated amplitudes of the first  $N_{\max}$  harmonics:

$$\begin{aligned} V(\theta, z) = & \sum_{n=-N_{\max}}^{N_{\max}} (C_n(z) \exp(-in\theta)) \\ & - \frac{A_s}{\pi} \sum_{n=1}^{N_{\max}} \frac{\sin(\theta - \theta_s)}{n} + \frac{A_s}{2} \begin{cases} -1 - \frac{\theta - \theta_s}{\pi}, & 0 \leq \theta \leq \theta_s \\ 1 - \frac{\theta - \theta_s}{\pi}, & \theta_s \leq \theta \leq 2\pi. \end{cases} \end{aligned} \quad (13)$$

The mean wave intensity was also calculated:  $I(z) = \frac{1}{2\pi} \int_0^{2\pi} V^2(z, \theta) d\theta = \sum_{n=-\infty}^{\infty} |C_n(z)|^2$ . With allowance for the asymptotic behavior of harmonics at high frequencies (i.e., at  $n > N_{\max}$ ) (11), the wave intensity can be represented as a finite sum

$$I(z) = C_0^2 + \sum_{n=1}^{N_{\max}} \left( 2|C_n(z)|^2 - \frac{A_s^2}{2\pi^2 n^2} \right) + \frac{A_s^2}{12}. \quad (14)$$

From the point of view of medical applications, the study of the propagation of intense harmonic waves (ultrasound therapy) and intense single pulses with shock fronts (extracorporeal lithotripsy) are of most interest. Therefore, we consider an initial acoustic signal in the form of a harmonic wave

$$p(\tau, x = 0) = p_0 \sin(\omega_0 \tau) \quad (15)$$

of frequency 1 MHz and amplitude 0.5–7 MPa, which corresponds to the pressure range used in ultrasound therapy, and a shock pulse with an exponential profile behind a shock front

$$p(\tau, x = 0) = \begin{cases} 0, & \tau < \tau_s \\ p_0 \exp\left(-\frac{\tau - \tau_s}{t_0}\right), & \tau > \tau_s. \end{cases} \quad (16)$$

Here,  $\tau_s$  is the time of the formation of the pulse shock front; the initial amplitude  $p_0 = 3$  MPa and the duration  $t_0 = 300$  ns of the pulse were set to be close to the parameters of the pulses used in lithotripters (at the focuser output, away from the focus [17]) or to the parameters of the pulses generated by the photoacoustic method in the plane-wave mode [18].

As was mentioned above, the sound velocity dispersion is relatively small. However, it noticeably affects the profile of the acoustic disturbance. Figure 2a presents the numerically calculated evolution of the profile  $V = p/p_0$  of an initially harmonic wave (15) in a medium with a linear frequency dependence of attenuation,  $\eta = 1$ , which corresponds to the parameters of butanediol (Fig. 1). Curve 1 represents the initial wave profile, and curve 2 represents the wave profile at the distance  $z = 0.3$  (8 cm) in the case of linear propagation,  $N = 0$ . Profiles 3 and 4 are calculated for the same distance in the case of a nonlinear propagation  $N = 10$  ( $p_0 = 4.5$  MPa) in the absence and presence of the sound velocity dispersion, respectively. One can see that the effect of dispersion manifests itself as an asymmetric distortion of the wave profile: the negative semiperiod becomes sharper, while the positive semiperiod is “protracted” so that the position of the peak of the wave increasingly lags behind the wavefront. Such an asymmetry of the profile is characteristic for media with dispersion, e.g., a relaxing medium [1, 18, 19]. In a dispersion medium, the shock front is shifted at the expense of the faster

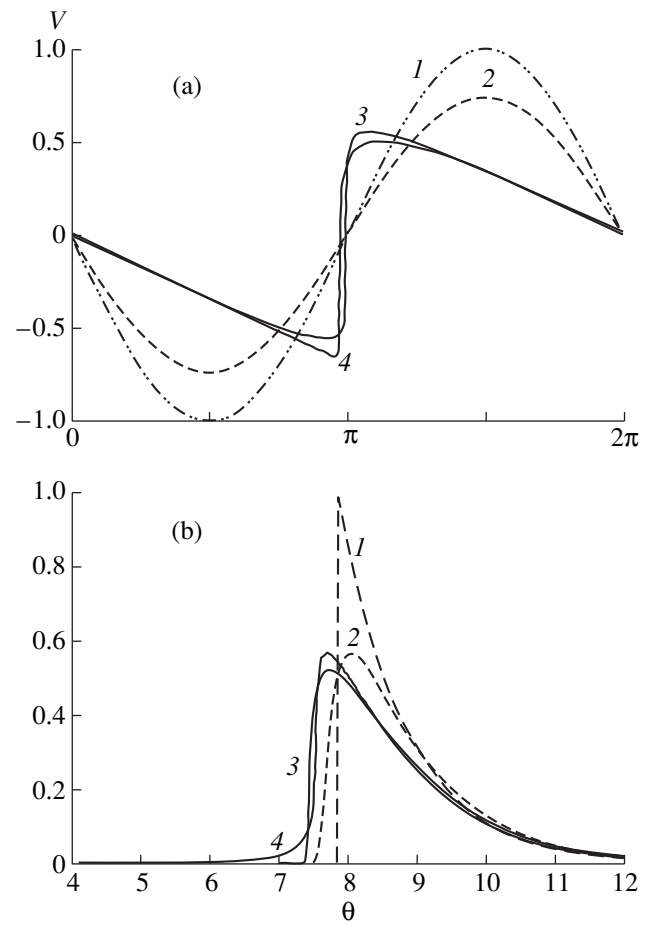


**Fig. 2.** Effect of nonlinearity, dissipation, and dispersion on the evolution of a wave profile in a medium with  $\eta = 1$ .

(a) Harmonic initial wave (curve 1); curves 2–4 correspond to  $z = 0.3$ : (2) profile calculated with allowance for only the attenuation ( $N = 0$ ); (3) profile in the presence of attenuation and nonlinearity ( $N = 10$ ); and (4) profile in the presence of attenuation, nonlinearity ( $N = 10$ ), and dispersion.

(b) Initial pulse with a shock front (curve 1); curves 2–4 correspond to  $z = 0.23$ : (2) profile in a linear medium ( $N = 0$ ) with attenuation and dispersion; (3) profile in a nonlinear medium ( $N = 3.3$ ) with attenuation and dispersion; and (4) profile in a nonlinear medium ( $N = 3.3$ ) with attenuation only.

propagation of higher frequencies forming the discontinuity.

In a similar way, the dispersion affects the profile of a shock pulse. Figure 2b presents the profile of the initial pulse (16) (curve 1) and the profiles of the pulse at the distance  $z = 0.23$  (6 cm) at which pronounced effects of both nonlinearity and dissipation can be observed. In the case of linear propagation (curve 2), the shock front broadens because of the attenuation of the high-frequency components. In the case of a nonlinear propagation (curve 3), the front of the pulse propagates faster, and the front width is less than in the case of linear propagation. Such a manifestation of nonlinear effects is well known. The aforementioned curves 2

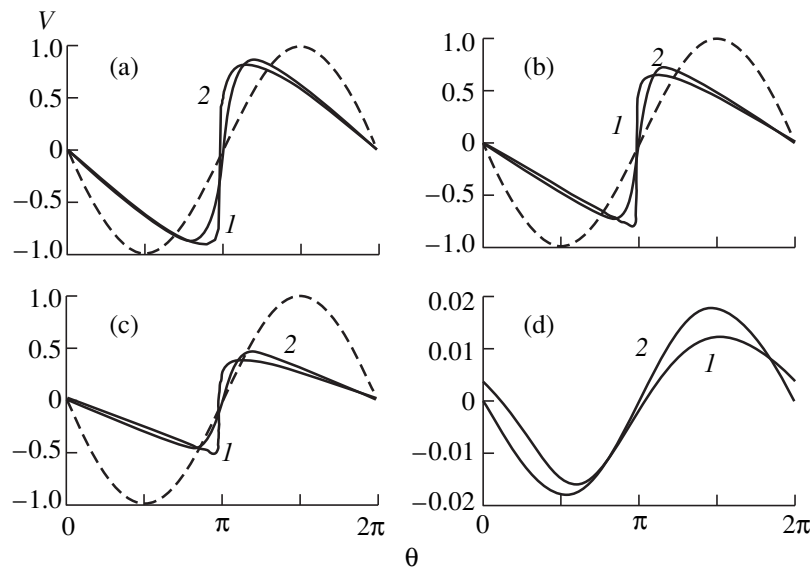


**Fig. 3.** Profiles of an initially harmonic wave (dashed curves) at different distances  $z =$  (a) 0.13, (b) 0.22, (c) 0.4, and (d) 3 in a nonlinear medium with different frequency power laws governing the attenuation:  $\eta = 1$  and 2 (numbers near the curves). The nonlinear parameter is  $N = 10$ .

and 3 are calculated with allowances made for the sound velocity dispersion. To illustrate the role of dispersion, we also present a nonlinear pulse profile calculated with allowance for the presence of attenuation but in the absence of dispersion (curve 4). Correlating profiles 3 and 4, one can see that the neglect of dispersion leads to the appearance of a lengthy precursor propagating faster than the shock front, which is a result of the violation of the causality principle. Besides, in the model without dispersion, the peak pressure of the signal is slightly overestimated, and the velocity of the shock front propagation is reduced.

In biological tissues, the frequency dependences of the attenuation coefficient vary from a linear law to an almost square one. The exponent of this power law is one of the parameters that affect the nonlinear evolution of the acoustic signal profile. This effect is illustrated in Fig. 3, which compares the wave profiles formed at different distances in media with linear ( $\eta = 1$ ) and a square-law ( $\eta = 2$ ) frequency dependences of the attenuation coefficient. The profiles are obtained for an initially harmonic wave. In the medium with the linear law ( $\eta = 1$ ), the shock front is formed earlier, it is narrower, and it lasts longer than in the medium with the square law ( $\eta = 2$ ). This occurs because in the medium with the square law, the high-frequency harmonics of the spectrum experience a stronger attenuation.

At large distances  $x \gg x_{at}$  (Fig. 3d) where the wave reverts to the harmonic form, the peak pressure amplitude in the medium with  $\eta = 1$  is less than in the medium with  $\eta = 2$ . This result may seem unexpected at first glance, because, in the medium with  $\eta = 2$ , all higher harmonics propagate with higher attenuation coefficients than in the medium with  $\eta = 1$ . The effect

is caused by the less intense generation of high-frequency spectrum components in the more dissipative medium, and, hence, by a lower attenuation at the arising shock fronts. Such an effect, which consists of the limitation of the efficiency of the wave energy redistribution toward the high-frequency spectrum region with increasing attenuation of the harmonics of the initial signal, can be used for controlling nonlinear wave interactions. This phenomenon should be most pronounced in a medium with resonance absorption at the second harmonic: in such a medium, the energy transfer to higher frequencies of the spectrum is limited, and the wave propagates almost without distortion [20].

For an initially harmonic wave, the change in the frequency dependence of attenuation from linear to a square-law one leads to some broadening of the shock front, which is illustrated in Fig. 4a. This figure presents the wave profiles calculated for the distance  $z = 0.5$  at  $N = 15$ , for media with different exponents  $\eta$  (the numbers near the curves) and the sound velocity dispersion corresponding to these media. One can see that an increase in  $\eta$  has practically no effect on the wave amplitudes, while a noticeable broadening of the shock front is observed. The front width increases several times as the frequency power law governing the attenuation changes from linear to a square one.

The exponent of the frequency power law also noticeably affects the absorption of the total wave energy in a nonlinear medium. Figure 4b shows the variation of the effective normalized attenuation coefficient  $\alpha_{eff}$  with distance, where the normalization of the coefficient is performed with respect to its value in the case of a linear wave propagation, and the quantity

$\alpha_{\text{eff}}$  is calculated from the variation in the wave intensity (14):

$$\alpha_{\text{eff}} = -\frac{dI/dx}{2\alpha_0 I}. \quad (17)$$

Different curves correspond to media with equal values of the attenuation coefficient  $\alpha_0$  at the fundamental frequency, but with different exponents of the frequency power law:  $\eta = 1, 1.5,$  and  $2$ . One can see that, at small distances, the effective attenuation coefficient is higher for the square law because of the stronger dissipation at high frequencies. However, after the formation of steep segments in the wave profile, the attenuation coefficient is higher in the medium with the linear law as a result of the more efficient nonlinear attenuation mode. The curves shown in Fig. 4b were calculated with allowances made for the dispersion. However, the corresponding dependences calculated by neglecting the dispersion proved to be virtually identical to those shown in Fig. 4b. Hence, although the dispersion affects the wave profile, it has no noticeable effect on the absorption of the wave energy.

The power law (2) is characterized by two parameters,  $\alpha_0$  and  $\eta$ , which play different roles in the evolution of the acoustic signal. Figure 5a shows the profiles of pulse (16) at the distance  $x = 6$  cm for media with different exponents of the power law (2) and a fixed parameter  $\alpha_0$  corresponding to the attenuation in butanediol at a frequency of 1 MHz. From this figure, one can see that an increase in the exponent leads to a noticeable broadening of the shock front, which can be explained by a stronger attenuation of the high-frequency spectrum components. At the same time, the variation in the exponent has no noticeable effect on the peak pressure value. By contrast, a change in the parameter  $\alpha_0$  leads to a change in the pulse amplitude. As the attenuation coefficient  $\alpha_0$  increases, the peak pressure decreases, while the width and the position of the shock front vary insignificantly (Fig. 5b). Figure 5b shows the pulse profiles corresponding to the same distance  $x = 6$  cm for media with a linear frequency dependence of the attenuation coefficient and different values of  $\alpha_0$  (numbers near the curves).

Thus, nonlinear interactions that occur in both periodic waves and pulsed fields depend on the parameters of the power law governing the frequency dependence of attenuation, especially for strongly nonlinear waves with discontinuities. Even a weak dispersion of sound velocity leads to noticeable distortions of the wave profile as compared to the case of a square-law frequency dependence of attenuation in the absence of dispersion. At the same time, the dispersion has virtually no effect on the dissipation of the energy of a nonlinear wave. The parameters of the power law governing the frequency dependence of attenuation affect the distortion of the profile of a propagating signal in different ways, especially in the case of a shock pulse: the exponent variations mainly affect the width of the pulse shock

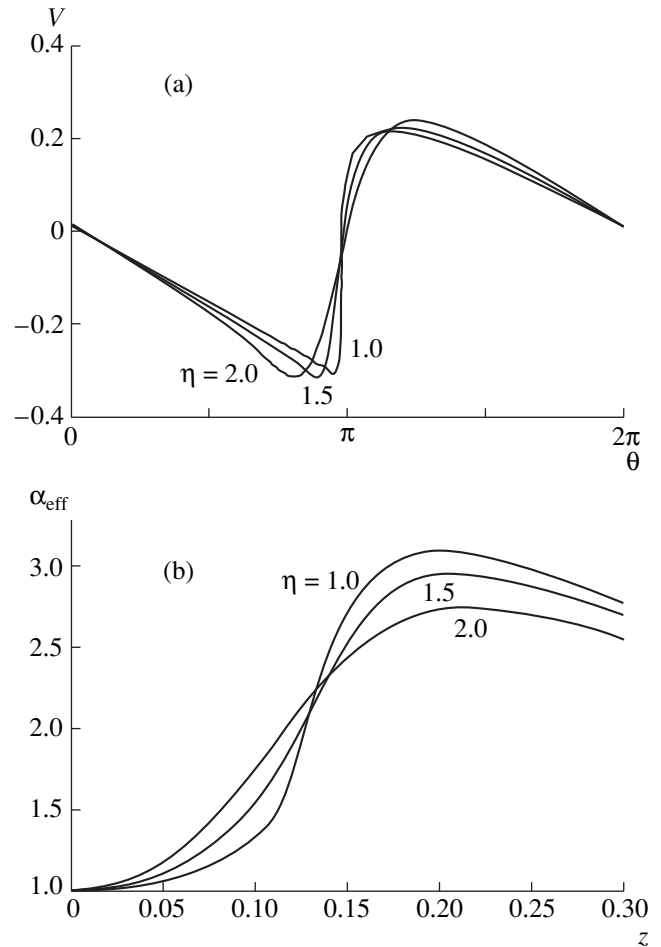


**Fig. 4.** Effect of the exponent  $\eta$  on the evolution of a wave in a nonlinear medium. At the input, a harmonic wave of frequency 1 MHz is set;  $\alpha_0 = 0.038 \text{ cm}^{-1}$ ; the nonlinear parameter is  $N = 15$ . (a) Wave profile at the distance  $z = 0.5$ ; (b) dependence of the effective attenuation coefficient on distance.

front, while the variations in the attenuation coefficient mainly affect the peak pressure value. This result allows one to discuss a fundamental possibility of the diagnostics of the parameters of attenuation in the medium by the form of a shock-wave pulse transmitted through it.

In closing, we discuss the problem of stability of a discontinuous wavefront propagating in a lossy medium obeying a frequency power law  $\alpha(\omega) \sim \omega^\eta$ . It has been found that the shock front of a wave propagating in a medium obeying a square law with  $\eta = 2$  is no mathematical discontinuity but has a finite width determined by the viscosity of the medium and the amplitude of the wave [1]. On the other hand, in all media with constant attenuation ( $\eta = 0$ ), the dissipation does not preclude discontinuities in the wave profile [21]. Discontinuities are also stable in relaxing media. Such media are characterized by a constant value of the attenuation coefficient at high frequencies [19]. As far

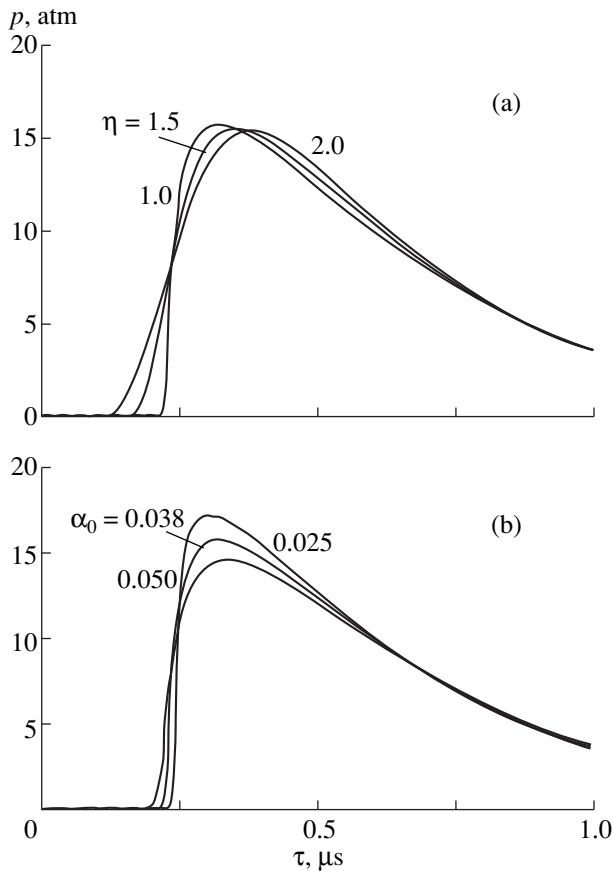


**Fig. 5.** Effect of the parameters of the power law (2),  $\alpha_0$  and  $\eta$ , on the profile of the shock pulse transmitted through a layer of a nonlinear lossy medium. The input parameters of the pulse are  $p_0 = 30$  atm and  $t_0 = 0.3$   $\mu$ s; the distance in the medium is  $x = 6$  cm.

(a) Pulse profiles in media with equal attenuation coefficients  $\alpha_0 = \alpha(1 \text{ MHz}) = 0.038 \text{ cm}^{-1}$  and different exponents  $\eta = 1, 1.5, \text{ and } 2$ .

(b) Pulse profiles in media with equal exponents  $\eta = 1$  and different values of the attenuation coefficient  $\alpha_0 = 0.025, 0.038, \text{ and } 0.05 \text{ cm}^{-1}$ .

as we know, for the case of an arbitrary power law (2), the problem of the stability of a discontinuity had never been studied. Below, we demonstrate that the exponent  $\eta = 1$  is a critical value for a discontinuity, i.e., a discontinuity is unstable at  $\eta \geq 1$ .

Let a plane wave with a discontinuous wave profile be set at the medium input. Without loss of generality, we can assume that the wave is a periodic one. The dissipation of the wave energy is described by the expression

$$\frac{dI}{dx} = \sum_{n=1}^{\infty} 2\alpha_n I_n, \quad (18)$$

where  $I_n \sim |C_n|^2$  and  $\alpha_n = \alpha(n\omega_0) \sim n^\eta$  are the intensity of the  $n$ th harmonic and the corresponding attenuation

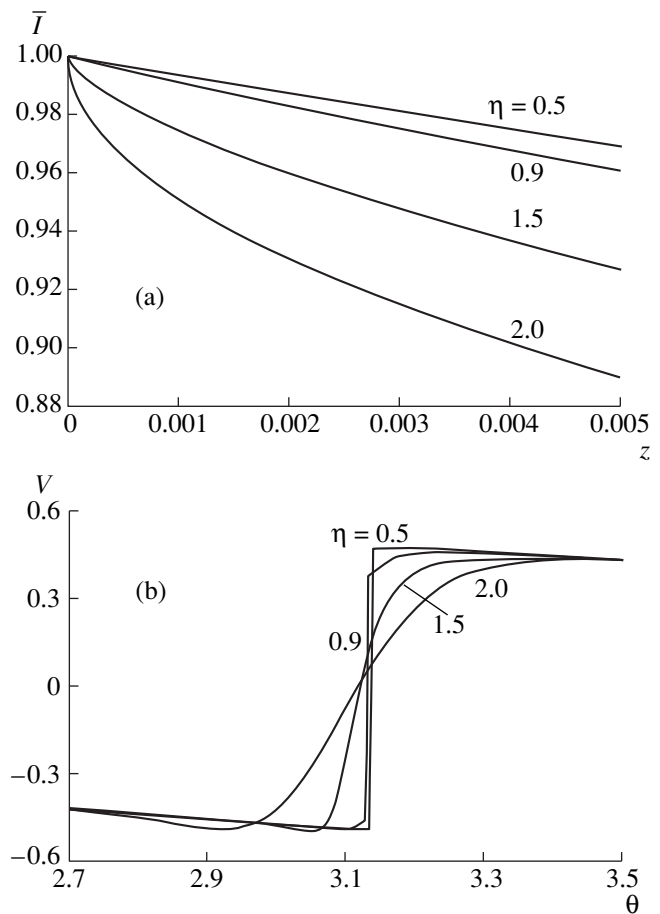


**Fig. 6.** Stability of the shock front of an initially sawtooth wave in media with different exponents  $\eta$  of the power law (2). (a) Dependence of the normalized intensity  $\bar{I} = I(z)/I(z=0)$  on the distance  $z$ ; (b) wave profile in the shock region at  $z = 0.005$ .

coefficient, respectively. At high frequencies, the spectrum of a discontinuous wave always has the asymptotic form (11), i.e.,  $|C_n| \sim n^{-1}$ . Hence, the decrease in the wave energy with distance is determined by a series whose terms at large  $n$  behave as  $n^{\eta-2}$ . At  $\eta \geq 1$ , series (18) diverges, i.e., the quantity  $dI/dx$  is infinite. If we assume that the high-frequency asymptotics (11) of the spectrum exists in an arbitrarily small interval of distances, we obtain an infinite value of the absorbed energy, which is impossible because of the finiteness of the intensity of the initial wave. Thus, in this case, the discontinuity is unstable. At  $\eta < 1$ , series (18) converges, and, hence, the existence of the discontinuity is possible.

As an illustration, Fig. 6 presents (a) the numerically calculated dependences of the intensity of an initially discontinuous wave on the distance  $z$  and (b) the profile of the wave in the shock region formed at  $z = 0.005$  in a nonlinear medium ( $N = 10$ ) for different exponents of the frequency power law governing the attenuation:  $\eta = 0.5, 0.9, 1.5, \text{ and } 2$ . The initial wave

was taken to be a sawtooth one with the discontinuity amplitude  $A_s = 1$ , and the intensity was normalized to its initial value at  $z = 0$ . One can see that, at  $\eta < 1$ , the derivative  $dI/dz$  at  $z = 0$  is finite, and the wave profile remains discontinuous in the course of the wave propagation. At  $\eta > 1$ , the intensity at  $z = 0$  decreases infinitely fast, and the initial discontinuity is smoothed out. As the exponent  $\eta$  increases, the effect of smoothing out is enhanced.

#### ACKNOWLEDGMENTS

This work was supported in part by the DARPA foundation, an NIH grant (no. DK 43881), and the Russian Foundation for Basic Research (project no. 98-02-17318).

#### REFERENCES

- O. V. Rudenko and S. I. Soluyan, *Theoretical Foundations of Nonlinear Acoustics* (Nauka, Moscow, 1975; Plenum, New York, 1977).
- M. B. Vinogradova, O. V. Rudenko, and A. P. Sukhorukov, *Theory of Waves* (Nauka, Moscow, 1990).
- Physical Principles of Medical Ultrasonics*, Ed. by G. Hill (Ellis Harwood, Chichester, 1986).
- C. W. Horton, Sr., *J. Acoust. Soc. Am.* **55**, 547 (1974).
- J. Y. Chapelon and D. Cathignol, in *Advances in Nonlinear Acoustics: Proceedings of 13th International Symposium on Nonlinear Acoustics* (Bergen, Norway, 1993).
- C. Chaussy and G. J. Fuchs, *J. Endourology* **141**, 782 (1989).
- Yu. A. Pishchal'nikov, O. A. Sapozhnikov, and V. A. Khokhlova, *Akust. Zh.* **42**, 412 (1996) [*Acoust. Phys.* **42**, 362 (1996)].
- V. A. Khokhlova, O. A. Sapozhnikov, L. A. Crum, *et al.*, in *Proceedings of the Ultrasonic World Congress* (Berlin, Germany, 1995), p. 1099.
- V. L. Ginzburg, *Akust. Zh.* **1**, 31 (1955) [*Sov. Phys. Acoust.* **1**, 32 (1955)].
- T. L. Szabo, *J. Acoust. Soc. Am.* **96**, 491 (1994).
- D. R. Bacon, Doctor of Philosophy Thesis (Bath University, UK, 1986).
- M. D. Collins, *J. Acoust. Soc. Am.* **84**, 2114 (1988).
- M. A. Averkiou, L. A. Crum, V. A. Khokhlova, *et al.*, in *Nonlinear Acoustics in Perspective: Proceedings of 14th International Symposium on Nonlinear Acoustics, Nanjing, China* (Nanjing University Press, 1996), p. 463.
- J. Tavakkoli, D. Cathignol, R. Souchon, *et al.*, *J. Acoust. Soc. Am.* **104**, 2061 (1998).
- M. O'Donnell, E. T. Jaynes, and J. G. Miller, *J. Acoust. Soc. Am.* **69**, 696 (1981).
- B. Cranz, in *Ultrasonic Symposium, 1994*.
- A. J. Coleman and J. E. Saunders, *Ultrasound Med. Biol.* **15**, 213 (1989).
- V. G. Andreev, Yu. A. Pishchal'nikov, O. A. Sapozhnikov, *et al.*, *Akust. Zh.* **45**, 13 (1999) [*Acoust. Phys.* **45**, 8 (1999)].
- A. L. Polyakova, S. I. Soluyan, and R. V. Khokhlov, *Akust. Zh.* **8**, 107 (1962) [*Sov. Phys. Acoust.* **8**, 78 (1962)].
- O. V. Rudenko, *Akust. Zh.* **29**, 398 (1983) [*Sov. Phys. Acoust.* **29**, 234 (1983)].
- O. A. Vasil'eva, A. A. Karabutov, E. A. Lapshin, and O. V. Rudenko, *Interaction of One-Dimensional Waves in Dispersion-Free Media* (Mosk. Gos. Univ., Moscow, 1983).

Translated by E.M. Golyamina

# Numerical Calculation for a Nonlinear Acoustic Impulse Diffracted by a Rectangular Ledge

V. I. Kondrat'ev and Yu. S. Kryukov

Research Institute of Applied Acoustics, a/ya 36, Dubna, 141980 Russia

e-mail: niipa@dubna.ru

Received February 8, 1999

**Abstract**—A computer model is developed for describing the diffraction of a nonlinear acoustic impulse signal by the irregularities of a perfectly rigid boundary. The model is based on the finite-difference method with the use of the MacCormack explicit scheme for solving the initial boundary-value problem formulated for a system of nonlinear equations of gas dynamics. The accuracy of the numerical calculations is estimated. The calculations are performed for the diffraction of the signal by ledges that occur at the irregular boundary. The results of the calculations are correlated with the estimates made by the Maekawa empirical theory. © 2000 MAIK “Nauka/Interperiodica”.

Most studies of the diffraction of acoustic impulse signals use the linear empirical diffraction theories [1, 2], which are based on the expansion of the signal into a Fourier series and take into account the ratio of the geometric dimensions of the obstacle to the wavelength of the corresponding spectral component of the signal. Although these theories are approximate, a great body of experimental data on the diffraction of impulses by vertical obstacles agree well with these theories [3].

The purpose of our study is the development of a finite-difference numerical model for the calculation of the signal diffraction by obstacles of different shape. The model is based on the numerical solution of a non-stationary initial boundary-value problem for gas dynamics equations in a semibounded region with an irregular, perfectly rigid lower boundary containing various kinds of ledges and grooves. In this paper, we use the MacCormack finite-difference scheme [4] the application of which to nonlinear acoustic impulses provides a sufficient rate of calculation and a fair accuracy of the results. This scheme was tested in the calculation of the interaction of acoustic impulses with thermics (hot gas regions) [5], where the region of calculation was a regular one with smooth uniform boundaries.

In this paper, we propose and justify the method of modeling for an irregular region of calculation with nonuniform boundaries of arbitrary configuration.

Let us consider a two-dimensional semibounded region  $\Omega$  filled with a homogeneous air medium (Fig. 1). We introduce the Cartesian coordinates  $Oxy$ . Figure 1 schematically represents the irregular lower boundary with breakpoints at  $x = x_2$ ,  $x = x_3$ , and  $x = x_4$ . The impulse occupies the interval  $(x_0, x_1)$  at the instant  $t_0 = 0$ . To describe the propagation of the impulse of a given form in a two-dimensional homogeneous air medium, we

use the system of nonlinear equations for an incompressible fluid [4]:

$$\begin{aligned} \frac{\partial \rho}{\partial t} + \frac{\partial(\rho V_x)}{\partial x} + \frac{\partial(\rho V_y)}{\partial y} &= 0, \\ \frac{\partial(\rho V_x)}{\partial t} + \frac{\partial(\rho V_x^2 + p)}{\partial x} + \frac{\partial(\rho V_x V_y)}{\partial y} &= 0, \\ \frac{\partial(\rho V_y)}{\partial t} + \frac{\partial(\rho V_x V_y)}{\partial x} + \frac{\partial(\rho V_y^2 + p)}{\partial y} &= 0, \\ \frac{\partial \varepsilon}{\partial t} + \frac{\partial((\varepsilon + p)V_x)}{\partial x} + \frac{\partial((\varepsilon + p)V_y)}{\partial y} &= 0, \end{aligned} \quad (1)$$

where  $\rho$ ,  $p$ ,  $V_x$ , and  $V_y$  are the physical parameters of the medium, namely, the density, the pressure, and the projections of the velocity onto the  $Ox$  and  $Oy$  axes, respectively;  $\varepsilon = \frac{p}{\gamma - 1} + \frac{\rho}{2}(V_x^2 + V_y^2)$  is the total energy; and  $\gamma$  is the specific-heat ratio.

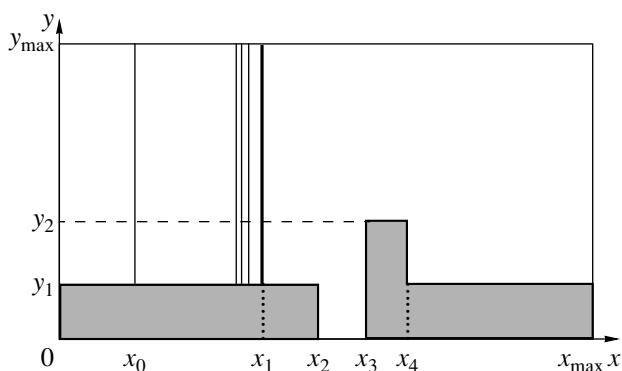


**Fig. 1.** Schematic diagram of the irregular region of calculation.

To specify the travelling wave problem, it is necessary to determine the initial conditions at the instant  $t_0 = 0$ . We assume that, at  $t_0 = 0$ , we have  $V_y(x, y) = 0$  and  $V_x(x, y) = u_1(x)$ , where  $x \in [x_0, x_1]$ , i.e., we have a wave with a plane wavefront travelling toward the obstacle. We set the values of  $p$  and  $\rho$  at the instant  $x_0 = 0$  in the form of the solution for an ordinary travelling wave in a polytropic gas [6]:

$$\begin{aligned} \rho &= \rho_0 \left( 1 + \frac{\gamma - 1}{2} \frac{V_x}{a_0} \right)^{\frac{2}{\gamma - 1}}, \\ p &= p_0 \left( 1 + \frac{\gamma - 1}{2} \frac{V_x}{a_0} \right)^{\frac{2\gamma}{\gamma - 1}}, \end{aligned} \quad (2)$$

where  $\rho_0$ ,  $p_0$ ,  $V_{x0}$ , and  $V_{y0}$  are the parameters of the medium in an unperturbed gas and  $a_0$  is the sound velocity in an unperturbed gas.

*Boundary conditions.* The calculations are performed in an inhomogeneous, piecewise uniform region. At the irregular lower boundary, the impermeability conditions are set:  $\frac{\partial \mathbf{V}}{\partial \mathbf{n}} = 0$ , where  $\mathbf{V} = (V_x \cdot i, V_y \cdot j)$  and  $\mathbf{n}$  is the unit vector normal to the lower boundary.

At the left and right boundaries of the region of calculation, as well as at the upper boundary, the conditions of the absence of the backward wave reflection are set.

Let us pass to the dimensionless parameters  $\rho'$ ,  $p'$ ,  $V'_x$ ,  $V'_y$ ,  $x'$ ,  $y'$ , and  $z'$  by determining their values relative to the values of the physical parameters of an unperturbed medium:

$$\begin{aligned} \rho' &= \frac{\rho}{\rho_0}; \quad V'_x = \frac{V_x}{a_0}; \quad V'_y = \frac{V_y}{a_0}; \quad p' = \frac{p}{p_0}; \quad x' = \frac{x}{L}; \\ y' &= \frac{y}{L}; \quad t' = \frac{at}{L}, \end{aligned} \quad (3)$$

where  $\rho_0$ ,  $p_0$ , and  $a_0$  are the density, pressure, and sound velocity in an unperturbed medium and  $L$  is some characteristic linear dimension.

Using expressions (3) and the equality  $\rho_0 a_0^2 = \gamma p_0$ , we represent the system of equations (1) in a compact vectorial form:

$$\frac{\partial q}{\partial t'} + \frac{\partial F_x}{\partial x'} + \frac{\partial F_y}{\partial y'} = 0, \quad (4)$$

where

$$\begin{aligned} q &= \begin{bmatrix} \rho' \\ \rho' V'_x \\ \rho' V'_y \\ \frac{p'}{\gamma(\gamma - 1)} + \frac{\rho'(V_x'^2 + V_y'^2)}{2} \end{bmatrix}; \\ F_x &= \begin{bmatrix} \rho' V'_x \\ \rho' V_x'^2 + \frac{p'}{\gamma} \\ \rho' V_x'^2 V_y'^2 \\ V'_x \left( \frac{p'}{\gamma - 1} + \frac{\rho'(V_x'^2 + V_y'^2)}{2} \right) \end{bmatrix}; \\ F_y &= \begin{bmatrix} \rho' V'_y \\ \rho' V_x'^2 V_y'^2 \\ \rho' V_y'^2 + \frac{p'}{\gamma} \\ V'_y \left( \frac{p'}{\gamma - 1} + \frac{\rho'(V_x'^2 + V_y'^2)}{2} \right) \end{bmatrix}. \end{aligned} \quad (5)$$

We introduce a regular rectangular grid in the entire region of calculation,  $\Omega_{j,i} = (x_j = x_{j-1} + \Delta x; y_i = y_{i-1} + \Delta y)$ , and define the discretization of the process in time,  $t^n = t^{n-1} + \Delta t$ , where  $\Delta x$ ,  $\Delta y$ , and  $\Delta t$  are the intervals of discretization in the spatial coordinates and in time, respectively. To obtain a numerical solution to the hyperbolic system of equations (4) with the initial and boundary conditions, we use the MacCormack explicit finite-difference scheme [4]:

$$\begin{aligned} q_{j,i}^* &= q_{j,i}^n - \frac{\Delta t'}{\Delta x'} (F_{xj+1,i}^n - F_{xj,i}^n) \\ &\quad - \frac{\Delta t'}{\Delta y'} (F_{yj,i+1}^n - F_{yj,i}^n), \\ q_{j,i}^{n+1} &= \frac{q_{j,i}^n - q_{j,i}^*}{2} - \frac{\Delta t'}{2\Delta x'} (F_{xj,i}^* - F_{xj-1,i}^*) \\ &\quad - \frac{\Delta t'}{2\Delta y'} (F_{yj,i}^* - F_{yj,i-1}^*). \end{aligned} \quad (6)$$

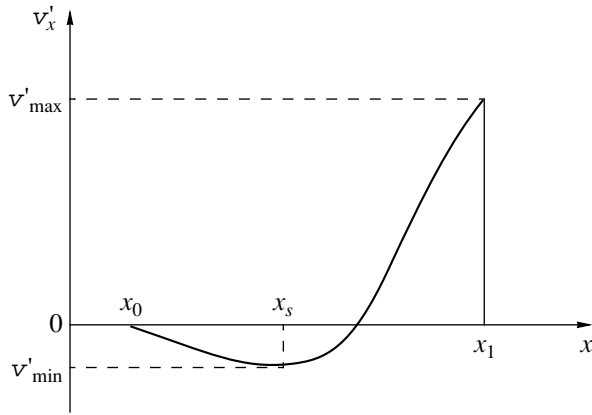


Fig. 2. Velocity profile of the initial nonlinear impulse.

For this scheme, a limitation must be imposed on the mesh width of the grid  $\Delta t'$  according to the Courant condition:

$$\frac{\Delta t'}{\Delta x'} \left( \sqrt{V_x'^2 + V_y'^2} + a \right) \leq 1, \quad (7)$$

where  $a$  is the local sound velocity.

In the finite-difference interpretation, the conditions, which are set at the free boundaries of the region where “inverse” waves are absent, are reduced to the equality of the gradients of the corresponding parameters at the adjacent meshes of the grid [7]. For each of the physical parameters at the vertical left and right boundaries and at the horizontal upper boundary, these conditions have the form:

$$\left( \frac{\partial \varphi}{\partial x} \right)_j = \left( \frac{\partial \varphi}{\partial x} \right)_{j+1}, \quad \left( \frac{\partial \varphi}{\partial y} \right)_i = \left( \frac{\partial \varphi}{\partial y} \right)_{i+1}, \quad (8)$$

where  $\varphi$  is any of the physical parameters:  $\rho$ ,  $p$ ,  $V_x$ , or  $V_y$ . At the lower boundary consisting of vertical and horizontal segments, the impermeability conditions are set for the corresponding velocity components:  $V_{xj,i} = -V_{xj+2,i}$  for a horizontal boundary segment and  $V_{yj,i} = -V_{yj,i+2}$  for a vertical boundary segment.

Taking into account that, in the presence of stepped profiles of nonlinear impulses, the difference approximation of differential equations (4) may give rise to a strong diffusion that will smooth out the stepped impulse profile, we apply the method of flow correction developed by Boris and Book [8]. The method is based on the idea that the introduction of a special antidiffusion limitation does not lead to the appearance of new minima and maxima in the numerical solution, as well as to an enhancement of the existing extrema. We note that the method of flow correction requires the use of a

stronger condition of the scheme stability as compared to expression (7):

$$\left( \sqrt{V_x'^2 + V_y'^2} + a \right) \frac{\Delta t'}{\Delta x'} < 0.4. \quad (9)$$

On the basis of the aforementioned method, a computer code was developed in the FORTRAN-90 language in an HP-UX, X11 medium for a working station of the HP-715 type and in Power Fortran for the Windows 95 medium for IBM-PC compatible computers.

To estimate the accuracy of calculations, we considered the case of an impulse travelling along an ideal, perfectly rigid plane in a semibounded region. The initial distribution of the component  $V_x'$  of the impulse velocity at the instant  $t_0$  was given in the form of a stepped function with the trailing edge descending along the  $Ox$  axis by the parabolic law  $V_x' = A(x - x_s)^2 - \alpha x$  at  $x < x_1$  (Fig. 2), where  $A$  and  $\alpha$  are some given coefficients.

At the initial instant of time  $t_0$ , the leading edge of the impulse was set in the region of calculation at the distance  $x_1$ , and the trailing edge was set at the distance  $x_0$ . The spherical impulse was considered in the far zone of the source, so that the leading edge was set as a plane one in the region of calculation. The density and pressure in the impulse were calculated through the values of the relative velocity  $V_x'$  by formula (2).

The parameters of the region of calculation were  $y_{\max} = 20$  m and  $x_{\max} = 60$  m. The mesh width of the rectangular finite-difference grid was 0.2 m. The time step used in the calculations  $\Delta t' = \frac{\Delta t}{aL}$ , where  $l = 100$  m and  $a = 330$  m/s, was selected automatically based on condition (9). From the numerical calculations, we obtained the variation of the maximum signal amplitude with distance (Fig. 3). According to curve 1 in Fig. 3a, the maximum signal amplitude decreases by the law that is well approximated by the asymptotic formula [2]

$$p \approx \frac{p_0}{r \ln \left( \frac{r}{\alpha} \right)} \quad (\text{curve 2 in Fig. 3a}),$$

where  $\alpha = 9.31$  (a constant),  $r$  is the distance from the source to the point of signal reception, and  $p_0$  is the maximum amplitude of the signal at some characteristic distance from the source.

The corresponding profiles of the impulse propagating along a smooth rigid surface were calculated by finite-difference formulas (6). The results of these calculations are shown in Fig. 3b, where curve 1 represents the profile of the signal at the first step of calculation with the leading edge located at a distance of 30 m from the left boundary of the region of calculation, and curve 2 shows the signal profile at the 320th step of cal-

calculation, which corresponds to the position of the leading edge at a distance of 58 m from the left boundary of the same region. The relative pulse length  $l$  slightly increases at this distance and reaches the value 1.1, which agrees well with the estimates made by the formula

$l \approx \sqrt{\ln \frac{\Delta r}{\alpha}}$ , where  $\Delta r = r_1 - r$  is the difference between the distances traveled by the impulse [6].

Thus, both the fulfillment of the conditions of stability for the numerical scheme and the example of numerical calculation for the propagation of a spherical impulse in the far zone of the source over a perfectly rigid surface point to the fair accuracy of the numerical model.

Using the computer model described above, we studied the diffraction of a nonlinear impulse propagating over a plane surface by a rectangular ledge of height 1.6 m and width 0.4 m rising above this surface; we also studied the diffraction of a similar impulse by the combination of a groove 1.4 m wide and 1 m deep with an adjacent rectangular ledge of the same geometry. First, we present the results of the comparison of the waveform and spectrum obtained for the signal behind the ledge from the calculations by the finite-difference model and the Maekawa empirical theory. The calculations by the Maekawa theory were performed with the use of the diffraction formula for a rectangular obstacle of finite dimensions [1]:

$$p_d = p_0 \frac{1}{\sqrt{3.16}} \frac{\tanh(2\pi N_1)^{1/2} \tanh(2\pi N_2)^{1/2}}{(2\pi N_2)^{1/2}}, \quad (10)$$

where  $N_1 = 2 \frac{\delta_1}{\lambda}$  and  $N_2 = 2 \frac{\delta_2}{\lambda}$  are the Fresnel numbers

calculated for  $\delta_1$  and  $\delta_2$ , respectively; here,  $\delta_1$  and  $\delta_2$  are the differences between the path of the direct signal and the paths of the signals diffracted by the left and right corners of the ledge, respectively. In the calculations, the impulse was preliminarily represented in the form of a sum of spectral components with the help of the Fourier transform. Then, formula (10) was applied to each spectral component. For the spectral components of the diffraction signal  $p_d$ , the signal formed behind the obstacle was calculated by the inverse Fourier transform.

Figure 4a presents the results obtained by calculating the variations in the relative pressure levels at a fixed observation point behind the obstacle with the use of the finite-difference model (curve 1) and the Maekawa model (curve 2). Figure 4b shows the levels of the spectral densities of signals: the calculations by the finite-difference model (curve 1) and the Maekawa theory (curve 2). The observation point was set at a distance of 1 m from the ledge, at a height of 1 m above the rigid surface. Figure 4a demonstrates a fair agreement between the signal levels in the impulse compression zone where the relative pressures are equal to 1.35 in both cases. In the rarefaction zone of the impulse, the Maekawa theory yields somewhat higher values of the relative pressure as compared to the finite-difference model: 0.89 and 0.85, respectively. We note that, behind the barrier, the shape of the impulse calculated by the finite-difference model is characterized by two local maxima in the compression zone, which is a result of the superposition of the direct diffraction wave and the wave reflected from the lower boundary. For correspondingly selected observation points, this fact is supported by numerous experimental data [3, 9]. The spectral compositions of the impulses calculated by the two

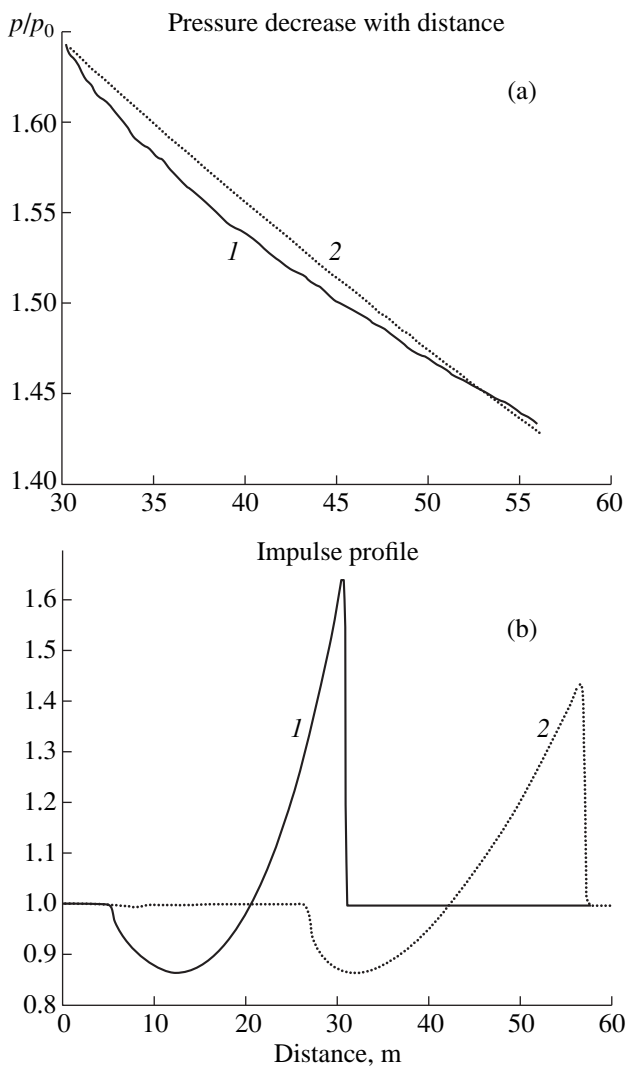


**Fig. 3.** Comparison of the accuracy of calculations for a particular case of a smooth rigid surface. (a) Variation of the relative pressure with distance: (1) finite-difference solution; (2) asymptotic solution by the Landau formula [6]. (b) Variation of the shape of the impulse with distance: (1) impulse profile at the first step of calculation; (2) impulse profile at the 320th step of calculation.

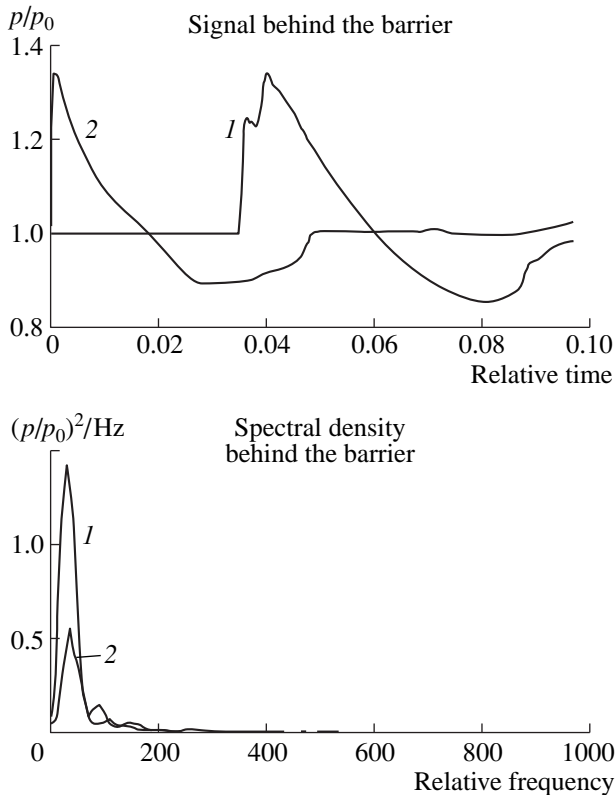


**Fig. 4.** Comparison of the numerical calculations performed for the diffraction of an acoustic impulse by a rectangular ledge with the calculations by the Maekawa theory [1]: (1) finite-difference solution; (2) Maekawa theory.

different models are close to each other, and the relative frequencies of the spectral maxima coincide (Fig. 4b).

The advantage of the finite-difference model is that it allows one to represent the diffraction process at successive instants in the entire region of calculation, rather than at a single point of observation.

The computer model is developed in the form of an interactive shell that allows a visual observation of the process. The monitor screen shows the distribution of the relative pressure  $p/p_0$  in the entire region of calculation at successive instants of time. The relative pressure is represented in the form of a color palette or isolines. Figures 5 and 6 show the isolines of relative pressure at successive instants of relative time  $t' = 0.09$  and  $0.14$ . Each of these figures, which represent the hard copies of the monitor screen, contains the following elements. The main window shows the isolines of the relative pressure of the impulse in the region of calculation for the pressure values varying from 0.6 to 1.7. The lower boundary of the region of calculation is marked by gray color. In the window on the lower right of the figure, the instant of relative time, for which the corresponding pressure distribution is obtained, is indicated against the dark background.

Now, we consider the results of calculations. Figure 5 shows the isoline patterns representing the process of the diffraction of a nonlinear impulse by a rectangular ledge. At the instant of relative time  $t' = 0.09$ , the leading edge of the oncoming impulse reaches the right boundary of the rectangular ledge, while, at the left boundary of the ledge, a reflected wave is formed, which propagates in the backward direction (Fig. 5a). The maximum relative pressure of the leading edge above the ledge is 1.539, and, in the reflected wave, the maximum relative pressure is 1.651. The following diffraction process can be seen in Fig. 5b that shows the pressure distribution at the instant  $t' = 0.14$ . Here, the wavefronts of the two diffraction waves, i.e., the wave reflected from the left boundary of the ledge and the wave propagating from the upper right corner of the obstacle, are clearly defined by dense isolines. The maximum pressure in the reflected wave is observed near the bottom, where the pressure is about 1.3. We note that the reflected wave travels through the rarefaction zone of the direct impulse, and, therefore, the intensity of this wave rapidly decreases. The shape of the pressure impulse in the reflected wave is mainly the same as the shape of the impulse of the direct wave but with a slight extension of the leading edge, which is related to the dimensions of the obstacle. Above the ledge, a rarefaction zone with a pressure of 1.03 is formed. In the initial impulse, the maximum pressure above the obstacle is 1.49. The pressure at the wavefront of the wave leaving the obstacle is 1.32. In the course of the propagation, the initial impulse passes the obstacle and “separates” from it. The wave leaving the obstacle is reflected from the rigid lower boundary and forms a new wave, which can be identified in Fig. 5b as a region of dense isolines behind the ledge, near the bottom. The pressure in the new wave is 1.36. After some time, the reflected wave catches up with the initial impulse so that its wavefront will coincide with the leading edge of the impulse. Before the ledge, a rarefaction zone is formed with a pressure of 0.88.

Figure 6 presents the isoline patterns for the process of the diffraction of a nonlinear impulse by a rectangular ledge positioned behind a groove. At  $t' = 0.09$ , the leading edge of the oncoming impulse reaches the right boundary of the rectangular ledge, while at the left boundary a reflected wave is formed, and this wave interacts with the groove (Fig. 6a). The maximum relative pressure in the groove before the ledge is 1.65. At the instant  $t' = 0.14$  (Fig. 6b), the maximum pressure in the reflected wave is also observed near the bottom, but in this case the pressure is 1.19. The pressure in the groove remains equal to 1.54, and an upward propagation of the wave reflected from the groove bottom is observed. In the rarefaction zone above the ledge, the pressure is 0.99. The maximum pressure above the ledge in the initial impulse is 1.49. The pressure at the wavefront of the wave leaving the ledge is 1.26, which

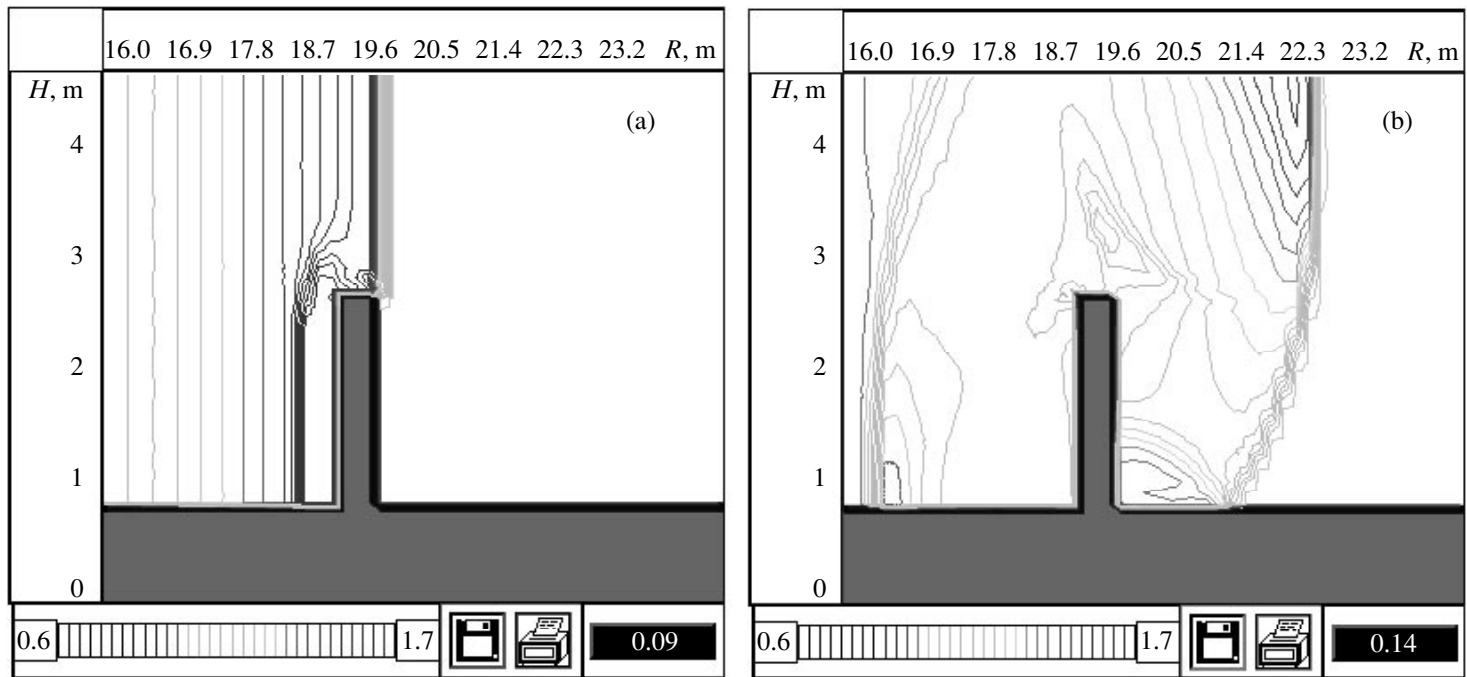


**Fig. 5.** Successive isoline patterns formed in the process of the diffraction of a nonlinear impulse by a rectangular ledge at the instants of relative time 0.09 and 0.14.

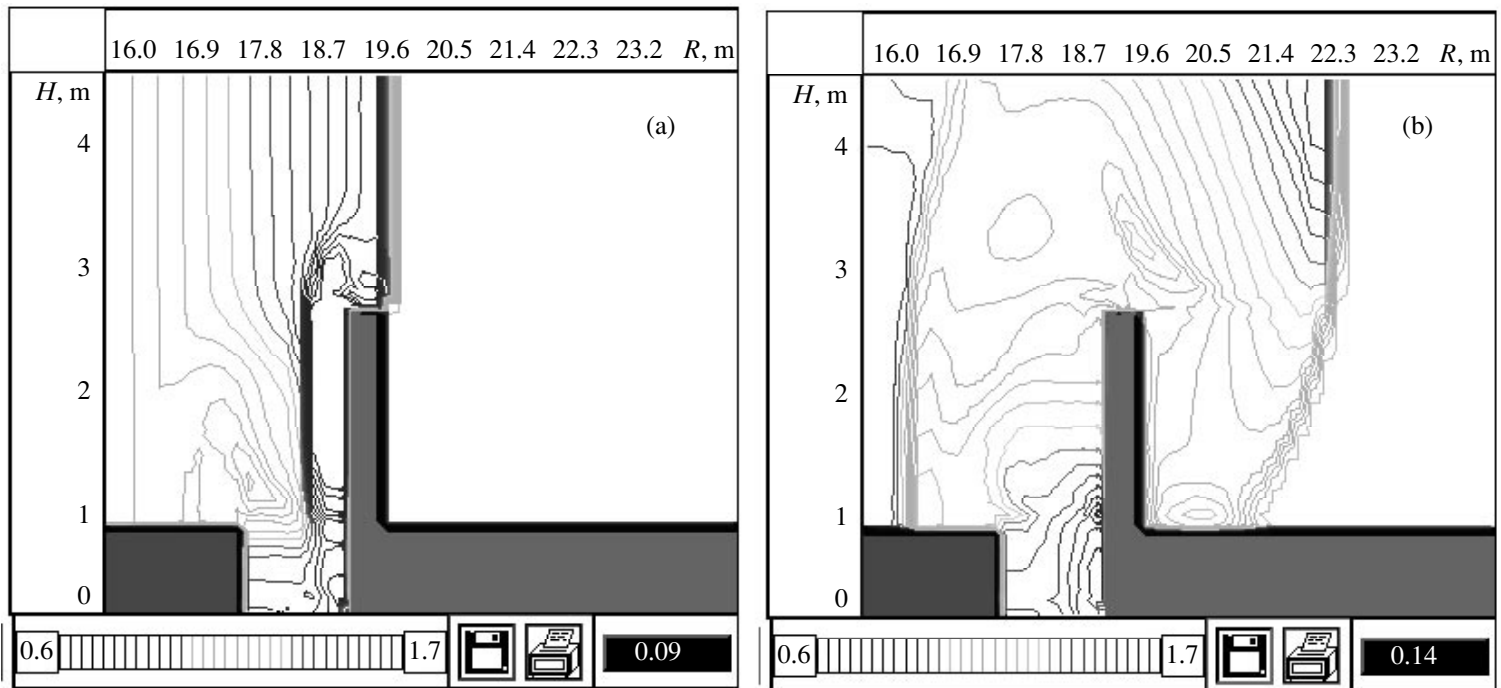


**Fig. 6.** Successive isoline patterns formed in the process of the diffraction of a nonlinear impulse by a groove combined with a rectangular ledge at the instants of relative time 0.09 and 0.14.

is somewhat lower than in the case shown in Fig. 5b. Behind the ledge, near the rigid boundary, the pressure is 1.25. On the whole, the presence of a groove leads to a decrease in the intensity of the diffraction wave formed by the ledge.

Thus, the proposed computer model based on the direct finite-difference solution of the system of gas-dynamics equations allows one to study the diffraction of a nonlinear impulse by an obstacle of an arbitrary shape. The numerical simulation described above reveals the mechanism of the formation of diffraction waves and makes it possible to determine the characteristic points of elevated and reduced pressures and the dynamics of their variation with time.

#### REFERENCES

1. Z. Maekawa, *Appl. Acoust.* **1**, 157 (1968).
2. H. Medwin, E. Childs, and G. M. Jebsen, *J. Acoust. Soc. Am.* **72**, 1005 (1982).
3. D. J. Saunders and R. D. Ford, *J. Acoust. Soc. Am.* **94**, 2859 (1993).
4. V. V. Zosimov and V. I. Kondrat'ev, in *Proceedings of 10th Jubilee Scientific-Engineering Conference on Aeroacoustics, Suzdal', Russia, 1992* (TsAGI, Moscow, 1992), Vol. 1, p. 5.
5. C. Fletcher, *Computational Techniques for Fluid Dynamics* (Springer, Berlin, 1988; Mir, Moscow, 1991), Vol. 2.
6. L. D. Landau and E. M. Lifshits, *Theoretical Physics*, Vol. 6: *Hydrodynamics* (Nauka, Moscow, 1986).
7. Yu. S. Kryukov, in *Proceedings of 5th Session of the Russian Acoustical Society "Problems of Geoacoustics: Methods and Means," Moscow, Russia, 1996* (Akust. Inst., Moscow, 1996), p. 38.
8. J. P. Boris and D. K. Book, *J. Comput. Phys.* **16**, 85 (1976).
9. S. T. Ho, I. J. Busch-Vishniac, and D. T. Blackstock, *J. Acoust. Soc. Am.* **101** (5), 2669 (1997).

*Translated by E.M. Golyamina*

# Amplitude Dependence of Internal Friction in Zinc

V. E. Nazarov

*Institute of Applied Physics, Russian Academy of Sciences,  
ul. Ul'yanova 46, Nizhni Novgorod, 603600 Russia*

*e-mail: nazarov@appl.sci-nnov.ru*

Received November 26, 1998

**Abstract**—Results of experimental and theoretical studies of the nonlinear loss and the resonance frequency shift in rod-type resonators made of annealed and unannealed zinc are presented. The experimental dependences are described in terms of the phenomenological equations of state allowing for the elastic nonlinearity. From the comparison of the theoretical dependences with the experimental results, the parameters of the hysteretic nonlinearity are determined. © 2000 MAIK “Nauka/Interperiodica”.

## INTRODUCTION

The main defects that determine the elastic and inelastic properties of crystalline solids are dislocations. Their behavior in the field of an elastic wave, namely, their motion and interaction with vacancies and interstitial or impurity atoms and with each other, determines the propagation velocity of the wave and its attenuation. The whole variety of the dislocation-caused effects that accompany the elastic wave propagation in crystals are called dislocation internal friction. To explain this phenomenon, a theory of mechanical damping due to dislocation was developed by Granato and Lucke [1–4] on the basis of a string model of a dislocation. The theory describes two types of the elastic energy loss. The loss of the first type occurs at low dynamical stresses and is called the amplitude-independent (linear) loss. This loss depends on frequency and is a consequence of the inelastic motion of dislocations in a viscous medium. The loss of the second type is called the amplitude-dependent (nonlinear) loss and is related to the difference in the behavior of a dislocation loop at the stages of loading and unloading of the crystal. This difference gives rise to a hysteretic form of the corresponding equation of state, i.e., of the dependence  $\sigma = \sigma(\epsilon, \dot{\epsilon})$ , where  $\sigma$  is the stress,  $\epsilon$  is the strain, and  $\dot{\epsilon}$  is the strain rate. The area of the hysteresis loop determines the nonlinear loss, and the average (over the wave period) value of the derivative  $\sigma'_\epsilon(\epsilon, \dot{\epsilon})$  determines the variation in the velocity of the wave propagation (or the defect of the elastic modulus). The damping decrement and the velocity variation exhibit similar dependences on the strain amplitude  $\epsilon_m$  of the wave, and their ratio is a constant value independent of  $\epsilon_m$ . In the theory developed by Granato and Lucke, the amplitude-dependent loss is assumed to be frequency independent.

The dislocation theory describing the amplitude-dependent internal friction provides an adequate quali-

tative (and in many cases quantitative) description of the experimental amplitude dependences of both the elastic modulus and the damping decrement in relatively pure crystals. However, for crystals containing impurities, the amplitude and frequency dependences observed in the experiment in most cases widely deviate from the theoretical predictions [2, 5–9]. Hence, for the development of the theory of amplitude-dependent internal friction, it is necessary to carry out experimental measurements of the amplitude and frequency dependences of nonlinear acoustic effects in different solids. Such experiments will also be useful for finding new media with strong acoustic nonlinearity, the determination of the mechanisms of their nonlinearity, and the development of the models and equations of state of these media.

To study the nonlinear effects in solids, it is necessary to use intense elastic waves, which can be easily obtained by the excitation of resonance oscillations in an acoustic resonator [10]. Such experiments were carried out with resonators made of polycrystalline copper and zinc subjected to heat treatment (annealing) [11, 12], as well as with resonators made of rock (granite and marble) [13]. In these materials, high acoustic nonlinearity was observed; the nonlinear effects were analytically described in terms of the phenomenological equations of state with allowances made for the elastic hysteresis.

This paper presents the results of an experimental study of the amplitude and frequency dependences of the effects caused by the amplitude-dependent internal friction (the nonlinear loss and the resonance frequency shift) in rod-type resonators made of polycrystalline zinc (99.95% Zn). In the experiments, two rods of length  $L = 35$  cm with square cross-sections 8 mm on a side were used. The rods were cut out of the same plate of material. The first rod (rod 1) was used as a reference one and was not subjected to annealing. The second rod (rod 2) was annealed during 50 h at a temperature of

350°C. The measurements were performed at room temperature.

EXPERIMENTAL TECHNIQUE

The block diagram of the experiment is shown in Fig. 1. A pumping piezoceramic transducer 1 served for the excitation of the resonator 2, which was fixed to a massive metal load 3 so that the boundary condition at one end of the rod was close to the condition at a perfectly rigid boundary. An accelerometer 4 was fixed at the other (free) end of the rod for measuring the pump wave amplitude. The mass of the accelerometer was sufficiently small to consider this rod boundary as an acoustically soft one. The pumping transducer excited low-frequency resonance vibrations in the rods at the frequencies of the first three longitudinal modes:  $F_1 \approx 2750$  Hz,  $F_2 \approx 8250$  Hz, and  $F_3 \approx 13550$  Hz. These frequencies correspond to a resonator with a hard boundary and a soft boundary, and the eigenfrequencies  $F_p$  of such a resonator are determined by the equation

$$F_p = F_1(2p - 1), \quad F_1 = c_0/4L, \quad p = 1, 2, 3, \dots \quad (1)$$

where  $c_0$  is the velocity of longitudinal waves in the rod and  $p$  is the number of a longitudinal mode. From this expression, we can estimate the velocity of a low-frequency longitudinal wave in the zinc rods used in the experiment:  $c_0 \approx 3.85 \times 10^5$  cm/s.

At a low amplitude of excitation (in the absence of nonlinear loss), the  $Q$ -factors of the resonators  $Q_p$  were as follows: for the unannealed rod,  $Q_1 = 546$ ,  $Q_2 = 339$ , and  $Q_3 = 139$ ; for the annealed rod,  $Q_1 = 395$ ,  $Q_2 = 159$ , and  $Q_3 = 133$ .

EXPERIMENTAL RESULTS

Figure 2 shows the dependences of the strain amplitude  $\epsilon_m$  (at resonance) on the amplitude  $u_0$  of the voltage across the pumping transducer for rods 1 and 2 at different frequencies of the resonator excitation. From the figure, one can see that the dependences  $\epsilon_m = \epsilon_m(u_0)$  are essentially nonlinear; this testifies to the presence of the amplitude-dependent loss in both unannealed and annealed zinc. For unannealed zinc, the nonlinear loss clearly manifests itself in the range  $10^{-6} \leq \epsilon_m \leq 10^{-5}$ , while at  $\epsilon_m \geq 10^{-5}$ , it becomes saturated: beginning from these amplitudes, the dependence is  $\epsilon_m \sim u_0$ , i.e., the loss becomes amplitude-independent (as at low amplitudes  $\epsilon_m \leq 10^{-6}$ ), but it is greater than at  $\epsilon_m \leq 10^{-6}$ . Similar dependences  $\epsilon_m = \epsilon_m(u_0)$  are observed for annealed zinc, except that in this case no saturation of nonlinear loss takes place.

Figure 3 shows the dependences of the resonance frequency shift  $\Delta F_p$  on the strain amplitude  $\epsilon_m$  for rods 1 and 2 at different frequencies of the resonator excitation.

From Fig. 3, it follows that, in an unannealed rod, at  $\epsilon_m \leq \epsilon_p^*$  we have  $\Delta F_p \sim \epsilon_m^2$ , and at  $\epsilon_m \geq \epsilon_p^*$  we have

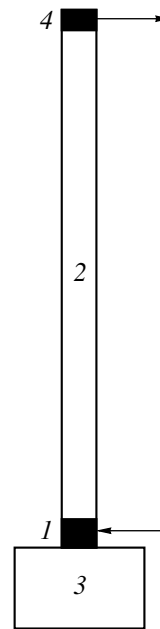


Fig. 1. Block diagram of the experimental setup: (1) pumping piezoceramic transducer; (2) rod-type resonator; (3) massive load; and (4) accelerometer.

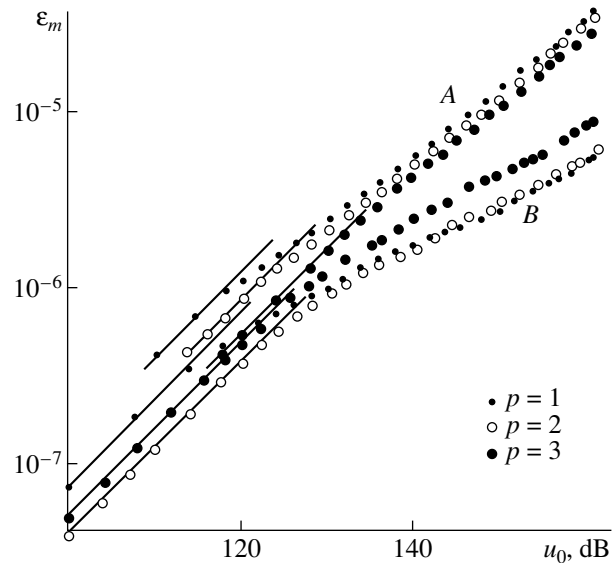
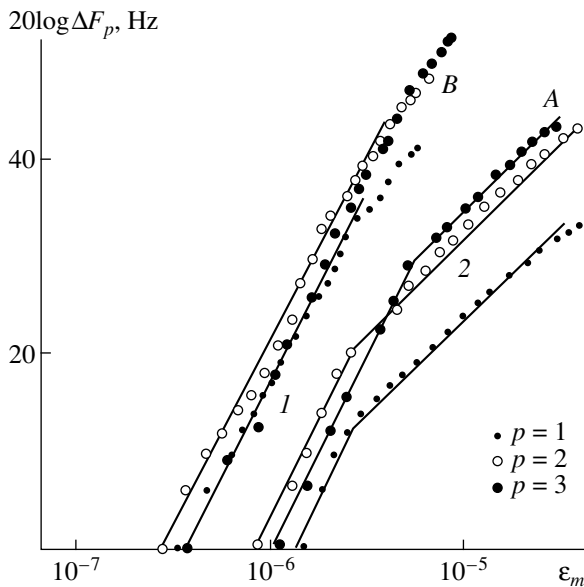


Fig. 2. Dependences of the strain amplitude  $\epsilon_m$  (at resonance) on the voltage amplitude  $u_0$  across the pumping transducer (in dB relative to 1  $\mu$ V) for rods (A) 1 and (B) 2 at different frequencies of the resonator excitation. The straight lines correspond to the dependence  $\epsilon_m \sim u_0$ .

$\Delta F_p \sim \epsilon_m$ . Here,  $\epsilon_p^*$  is the strain amplitude observed for the rod excited at the frequency  $F_p$  at which the dependence of the resonance frequency shift on the strain amplitude changes from quadratic to linear:  $\epsilon_1^* \approx 2.5 \times 10^{-6}$ ,  $\epsilon_2^* \approx 3.2 \times 10^{-6}$ , and  $\epsilon_3^* \approx 5 \times 10^{-6}$ .



**Fig. 3.** Dependences of the resonance frequency shift  $\Delta F_p$  on the strain amplitude  $\varepsilon_m$  for rods (A) 1 and (B) 2 at different frequencies of the resonator excitation. The straight lines correspond to the dependences (1)  $\Delta F_p \sim \varepsilon_m^2$  and (2)  $\Delta F_p \sim \varepsilon_m$ .

From Fig. 3, it also follows that, in the annealed rod, the dependence  $\Delta F_p \sim \varepsilon_m^2$  is observed in almost the entire strain range (except for the small region  $\varepsilon_m \geq \varepsilon_p^* \approx (3-5) \times 10^{-6}$ ).

The effects observed in the experiment cannot be described by the five-constant (or nine-constant) elasticity theory [14], because this theory does not allow for the nonlinear loss. The latter also cannot be explained by a decrease in the pump wave energy due to the generation of higher harmonics, because in the experiment their level was far below the amplitude of the fundamental wave.

In the theory of amplitude-dependent internal friction, the presence of the nonlinear loss and the defect of the elastic modulus are explained by the fact that the equation of state of the crystal is described by a hysteretic function; its analytical expression has the form [13, 15]

$$\sigma(\varepsilon, \dot{\varepsilon}) = E[\varepsilon - f(\varepsilon, \dot{\varepsilon})] + \alpha p \dot{\varepsilon}, \quad (2)$$

$$f(\varepsilon, \dot{\varepsilon})$$

$$= \begin{cases} \gamma_1 \varepsilon^n / n, & \varepsilon > 0, \dot{\varepsilon} > 0 \\ [(\gamma_1 + \gamma_2) \mathcal{E}^{n-1} \varepsilon - \gamma_2 \varepsilon^n] / n, & \varepsilon > 0, \dot{\varepsilon} < 0 \\ -\gamma_3 \varepsilon^n / n, & \varepsilon < 0, \dot{\varepsilon} < 0 \\ [(-1)^n (\gamma_3 + \gamma_4) \mathcal{E}^{n-1} \varepsilon + \gamma_4 \varepsilon^n] / n, & \varepsilon < 0, \dot{\varepsilon} > 0, \end{cases} \quad (3)$$

where  $\sigma$ ,  $\varepsilon$ , and  $\dot{\varepsilon}$  are the longitudinal stress, the strain, and the strain rate, respectively;  $E$  is Young's modulus ( $E = \rho c_0^2$ );  $\rho$  is the density;  $\alpha$  is the linear loss coefficient;  $f(\varepsilon, \dot{\varepsilon})$  is the nonlinear part of the equation of state;  $\mathcal{E} = \mathcal{E}(x)$  is the local strain amplitude;  $\gamma_i$  are the nonlinearity parameters;  $|\gamma_i \varepsilon_m^{n-1}| \ll 1$ ; and  $n > 1$ . (For a resonator with a hard boundary and a soft boundary, the local amplitude  $\mathcal{E}(x)$  is determined by the expression  $\mathcal{E}(x) = \varepsilon_m |\cos K_p x|$ , where  $K_p = \pi[2p - 1]/2L = 2\pi F_p/c_0$ .)

The values of the nonlinearity parameters  $\gamma_i$  and the exponent  $n$  can be determined (for both annealed and unannealed zinc) from the comparison of the theoretical calculations with the experimental results. From the analysis of the nonlinear function  $f(\varepsilon, \dot{\varepsilon})$  involved in the equation of state (2), we obtain [15]:

for unannealed zinc,  $n = 3$  at  $\varepsilon_m \leq \varepsilon_p^*$  and  $n = 2$  at  $\varepsilon_m > \varepsilon_p^*$ ;

for annealed zinc,  $n = 3$  (at  $\varepsilon_m \leq \varepsilon_p^*$ ).

In combination with the equation of motion [14, 16]

$$\rho U_{tt} = \sigma'_x(\varepsilon, \dot{\varepsilon}) \quad (4)$$

and the boundary conditions at the resonator ends

$$U(x=0, t) = A_0 \cos \Omega t, \quad (5)$$

$$U'_x(x=L, t) = 0$$

(here,  $U$  is the displacement,  $\varepsilon = U_x$ , and  $A_0$  and  $\Omega$  are the amplitude and the frequency of the wave produced by the pumping transducer), the equations of state (2) and (3) provide an adequate description of the amplitude dependences of the nonlinear loss and the resonance frequency shift for both annealed and unannealed rods.

The method of solving equations (2)–(5) was described in our previous publications [11, 15], and, below, we use the results presented in those papers.

For a rod, the strain amplitude is determined by the expression

$$\varepsilon_m = \frac{A_0 \Omega_p / L}{[(\delta + \delta_h)^2 + (\mu_p + \mu_h)^2 \Omega_p^4 / 4]^{1/2}}, \quad (6)$$

where  $\delta = \Omega - \Omega_p$ ,  $\mu_p = (\Omega_p Q_p)^{-1}$ ,  $\delta_h = 2\pi \Delta F_p$ , and  $\mu_h$  is the nonlinear loss coefficient; in addition:

for unannealed zinc at  $\varepsilon_m \leq \varepsilon_p^*$  and for annealed zinc, we have

$$\delta_h = -a_1 \varepsilon_m^2 \Omega_p, \quad \mu_h = b_1 \varepsilon_m^2 / \Omega_p, \quad (7)$$

$$a_1 = (\gamma_1 + \gamma_2 - \gamma_3 - \gamma_4) / 32 + (\gamma_1 - \gamma_2 - \gamma_3 + \gamma_4) / 128, \quad (8)$$

$$b_1 = (\gamma_1 + \gamma_2 - \gamma_3 - \gamma_4) / 16\pi,$$

Coefficients  $a_1$  and  $b_1$ 

Mode number, $p$	1		2		3	
	$a_1$	$b_1$	$a_1$	$b_1$	$a_1$	$b_1$
Unannealed zinc						
$\varepsilon_m \leq \varepsilon_p^*$	$2 \times 10^8$	$2 \times 10^8$	$1.9 \times 10^8$	$1.6 \times 10^8$	$7.5 \times 10^7$	$5.9 \times 10^7$
$\varepsilon_m \geq \varepsilon_p^*$	$5.1 \times 10^2$	$4.6 \times 10^2$	$4.9 \times 10^2$	$4.6 \times 10^2$	$4.2 \times 10^2$	$2.7 \times 10^2$
Annealed zinc						
$\varepsilon_m \leq \varepsilon_p^*$	$2.6 \times 10^9$	$3.4 \times 10^9$	$1.3 \times 10^9$	$2 \times 10^9$	$5.3 \times 10^8$	$7.5 \times 10^8$

 and for unannealed zinc at  $\varepsilon_m \geq \varepsilon_p^*$ , we have

$$\delta_h = -a_1 \varepsilon_m \Omega_p, \quad \mu_h = b_1 \varepsilon_m / \Omega_p, \quad (9)$$

$$a_1 = 4(\gamma_1 - \gamma_2 + \gamma_3 - \gamma_4) / 9\pi^2 + (\gamma_1 + \gamma_2 + \gamma_3 + \gamma_4) / 6\pi, \quad (10)$$

$$b_1 = 2(\gamma_1 + \gamma_2 + \gamma_3 + \gamma_4) / 9\pi^2.$$

From equations (7) and (9), it follows that, as in the Granato–Lucke theory, the ratio  $\delta_h / \mu_h \Omega_p^2$  does not depend on  $\varepsilon_m$ :  $\delta_h / (\mu_h \Omega_p^2) = -a_1 / b_1$ .

For both rods, the values of the coefficients  $a_1$  at different excitation frequencies can be found from the measured shifts of resonance frequencies.

To determine the coefficients  $b_1$  responsible for the nonlinear loss, we proceed as follows. Assuming that the amplitude  $A_0$  of the resonator excitation varies in direct proportion to the voltage amplitude  $u_0$  across the transducer, we use equation (6) (at  $\delta = -\delta_h$ ) to obtain the expression

$$\varepsilon_{m1} / \varepsilon_m = A_{01} / A_0 (1 + \mu_h(\varepsilon_m) / \mu_p). \quad (11)$$

Here,  $A_{01}$  and  $\varepsilon_{m1}$  are the amplitude of the transducer vibrations and the corresponding strain amplitude of the rod when the nonlinear loss in the resonator is small and cannot be observed;  $\varepsilon_m$  is the strain amplitude of the rod ( $\varepsilon_m > \varepsilon_{m1}$ ) excited by the transducer with the excitation amplitude  $A_0 > A_{01}$  when the nonlinear loss is substantial. Expression (11) determines the dependence of the nonlinear loss  $\mu_h(\varepsilon_m)$  on the strain amplitude  $\varepsilon_m$ :

$$\mu_h(\varepsilon_m) / \mu_p = (\varepsilon_{m1} / \varepsilon_m) (A_0 / A_{01}) - 1. \quad (12)$$

Using the data presented in Fig. 3, we can plot the dependences  $\mu_h(\varepsilon_m) / \mu_p$  on  $\varepsilon_m$  for the two rods under study (Fig. 4). From Fig. 4, one can see that the behavior of these dependences is as follows: for unannealed zinc, initially (at  $\varepsilon_m \leq \varepsilon_p^*$ )  $\mu_h(\varepsilon_m) \sim \varepsilon_m^2$ , then (at  $\varepsilon_m \geq \varepsilon_p^*$ ) a linear dependence  $\mu_h(\varepsilon_m) \sim \varepsilon_m$  takes place, and at even greater strains the linear loss tends to saturation,

i.e.,  $\mu_h(\varepsilon_m) = \text{const.}$ ; for annealed zinc, in almost the entire strain range (except for the small interval  $\varepsilon_m \geq \varepsilon_p^* \approx (3-5) \times 10^{-6}$  where the dependence of  $\mu_h(\varepsilon_m) / \mu_p$  on  $\varepsilon_m$  is close to a linear one), the dependence  $\mu_h(\varepsilon_m) \sim \varepsilon_m^2$  corresponding to the analytical dependence (7) is observed.

The table presents the values of the coefficients  $a_1$  and  $b_1$  determined for annealed and unannealed zinc from the comparison of expressions (7) and (12) with the experimental results shown in Figs. 3 and 4. (However, it should be noted that the estimates obtained for the parameters  $a_1$  and  $b_1$  for unannealed zinc at  $\varepsilon_m \geq \varepsilon_p^*$  are approximate, because in this case the nonlinear loss and the resonance frequency shift are determined

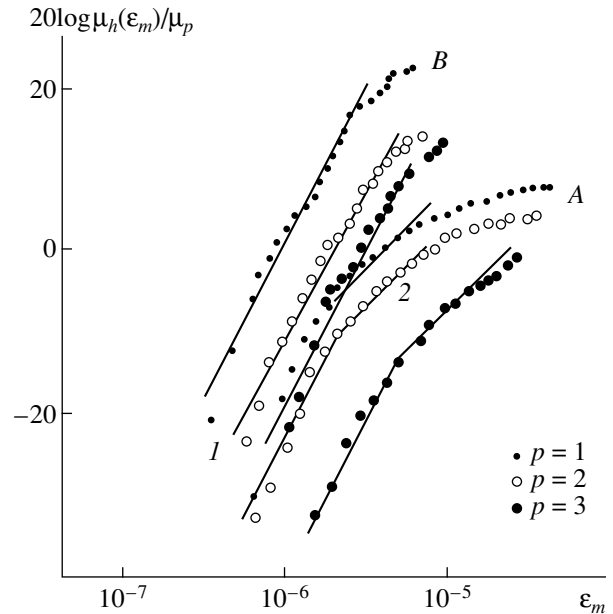


**Fig. 4.** Dependences of  $\mu_h(\varepsilon_m) / \mu_p$  on the strain amplitude  $\varepsilon_m$  for rods (A) 1 and (B) 2 at different frequencies of the resonator excitation. The straight lines correspond to the dependences (1)  $\mu_h(\varepsilon_m) \sim \varepsilon_m^2$  and (2)  $\mu_h(\varepsilon_m) \sim \varepsilon_m$ .

by the combined effect of nonlinearities that occur at both  $\epsilon_m \leq \epsilon_p^*$  and  $\epsilon_m \geq \epsilon_p^*$ .)

From the table, one can see that, with increasing mode number, i.e., with increasing frequency of the resonator excitation, the values of the coefficients  $a_1$  and  $b_1$  (and, consequently, the values of the nonlinearity parameters  $\gamma_{1-4}$ ) noticeably decrease for both annealed and unannealed zinc, while their ratio remains virtually constant. As the frequency increases by a factor of five, the values of the coefficients  $a_1$  and  $b_1$  decrease: for unannealed zinc, by a factor of three at  $\epsilon_m \leq \epsilon_p^*$  or by a factor of nearly two at  $\epsilon_m \geq \epsilon_p^*$ ; for annealed zinc, by a factor of four. From the comparison between the first and the third rows of the table (at  $\epsilon_m \leq \epsilon_p^*$  when  $n = 3$  for both annealed and unannealed zinc), it also follows that the annealing of zinc at 350°C during 50 h leads to an increase in its hysteretic nonlinearity almost by a factor of ten.

#### SUMMARY

The amplitude and frequency dependences of the nonlinear loss and the resonance frequency shift in rod-type resonators made of annealed and unannealed zinc were studied experimentally. The amplitude dependences observed in the experiment were described in terms of the phenomenological equations of state with their nonlinear parts incorporating a hysteresis with the exponents:  $n = 3$  (at  $\epsilon_m \leq \epsilon_p^* \approx (2.5-5) \times 10^{-6}$ ) and  $n = 2$  (at  $\epsilon_m \geq \epsilon_p^*$ ) for unannealed zinc;  $n = 3$  for annealed zinc (at  $\epsilon_m \leq \epsilon_p^* \approx (3-5) \times 10^{-6}$ ). The comparison of the analytical calculations with the experimental results showed that the annealing of zinc leads to an increase in its hysteretic nonlinearity, and the latter is frequency-dependent decreasing with increasing frequency. This conclusion will be used for the interpretation of the results of our next experiments with the same rods.

#### ACKNOWLEDGMENTS

This work was supported in part by the Russian Foundation for Basic Research (project no. 98-05-64683).

#### REFERENCES

1. A. Granato and K. Lucke, *J. Appl. Phys.* **27**, 583 (1956).
2. *Ultrasonic Methods for Studying Dislocations*, Ed. by L. G. Merkulov (Inostr. Lit., Moscow, 1963).
3. A. Granato and K. Lucke, in *Physical Acoustics: Principles and Methods*, Ed. by W. P. Mason (Academic, New York, 1965; Mir, Moscow, 1969), Vol. 4A, pp. 226–276.
4. R. Truell, Ch. Elbaum, and B. Chick, *Ultrasonic Methods in Solid State Physics* (Academic, New York, 1969; Mir, Moscow, 1972).
5. A. S. Novick, *Phys. Rev.* **80**, 249 (1950).
6. Y. Xiki, *J. Phys. Soc. Jpn.* **13**, 1138 (1958).
7. S. B. Kustov, S. N. Golyandin, A. V. Nikiforov, *et al.*, *Fiz. Tverd. Tela* **31**, 260 (1989) [*Sov. Phys. Solid State* **31**, 326 (1989)].
8. S. N. Golyandin and S. B. Kustov, *Fiz. Tverd. Tela* **34**, 3796 (1992) [*Sov. Phys. Solid State* **34**, 2031 (1992)].
9. S. N. Golyandin and S. B. Kustov, *Fiz. Tverd. Tela* **37**, 3248 (1995) [*Phys. Solid State* **37**, 1786 (1995)].
10. C. Campos-Pozuelo and J. A. Gallego-Juáres, *J. Acoust. Soc. Am.* **97**, 875 (1995).
11. V. E. Nazarov, L. A. Ostrovskii, I. A. Soustova, *et al.*, *Akust. Zh.* **34**, 491 (1988) [*Sov. Phys. Acoust.* **34**, 285 (1988)].
12. V. E. Nazarov, in *Proceedings of the IX International Conference on Interactions of Defects and Inelastic Phenomena in Solids* (Tula, Russia, 1997), p. 88.
13. S. V. Zimenkov and V. E. Nazarov, *Fiz. Zemli*, No. 1, 13 (1993).
14. L. K. Zarembo and V. A. Krasil'nikov, *Introduction to Nonlinear Acoustics* (Nauka, Moscow, 1966).
15. V. E. Nazarov and A. M. Sutin, *Akust. Zh.* **35**, 711 (1989) [*Sov. Phys. Acoust.* **35**, 410 (1989)].
16. L. D. Landau and E. M. Lifshits, *Theory of Elasticity* (Nauka, Moscow, 1987).

*Translated by E.M. Golyamina*

# Cerenkov-Type Magnetoacoustic Oscillations in a Viscoelastic Cylinder

E. B. Postnikov and S. V. Sobolev

Kursk State Pedagogical University, ul. Radishcheva 33, Kursk, 305000 Russia

e-mail: kgpu@pubsovtest.ru

Received February 4, 1999

**Abstract**—The conditions of the resonance excitation and energy dissipation are considered for magnetoacoustic oscillations generated in a conducting cylinder by a travelling current wave coaxial with the cylinder. Expressions are obtained for the distributions of the power density of the sources of Joule and viscous heating. On the basis of these expressions, a numerical solution is obtained to the heat-transfer equation with the boundary conditions of the third kind. It is shown that, under such conditions, the temperature field formed in the cylinder has nearly zero gradients, and both the time required for the magnetothermoacoustic treatment of the sample and the corresponding power consumption are considerably reduced. © 2000 MAIK “Nauka/Interperiodica”.

The study of acoustic waves propagating in a solid in the presence of a strong constant magnetic field has become of special importance in relation to the development of new technologies of materials treatment and nondestructive testing, as well as to the improvement of the elements of measuring equipment [1–5]. In particular, the treatment of materials under the aforementioned conditions considerably improves their physical-mechanical properties and reduces the time of the processes and the power consumption [3]. In this connection, the theoretical studies concerned with the formulation and solution of two-dimensional problems of magnetoelasticity seem to be fairly topical [6].

In this paper, we consider the mechanism of the Cerenkov-type excitation of magnetoacoustic waves and the dissipation of their energy in a homogeneous nonmagnetic ( $\mu = 1$ ) infinite cylinder of radius  $R$ ; the conductivity of the cylinder material is  $\sigma$ , and the cylinder is placed in a constant uniform magnetic field  $\mathbf{B} = (0, 0, B)$ . The source of perturbation is a travelling wave with the current density

$$\mathbf{j} = \{0, j \exp[i(k_0 z - \omega t)] \delta(r - R_0), 0\}, \quad R_0 > R, \quad (1)$$

$$j = \text{const}, \quad \text{Im} j = 0.$$

We use the cylindrical coordinates  $r, \varphi, z$ . We assume that the phase velocity of the wave  $v = \omega/k_0$  exceeds the propagation velocity of purely transverse  $c_\perp$  or purely longitudinal  $c_\parallel$  waves.

A similar problem of the generation of magnetoacoustic waves in a halfspace was considered by Sobolev [4] without regard for the dissipation.

The only nonzero component of the vector potential  $\mathbf{A} = \{0, A(r) \exp[i(k_0 z - \omega t)]\}$  of the electromagnetic

field induced by the current wave (1) satisfies the Poisson equation

$$\Delta A = -\mu_0 j \delta(r - R_0)$$

and can be expressed through the modified Bessel functions  $I_1(k_0 r)$  and  $K_1(k_0 r)$ :

$$A = \mu_0 j R_0 \begin{cases} K_1(k_0 R_0) I_1(k_0 r) & \text{at } r < R_0 \\ I_1(k_0 R_0) K_1(k_0 r) & \text{at } r > R_0. \end{cases} \quad (2)$$

The vector potential of the field “reflected” from the cylinder surface is described by the expression

$$A = \alpha K_1(k_0 r), \quad \alpha = \text{const}. \quad (3)$$

In expressions (2) and (3), as well as in all expressions below, the factor  $\exp[i(k_0 z - \omega t)]$  is omitted.

The initial system of equations describing the magnetoacoustic oscillations of the cylinder medium has the form [1]

$$\begin{cases} \frac{\partial^2 \mathbf{u}}{\partial t^2} = \left( c_\perp^2 + \gamma_\perp \frac{\partial}{\partial t} \right) \Delta \mathbf{u} + \left[ \left( c_\parallel^2 + \gamma_\parallel \frac{\partial}{\partial t} \right) \right. \\ \left. - \left( c_\perp^2 + \gamma_\perp \frac{\partial}{\partial t} \right) \right] \text{grad div } \mathbf{u} - c_a^2 \frac{\mathbf{B}}{B^2} \times \text{rot } \mathbf{b} \\ \Delta \mathbf{A} - \mu_0 \sigma \frac{\partial \mathbf{A}}{\partial t} = -\mu_0 \sigma \frac{\partial \mathbf{u}}{\partial t} \times \mathbf{B}, \quad \mathbf{b} = \text{rot } \mathbf{A}. \end{cases} \quad (4)$$

Here,  $\mathbf{u} = (u_r, 0, u_z)$  is the vector of particle displacements in the medium,  $c_a$  is the Alfphen velocity,  $\mathbf{b}$  is the perturbation of the magnetic field, and the coefficients  $\gamma_\perp$  and  $\gamma_\parallel$  are expressed through the bulk  $\zeta$  and shear  $\eta$  viscosities according to the formulas  $\gamma_\perp = \eta/\rho$  and  $\gamma_\parallel = (\zeta + 4\eta/3)/\rho$ . Taking into account that in solids, even at

$B \sim 10$  T, the condition  $c_a \ll c_\perp < c_\parallel$  is satisfied and introducing the “transverse”  $\mathbf{u}_\perp$  and “longitudinal”  $\mathbf{u}_\parallel$  components of the displacement vector  $\mathbf{u} = \mathbf{u}_\perp + \mathbf{u}_\parallel$  so that the conditions  $\text{div} \mathbf{u}_\perp = 0$  and  $\text{rot} \mathbf{u}_\parallel = 0$  are satisfied, we obtain a system of equations that is equivalent to system (4):

$$\frac{\partial^2 \mathbf{u}_\perp}{\partial t^2} = \left( c_\perp^2 + \gamma_\perp \frac{\partial}{\partial t} \right) \Delta \mathbf{u}_\perp, \quad (5)$$

$$\frac{\partial^2 \mathbf{u}_\parallel}{\partial t^2} = \left( c_\perp^2 + \gamma_\perp \frac{\partial}{\partial t} \right) \Delta \mathbf{u}_\parallel, \quad (6)$$

$$\Delta \mathbf{A} - \mu_0 \sigma \frac{\partial \mathbf{A}}{\partial t} = -\mu_0 \sigma \frac{\partial \mathbf{u}}{\partial t} \times \mathbf{B}. \quad (7)$$

We assume that the skin depth is small compared with the cylinder radius  $R$ . Then, at the cylinder surface, the vector potential satisfies the following boundary conditions:

$$A|_{R+0} - A|_{R-0} = 0, \quad \frac{\partial A}{\partial r} \Big|_{R+0} - \frac{\partial A}{\partial r} \Big|_{R-0} = -\mu_0 j_0, \quad (8)$$

where  $j_0$  is the effective surface current density to be determined.

The two other boundary conditions necessary for obtaining a unique solution to the problem express the condition of the continuity of the momentum flux at  $r = R$  and have the form

$$\begin{aligned} & \left( c_\perp^2 + \gamma_\perp \frac{\partial}{\partial t} \right) \left( \frac{\partial u_z}{\partial r} + \frac{\partial u_r}{\partial z} \right) = 0, \\ & \left[ \left( c_\parallel^2 + \gamma_\parallel \frac{\partial}{\partial t} \right) - 2 \left( c_\perp^2 + \gamma_\perp \frac{\partial}{\partial t} \right) \right] \left( \frac{\partial u_z}{\partial z} + \frac{u_r}{r} \right) \\ & + \left( c_\parallel^2 + \gamma_\parallel \frac{\partial}{\partial t} \right) \frac{\partial u_r}{\partial r} = \frac{B}{\rho} j_0. \end{aligned} \quad (9)$$

From equations (5) and (6), it follows that at  $v > c_\parallel$  both oscillation branches, i.e., the modified transverse and longitudinal ones, are excited with the wave numbers  $\kappa_{\perp, \parallel} = k_{\perp, \parallel} + i\omega^3 \gamma_{\perp, \parallel} / 2k_{\perp, \parallel} c_{\perp, \parallel}^4$  where  $k_{\perp, \parallel} = k_0[(v/c_{\perp, \parallel})^2 - 1]^{1/2}$ . In this case, we have

$$\begin{aligned} u_r &= k_0 \alpha_1 J_1(\kappa_\parallel r) + i \kappa_2 \alpha_2 J_2(\kappa_\parallel r), \\ u_z &= i \kappa_1 \alpha_1 J_0(\kappa_\perp r) + k_0 \alpha_2 J_0(\kappa_\parallel r). \end{aligned} \quad (10)$$

Here,  $\alpha_{1,2}$  are constants determined from the boundary conditions (8) and (9), and  $J_{0,1}(\kappa_{\perp, \parallel} r)$  are the Bessel functions of the first kind. If the phase velocity of the current wave satisfies the inequality  $c_\perp < v < c_\parallel$ , oscillations with the wave number  $\kappa_\perp$  are excited in the cylinder bulk. The second branch of oscillations with the wave number  $k_\parallel$  represents a modified Rayleigh surface

wave exponentially decaying with distance from the cylinder surface toward its axis.

Substituting expressions (10) into the right-hand member of equation (7), we determine the vector potential of the electromagnetic field in the cylinder material. Using this vector potential and the known formulas  $\mathbf{e} = -\partial \mathbf{A} / \partial t$ ,  $\mathbf{b} = \text{rot} \mathbf{A}$ , we determine the components of the perturbations of the electric and magnetic field:

$$e_\phi = i\omega(k_0 \alpha_1 \beta_1 J_1(\kappa_\perp r) + i \kappa_2 \alpha_2 \beta_2 J_1(\kappa_\parallel r)),$$

$$e_r = e_z = 0,$$

$$b_r = -ik_0(k_0 \alpha_1 \beta_1 J_1(\kappa_\perp r) + i \kappa_2 \alpha_2 \beta_2 J_1(\kappa_\parallel r)),$$

$$b_z = k_0 \kappa_1 \alpha_1 \beta_1 J_0(\kappa_\perp r) + i \kappa_2^2 \alpha_2 \beta_2 J_0(\kappa_\parallel r), \quad b_\phi = 0,$$

where  $\beta_{1,2} = i\omega \mu_0 \sigma B / (\kappa_{\perp, \parallel}^2 + \kappa_0^2 - i\omega \mu_0 \sigma)$ .

The cylinder is heated at the expense of the viscous and Joule dissipation of the energy of coupled acoustic and electromagnetic oscillations. The heating of the cylinder is most efficient at resonance conditions [3]. The distributions of the oscillation-period average powers of the viscous and Joule heat sources along the cylinder radius,  $q_\gamma(r)$  and  $q_\sigma(r)$ , have the form

$$\begin{aligned} q_\gamma(r) &= \frac{\rho \omega^2}{2q_1} \left[ 2\gamma_\perp \left( \frac{1}{2} \left| \frac{\partial u_r}{\partial z} + \frac{\partial u_z}{\partial r} \right|^2 + \left| \frac{u_r}{r} \right|^2 \right. \right. \\ & \left. \left. + \left| \frac{\partial u_r}{\partial r} \right|^2 + \left| \frac{\partial u_z}{\partial z} \right|^2 \right) + (\gamma_\parallel - 2\gamma_\perp) \left| \frac{\partial u_r}{\partial r} + \frac{\partial u_z}{\partial z} + \frac{u_r}{r} \right|^2 \right], \quad (11) \end{aligned}$$

$$q_\sigma(r) = \frac{\omega^2}{2\sigma q_2} \left| \frac{1}{\mu_0} \text{rot} \mathbf{b} \right|^2.$$

In expressions (11), the dimensionless factors are determined by the formulas

$$q_1 = \frac{(BjR_0 K_1(k_0 R))^2}{\rho c_\parallel R^3},$$

$$q_2 = \frac{\sigma R B^2 (BjR_0 K_1(k_0 R))^2}{c_\perp \rho c_\parallel R^3}.$$

As an example, we consider the resonance oscillations of a cylinder of radius  $R = 0.25$  m made of material with the properties of aluminum [7]. We assume that the velocity of the current wave is  $v = 8000$  m/s. The values of  $k_0$ , which correspond to the maximum amplitudes of mechanical and electromagnetic oscillations, are determined from the condition of the minimum value of the principal determinant of the system of boundary conditions (8) and (9). The distributions (11) corresponding to the first resonance value  $k_0 = 11.8$  are shown in Figs. 1 and 2. One can see that, in contrast to the case of a purely induction heating, the distribution of the heat

sources extends into the cylinder volume, and the main contribution to heating is made by internal friction.

The radial distribution of the temperature  $T$  that occurs in the cylinder at any given moment can be determined by solving the axially symmetric heat-transfer equation, which has the following dimensionless form:

$$\frac{\partial \Theta}{\partial Fo} = \frac{\partial^2 \Theta}{\partial \xi^2} + \frac{1}{\xi} \frac{\partial \Theta}{\partial \xi} + \frac{q_\gamma}{q_1} + \frac{q_\sigma}{q_2}, \tag{12}$$

$$\Theta = (T - T_0) c \rho a / R^2 q_1$$

with the initial

$$\Theta = 0 \text{ at } Fo = 0 \tag{13}$$

and boundary

$$\frac{\partial \Theta}{\partial \xi} = Bi \Theta \text{ at } r = R \tag{14}$$

conditions.

Here,  $Fo = at/R^2$  is the Fourier number,  $\xi = r/R$  is the dimensionless coordinate,  $Bi = HR$  is the Bio criterion,  $a$  is the thermal diffusivity,  $c$  is the specific heat,  $\rho$  is the density of the cylinder material, and  $H$  is the heat-transfer coefficient characterizing the heat transfer to the surrounding medium.

Figure 3 presents the solution to problem (11)–(15) for the Fourier numbers from 0.2 to 2.0 and the Bio criterion taken equal to 0.1. The solution was obtained by the grid method [8]. From the curves, one can see that the temperature field in the cylinder proves to be a low-gradient one, which in its turn has a beneficial effect on the structure of the heated material of the body under consideration. Such a behavior of the temperature field is caused by the fact that the power density of the viscous heat sources varies only weakly over the major part of the cylinder cross-section (0.2–1) $R$  (Fig. 1). The increase in the power density near the cylinder axis is compensated by an intense heat flow due to the high thermal conductivity of the metal. As a result, only a weak slope of the temperature curves is observed.

Thus, the excitation of high-frequency electromagnetic oscillations in electrically conducting bodies by external sources in the presence of a strong constant magnetic field leads to the generation of magnetoacoustic oscillations in the bulk of the body. At resonance conditions, the magnetic field promotes a virtually unobstructed energy transfer from the source to the bulk of the body under treatment, while the energy dissipation due to the Joule loss and the internal friction provides a uniform heating of the body and makes it

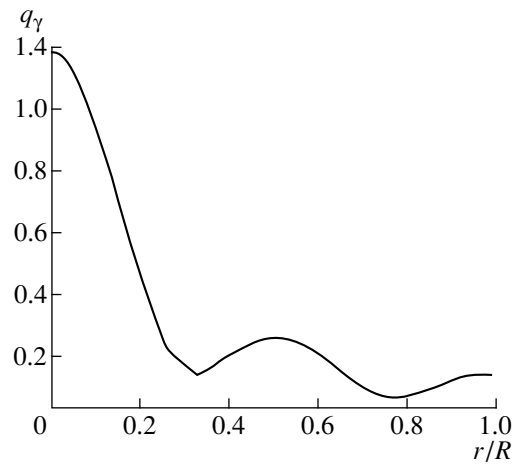


Fig. 1.

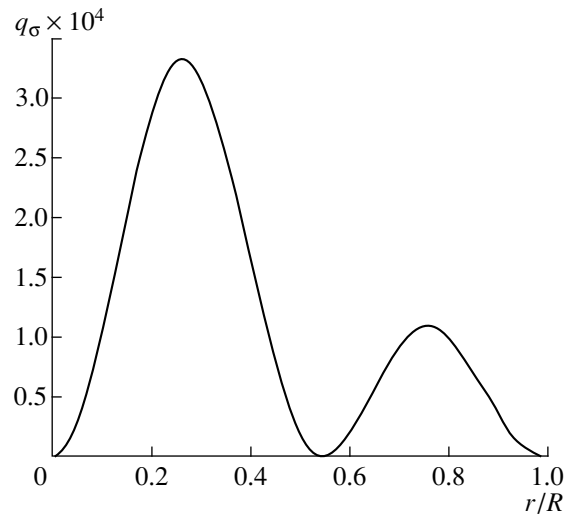


Fig. 2.

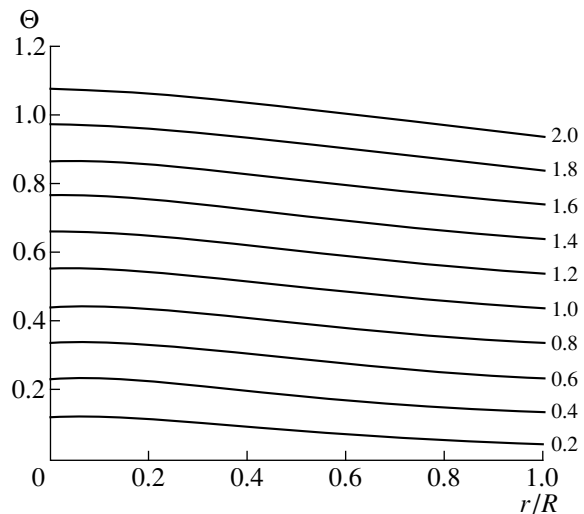


Fig. 3.

possible to considerably reduce the treatment time and the power consumption.

#### REFERENCES

1. Ya. S. Podstrigach, Ya. I. Burak, and V. F. Kondrat, *Magnetoelasticty of Electrically Conducting Bodies* (Naukova Dumka, Kiev, 1982).
2. A. É. Mikel'son and Z. D. Chernyĭ, *Electrodynamical Excitation and Measurement of Oscillations in Metals* (Zinatne, Riga, 1979).
3. M. I. Kiselev and S. V. Sobolev, in *Physicochemical Processes of Materials Treatment by Concentrated Energy Flows* (Nauka, Moscow, 1989), pp. 220–226.
4. S. V. Sobolev, *Akust. Zh.* **42**, 580 (1996) [*Acoust. Phys.* **42**, 512 (1996)].
5. R. Collins, W. D. Dover, J. R. Bowler, and K. Miya, *Non-destructive Testing of Materials. Studies in Applied Electromagnetics and Mechanics* (1995).
6. A. DeSimone and G. Dolzmann, *Arch. Rational Mech. Anal.* **144**, 107 (1998).
7. *Physical Quantities: Handbook*, Ed. by I. S. Grigor'ev and E. Z. Meilikhov (Énergoatomizdat, Moscow, 1991).
8. P. P. Yushkov, in *Proceedings of the Leningrad Technological Institute of Refrigeration Industry* (Leningrad, 1956), Vol. 14, pp. 315–323.

*Translated by E.M. Golyamina*

# Spectra of Ocean Noise Generated by Breaking Wind Waves

G. A. Postnov

*Shirshov Oceanology Institute, Russian Academy of Sciences,  
Nakhimovskii pr. 36, Moscow, 117851 Russia*

*e-mail: nosoff@chip.sio.rssi.ru*

Received September 15, 1998

**Abstract**—A dynamical model of a cloud of air bubbles produced by breaking wind waves is developed on the basis of experimental data. For moderate wind speeds, the bubble cloud is represented by a hemisphere with its plane surface being coincident with the water surface and with new radiating bubbles emerging at its center. The frequency spectra of noise generated by bubbles at different stages of the cloud development are calculated with allowance for the multiple scattering of sound in the cases of a soft surface and an absorbing surface. The computational results are found to agree well with the experimental data. The angular spectrum of noise is estimated on the basis of a simplified model, and this estimate is found to quantitatively agree with the spectrum observed in the experiment. © 2000 MAIK “Nauka/Interperiodica”.

Currently, one can state with assurance that the dynamical (i.e., depending on the local wind speed) component of ocean noise observed at relatively high frequencies is caused by damped oscillations of excited air bubbles, which are formed as a result of the interaction of wind with the ocean surface. The main process that leads to the formation of bubbles in water is the breaking of wind waves. There exists no theoretical model for describing the dynamics of collective bubble motion in this process. Therefore, to calculate the characteristics of noise produced by breaking waves, one has to use a model based on the experimental data.

The characteristics of bubbles and the noise they produce were studied in many laboratory-scale and full-scale experiments (e.g., [1–4]). In some publications, the frequency and angular spectra of ocean noise were calculated on the basis of simple models. For example, Kennedy and Szlyk [5] calculated the spectra for a homogeneous ocean model with a horizontally uniform layer of radiating bubbles. Mendus and Postnov [6] performed a similar calculation for a more realistic ocean model with allowance for multiple scattering from the surface and the passive bubble layer. Norton *et al.* [7] took into account the presence of random bubble clouds near the ocean surface. In these publications, the calculations were performed on the basis of the ray approach. Other theoretical studies [8–11] were based on mode calculations. In papers [5–10], the sources of radiation were uniformly distributed over the surface layer. In the model considered by Oguz [11], the noise sources were uniformly distributed over the plane surfaces of hemispherical clouds of passive bubbles; the sound velocity in these clouds was constant but different from the sound velocity in water, and the hemispheres themselves were randomly distributed

under the surface of a homogeneous ocean. However, the experimental data show that the structure and shape of bubble clouds strongly depends on the conditions of wave breaking [12, 13]. The common disadvantage of all known models is the unduly simplified representation of the noise generation by a local source. The use of a more adequate model of a local source may lead to a considerable refinement of its radiation characteristics, as well as to an improvement of the overall picture of the noise field in the ocean. This paper presents an attempt to construct a model of the noise generation by a single breaking wave.

The direct observations of breaking wind waves in the ocean allow one to distinguish between the following typical conditions of wave breaking:

- (a) formation of local cusps on the peaks of swell or wind waves; the breaking of these cusps produces more or less round spots of foam; such conditions are observed when the wind speed is  $v = 4\text{--}7$  m/s,
- (b) formation of elongated ridges of swell or wind waves; the ridges break on the lee slopes of waves; such conditions occur at  $v = 8\text{--}12$  m/s,
- (c) separation of wind wave ridges by wind with their subsequent incidence on the wave slope; the conditions occur at  $v \geq 12$  m/s.

According to Kolaini [2], the aforementioned conditions are called as follows: (a) weak spilling, (b) spilling, and (c) plunging. However, it seems more adequate to use the term “rolling” for (a) and (b) and the term “turnover” for (c).

For conditions (a) (weak rolling), we can use a model that describes the space-time structure of bubble clouds on the basis of experimental data. We consider the propagation of the radiation generated by a single

bubble with a given spectrum and given coordinates through a cloud of passive bubbles. The total noise level away from the cloud is determined by the sum of noise intensities produced by all radiating bubbles.

The primary source of noise in the ocean is taken to be an air bubble immediately after its formation (an active bubble). One can assume that the bubble oscillations that lead to sound radiation are caused either by the difference between the air pressure in the bubble and the pressure in the surrounding medium or by the deviation of the initial bubble shape (at the instant of its capture) from a sphere. In the first case, the bubble is expected to perform radial oscillations, while in the second case multipole oscillations can be excited [14]. Another possible mechanism of bubble excitation is the resonance excitation by a turbulent flow of water [15]. According to the experimental data [1], more than 65% of all bubbles perform radial oscillations, and the radiation intensity of these bubbles is much higher than that produced by the rest of the bubbles. Hence, we can assume that an active bubble of radius  $a_0$  radiates as a monopole with the resonance frequency  $f_a = 3/a_0$ , where  $a_0$  is in meters and  $f_a$  is in hertz. In the experiments, it was also found that, for most of the bubbles, the time dependence of the pressure generated by a bubble at a distance  $r$  has the form

$$p(t) = \frac{P_0 a_0}{r} \exp(-bt) \sin 2\pi f_a t, \quad (1)$$

where  $b = \pi f_a \delta$  and  $\delta$  is the damping factor, for which the expression can be found in the literature (e.g., in [16]); the latter quantity can be approximated by the expression  $\delta \approx 0.014(1 + 0.03 f_a^{1/2})$ . From formula (1), it follows that, within a time interval about  $2/b$ , the radiation intensity of a bubble becomes negligible and the bubble transforms to the passive state. For subsequent calculations, we need to know the spectrum  $S$  of the radiation of a single bubble. The spectrum can be determined by applying the Fourier transform to formula (1). The expression for the spectrum has the form

$$S = P_0 a_0 f_a [(2\pi)^2 r (f^2 - f_a^2 + i f_a \delta)]^{-1}. \quad (2)$$

According to the experiment [1], the pressure amplitude  $P_0 a_0 / r$  at  $r = 1$  m does not depend on  $a_0$  (at least for  $a_0 > 0.0001$  m) and lies within 0.2–1 Pa.

Formula (2) refers to the case of a bubble located at a constant depth. It is well known that the resonance frequency of bubble oscillations depends on the external pressure and, hence, on the bubble depth  $z$ . This fact was confirmed experimentally [1]. In addition, if the velocity of the bubble motion relative to the surface is sufficiently high, the resonance peak of the spectrum  $S$  may broaden. However, according to the experimental data [1], most of the bubbles exhibit no variations of their resonance frequency within the time of radiation; therefore, the calculations described below are performed on the basis of spectrum (2).

Detailed quantitative estimates for the process of air bubble formation by breaking waves were obtained by Lamarre and Melville [12]. These estimates were based on a laboratory experiment with waves generated by mechanical devices. Below, we use the data obtained from these experiments. It was found that, within the first 0.5 s after wave breaking, the shape of the bubble cloud is akin to a hemisphere with its plane surface being coincident with the water surface. Then, the capture of new bubbles terminates, the bubble cloud moves to deeper water layers, and its shape becomes almost spherical. Based on these data, we select the model of a bubble cloud in the form of a hemisphere with its plane surface coincident with the water surface. Approximating the experimental data [12], we can represent the relative air content in water  $V(r, t)$  (where  $r$  is the distance from the center of the plane surface of the hemisphere and  $t$  is the time that elapsed from the onset of breaking) in the form

$$V(r, t) = V_0(t) \exp(-\gamma(t)r), \quad (3)$$

where the parameters can be approximated by the expressions

$$V_0 \approx (20t)^{-1}, \quad 0.1 < t < 0.5 \text{ s}, \quad \gamma \approx 1.6t^{-1/2}, \quad \gamma [\text{m}^{-1}].$$

Unfortunately, no data on the dependence of the captured air volume on the wind speed can be found in the literature.

If we know the solution to the problem of the radiation intensity  $i(\mathbf{r}_0, f, \varphi, \theta)$  in the far zone in the direction with the angular coordinates  $\varphi, \theta$  for a sound source positioned at the distance  $\mathbf{r}_0$  from the cloud center, the radiation intensity of an active bubble of radius  $a_0$  will have the form

$$I(\mathbf{r}_0, a_0, f, \varphi, \theta) = i(\mathbf{r}_0, f, \varphi, \theta) |S(a_0, f)|^2 (r/P_0 a_0)^2.$$

For a great number of active bubbles with the spectra of type (2), random amplitudes, and the times of formation described by a Poisson process, the mean spectrum of their noise intensity can be expressed by the Campbell formula

$$I(f, \varphi, \theta) = \int q(a_0) \langle I(\mathbf{r}_0, a_0, f, \varphi, \theta) \rangle da_0, \quad (4)$$

where  $\langle \rangle$  means averaging over all coordinates  $\mathbf{r}_0$ . Here,  $q da_0$  is the number of bubbles formed in a unit time with the radii from  $a_0$  to  $a_0 + da_0$ . This quantity can be estimated by the formula

$$q \approx n(a_0) \frac{dV_0}{dt} \Delta t,$$

where  $\Delta t$  is the characteristic time of bubble radiation,  $\Delta t \approx 0.3a_0/(\pi\delta)$ , and  $\frac{dV_0}{dt}$  is the rate of change of the air

volume in the cloud; the latter can be estimated using the experimental data (e.g., from [12]). In what follows, we will assume that the distribution of active bubbles in

size  $n(a_0)$  coincides with the distribution  $n(a)$  for passive bubbles. This assumption is based on the fact that the processes of rising to the surface for large bubbles and the dissolution of small bubbles, i.e., the processes that lead to changes in the aforementioned distribution with time, are sufficiently slow.

The relationship between the quantity  $V$  and the function  $n(a)$  is determined by the formula

$$V = 4\pi/3 \int_{a_{\min}}^{a_{\max}} n(a)a^3 da, \quad (5)$$

and the relationship between  $v_0$  and  $V$  for approximation (3) is determined by the formula

$$v_0 = 2\pi \int_0^{\infty} r^2 V(r, t) dr = 4\pi V_0 / \gamma^3. \quad (6)$$

In the general case, the calculation of  $i(\mathbf{r}_0, f, \varphi, \theta)$  is extremely complicated. For an arbitrary geometry of the problem, the solution is possible only by the methods of the geometric diffraction theory, whereas, for clouds with large values of  $V$ , these methods lead to considerable errors [18]. Hence, we try to find the solution with allowance for the multiple scattering in the Twersky approximation [17]. In addition, we assume that the capture of bubbles occurs at the center of the hemisphere at the water surface, at  $r = 0$ . The average distance  $l$  between active bubbles and this point can be estimated as  $l = \langle |\mathbf{r}_0| \rangle \approx s/b$ , where  $s$  is the mean rate of cloud expansion. With allowance for the experimental data [12], the latter quantity can be set equal to 1 m/s. Then, we can conclude that  $l$  is relatively small, and, in calculating the scattered field, we can assume that the source is located at  $r = r_0 = 0$ .

Another difficulty is caused by the absence of data on the characteristics of the water surface in the process of bubble capture. It is expedient to perform the calculations for two limiting cases: a perfectly soft plane surface and an absorbing surface. The comparison of the computational results with the experimental frequency spectra of noise produced by breaking waves will allow us to judge the validity of these models.

For a hemispherical cloud with a source at the center of its plane surface, the pressure  $p$  will be a function of the distance  $r$  and the angle  $\theta$ . This fact considerably complicates the solution of the Twersky integral equation. For the sake of simplification, we seek the field in the direction  $\theta = \pi$  (i.e., in the downward direction normal to the water surface).

If the dimensions of the scatterers are much less than the distance between them, i.e., the scattering characteristics are independent of the position of the

bubble in the cloud [17], the equation for the mean (coherent) acoustic field has the form

$$p(\mathbf{r}) = p_0(\mathbf{r}) + \int_0^{\infty} \int_{\Omega} p(\mathbf{r}') u(\mathbf{r}, \mathbf{r}') n(a, \mathbf{r}') da d\mathbf{r}', \quad (7)$$

where  $p_0 = \exp(ik_0 r)/r$  and  $u$  is the scattering operator. According to the data reported in the literature [3], we set  $n = n_0(a) \exp(-\gamma r')$ , where  $n_0$  is the density of bubble distribution in the vicinity of the point  $r = 0$ , this quantity being determined by formula (5) at  $V = V_0$ . For an absorbing surface in the far-zone approximation, the operator  $u$  has the form  $u = \sigma \exp(ik_0 \rho) / \rho$ , where  $\rho = (r^2 + r'^2 - 2rr'y)^{1/2}$ ,  $k_0$  is the wave number for water without bubbles,  $\sigma$  is the scattering amplitude (for free space,  $\sigma = a/L$ ,  $L = (300af)^{-2} - 1 - i\delta$ , and  $y$  is the cosine of the angle between the vectors  $\mathbf{r}$  and  $\mathbf{r}'$ ). Then, in the spherical coordinate system, expression (7) can be represented in the form

$$p(r) = p_0(r) + 2\pi J_0 \int_{a_0}^{\infty} \int_0^1 p(r') r'^2 \times \exp(-\gamma r') \frac{\exp(ik_0 \rho)}{\rho} dr' dy,$$

where  $J_0 = \int_0^{\infty} \frac{n_0(a)a}{L} da$ .

Integrating with respect to  $y$  at  $r \gg r'$  (virtually, at  $r \gg 1/\gamma$ ) and neglecting the finite size of the radiating bubble, we obtain a degenerate Fredholm equation

$$p(r) = p_0(r) + M \int_0^{\infty} p(r') \frac{r'}{r} \exp(ik_0 r - \gamma r') \times (1 - \exp(-ik_0 r')) dr', \quad (8)$$

where  $V = 2\pi J_0 / ik_0$ . The solution to this equation has the form

$$p(r) = \frac{\exp(ik_0 r)}{r} \left[ 1 - \frac{2\pi J_0}{\gamma(ik_0 - \gamma)} \right]^{-1}. \quad (9)$$

For the model of a hemispherical cloud with a perfectly soft plane surface, the source located at the center of the surface will be considered as a dipole with the base  $2z$ , where  $z$  is a random variable with the average value  $\langle z \rangle = 2l/\pi$ . In the equation for the mean acoustic field (7), the operator  $u$  for  $\theta = \pi$  can be represented as

$$u = \sigma \left[ \frac{\exp(ik_0 \rho^+)}{\rho^+} - \frac{\exp(ik_0 \rho^-)}{\rho^-} \right], \text{ where } \rho^{\pm} = (r^2 +$$

$r'^2 - 2rr'y)^{1/2}$  and  $\sigma = a/L \left[ L + \frac{a}{2z} \exp(2ik_0 z) \right]$  (for a bubble at the distance  $z = r'y$  from the surface) [18].

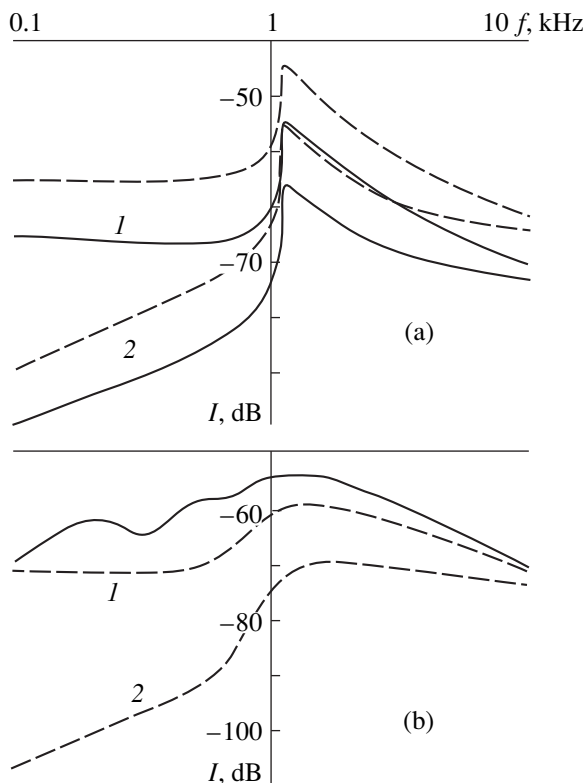


**Fig. 1.** Frequency spectra of noise produced by a single breaking wind wave: (a)  $\kappa = 3$ ,  $a_{\max} = 0.003$  m; (b)  $\kappa = 3$ ,  $a \leq 0.001$  m and  $\kappa = 5$ ,  $a > 0.001$  m. (1) An absorbing surface and (2) a soft surface;  $t =$  (solid lines) 0.1 and (dashed lines) 0.5 s; the thick line shows the experimental data.

The solution of equation (7) is fairly difficult. A simplification is possible in the case of a factorable function  $p(r', y)$ . It is easy to verify that at small  $k_0 z$  the relation  $p(r', y) \approx p(r')2ik_0 r'y$  is valid. To reduce equation (7) to a degenerate one, we replace the quantity  $\sigma$  by its upper bound, which has the form  $\sigma = a/L'$ , where  $L' = (300af)^2 - 1 + i0.0007a^{-1/2}$ . Performing these substitutions in (7) and integrating with respect to  $a$  and  $y$ , we obtain for  $r \gg 1/\gamma$ :

$$p(r) = p_0(r) + M' \int_0^\infty p(r') \frac{r'}{r^2} \times \left[ (i/k_0 + r) \sin \frac{2k_0 r'}{2} + \frac{ir'}{2} \cos k_0 r' \right] \exp(ik_0 r - \gamma r') dr', \tag{10}$$

where  $M' = \frac{16}{k_0} \int_0^\infty \frac{n_0(a)a}{L'} da$  and  $p_0 = \frac{P_0 a_0}{r} \exp(ik_0 r)(1 - \exp(2ik_0 z))$ . This degenerate equation can be solved by a conventional method, but since its solution is cumbersome, we do not present it here. In the expression for  $p_0$ , we have  $k \neq k_0$  in the general case, because, between the radiating bubble and the surface, other bubbles that

affect the sound velocity may be present. If we replace  $z$  by its average value  $\langle z \rangle \approx \frac{5a_0}{1 + 0.055/a_0^{1/2}}$ , the number of such bubbles will be small, and the quantity  $k$  can be estimated using the approximation of a quasi-homogeneous medium. We note that  $\langle z \rangle$  may be underestimated, because most of the bubbles begin radiating at  $z > 6a_0$  [2]. On the other hand, the experiments described by Medwin and Beaky [1] refer to another mechanism of bubble capture than that considered in this paper. Hence, the parameters  $l$  and  $k$  of the model should be corrected according to the results of the comparison of the calculated noise spectra with the experimental ones.

Similarly, we can find the approximate solutions of the Twersky equation for the incoherent component of the scattered intensity. These equations have the form [17]

$$i = |p(\mathbf{r})|^2 + \int \left[ \int_0^\infty n(a, \mathbf{r}') v(\mathbf{r}, \mathbf{r}') |p(\mathbf{r}')|^2 da \right] d\mathbf{r}',$$

where  $p$  is the solution to equation (8) or (10) and  $v$  satisfies the integral equation

$$v(\mathbf{r}, \mathbf{r}') = u(\mathbf{r}, \mathbf{r}') + \int \left[ \int_0^\infty v(\mathbf{r}', \mathbf{r}'') u(\mathbf{r}, \mathbf{r}'') n(a, \mathbf{r}'') da \right] d\mathbf{r}''.$$

Without dwelling on the details of computations, we present the expression for  $i(r_0 = 0, a_0, f, \theta = \pi)$  used in the calculations:

$$i \approx |p(r)|^2 + 2\pi J_1 r \int_0^\infty v |p(\mu r)|^2 E_1(2\beta_0 r(1 - \mu)) d\mu, \tag{11}$$

where  $J_1 = \int_0^\infty \frac{n_0(a)a^2}{|L|^2} da$ ,  $E_1$  is an integral exponential function and  $\beta_0$  is the coefficient of wave attenuation in a bubble cloud with the concentration  $V = V_0$ . This coefficient is calculated in the approximation of a quasi-homogeneous medium, and the expression for it can be found in, e.g., [16].

Figure 1 presents the calculated frequency spectra of noise generated by breaking waves; the spectra were calculated by formula (4) with the intensities  $i(r_0 = 0, a_0, f, \theta = \pi)$  calculated by formula (11). For a reflecting surface, the averaging over  $z$  was performed on the assumption that the distribution has the form  $w(z) = \exp(-z/\langle z \rangle)$ ; the term  $|p|^2$  involved in expression (11)

was multiplied by  $(2k\langle z \rangle)2/(1 + 2(k\langle z \rangle)^2)$ . In the calculations, we used the conventional approximation

$$n(a) = n_0 a^{-\kappa}, \quad a_{\min} \leq a \leq a_{\max},$$

$$n_0 = V \frac{1 - \kappa/4}{a_{\max}^{4-\kappa} - a_{\min}^{4-\kappa}}, \quad (12)$$

$$a_{\min} = 0.00003 \text{ m}, \quad a_{\max} = 0.003 \text{ m}.$$

The value of  $\kappa$  may vary widely; according to [11], it should fall within the interval from 1 to 8, but its most probable values are 3–5. Figure 1a shows the spectra for  $\kappa = 3$ . In the formulas that were used for calculating the spectrum in the case of a reflecting surface, we took  $k = k_0$ . In Fig. 1b, the thick line shows the smoothed experimental spectrum of noise observed for the weak rolling conditions by Kolaini [2]. We selected the spectrum obtained in laboratory conditions instead of the full-scale ones for the following reasons:

(1) The structure of the bubble density in the cloud was also determined in the laboratory experiment [12]. Therefore, it seems to be more correct to test the validity of the model by the comparison with the experiment for which the parameters of the cloud are known.

(2) In the publications describing the noise of breaking waves in the sea (e.g., [3]), unsmoothed spectra of the sum of the wave breaking noise and background noise are presented. If we subtract the background spectrum and perform the smoothing procedure, we obtain a result close to that presented in [2]. We note that the experimental spectrum of noise presented in [20] for the turnover conditions in the surf zone is also quite close to the laboratory spectrum.

The comparison of the experimental spectrum with the calculated curves suggests the following conclusions:

(a) At frequencies above 1 kHz, the calculated and experimental curves agree well with each other. The presence of a sharp peak in the calculated curves near  $f = 1$  kHz is explained by the choice of the function  $n(a)$ , which terminates at the resonance frequency 1 kHz. We can assume that the real distribution  $n(a)$  has no discontinuities at large  $a$ . This assumption is confirmed by the experimental data [20]. The result of the calculation of  $I(f)$  performed for the approximation  $\kappa = 3$  at  $a < 0.001$  m and  $\kappa = 5$  at  $a > 0.001$  m (which is close to the approximation obtained in [20]) is presented in Fig. 1b. One can see that the aforementioned broken-line approximation of  $n(a)$  provides a better agreement with the experiment than the discontinuous approximation (12).

(b) At the frequencies below 1 kHz, the curves obtained for the absorbing surface are closer to the experimental data than the curves for the reflecting surface. In addition to the assumption that the surface should possess absorbing properties, there exists another mechanism that could provide a better agreement between the calculations and the experiment: a

decrease in the sound velocity in the surface layer. According to Lamarre and Melville [12], the sound velocity measured at the center of the cloud may be as low as 20 m/s.

To chose between the aforementioned factors, it is necessary to consider additional experimental data. For example, we could compare the calculated and experimental angular spectra of noise produced by breaking waves. Unfortunately, a rigorous calculation of angular spectra with allowance for multiple scattering is quite complicated, while the only known experimental angular spectrum obtained for a single breaking wave [19] covers only a limited range of angles. However, such a comparison would be useful for our study. We proceed from the assumption that the angular dependence of the intensity is mainly determined by the interference of the direct and surface-reflected coherent components of the signal generated by a point source at the frequency  $f$  at the distance  $l$  from the surface. The effect of the cloud on the complex sound velocity can be taken into account by using the approximation of a quasi-homogeneous medium. The aforementioned assumption is based on the fact that  $l$  is small, the number of passive bubbles within this distance is also small, and one can expect that the effect of multiple scattering on a wave propagating from the source to the surface is negligible. We can show that, in a bubble cloud with the concentration  $V$ , the complex sound velocity is determined by the expression

$$\frac{1}{c} = \left[ \frac{(1-V)^2}{c_0^2} + \frac{1-V}{\pi f^2} \int_0^\infty \frac{an(a)da}{D - i\delta} \right]^{1/2}.$$

Then, the attenuation coefficient is  $\beta = 2\pi f \text{Im}(1/c(r))$ . Setting  $\beta = \beta_0 \exp(-\gamma r)$  for the cloud and taking into account that  $l \ll 1/\gamma$ , we obtain (here, we neglect the factor independent of  $\theta$ ):

$$I(\theta) = 1 + \exp 2\xi - \frac{\exp \xi}{1 + (4\pi f \text{Re}(c^{-1}(l))l \cos \theta)^2}, \quad (13)$$

$$\xi \approx 2\beta_0 l \cos \theta.$$

The surface is assumed to be smooth and totally reflecting. The presence of a surface roughness can be described by an additional term in the expression for  $\xi$ . However, since no information on the statistical characteristics of the surface in the wave breaking area is available, the inclusion of this factor makes no sense.

Figure 2 shows the angular spectra calculated by formula (13) for the cloud parameters at  $t = 0.5$  s, for the frequencies 0.5 and 1 kHz with the quantity  $\beta$  approximated as described in [16]. The calculated diagrams qualitatively agree with the experimental data [19]. Therefore, we can conclude that, in calculating the radiation of active bubbles near the water surface, it is necessary to take into account the decrease in the sound velocity even when the distance between the bubble and the surface is small. Evidently, the problem

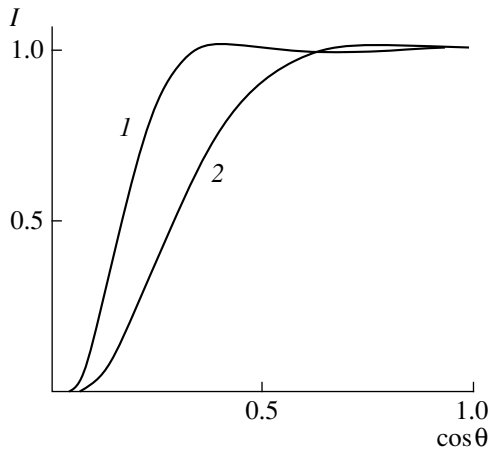


Fig. 2. Angular spectra of noise produced by a single breaking wave:  $f = (1)$  0.5 and  $(2)$  1 kHz.

of calculating the angular spectra of noise produced by breaking waves requires further investigation.

The current knowledge of the processes of noise generation by air bubbles in the ocean allows us to outline the future model of a local noise source. The intensity of noise should be determined by the summation of the intensities of at least the following processes:

rolling (at frequencies  $> 0.1$  kHz),  
turnover (at frequencies  $< 1$  kHz),

and formation of a turbulent vertical flow in the wave breaking area, this flow causing the excitation of the "old" passive bubbles (at frequencies  $> 1$  kHz).

The relative contributions of these processes to noise depend on the wind speed  $v$ , and they should be determined experimentally.

The model of noise at  $v < 7$  m/s is described in this paper. The model of rolling noise at  $v > 7$  m/s is fairly complicated; presumably, the rolling process can be considered in the first approximation as a random sequence of several processes described above, because a long wave never simultaneously breaks along its full length. The model of noise produced by the turnover processes is not developed in detail; however, according to Kolaini *et al.* [13], the simplest model of a spherical quasi-homogeneous cloud adequately describes the turnover noise spectrum near the resonance. Here, we should mention the study concerned with the formation of the noise field in a coastal zone where the turnover of waves has its specific features related to the effect of the bottom [20]. Special approaches to estimating the noise of bubbles excited by turbulence are described by Kolaini and Goumilewski [21].

In closing, it should be noted that the progress in the development of the model of a local source of ocean noise essentially depends on the progress in obtaining the data on the dynamics of the water bulk in the presence of breaking waves.

#### ACKNOWLEDGMENTS

This work was supported in part by the Russian Foundation for Basic Research (project no. 96-15-98367).

#### REFERENCES

1. H. Medwin and M. Beaky, *J. Acoust. Soc. Am.* **86**, 1124 (1989).
2. A. Kolaini, *J. Acoust. Soc. Am.* **103**, 300 (1998).
3. D. Farmer and Li Ding, *J. Acoust. Soc. Am.* **92**, 397 (1992).
4. S. Stolte, in *Proceedings of Conference on Oceans, 1994*, Vol. 2, p. 17.
5. R. Kennedy and T. Szlyk, *J. Acoust. Soc. Am.* **89**, 673 (1991).
6. V. I. Mendus and G. A. Postnov, *Akust. Zh.* **39**, 1107 (1993) [*Acoust. Phys.* **39**, 582 (1993)].
7. G. Norton *et al.*, *J. Acoust. Soc. Am.* **103**, 3256 (1998).
8. V. I. Mendus and G. A. Postnov, *Akust. Zh.* **40**, 316 (1994) [*Acoust. Phys.* **40**, 288 (1994)].
9. Z. Ye, *J. Acoust. Soc. Am.* **102**, 788 (1997).
10. T. Yang and K. Yoo, *J. Acoust. Soc. Am.* **101**, 2541 (1997).
11. H. Oguz, *J. Acoust. Soc. Am.* **93**, 2417 (1993).
12. T. Lamarre and W. Melville, *J. Acoust. Soc. Am.* **95**, 1317 (1994).
13. A. Kolaini *et al.*, *J. Acoust. Soc. Am.* **94**, 2809 (1993).
14. M. Longuet-Higgins, *J. Acoust. Soc. Am.* **87**, 652 (1990).
15. H. Pumphrey and J. Williams, *IEEE Trans. OE-15* (4), 268 (1990).
16. C. Clay and H. Medwin, *Acoustical Oceanography. Principles and Applications* (Wiley, New York, 1977; Mir, Moscow, 1985).
17. A. Ishimaru, *Wave Propagation and Scattering in Random Media* (Academic, New York, 1978; Mir, Moscow, 1982), Vol. 2.
18. Z. Ye and C. Feuillade, *J. Acoust. Soc. Am.* **102**, 798 (1997).
19. G. A. Postnov, *Akust. Zh.* **44**, 527 (1998) [*Acoust. Phys.* **44**, 452 (1998)].
20. G. Deane, *J. Acoust. Soc. Am.* **102**, 2671 (1997).
21. A. Kolaini and A. Goumilewski, *J. Acoust. Soc. Am.* **101**, 218 (1997).

*Translated by E. M. Golyamina*

# Sound Scattering by Density Discontinuities in Media with Temperature or Salinity Stratification

V. E. Prokhorov

*Institute of Problems of Mechanics, Russian Academy of Sciences,  
pr. Vernadskogo 101 (1), Moscow, 117526 Russia*

*e-mail: prohorov@ipmnet.ru*

Received December 27, 1998

**Abstract**—In a stratified liquid flow about an obstacle, acoustically contrasting thin layers whose scattering properties considerably depend on the stratification type are formed. High initial scattering levels and short lifetimes are characteristic of layers with temperature stratification. On the contrary, relatively low initial levels characterize the scattering from layers with salinity stratification, while their lifetimes are two orders of magnitude longer. The experimental envelopes obtained for the decay of scattering from a layer in the wake behind a two-dimensional circular cylinder agree well with the theoretical predictions. The values of the reflection coefficient calculated using the hydrodynamic similarity principle for a single concentration level in real sea conditions fit well into the range of experimental scattering levels. © 2000 MAIK “Nauka/Interperiodica”.

The scattering of ultrasound by thin high-gradient interlayers was investigated in laboratory experiments [1, 2]. In these experiments, the interlayers were formed as outer shells of the wake behind a two-dimensional circular cylinder in a liquid with the salinity stratification. From the simultaneous analysis of the schlieren patterns and vertical backscattering profiles, it follows that almost all scattering power was reflected from the interlayers, and only a small portion (a few percent) was reflected from the three-dimensional microstructural inhomogeneities of the wake [2]. The backscattering coefficients measured for different flow modes were recalculated into equivalent (in power) dimensionless cross-sections of volume scattering, and these values were found to be of the same order of magnitude as the corresponding data of full-scale experiments [3]. Exhaustive investigations [4] showed that, even at a relatively early stage of flow, the shells of a two-dimensional wake are transformed under the buoyancy forces to flat, nearly horizontal layers sufficiently thin in comparison with the sound wavelength ( $\lambda = 0.15$  cm in [4]). The experimental vertical backscattering coefficient was found close to the theoretical value calculated from contact measurements of the density drop and the shell thickness by using the formulas of geometric acoustics [5]. In the experiments on oblique sounding, it was found that, at the stage of a well-developed wake, only the specular component of the scattering is observed [4, 5]. This fact testifies to the smallness of the Rayleigh parameter  $2kh\sin\varphi$  ( $k = 2\pi/\lambda$ ,  $\varphi$  is the grazing angle relative to the boundary, and  $h$  is the characteristic height of roughness); this means that the characteristic height of roughness of the reflecting boundary is small in comparison with the wavelength [6].

An acoustical contrast appears due to the formation of density discontinuities when the flow interacts with a solid body. This interaction causes some portion of liquid in the region before the body to acquire a vertical component of velocity  $w$  that is sufficient for this portion of liquid to rise to a height  $z_0$  and to flow into the wake. In this case, the density differential between the raised particle of density  $\rho$  and the surrounding liquid will be  $\delta\rho = \gamma z_0$ , where  $\gamma = d\rho/dz$  is the density gradient in the surrounding liquid. To estimate the maximum value of  $z_0$ , we set  $w$  equal to the flow velocity  $u$ . Then, equating the work of the particle against the buoyancy forces  $\int_0^{z_0} g\gamma\rho dz$  to its kinetic energy  $\rho u^2/2$ , we obtain  $z_0 = u/N$ , where  $N = (g\gamma/\rho)^{1/2}$  is the buoyancy frequency. Substituting  $z_0$  into the expression for  $\delta\rho$ , we find the relative density differential in the form

$$\rho' = \delta\rho/\rho = uN/g. \quad (1)$$

In the laboratory experiments [4, 5], the velocity  $u$  varied in a range 0.1–0.2 cm/s, and the buoyancy frequency remained intact and equal to  $N = 1.1$  s<sup>-1</sup>. Substituting these values in (1), we obtain  $\rho' = 1.1 \times 10^{-4}$ – $2.2 \times 10^{-4}$ , which is in a good agreement with the direct measurements that yield the values  $1 \times 10^{-4}$ – $2 \times 10^{-4}$ .

The processes generating the density-type boundaries are universal, and the hydrodynamic similarity makes it possible to extend the data of the laboratory studies of flows around obstacles [1, 2, 4, 5] to similar processes in the ocean, in the currents behind elevated regions near the bottom, in shallow waters, and in the shelf zone, especially if the currents are well developed and the pycnocline is sharp.

To satisfy the similarity condition, one should require that the product  $uN$  (and, correspondingly,  $\rho'$ ) varies only slightly when the model conditions are changed to the full-scale conditions. For the ocean, we estimate the average buoyancy frequency at about  $5 \times 10^{-3} \text{ s}^{-1}$ , which is less than the corresponding laboratory value by a factor of about 200. Then, as follows from (1), one obtains the full-scale value of  $\rho'$  the same as in laboratory experiments for the velocities between 0.2 and 0.4 m/s, which are typical of the ocean. Consequently, for the buoyancy frequency and the flow velocity characteristic of the ocean, the layers with the density differentials of the order of magnitude same as in the laboratory basin will be formed in the wake behind an elevation of height  $H > z_0 = u/N$ . Additionally, taking into account the fact that the laboratory salt solution and seawater have nearly equal coefficients of molecular exchange (the thermal diffusivity  $k_T$  and the salt diffusion coefficient  $k_S$ ), we deduce that the thickness of the transition region in full-scale conditions will be of the same order of magnitude as in the laboratory basin.

Taking into account the fact that sea sonars use wavelengths far exceeding the above value of 0.15 cm, it would appear reasonable that the reflectivity of these layers will be as efficient as the reflectivity of their laboratory analogs. Here, we deal with the coherent specular reflection from a smooth solid layer rather than with the scattering from a biological or other-type suspension that also can cause coherent scattering, especially if such a suspension is concentrated in a layer that is thin in comparison with the wavelength. The most essential difference is that a suspension scatters coherently not only in the specular direction, but also in all other directions, including backwards. Another difference lies in the relationship between the coherent and incoherent components; for a layer of discrete particles, this relationship depends on the total particle number [7].

In a particular case of vertical sounding, the specular reflection from a solid layer is similar to the scattering from a layer with suspended particles, and both types of scattering can be described by the same equation of underwater sounding [8]:

$$10 \log(I_r/I_0) = J + 10 \log A - 40 \log r, \quad (2)$$

where  $I_r$  and  $I_0$  are the scattered and transmitted intensities at the point of reception,  $J = 10 \log n^2$ ,  $n = (I_s/I_i)^{0.5}$  is the scattering coefficient of the surface,  $I_i$  and  $I_s$  are the intensities of the incident and scattered waves at a distance of 1 m,  $r$  is the distance of the scattering surface from the sonar,  $A = 0.5c\tau\Psi r$ ,  $c$  is the velocity of sound,  $\tau$  is the duration of the signal sample,  $10 \log \Psi = 10 \log(2\theta/\pi) + 6.9$ , and  $\theta$  is the angular halfwidth of the directivity pattern.

In sea measurements, it is common practice to consider that the scattering is caused by volume inhomogeneities whose dimension far exceeds the wavelength. For

this reason, the processing is performed according to another algorithm that coincides with (2) only in the form

$$10 \log(I_r/I_0) = J_V + 10 \log V - 40 \log r,$$

but where  $V = 0.5c\tau\Psi r^2$  and  $10 \log \Psi = 20 \log(2\theta/\pi) + 7.7$  [8]. Thus, the scattering intensity  $I_r/I_0$  recorded at the point of reception can be transformed into the volume ( $J_V = 10 \log n_V^2$ ) or surface ( $J$ ) backscattering strength, depending on the accepted model of scattering. These quantities are related through an obvious relationship

$$\begin{aligned} J - J_V &= 10 \log(n/n_V)^2 \\ &= 10 \log(2\theta/\pi) + 10 \log r + 1.2, \end{aligned} \quad (3)$$

which will be used below to transform the volume scattering measure into surface scattering measure.

Thus, the data obtained in the laboratory conditions point to the fact that the interaction of sea currents with obstacles can form density discontinuities (boundaries) contrasting in the field of sound scattering. The question arises of what the contribution of these discontinuities to the total scattering recorded by the sonar is.

In this connection, a topical problem is to theoretically investigate the scattering properties of a thin density-discontinuity layer formed in a stratified liquid and developing according to the diffusion law. Because the ocean is stratified in temperature and salinity, it appears reasonable to investigate and compare the scattering properties of both types of stratification.

We will consider a flat stationary layer whose stratification parameter (temperature  $T$  or salinity  $S$ ) is described by a linear function of depth at the initial moment and is deformed with time under the action of diffusion. We will investigate the evolution of the layer in the most general form, by using the equation of diffusion  $\partial S/\partial t = k_S \Delta S$ , and formally change  $S$  and  $k_S$  for  $T$  and  $k_T$ , respectively, to consider the temperature stratification. This approach is applicable for sufficiently thin layers of temperature and salinity discontinuity; namely, for the layers whose width is below the minimum internal scale of turbulence [9]. Below, we will deal only with the type of layers that are smoothed out according to laws of molecular diffusion.

We will assume that the gradient within the layer far exceeds its values outside the layer, so that the liquid on both sides of the layer can be considered as a homogeneous liquid with a constant salinity  $\pm s$  (or temperature  $\pm T$ ) without loss of essential features. Then, the initial distribution (at  $t = 0$ ) for an interlayer of thickness  $\delta$  located at  $z = 0$  in a medium occupying the depth interval  $-\infty < z < \infty$  can be given in the form:

$$S_0 = \begin{cases} -s, & -\infty < z < -\delta/2 \\ z2s/\delta, & -\delta/2 < z < \delta/2 \\ s, & \delta/2 < z < \infty. \end{cases} \quad (4)$$

The current distribution at moment  $t$  is determined by the known solution of the Fourier equation [10]

$$S(z, t) = 0.5(\pi k_s t) \int_{-\infty}^{\infty} S_0(y) \exp\{-(z-y)^2/4k_s t\} dy.$$

Substituting (4) in this equation and introducing the quantities

$$\begin{aligned} x &= z/\delta, \\ x_c &= 2(k_s t)^{0.5}/\delta, \end{aligned} \quad (5)$$

we represent it as a sum whose terms are the canonic expressions like the error function  $\operatorname{erf}(x) = 2(\pi)^{-0.5} \int_0^x e^{-x^2} dx$  and exponents. Omitting intermediate transformations, we finally obtain the current distribution of salinity in the form

$$\begin{aligned} S(x, x_c) &= (x + 0.5) \operatorname{erf}\left(\frac{x + 0.5}{x_c}\right) \\ &\quad - (x - 0.5) \operatorname{erf}\left(\frac{x - 0.5}{x_c}\right) \\ &\quad + \frac{x_c}{\sqrt{\pi}} \left( \exp\left(-\left(\frac{x + 0.5}{x_c}\right)^2\right) - \exp\left(-\left(\frac{x - 0.5}{x_c}\right)^2\right) \right). \end{aligned} \quad (6)$$

The diffusion smoothes out and broadens the transition region with retaining the amplitude of the differential approximately constant and equal to  $2s$  (see Fig. 1). We specify the current dimensionless thickness as the thickness corresponding to the threshold value of the property under study 0.98. It can be shown that, for any curve in Fig. 1, this thickness is achieved at the point with the coordinate

$$x = x_b = 1/\operatorname{erf}(0.5/x_c), \quad (7)$$

which is the abscissa of the point of intersection of two straight lines: the secant  $y = x \operatorname{erf}(0.5/x_c)$  and the asymptote  $y = 1$ . In this case, the amplitude of the salinity drop across the transition region will be  $\delta S = 1.96s \approx 2s$ , and, according to (5), the absolute width of the transition region will be

$$d = 2\delta x_b. \quad (8)$$

For normal incidence of a plane sound wave, the reflection coefficient of the smooth transition region shown in Fig. 1 can be specified in the form [11, 12]

$$n^2 = \sin^2[\zeta \ln(1 + \eta)] / \{4\zeta^2 + \sin^2[\zeta \ln(1 + \eta)]\},$$

where  $\zeta = (B^2 - 0.25)^{0.5}$ ,  $B = kd/\eta$ ,  $k = 2\pi/\lambda$  is the sound wave number, and  $\eta = \delta R/R$  is the relative differential of the acoustic impedance  $R = \rho c$  (this differential is determined by the corresponding drops in density  $\delta\rho$  and sound velocity  $\delta c$  through the relationship  $\eta = \delta\rho/\rho + \delta c/c$ ). In liquid solutions, the absolute differentials of

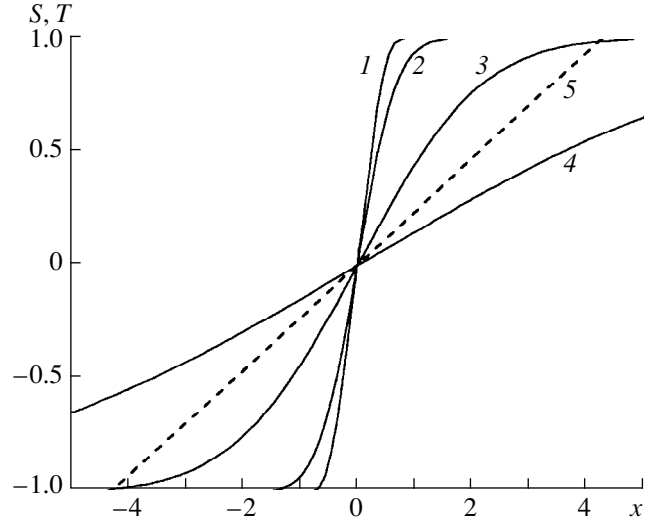


**Fig. 1.** Current distributions of salinity ( $S$ , curves 1 and 2) and temperature ( $T$ , curves 3 and 4) calculated according to expression (5) for  $\delta = 0.1$  cm. The time is 10 (curves 1 and 3) and 100 s (curves 2 and 4). Curve 5 is the secant  $y = x \operatorname{erf}(0.5/x_c)$ .

the properties are normally less than the corresponding mean values by several orders of magnitude. Because of this, we have  $\ln(1 + \eta) \approx \eta$  and  $B \gg 1$ , which makes it possible to reduce the formula for  $n$  to the form

$$n = 0.5\eta |\sin(kd)|/kd. \quad (9)$$

The quantities  $\delta\rho$  and  $\delta c$  involved in the expression for  $\eta$  are expressed in terms of the differentials of temperature  $\delta T$  or salinity  $\delta S$ . In the latter case,

$$\delta\rho/\rho = \beta_\rho \delta S, \quad \delta c/c = \beta_c \delta S,$$

where  $\beta_\rho = 0.8 \times 10^{-3}(\%)^{-1}$  and  $\beta_c = 0.7 \times 10^{-3}(\%)^{-1}$ .

In the case of a layer with temperature stratification, one should replace  $\beta_\rho$  and  $\beta_c$  by  $\alpha_\rho = -0.2 \times 10^{-3} \text{ deg}^{-1}$  and  $\alpha_c = 2 \times 10^{-3} \text{ deg}^{-1}$ , respectively.

Because interlayers are formed in the field of mass forces, it is convenient to measure the amplitude of the drop in the density units common for both types of stratification. These units offer us a possibility of comparing the scattering levels of temperature and salinity layers characterized by equal density differentials. Substituting  $\delta S = \delta\rho/(\rho\beta_\rho)$  and  $\delta T = \delta\rho/(\rho\alpha_\rho)$  in (9), we obtain for the salinity and temperature layers, respectively:

$$n_S = 0.5(1 + \beta_c/\beta_\rho)(\delta\rho/\rho) |\sin(kd_S)|/kd_S, \quad (10)$$

$$n_T = 0.5(1 + \alpha_c/\alpha_\rho)(\delta\rho/\rho) |\sin(kd_T)|/kd_T. \quad (11)$$

The current thicknesses  $d_T$  and  $d_S$  of the temperature and salinity layers, respectively, are determined from (8) taking into account (7) and (5).

Structurally identical formulas (10) and (11) are given separately to emphasize the essential differences in the dynamics of the scattering by temperature and

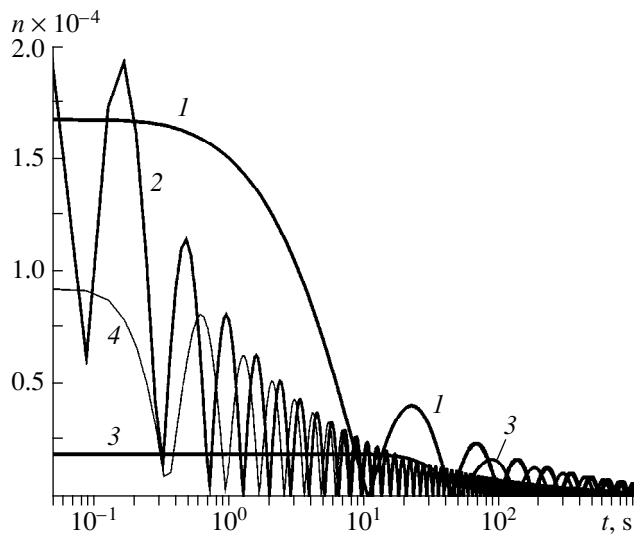


**Fig. 2.** Scattering coefficient calculated for the wavelength  $\lambda = 0.15$  cm for salinity (curves 1 and 3) and temperature layers (curves 2 and 4). The initial layer thickness is  $\delta = 0.01$  (curves 1 and 2) and 0.1 cm (curves 3 and 4).

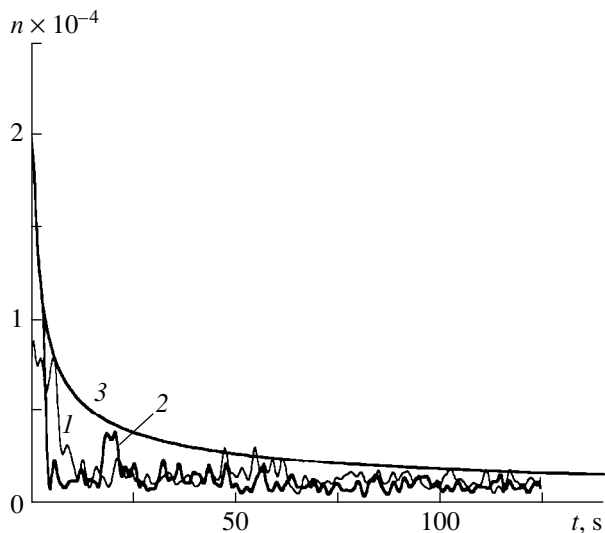


**Fig. 3.** Scattering by the lower (curve 1) and upper (curve 2) shells of the wake behind a two-dimensional cylinder. Curve 3 presents the envelope of the amplitudes  $A_S$  obtained from formula (10).

salinity layers, which is evidenced by the behavior of the time dependent scattering coefficient  $n(t)$  shown in Fig. 2. For the initial parameters to agree with the experimental data, their particular values—the wavelength  $\lambda = 0.15$  cm, the density differential  $\delta\rho/\rho = 2 \times 10^{-4}$ , and the layer thickness  $\delta = 0.1$  and 0.01 cm—were taken from the laboratory experiments [4, 5].

As may be seen, appreciable scattering levels for temperature and salinity layers correspond to radically different temporal regions. The ratio of the scattering amplitudes of temperature and salinity layers is  $n_T/n_S = (1 + \alpha_c/\alpha_p)/(1 + \beta_c/\beta_p) \approx 4.7$  at the initial instant of time

(see (10) and (11)); this ratio becomes less than unity already at the initial stage, and at the final stage ( $t > 50$  s), the scattering from the salinity layer predominates.

Note that the effect of the initial layer thickness on the amplitude and phase of scattering gradually disappears, so that, at later stages, the scattered field “forgets” the initial dimensions of the interlayers.

Figure 3 shows the experimental coefficient of the vertical backscattering from the upper and lower boundaries of the wake behind a two-dimensional cylinder in water with salinity stratification. The curves were obtained from the data of the laboratory experiments [4, 5] by special processing. The following parameters of echo sounding were maintained during the experiments:  $\lambda = 0.15$  cm; the pulse duration and pulse repetition period were  $\tau = 40$   $\mu$ s and 0.16 s, respectively. The measured interlayer thickness (about 0.1 cm) nearly coincided with the resolution limit of the electric conductivity sensor. An appreciable difference between curves 1 and 2 in the high-frequency components is caused by nonstationary oscillations of the scattering direction due to the wave and weak vortex motions of shells. It is clear that the selection of the characteristic oscillations caused by the resonance values of thickness, which periodically occur in the process of the diffusion expansion of the layer, presents a difficult problem against this background. Nevertheless, the amplitudes and the general behavior of the decay satisfactorily agree with the theoretical envelope  $A_S = 0.5(1 + \beta_c/\beta_p)(\delta\rho/\rho)/kd_S$  (curve 3) of the reflection coefficient of the salinity layer (curve 1 in Fig. 2), which is evidence in favor of the diffusion mechanism of the scattering evolution.

The theoretical curves in Fig. 2 clearly show the temporal boundary  $\tau_S$  separating the region where the scattering by temperature layers predominates from the regions where the scattering by salinity layers predominates, the latter case corresponding to greater times. From (10) and (11), it follows that, for equal density differentials  $\delta\rho/\rho$ , the ratio of the scattering amplitudes for the salinity ( $A_S$ ) and the temperature ( $A_T$ ) layers  $\xi = A_S/A_T = (1 + \beta_c/\beta_p)d_T/[(1 + \alpha_c/\alpha_p)d_S]$  can be represented as a function of a single argument  $\chi = t/\delta^2$  whose dimension is inversely proportional to the diffusion coefficient. Figure 4 shows the ratio  $\xi$  as a function of  $\chi$ . From this curve, it follows that  $\tau_S/\delta^2 = 1236$  s/cm<sup>2</sup>. For the considered cases, i.e.,  $\delta = 0.01$  and 0.1 cm, the threshold time is 0.14 and 14 s, respectively; this quantity rapidly increases with the initial thickness, which could be considered as evidence in favor of the predominant role of the scattering by sufficiently thick temperature layers. However, because of the large values of  $k_T$ , the temperature layer soon reaches a certain thickness  $l_0$  starting from which turbulent diffusion comes into play [9]; as a result, the layer is smoothed out much faster and finally loses its scattering properties.

It is reasonable to specify  $l_0$  as the internal scale of turbulence  $l_0 = \{(-B(0)/2B''(0))\}^{1/2}$  where  $B(r)$  is the

correlation function of the flow velocities [13]. According to full-scale measurements [13], the scale  $l_0$  for the ocean lies between 0.8 and 1.8 cm, and we can use  $l_0 = 1$  cm as a rough estimate. Figure 5 shows the layer thickness  $d(t)$  versus time (in hours) for several values of the initial thickness  $\delta$ . One can see that for all  $\delta < 1$  cm, the times required for the temperature and salinity layers to achieve the limiting thickness  $d = l_0 = 1$  cm are about  $t_T \approx 0.02$  and  $t_S \approx 2$  h, respectively.

According to these considerations, we constructed two curves  $n(t)$  for the characteristic frequencies 24 and 5 kHz ( $\lambda = 6.25$  and 30 cm) commonly used in echo sounding (Fig. 6). In constructing, we used the initial density differential  $\delta\rho/\rho = 2 \times 10^{-4}$  and the initial thickness 0.1 cm. Similar to Fig. 5, the temporal scale is given in hours for the purpose of correlating them with the actual observation times. The solid portions of curves correspond to a region where the molecular theory is applicable. Their analytical extensions corresponding to the zone of turbulent diffusion are shown by dotted curves. The temperature layer rapidly reaches the zone of turbulent diffusion, where it is smoothed out and loses the acoustical contrast. At the same time frame a singular salinity interlayer is developed according to the molecular diffusion law within a much longer time and provides a considerably higher backscattering coefficient.

Above, we mentioned that the equation of underwater sounding (2) does not describe the specular reflection excluding the particular case of vertical backscattering. For this particular case, we can compare the theoretical scattering coefficients with the data of full-scale measurements. To realize this comparison, one should use formulas (3) to preliminarily transform the full-scale data (generally given in terms of volume scattering) to the coefficients of surface scattering. For the case of vertical sounding, this transformation is equivalent to replacing the layer of volume inhomogeneities with a single reflecting surface that creates the scattering intensity at the point of reception  $I_r/I_0$  coincident with the intensity of the scattering by volume inhomogeneities.

The horizontal dashed lines in Fig. 6 show the upper and lower boundaries of the surface backscattering (reflection) coefficient equivalent (in  $I_r/I_0$ ) to the volume scattering strength  $J_V$  ranging from  $-90$  to  $-80$  dB; these strengths correspond to those measured in certain regions of the ocean at a depth of about 200 m at frequencies of 24 and 5 kHz [8]. As may be seen, the scattering level of the salinity transition region remains within these boundaries during the time  $t_S$  nearly coincident with the actual duration of echo sounding. Although the scattering from the temperature discontinuity layer appreciably exceeds the upper boundary, its duration  $t_T$  is very short.

A consequence of this difference in the lifetimes must be an appreciable difference of salinity and temperature layers in the horizontal dimensions of the

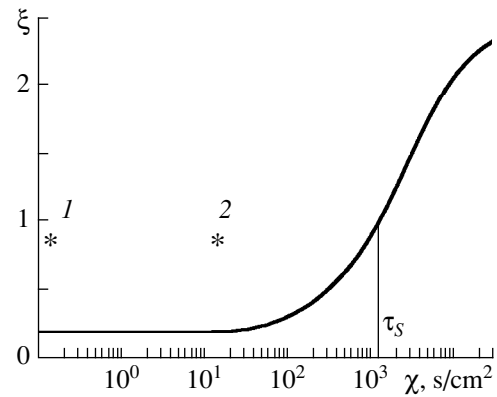


**Fig. 4.** Ratio  $\xi$  of the envelopes of the scattering levels of the temperature and salinity layers with equal density drops versus  $\chi = t/\delta^2$ . The abscissas of asterisks 1 and 2 are equal to threshold times (in seconds) for the layers of thickness 0.01 and 0.1 cm, respectively.

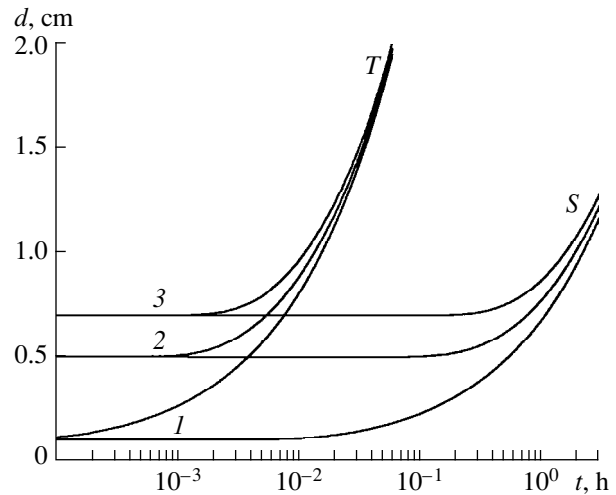


**Fig. 5.** Current thickness of salinity (S) and temperature (T) layers with the initial thickness  $\delta = (1)$  0.1, (2) 0.5, and (3) 0.7 cm.

acoustically contrasting zones. As an example, we consider the case of a flow about a single extended obstacle oriented across the flow. Such a configuration is analogous to the laboratory flow behind a two-dimensional cylinder (more precisely, to its upper half). In this case, a sole surface of density discontinuity will be formed in the wake, and its thickness will increase with the distance from the obstacle. The reflectivity of the surface will be substantial only within the temporal interval of the molecular diffusion,  $t_S$  or  $t_T$ , depending on the stratification type. For the average velocity  $u = 0.4$  m/s, the size (along the stream) of the acoustically contrasting zone will be  $ut_S \approx 2900$  m or  $ut_T \approx 29$  m for the salinity and temperature stratification, respectively. The second value is comparable with the transverse dimension of the spot insonified by the sonar, while the first value far

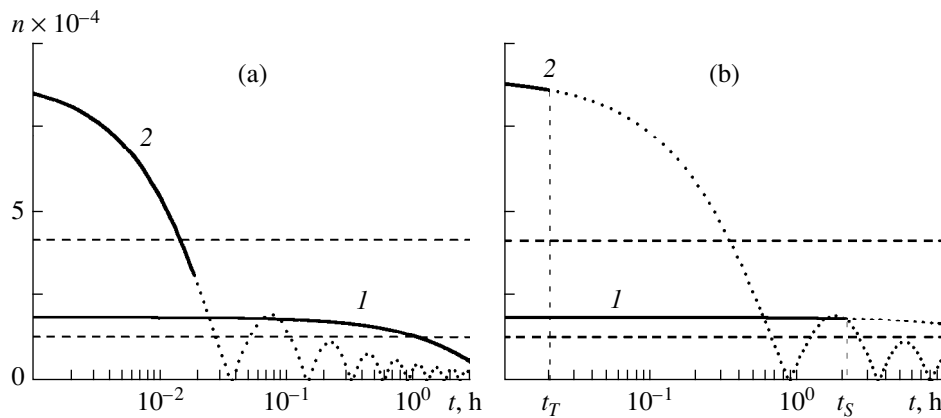


**Fig. 6.** Scattering coefficients (10) and (11) of (1) salinity and (2) temperature layers for  $\delta\rho/\rho = 2 \times 10^{-4}$ ,  $\delta = 0.1$  cm, and  $\lambda =$  (a) 6.25 and (b) 30 cm. The dotted lines are out of the scope of the molecular diffusion approximation. The dashed horizontal lines show the range of the reflection coefficient equivalent to  $J_V$  from  $-90$  to  $-80$  dB.

exceeds this dimension. This fact can be essential in an actual search for such inhomogeneities in the ocean.

To conclude, we list the main results.

A mechanism of the reflection from the density boundaries that appear in the bulk of a stratified liquid and develop according to the molecular diffusion laws is proposed. The amplitude and dynamical characteristics of scattering strongly depend on the type of stratification. For the same initial parameters (the density differential and the thickness), the initial backscattering level of the temperature layer is 4.7 times higher than the corresponding level of the salinity layer; however, the salinity layers are characterized by a longer duration of scattering, which exceeds the corresponding duration for the temperature layers by an order of magnitude. For a salinity layer, the evolution dependences and the amplitudes of scattering calculated in accordance with the theory agree well with the results of the laboratory experiments.

Theoretical results are extended to the full-scale conditions with allowance for the turbulence of the ocean. Because of the turbulence, the effect of the temperature discontinuity on the scattering is significant only at the initial stage. By contrast, the salinity layer develops to its limiting thickness within a considerably longer time interval, owing to which the duration of the scattering appears to be about the actual duration of measurements in the ocean, and the scattering amplitude falls into the interval of the possible levels of surface scattering.

#### ACKNOWLEDGMENTS

I am grateful to V.V. Mitkin for his assistance in the experiment.

The work was supported by the Russian Foundation for Basic Research, project no. 97-01-01013.

#### REFERENCES

1. V. E. Prokhorov and Yu. D. Chashechkin, Dokl. Akad. Nauk **336**, 398 (1994).
2. V. E. Prokhorov and Yu. D. Chashechkin, Akust. Zh. **41**, 908 (1995) [Acoust. Phys. **41**, 804 (1995)].
3. V. P. Shevtsov, A. S. Salomatina, and V. I. Yusupov, Okeanologiya **28**, 376 (1988).
4. V. V. Mitkin, V. E. Prokhorov, and Yu. D. Chashechkin, Akust. Zh. **45**, 380 (1999) [Acoust. Phys. **45**, 336 (1999)].
5. V. E. Prokhorov, in *Proceedings of 9th International Symposium on Acoustic Remote Sensing "ISARS'98"*, Wien, Austria (1998), p. 37.
6. L. M. Brekhovskikh and Yu. P. Lysanov, *Fundamentals of Ocean Acoustics* (Springer, Berlin, 1982; Gidrometeoizdat, Leningrad, 1982).
7. N. Gorska and Z. Klusek, J. Acoust. Soc. Am. **104**, 141 (1998).
8. R. J. Urlick, *Principles of Underwater Sound* (McGraw-Hill, New York, 1975).
9. K. N. Fedorov, *Thin Thermohaline Structure of Ocean Waters* (Nauka, Moscow, 1976).
10. L. D. Landau and E. M. Lifshits, *Fluid Mechanics* (Nauka, Moscow, 1986; Pergamon, Oxford, 1987).
11. J. Rayleigh, *The Theory of Sound* (Dover, New York, 1945; GITTL, Moscow, 1955), Vol. 2.
12. V. A. Shutilov, *Fundamentals of Physics of Ultrasound* (Izd. Len. Univ., Leningrad, 1980).
13. *Physics of Ocean* (Nauka, Moscow, 1978), Vol. 1: *Hydrophysics of Ocean*, Ch. 4, Sect. 5.

Translated by A.G. Vinogradov

# Experimental Study of the Effect of Internal Waves on the Frequency Interference Structure of the Sound Field in Shallow Sea

A. N. Rutenko

*Pacific Institute of Oceanology, Far-East Division, Russian Academy of Sciences,  
Baltiĭskaya ul. 43, Vladivostok, 690041 Russia*

*e-mail: pacific@online.marine.su*

Received February 26, 1999

**Abstract**—In-sea studies are discussed on the effect of internal waves on the frequency interference structure of the sound field propagating along a fixed path in the shelf zone of the Sea of Japan. The studies are based on the continuous transmission of a sound signal frequency-modulated by a sinusoid in the frequency band 306–328 Hz. The experiment includes synchronous measurements of the sound field and the water temperature at different depths with the use of a vertical acoustical-hydrophysical measuring system installed 260 m away from the source, at a point with a 38-m depth of water. It is shown that the intensity of sound signals with frequencies differing by as little as 4% vary with different amplitudes, sometimes even in opposite phases, because of the effect of internal waves. These differences are maximum at the depths corresponding to the interference minima in the vertical distribution of the received sound field. © 2000 MAIK “Nauka/Interperiodica”.

In the propagation of sound waves generated by a point source, an intricate space-frequency distribution of the acoustic energy is formed in the sea waveguide. This distribution is known as the fine interference structure. The structure is stable if only coherent waves participate in the superposition, and the methods of acoustic interferometry [1] can be successfully applied to monitor the dynamics of the water bulk and the acoustic parameters of the bottom. In natural media, the coherence may be destroyed by the fluctuations of the refractive index, which affect the amplitude and phase of the interfering waves. The experimental and theoretical studies [2–7] showed that internal waves (IW) significantly affect the sound propagation in the irregular shallow-water waveguides which are typical for shelf zones of tidy seas with a water density stratification. The sound refraction and scattering due to the sound speed inhomogeneities produced by IW lead to the interaction of the propagating acoustic modes, and this process may have a resonant nature [3]. The interaction causes an energy transport from lower to higher modes and results in the “washing out” or disappearance of the regular interference structure, and in a more uniform insonification of the entire water column [4].

The effect of a nonlinear IW (a soliton) moving in the waveguide on the propagation of pulsed sound signals linearly frequency-modulated within the band

728–885 Hz was experimentally and theoretically studied by Konyaev *et al.* [5]. They showed that, in shallow sea regions, even weak disturbances of the sound channel can lead to significant changes in the amplitudes of the received signals. These changes can be caused by the intermode interaction induced by the medium inhomogeneities, the amplitude variations in the received sound signals depending on the distance to the inhomogeneity and increasing at most “sensitive” points on the path.

The aforementioned facts show the importance of special studies of the effect of IW on the propagation of wide-band sound signals. Such studies are reported in this paper.

The measurements were carried out at the shelf of the Sea of Japan, on a fixed path 260 m in length [6], with the sound transmitter installed at the depth 26 m and a MOLLUSK-96 vertical acoustical-hydrophysical measuring system placed at a point with the 38-m sea depth. With this system, the acoustic pressure was measured simultaneously at eight horizons within the frequency band 20–600 Hz, the hydrophones P.1, ..., P.8 of the system being vertically spaced at 4.5 m from each other. The measuring system was equipped with five point temperature sensors to measure the water temperature and with a 20-m-long resistor-type distributed temperature sensor (DTS) to monitor the variations in the mean temperature of the water layer. The

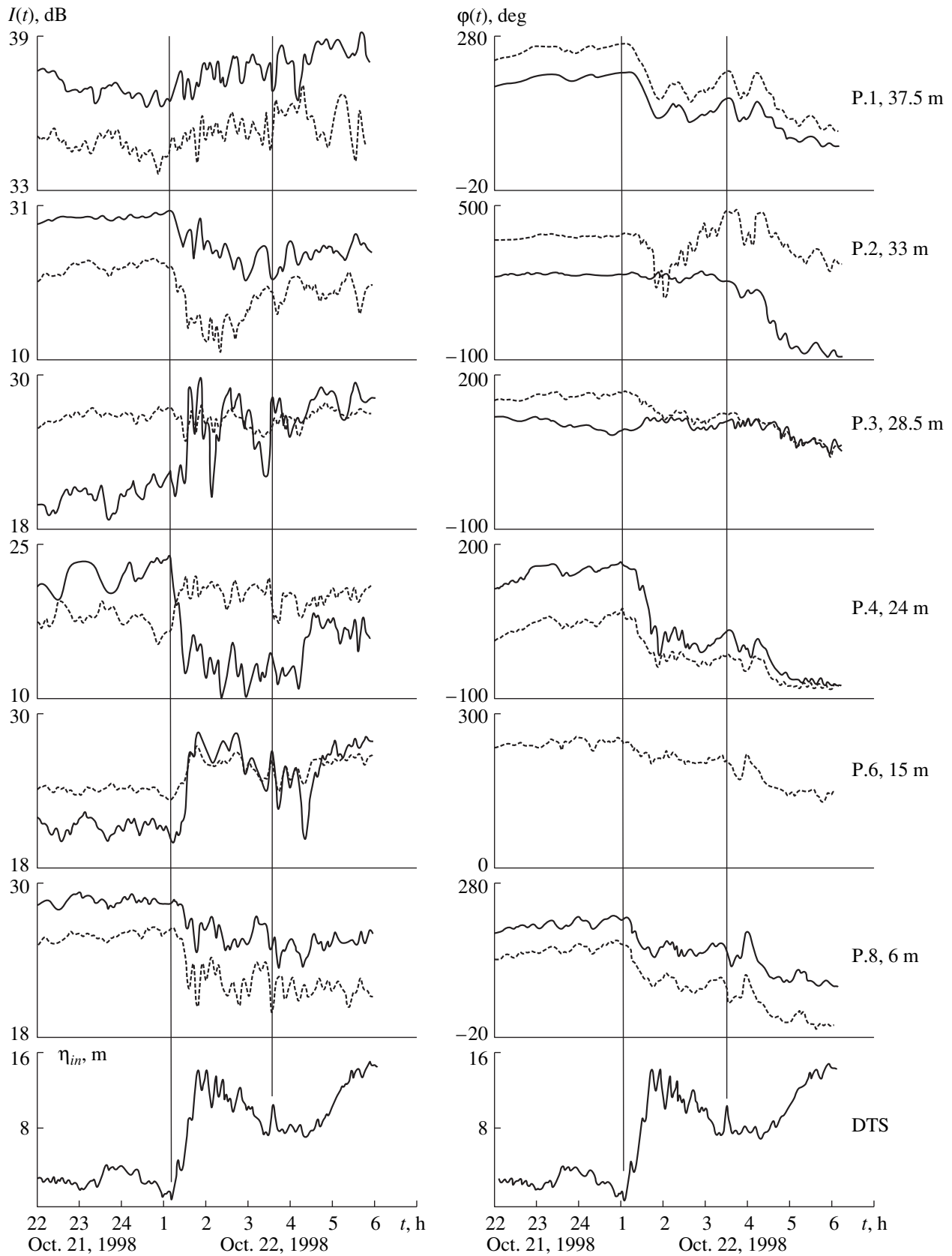


**Fig. 1.** Measured IW profiles  $\eta_{in}$  (DTS) and the variations of the intensity  $I$  and phase  $\varphi$  of sound signals at frequencies of 310 HZ (solid curves) and 324 Hz (dashed curves).

sound signal frequency-modulated within the band 306–328 Hz was continuously generated by the transmitter. The modulation signal was a sinusoid of the frequency 0.6 Hz. Autumn-like water stratification existed along the path. The measurements illustrate the effect of the internal tide and short IW on the frequency interference structure of the received sound signals at different depths.

Figure 1 shows the experimental results obtained on October 21–22, 1998. The synchronous sequences of the acoustic data were entered into a computer, upon digitizing with the sampling frequency  $f_D = 1250$  Hz. The same procedure was performed with the temperature data, the sampling frequency being  $f_D = 78.125$  Hz in this case. After collecting 4096 samples from each acoustic channel, the data input was terminated, and the periodograms  $G(\omega)$  and mean temperatures were calculated with the use of the FFT algorithm. Complex values of the periodograms were stored for the chosen frequency band. These values were subsequently used to estimate the power spectra  $\hat{G}(\omega)$ , the intensities  $I$ , and the phases  $\phi$  of the acoustic signals at the specified frequencies (see [7]). Then a new cycle of data input began. In such a way, at time intervals  $\Delta t \approx 7$  s, the synchronous sequences for the following quantities were obtained: the water temperature measured with the integrating DTS instrument, the intensity  $I$  and phase  $\phi$  of the sound signals received by the hydrophones P.1, ..., P.8 at the chosen frequencies, and the files of the values of  $G(\omega)$  for the frequency band 306–328 Hz.

In Fig. 1, plots of the IW profiles  $\eta_{in}(t)$  obtained with the DTS are presented. According to these plots, the wave of internal tide has filled the path with relatively cold near-bottom water. The temperature difference between the surface and near-bottom water layers increased up to 9°C (the temperatures measured by the point sensors are not shown). Accordingly, the temperature gradient in the thermocline also increased: it became equal to about 1°C/m. The changes in the temperature field significantly affected the propagation of the sound waves. In Fig. 1, the variations of  $I$  and  $\phi$  are plotted for the sound signals with frequencies of 310 and 324 Hz. Figure 2 shows the sonograms  $\hat{G}(\omega)$  for the frequency-modulated sound signals received by the vertical hydrophone array. These sonograms illustrate the effect of IW on the frequency interference structure of the sound field at different depths. Figure 1 shows that the values of  $I$  measured for the signals whose frequencies differ by as little as 14 Hz (4%) vary with different amplitudes, even in opposite phases (plots P.4 in Fig. 1), and these differences are maximum for the horizons that correspond to the interference minima in the vertical distribution of the received sound field. According to Fig. 1, the frequency dependence of the signal phase of the IW-induced variations is much weaker than that of the intensity.

The effect of IW on the acoustic field is illustrated by Fig. 2 for the frequency band 307–327 Hz. The changes in  $\hat{G}(\omega)$  are smallest near the bottom (P.1) and near the sea surface (P.8, the depth 6 m). This phenomenon is related to the features of the vertical interference structure of the sound field. To prove this statement, we present Fig. 3, which shows the results of the vertical profiling of the cw sound field at a frequency of 315 Hz. The profiling was carried out at two points of the path, with the use of the BURUN-96 probe that performs synchronous measurements of the sound pressure, sound speed, and hydrostatic pressure [6]. These measurements were carried out on October 21, 1996, at 150 m from the sound source, at a point with a 28-m sea depth (plots 1), and near MOLLUSK-96 (plots 2). During the measurements, nearly two-layered stratification existed on the path with the near-bottom pycnocline, this situation being close to the water stratification for the experiment at hand for the time interval from 22.00, October 21 to 01.00, October 22, 1998 (see Fig. 1). According to the plot of  $I(z)$  (the solid curve in Fig. 3), the interference maxima are near the sea surface and bottom, while a deep minimum exists in the pycnocline layer (see plot of  $C(z)$ , the solid curve). It is natural to expect that maximum intensity variations of the sound field, which are caused by IW propagating along the path, occur at the horizons of the interference minima in the vertical distribution  $I$ , because these minima are significantly narrower than the maxima, and the vertical displacements of the pycnocline can lead to wider variations of  $I(z)$  at these depths as compared to the depths corresponding to the relatively smooth interference maxima in  $I(z)$ . The plots of  $\phi(z)$  in Fig. 3 also agree with the measurements illustrated by Fig. 1. The phase of the sound signal decreases as the pycnocline rises to the sea surface.

Let us consider the effect of a sole nonlinear IW on the sound field in more detail. Figure 4 presents the plots of  $\eta_{in}$  and variations of  $I$  and  $\phi$  in the sound field at frequencies of 307, 317, and 327 Hz. This data were obtained at different horizons during the passage of a sole internal wave (IW.1) along the path. The plots show that the effect of IW.1 on the sound field exhibits both frequency and vertical selectivity. The variations of  $I$  are maximum for the interference minima in the distributions  $I(z, \omega)$  (see plot  $I(t)$  for the 317-Hz signal received by the hydrophone P.2). The frequency dependence of the signal phase variations is less pronounced than that of the intensity variations. One can note that the variations of  $\phi$  are nearly in phase at different depths, in agreement with the vertical profiles  $\phi$  (see Fig. 3).

The acoustic path was oriented along the typical propagation direction for short IW in this shelf region of the Sea of Japan [8]. According to Fig. 4, the crest of IW.1 came to the acoustic path at 3.32 a. m. and, as the

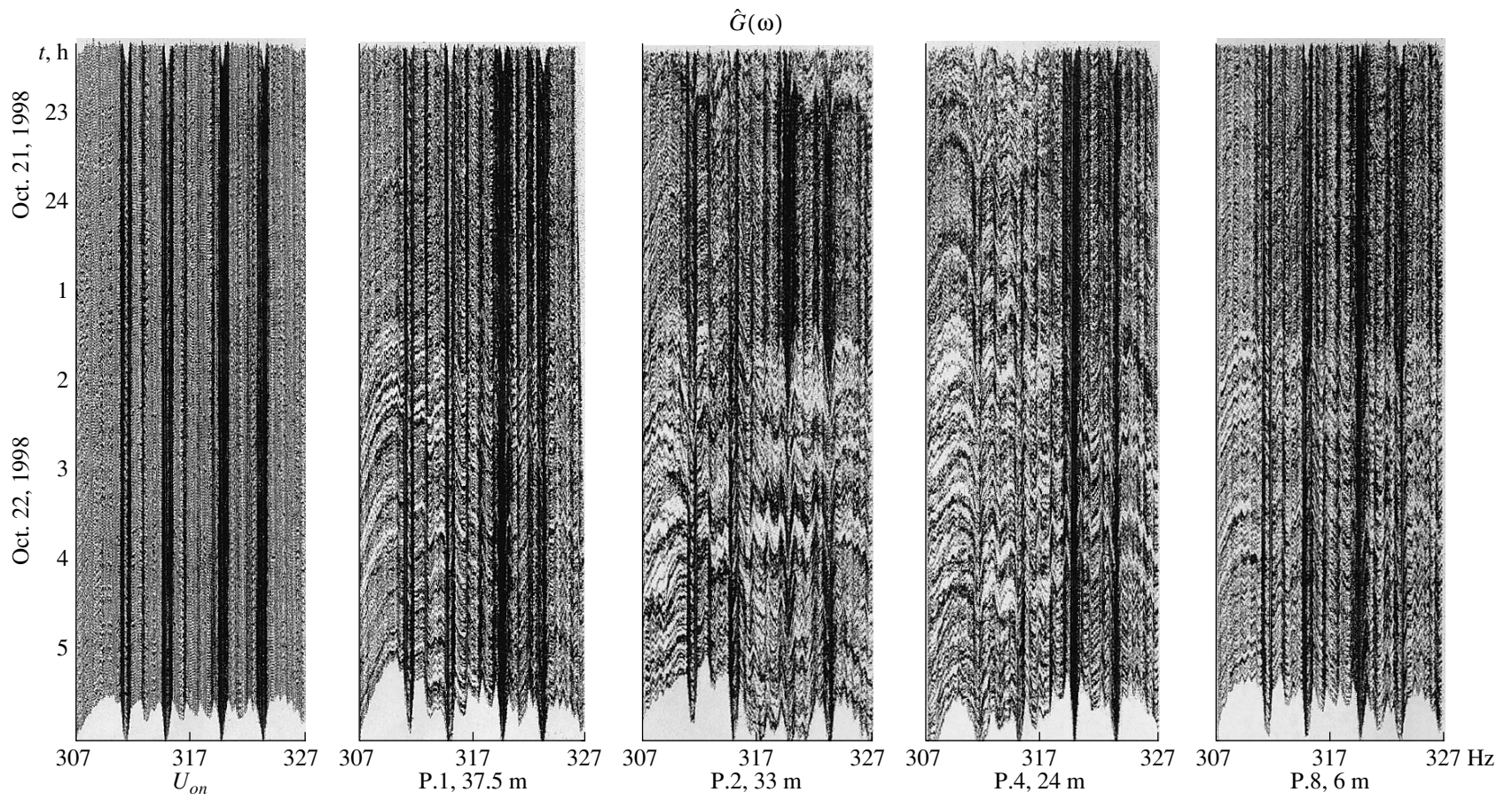


**Fig. 2.** Sonograms  $\hat{G}(\omega)$  for the frequency-modulated sound signals transmitted ( $U_{on}$ ) and received by the hydrophones P.1, P.2, P.4, and P.8 of the MOLLUSK-96 measuring system.

$\varphi(z)$  plots show (in view of the fact that the signal phase decreases as the IW cause the thermocline rise), passed over the sound source at 3.32 a.m. It means that the mean propagation velocity of IW.1 was about 0.22 m/s, which, in view of the sea depth change from 38 m at the observation point to 26 m at transmission one, agrees both with the theory of IW and with the in-sea measurements [8, 9]. Thus, the plots of Fig. 4 quantitatively and qualitatively characterize the changes in the sound field, which are caused by a sole IW propagating along the acoustic path. From the profile  $\eta_{in}$  of IW.1, a spatial scale can be estimated for the sound speed field inhomogeneity that propagates with the phase velocity of the IW:  $\Delta x \approx 140$  m,  $\Delta z \approx 4$  m. The strong influence of IW.1 on the propagation of the sound waves may be explained by their resonant interaction with the “acoustic inhomogeneity” induced by the IW. The table summarizes the results of a numerical experiment carried out with the MOATL [10] computer code for the acoustic path that was similar to that of the in-sea experiment in its geometry and water stratification. The wave num-

bers  $k_n$  and the group velocities  $V_g^{(n)} = \frac{\Delta\omega}{\Delta k_n}$  were calcu-

lated for eight modes of the sound field with the frequency 315 Hz. The calculations were carried out for two cases: without any IW on the path and, with a disturbance with spatial parameters of IW.1 formed in the dependence  $C(x, z)$  of the water layer on the path near the reception point.

The parameters of the propagating sound waves were calculated in the adiabatic approximation, neglecting the mode interaction. Nevertheless, the calculations allow one to obtain quantitative estimates, to explain the variations of the signal phase, which were experimentally observed during the passage of the IW.1 soliton along the path (Fig. 4), and to estimate the possibility for the resonant interaction of the modes [3]. According to the calculations and measurements, we have:  $h_{in} \approx \lambda$ ,  $k_{in} \cong k_1 - k_3 \cong k_2 - k_5$ . Here,  $h_{in}$  is the height of IW.1,  $\lambda$  is the acoustic wavelength,  $k_{in}$  is the wave number of IW.1, and  $k_n$  is the wave number for the  $n$ th acoustic mode. Hence, IW.1 could lead to the resonant interaction of the first acoustic mode with the third one, this interaction being accompanied by the transport of the acoustic energy and changes in the space-frequency interference structure of the sound field at the reception point. The plots of  $I$  shown in Fig. 4 confirm the frequency selectivity (resonance) in the interaction of the sound waves with IW.1. According to the plots P.2 of Fig. 4, the level of the 317-Hz signal decreased on average by 12 dB during the passage of IW.1 over the path, the level of the 307-Hz signal decreased by 4 dB, and that of the 327-Hz signal remained nearly unchanged. The propagation of IW.1 along the acoustic path caused variations of  $\varphi$  (see plots P.1, P.6, and P.8 of Fig. 4 within the time interval bounded by the two vertical

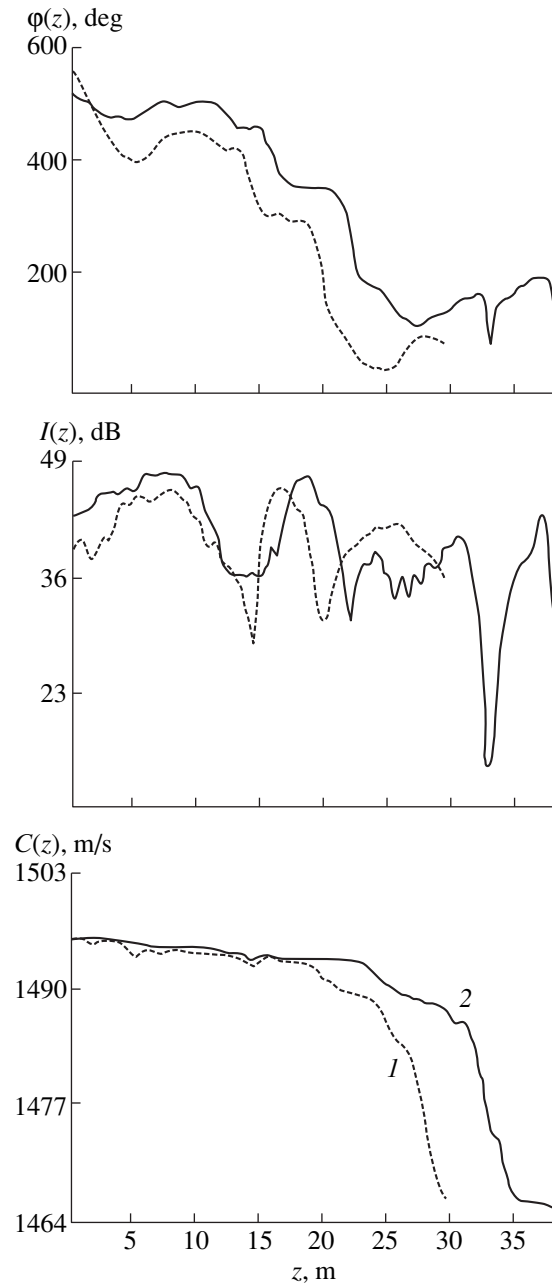


**Fig. 3.** Vertical profiles of the sound speed  $C$ , intensity  $I$ , and phase  $\varphi$  of the acoustic field at the frequency 315 Hz. The measurements of October 21, 1996, with the BURUN-96 probe, at 150 m from the sound source (dashed curves) and near the MOLLUSK-96 (solid curves).

lines). These variations corresponded to a more rapid spread of the acoustic energy, though, on average, more cold water came to the path (see the IW.1 profile in Fig. 4). After IW.1 had passed over the sound source, the signal phases measured at different depths became nearly equal to those observed prior to the passage of IW.1.

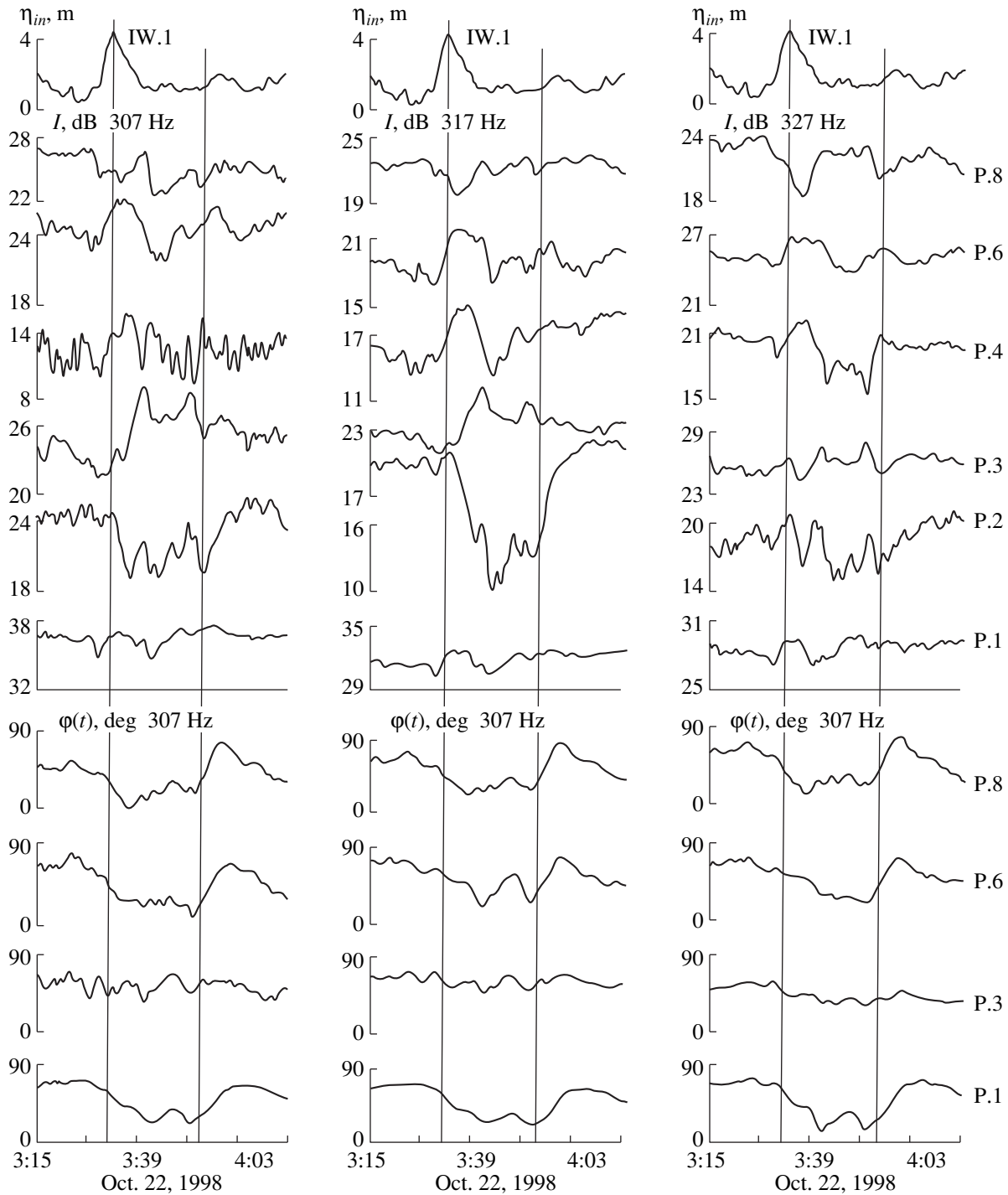


**Fig. 4.** Profile of the IW.1 soliton (curve  $\eta_{in}$ ) propagating along the acoustic path and the variations of the intensity  $I$  and phase  $\varphi$  of the sound field at frequencies of 307, 317, and 327 Hz. The measurements with the MOLLUSK-96 system.

The numerically obtained results summarized in the table agree with the in-sea experiment:  $V_g$  increased for most acoustic modes propagating over the path where IW.1 existed. Note that the maximum velocity  $V_g^{(2)} =$

1486 m/s corresponds to the second mode propagating over the path without IW, while, in the presence of IW.1, the third mode is the fastest ( $V_g^{(3)} = 1485$  m/s) to transport the acoustic energy, and its amplitude could

Table

Mode no.	$k, \text{m}^{-1}$	$V_g, \text{m/s}$	
		without IW	with IW.1
1	1.31	1468	1468
2	1.28	1486	1484
3	1.27	1481	1485
4	1.26	1464	1466
5	1.24	1438	1440
6	1.21	1411	1413
7	1.18	1378	1379
8	1.14	1339	1339

become higher at the expense of the first mode owing to their resonant interaction with IW.1.

#### ACKNOWLEDGMENTS

I am grateful to L. K. Bugaeva for her assistance in the numerical experiment. The work was supported by the Russian Foundation for Basic Research (project no. 96-02-16114).

#### REFERENCES

1. E. F. Orlov and G. A. Sharonov, *Interference of Sound Waves in the Ocean* (Dal'nauka, Vladivostok, 1998).
2. B. G. Katsnel'son and V. G. Petnikov, *Acoustics of Shallow Sea* (Nauka, Vladivostok, 1997).
3. J.-X. Zhou, X.-Z. Zhang, and P. H. Rogers, *J. Acoust. Soc. Am.* **90**, 2042 (1991).
4. D. Tielburger, S. Finette, and S. Wolf, *J. Acoust. Soc. Am.* **101**, 789 (1997).
5. K. V. Konyaev, D. E. Leikin, K. D. Sabinin, *et al.*, *Akust. Zh.* **44**, 476 (1998) [*Acoust. Phys.* **44**, 407 (1998)].
6. L. F. Bondar', A. V. Gritsenko, A. N. Rutenko, *et al.*, in *Proceedings of Brekhovskikh's Advanced-Study School "Ocean Acoustics"* (Geos, Moscow, 1998), pp. 178–182.
7. A. N. Rutenko, *Akust. Zh.* **43**, 98 (1997) [*Acoust. Phys.* **43**, 84 (1997)].
8. A. N. Serebryanyĭ, *Okeanologiya* **25**, 744 (1985).
9. A. N. Rutenko, *Morskoĭ Gidrofiz. Zh.*, No. 3, 58 (1989).
10. J. F. Miller and S. N. Wolf, Technical Report of the Naval Research Laboratory (Washington, 1980).

*Translated by E.A. Kopyl*

# Effect of the Dimensions and Curvature of a Radiating Surface on the Efficiency of Its Noise-Reduction Coating

V. B. Stepanov

Andreev Acoustics Institute, ul. Shvernika 4, Moscow, 117036 Russia

e-mail: bvp@akin.ru

Received February 26, 1999

**Abstract**—The efficiency of a noise-reduction coating [1] consisting of passive oscillators arranged on a vibrating surface is studied in relation to the surface dimensions and curvature. Model calculations performed for plane, cylindrical, and spherical surfaces show that, in the frequency range where the wave dimensions of oscillators do not exceed the half-wavelength of sound in air, the efficiency of the coating remains the same as in the case of a boundless plane surface performing pistonlike vibrations. © 2000 MAIK “Nauka/Interperiodica”.

Earlier, a noise-reduction coating consisting of plane passive oscillators arranged on a radiating surface in a checkerboard pattern was proposed [1]. The period of the pattern  $D$  was less than the sound wavelength in air. Owing to such an arrangement, in the frequency range where the phase shift between the oscillator surfaces and the neighboring free areas is  $\frac{\pi}{2} \leq \theta \leq \frac{3}{2}\pi$ , the

initial surface distribution of vibration is transformed to a periodic one (with the period  $D$ ), which results in a considerable reduction in sound radiation. According to the results of both calculation and experiment, a coating consisting of oscillators of size  $d = D/2 = 0.025$  m on a plane surface of dimensions  $0.7 \times 0.45$  m<sup>2</sup> reduces the radiated power in a given frequency range on average by 6–8 dB in a frequency band of 1.5–2 octaves. This result offers strong possibilities for the practical application of such coatings. In view of the interest taken by many researchers and engineers in the development of new types of sound-absorbing coatings and methods of noise reduction in different structures [2–6], it is worthwhile to study in more detail the efficiency of the proposed coating [1] and to determine its dependence on the dimensions and curvature of the radiating surface.

The sound power was determined by the numerical integration of the intensity  $I = P^2/\rho_0 c_0$  over the surface  $S_1$  of an imaginary hemisphere of radius  $r_1$  with the origin at the center of the radiating surface  $S$  ( $r_1 \gg \lambda_0$ ,  $r_1 \gg A^2/\lambda_0$ , where  $\lambda_0$  is the sound wavelength in air and  $A$  is the maximum dimension of the surface  $S$ ). The pressure  $P$  at the surface  $S_1$  was calculated by the Helmholtz–Huygens formula [7]. For some specific cases of this problem, numerical estimates were performed with the use of the Green’s function taking into account the diffraction and reflection of sound waves at the curved surface of the radiating body. These estimates showed that, owing to the integral nature of the sought-for radi-

ation power, the necessary calculations can be performed in the high-frequency approximation by the Kirchhoff formula:

$$P(M) = \frac{1}{4\pi} \int_S \frac{e^{j\xi_0 r_M}}{r_1} V_S [j\omega \rho_0 (\cos(n, \hat{r}_M) - 1)] dS. \quad (1)$$

Here,  $V_S$  is the distribution of the normal component of the particle velocity over the integration surface  $S$ . This distribution is determined by the particle velocity of the main surface within the free areas between the oscillators and by the particle velocity of the surfaces of the radiating oscillators. The latter velocity is determined from relation (12) of the cited paper [1]:

$$V_{S1} = V_{S0} \left( \cos \tilde{\varphi}_1 - \frac{m_2}{m_1} \tilde{\varphi}_1 \sin \tilde{\varphi}_1 \right), \quad (2)$$

where  $V_{S0}$  is the particle velocity of the main surface at the point corresponding to the geometric center of the oscillator,  $\tilde{\varphi}_1 = \omega h_1 / \tilde{c}_1$  is the wave thickness of the elastic element of the oscillator,  $\tilde{c}_1 = c_1 (1 - j\eta_1/2)$  is the complex velocity of the longitudinal wave,  $m_1 = \rho_1 h_1$  is the surface mass of the elastic element, and  $m_2 = \rho_2 h_2$  is the surface mass of the undeformable plate attached to the element and emitting sound from its outer surface. It was assumed that the elastic element was made of rubber of thickness  $h_1 = 5 \times 10^{-3}$  m ( $\rho_1 = 750$  kg/m<sup>3</sup>,  $c_1 = 46$  m/s, and  $\eta_1 = 0.2$ ), and the relative mass of the plate ( $\rho_2 = 2.7 \times 10^3$  kg/m<sup>3</sup> and  $h_2 = 2 \times 10^{-3}$  m) was  $m_2/m_1 = 1.43$ . In plan, the oscillators and the free areas between them have the form of squares of side  $d$ .

First, we determined the dependences of the coating efficiency on the transverse wave dimension of a single oscillator  $\xi_0 d$  ( $\xi_0 = \omega/c_0$  is the wave number in air) and on the dimensions of the radiating surface. The geometric conditions of an efficient suppression of radiation

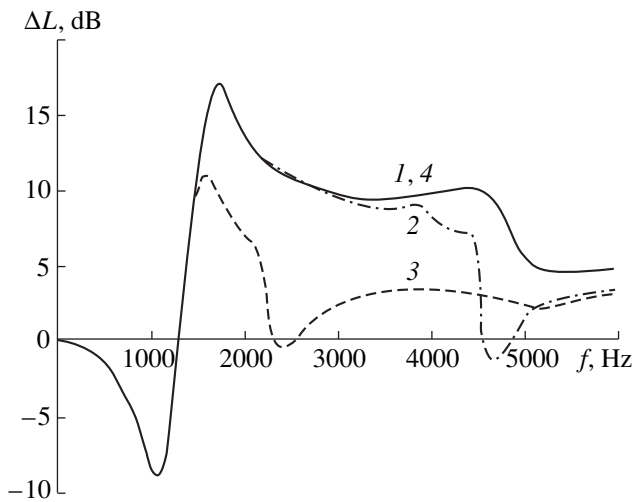


**Fig. 1.** Dependence of the reduction in the radiation power of an oscillating piston of dimensions  $1.4 \times 1.0 \text{ m}^2$  on frequency for different transverse dimensions  $d$  of the oscillators applied to its surface. Curves 1, 2, and 3 correspond to  $d = 0.025, 0.05,$  and  $0.1 \text{ m}$ , respectively. Curve 4 (coincident with curve 1) corresponds to the efficiency of a coating consisting of oscillators with  $d = 0.025 \text{ m}$  on a boundless piston.

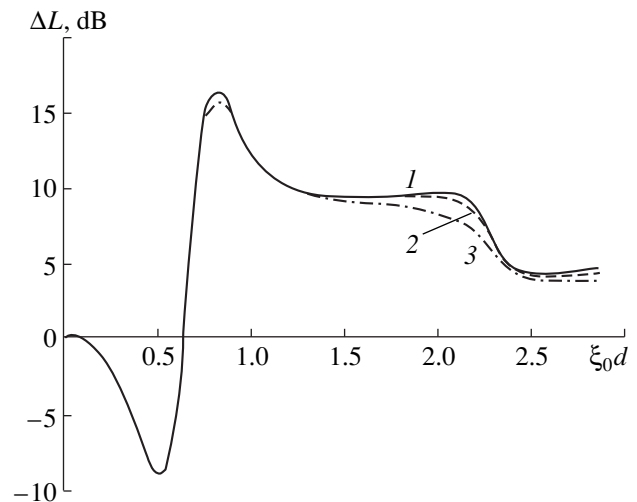


**Fig. 2.** Dependence of the reduction in the radiation power on the wave dimensions of oscillators for different values of the side  $A$  of a square oscillating piston. Curves 1, 2, and 3 correspond to  $A = 1.4, 0.1,$  and  $0.05 \text{ m}$ , respectively. The transverse dimension of the oscillators is in all cases  $d = 0.025 \text{ m}$ ;  $\xi_0$  is the wave number in air.

were obtained analytically in the previous paper [1], and they have the form:  $\xi_0 d \leq \pi$  for a boundless plane surface performing pistonlike vibrations and  $\xi_0 d \ll 1$  for a surface of limited dimensions. In the first case, the calculation was performed for an oscillating plane piston the dimensions of which,  $1.4 \times 1.0 \text{ m}^2$ , far exceeded (by a factor of ten or more) the size  $d$  of the oscillator. Figure 1 shows the frequency characteristics of the coating efficiency expressed in terms of the reduction in the total radiation power of the aforementioned piston for different oscillator dimensions  $d$  (curves 1–3). For comparison, curve 4 shows the efficiency of the coating ( $d = 0.025 \text{ m}$ ) mounted on a boundless surface performing pistonlike vibrations. From the behavior of the curves, one can conclude that, if the condition  $\xi_0 d \approx 2.8\text{--}3.0$  is satisfied, the efficiency of the coating is in all cases the same as that obtained for a boundless piston.

Figure 2 presents the dependence of the efficiency of a coating consisting of oscillators with  $d = 0.025 \text{ m}$  on the wave dimension of the oscillator for different values of the side  $A$  of the square oscillating piston. Even in the case  $A/d = 2$  (curve 3), when only one coating link including an oscillator and an adjacent free area fits into the piston surface along its length and width, the efficiency of the coating for all reasonable values of the oscillator dimensions,  $\xi_0 d < 3.0$ , only slightly (by 1–2 dB) differs from the efficiency at  $A/d = 56$  (curve 1) that is fully coincident with the efficiency of the coating on a boundless piston. The fact that at  $\xi_0 d < 3.0$  the effect of coating does not depend on the dimensions of the radiating surface means that the acoustic interaction between the oscillators and the free

surface areas, i.e., the interaction responsible for the suppression of sound radiation, occurs to the same extent within every pair containing an oscillator and an adjacent free area. This testifies to the pointlike nature of such a pair, which allows a local compensation of the volume velocity of the free area vibration by the antiphase component of the volume velocity of the adjacent oscillator.

Next, we studied the efficiency of the coating in the presence of one-dimensional and two-dimensional radiating distributions of the particle velocity on a plane surface of dimensions  $1.4 \times 1.0 \text{ m}^2$ . The one-dimensional and two-dimensional distributions were set in the form:  $V_{s0} = V_0 \sin \xi_x x e^{-j\omega t}$  ( $\xi_x < \xi_0$ ) and  $V_{s0} = V_0 \sin \xi_x x \sin \xi_y y e^{-j\omega t}$  ( $\xi_x^2 + \xi_y^2 < \xi_0^2$ ), respectively. In the one-dimensional case, the calculations showed that at  $\xi_0 d < 3$  the periodic behavior of the velocity distribution and variations in its scale do not affect the coating efficiency, which is coincident with that obtained for pistonlike surface vibrations. This fact is explained by the constancy of the amplitude and phase of the particle velocity of the surface along the  $y$  axis. Owing to this constancy, the acoustic interaction that occurs in the oscillator–free area pairs oriented in a given direction is of the same magnitude as in the case of the pistonlike surface vibration. In the case of a two-dimensional velocity distribution, a drop in the amplitude of the particle velocity of the main surface occurs at the shoulder  $d$  of every interacting pair, and the magnitude of this drop is different for different pairs. The deviation of the drop for each specific pair from the average drop value obtained for the entire surface determines the differ-

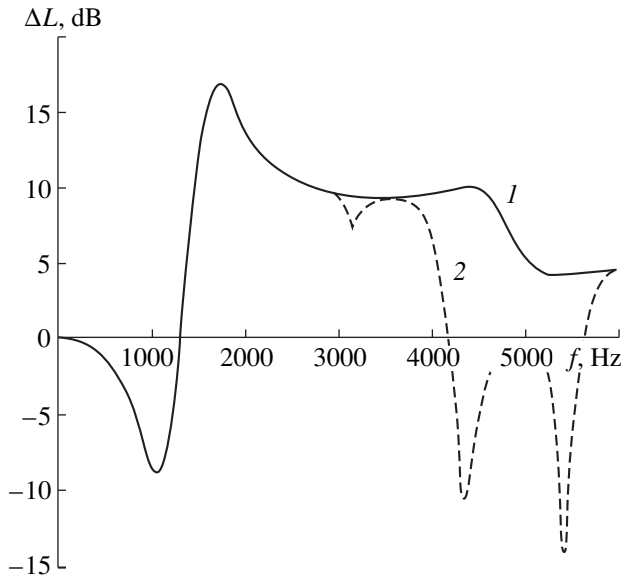


**Fig. 3.** Dependence of the reduction in the radiation power on frequency for the lateral surface of a fluctuating cylinder of height 1 m and radius  $R = 0.22$  m, and for an oscillating flat piston of equal area ( $1.4 \times 1.0$  m<sup>2</sup>). Curve 1 corresponds to the cylinder and the piston with the oscillators of size  $d = 0.025$  m, and curve 2 corresponds to the same cylinder with  $d = 0.05$  m.

ence in the coating effects at the surfaces with a constant (piston) and sinusoidal spatial distributions of the velocity amplitude. The maximum estimate of this difference has the form

$$\Delta L = 20 \log \frac{1 + \frac{\pi^2}{8} \sin \xi_x d \sin \xi_y d}{\cos(\xi_x + \xi_y)d + \sin \xi_x d - \sin \xi_y d}, \quad (3)$$

where the value of  $\Delta L$  does not exceed 2 dB for the oscillator wave dimensions varying within the range  $\xi_{x,y}d \leq \pi/4$ . The results of calculations well agree with this estimate. For example, for  $\xi_0 d < 3$  and  $\xi_{x,y}d \leq \pi/4$ , the coating efficiency is practically the same as in the case of the piston, and it decreases by 1–1.5 dB only when  $\xi_{x,y}d$  approaches  $\pi/4$ . For the radiating components of the velocity distribution, the relation  $\xi_x^2 + \xi_y^2 < \xi_0^2$  is valid. Then, with allowance for the range of reasonable values of the parameters  $\xi_0 d$  and  $\xi_{x,y}d$ , we can expect a result similar to that mentioned above for the case of a surface with an arbitrary spatial distribution of the particle velocity. The experiment described in the previous paper [1] demonstrated a high efficiency of the coating on a flexurally vibrating plate excited in one-third-octave bands of “white noise.”

The dependence of the coating efficiency on the curvature of the radiating surface was determined for a fluctuating cylinder (with nonradiating end-walls) and a sphere. To make the comparison of the results more

convenient, the surface areas of these bodies were taken to be equal to the surface area of a flat piston of dimensions  $1.4 \times 1.0$  m<sup>2</sup>. Therefore, the 1 m-high cylinder had the radius  $R = 0.22$  m, and the sphere had the radius  $R = 0.33$  m. In the first case, the oscillators had the form of squares of side  $d$ , and in the second case, they were spherical quadrangles having the same area and formed by intersecting parallels and meridians. Figure 3 illustrates the relative efficiency of the coating on the cylinder for the oscillator size  $d = 0.025$  and  $0.05$  m ( $R/d \approx 9$  and  $4.4$ , respectively). In the frequency range under study, 0–6000 Hz ( $\xi_0 d \approx 3$ ), the efficiency of the coating consisting of oscillators with  $d = 0.025$  (curve 2) is equal to that of the coating on a boundless piston (curve 1). In the case  $d = 0.05$  m, no difference in the effects of coating is observed up to the frequency 3000 Hz, which also corresponds to the wave dimension of oscillators  $\xi_0 d \approx 3$ . In addition, despite the curvature of the cylinder surface, which adversely affects the conditions of the medium flow around a circle, the coating efficiency close to the limiting one is also retained for the cylinder at  $\xi_0 d > 3$  up to almost 4000 instead of 3000 Hz observed in the case of the piston (curves 2 in Figs. 3 and 1, respectively). This result is explained by the fact that at  $\xi_0 d > 3$  the interacting pair consisting of an oscillator and an adjacent free area cannot be considered as a point. Now, the previous degree of compensation of the volume velocity of free area vibrations can be achieved only when every free area is surrounded by oscillators on all sides, and each oscillator interacts with the free area only through the adjacent part of its surface. In this case, partially uncompensated sources of volume velocity appear along the perimeter of the radiating surface, which leads to a reduction in the coating efficiency. In the case of a piston, the number of such uncompensated sources is greater than in the case of a cylinder, because of the closure of the cylindrical surface in the angular coordinate. Finally, with the same dimensions of oscillators, the efficiency of the coating on a sphere is coincident with that on a boundless piston up to  $\xi_0 d \approx 4$ , which can be explained by the absence of uncompensated vibrating areas owing to the complete closure of the spherical surface.

Thus, the results of this study allow us to conclude that up to the values  $\xi_0 d \approx 3$ ,  $\xi_{x,y}d \approx \pi/4$ , the efficiency of the noise-reduction coating in all cases considered above is the same as in the case of a boundless plane surface performing pistonlike vibrations. Then, to calculate the reduction in the noise radiation power after the application of the proposed coating, it is possible to use formula (4) from the previous paper [1]:

$$\Delta L = 10 \log \frac{4}{\left| 1 + \frac{V_{S1}}{V_{S0}} \right|^2}. \quad (4)$$

Here,  $V_{S1}/V_{S0}$  is the relative particle velocity of the oscillator surface, and this quantity is determined by relation (2).

## REFERENCES

1. V. B. Stepanov, Akust. Zh. **44**, 532 (1998) [Acoust. Phys. **44**, 456 (1998)].
2. V. V. Tyutekin, Akust. Zh. **43**, 681 (1997) [Acoust. Phys. **43**, 589 (1997)].
3. R. N. Viktorova and V. V. Tyutekin, Akust. Zh. **44**, 331 (1998) [Acoust. Phys. **44**, 275 (1998)].
4. N. Atalla, R. Panneton, and J.-F. Allard, Acustica **83**, 891 (1997).
5. G. Maidanik and K. J. Becker, J. Acoust. Soc. Am. **104**, 2628 (1998).
6. Kosuke Nagaya and Lianjin Li, J. Acoust. Soc. Am. **104**, 1466 (1998).
7. L. F. Lependin, *Acoustics* (Vyssh. Shkola, Moscow, 1978).

*Translated by E.M. Golyamina*

# Developments in Indirect Methods for Estimating Fish Target Strength<sup>1</sup>

A. Stepnowski

Technical University of Gdansk, Acoustics Department, 80-952 Gdansk, Poland

E-mail: deans@pg.gda.pl

Received October 15, 1998

**Abstract**—The paper discusses *in situ* indirect methods of fish target strength (TS) estimation in terms of possible improvements in the existing so-called “conventional” methods. In this context, the novel inverse techniques (both iterative and direct)—most recently applied to the problem in question—were not analyzed but only shortly reviewed along with the other indirect techniques. Instead, the emphasis was given to the newly developed extensions of conventional methods. © 2000 MAIK “Nauka/Interperiodica”.

The solution of the problem of TS-estimation requires finding the unknown probability density function (PDF) of target strength from acoustic echoes, which can be estimated by solving so-called “single-beam single target integral equation,” relating PDF’s of echo variable, target strength and beam pattern of the echo sounder transducer. Depending on the domain (logarithmic or absolute values) the equation takes the form of the convolution or Fredholm equation of the first kind which, as was shown, can be represented by so called “Mellin convolution.” Two possible approaches, constituting the extensions in question, were proposed for each domain, viz.: the Characteristic Function Ratio method and the Discrete Mellin Transform method. The target strength PDF’s estimates derived from both methods using simulations were also presented.

## 1. INTRODUCTION

To assess fish population estimates from echo integrator surveys the reliable estimates of the average target strength (TS) or back-scattering cross-section ( $\sigma_{bs}$ ) of individual fish must be known to properly scale an echo integration data to absolute estimates of fish density and hence biomass estimates [6, 8, 24]. Also, these TS-estimates are required to calculate sampled volume of echosounder when using the echo counting technique [13]. Additionally, variations in mean target strength are thought to be among the dominant sources of non-survey errors in acoustic population estimates derived from echo integration [15].

There are three principal approaches to fish target strength estimation [9]:

theoretical,

*ex situ* measures on dead or alive fish under controlled (experimental) conditions,

*in situ* measures on free-swimming fish in their natural habitat.

As it is known [9, 10, 15], TS-data obtained from the theoretical and *ex situ* methods are often not reliable and consistent with *in situ* results as many factors are likely to influence fish target strength (migration, aspect, behaviors, physiological state) and may differ with respect to time and place. Therefore, the measurement of fish target strength *in situ*, is thought to be the most reliable and recommended estimation strategy [6, 12].

Figure 1 shows, that *in situ* methods of TS measurement require removing the effect of unknown random location of fish in the acoustic beam  $b(\theta, \varphi)$  - i.e., beam pattern factor, that can be achieved either directly from each individual echo, or indirectly by processing collections of echoes.

Direct methods are generally more complex and costly than indirect techniques because they require a special configuration of the echo sounder transducer providing multiple beam (dual-, split-, or quasi-ideal-beam) and multi-channel echo sounder receiver [6, 15, 23].

Indirect methods are attractive because they use the same single-beam echo sounder as used for routine echo integration surveys, but they require knowledge of the transducer’s beam pattern and assume uniform distribution of fish in sampled volume of water that might be often not the case [6, 9]. Indirect methods can be either parametric with respect to the target strength probability density function (PDF), or non-parametric [2, 7].

Graphical presentation of the relations between PDF’s of three variables in question (i.e., echo value, beam pattern and target strength) is shown in Fig. 2. In logarithmic domain the measured echo level PDF  $p_E(E)$

<sup>1</sup> This article was submitted by the author in English.

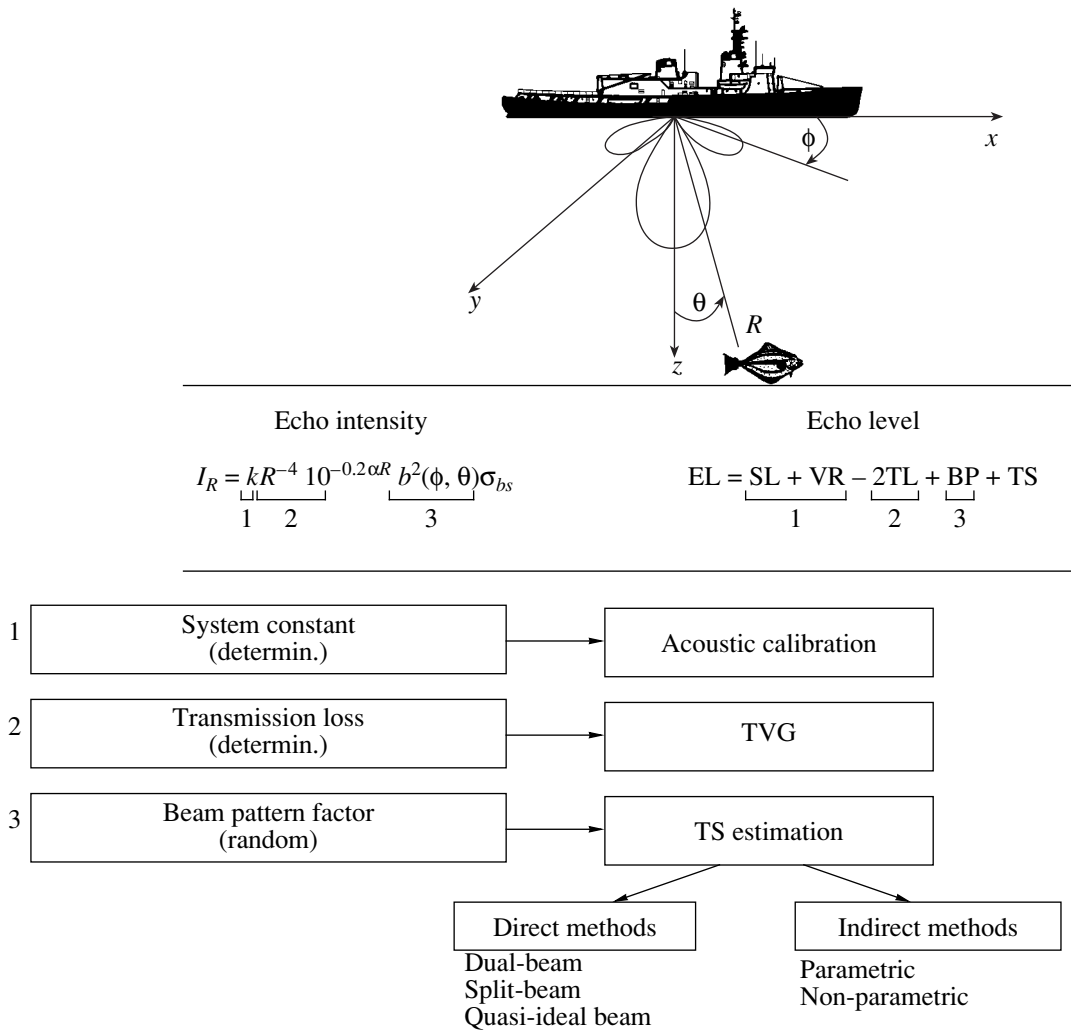


**Fig. 1.** The concept of *in situ* fish target strength estimation by direct and indirect methods in the context of removing of the beam pattern factor.

results from the convolution of  $p_B(B)$  and  $p_{TS}(TS)$  PDF's.

$$p_E(E) = \int_0^\infty p_{TS}(TS)p_B(E - B)dTS. \quad (1)$$

In absolute domain the echo amplitude PDF  $p_e(e)$  is related with beam pattern  $p_b(b)$  and backscattering cross section  $p_\sigma(\sigma_{bs})$  PDF's by a "single-beam" integral equation:

$$p_e(e) = \int_0^\infty p_b(b)p_{\sqrt{\sigma}}(e/b)db/b. \quad (2)$$

Therefore, estimation of target strength PDF from fish echoes requires deconvolution of (1), whereas estimation of the PDF  $\sigma_{BS}$  from fish echoes requires solving of the integral equation (2).

## 2. REVIEW OF EXISTING INDIRECT *IN SITU* TS-ESTIMATION METHODS

### 2.1. Conventional Methods

According to common opinion indirect TS-estimation methods had been introduced by Craig and Forbes [3] who applied statistical correction of the measured echo level PDF to the target strength PDF, using directivity PDF represented by circular areas covered by cross-sections of the beam pattern. Matrix inversion of the set of linear equations obtained in this way leads to the solutions—the TS histogram, often unreliable and strongly dependent on the actual target strength PDF [6, 15].

Ehrenberg was the next who formulated the inverse problem of TS estimation in terms of a Volterra integral equation of the first kind and used an *n*th-degree polynomial approximation to solve it for the unknown  $\sigma_{bs}$  PDF [6]. The unknown polynomial coefficients were

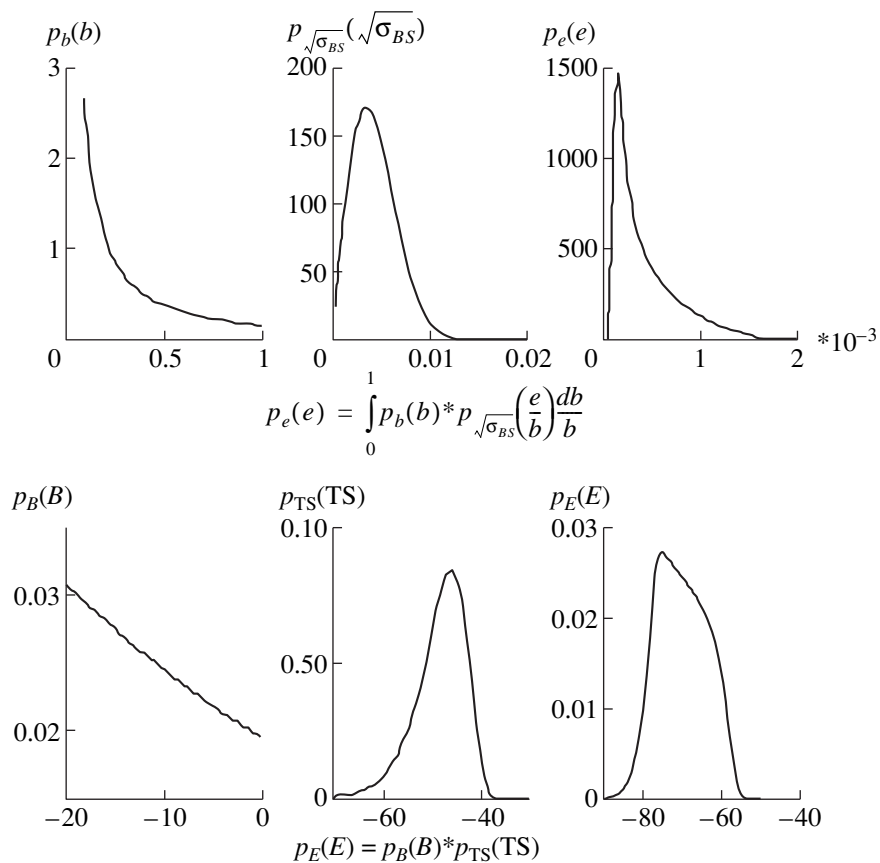


**Fig. 2.** Typical form of beam pattern PDF, target strength PDF and echo PDF in (a, b, c) absolute and (d, e, f). Logarithmic domain.

evaluated simultaneously by a least square fit. The drawback of the method is its ability to generate ill-conditioned simultaneous equations for the higher degree polynomials.

This method was modified by Robinson [21] by subdividing the  $p(\sigma_{bs})$  estimate space into a number of sub-intervals and fits low order polynomials (of  $n < 3$ ) to the unknown  $\sigma_{bs}$  PDF. For the actual PDF's with a larger standard deviation ( $>2.5$  dB) the simultaneous equations to be solved may become ill-conditioned, as in the Ehrenberg method, which may result in underestimating the mean target strength [21]. Robinson also found that within his method, modal artifacts are possible due to fitting multiple cubics.

Petersen and Clay [2] introduced parametric method, further modified by Ehrenberg, by using the Rayleigh distribution to model the unknown  $p(\sigma_{bs})$  PDF. The technique adjusts the unknown parameter in the Rayleigh distribution until this theoretical echo amplitude PDF and measured histogram show closest possible agreement. However, these techniques should only be employed when the Rayleigh-distributed on-axis amplitude holds. Ehrenberg [7] derived a general expression for the beam pattern factor PDF, further developed by Moszynski [19], and noted that the Ray-

leigh model is valid only for fish length to a wavelength ratio greater than 25. Clay and Heist [2] found that two-parameter Rice PDF was justified and that both fish activity and length condition the Rice parameters.

Lindem [14] modified Craig and Forbes' method by setting all negative estimates to zero. He also correlated fish length with modes in the indirect estimates.

Clay [1] formulated Craig and Forbes' method in terms of deconvolution of PDF's. The "single-beam" integral equation was first formulated in terms of voltages and converted to a convolution integral by a change of variables. The numerical deconvolution has been implemented using the Z-transform polynomial long division. However, the deconvolution of actual data demonstrates oscillations and drifts in the results, especially for small echo amplitudes and low signal-to-noise ratio.

Miinalainen and Eronen [17] used a least-squares method, but concluded that the use of non-negative least squares for deconvolution was too time consuming and subject to noise. Therefore, they used a modified singular value decomposition (SVD) routine in which all negative values in the solution were converted to zeros.

Rudstam *et al.* [22] used Clay's deconvolution with Rice PDFs fitted *a posteriori* to estimate fish target

strength and density. The use of Rician PDF is questionable because bumpiness in deconvolved data could be artifactual, but not the result of a combination of Ricians (fitted for fish size groups).

Although deconvolution and related conventional techniques often suffer from modal artifacts, (which may be treated as a result of data undersampling) if large sample sizes are provided, they offer better estimates as negative values of estimates are then largely avoided. On the other hand, *a posteriori* techniques and parametric techniques presume knowledge of the fish scattering model, which may not be available. Therefore, they can be over-constrained by the target strength PDF model and thus are not robust.

## 2.2. Novel Inverse Techniques Applied to Target Strength Estimation

A class of inverse techniques, both iterative and direct, recently applied for fish target strength estimation is partly avoid of the problems of ill-conditioned equations and matrix inversion, which deconvolution and other conventional methods reviewed so far suffer from. These techniques have been initiated by Hedgepeth [12], who introduced the so-called Expectation, Maximization and Smoothing–EMS methods. Some other techniques introduced recently are: Regularization [18, 28], Windowed Singular Value Decomposition (WSVD) [11, 18], and Wavelet Decomposition [5, 26].

**Expectation, Maximization and Smoothing (EMS)** performs its three-step iterative procedure on the “single-beam” integral equation (1) transformed to a linear matrix equation:  $z = \mathbf{Kx}$ . In the first step the statistics of  $z(x)$  is estimated as a conditional expectation. Second step calculates the maximum likelihood estimates. The last, third step in every iteration, smoothes solution  $x$  using Gaussian kernel with locally weighted end points. The EMS constrains estimates to be positive and reduces the time needed to converge by smoothing groups of estimates per iteration [12].

**Regularization method** deals with the considered linear inverse problems in terms of the reconstruction of an unknown function  $f(\cdot)$  (*target strength PDF*) out of the observed function  $z(\cdot)$  (*echo PDF*). Thus, the “single-beam” integral equation can be transformed to a linear operator equation:  $z(u) = (Kf)(u) + n(u)$ , where  $K$  is the linear operator (beam pattern PDF matrix).

One way to solve this problem is to apply square regularization introduced by Tichonov *et al.* [28], according to which the solution estimate (target strength PDF estimate vector) is obtained as:  $\hat{f}_\lambda = (K^*K + \lambda I)^{-1}K^*z$ , where  $I$  identity matrix,  $K^*$  transpose of matrix  $K$ ,  $\lambda$  regularization parameter,  $z$  vector of the echo PDF, [26].

**Singular Value Decomposition (SVD)** as applied to solution of ill-posed problems substitute a simple operator inversion  $K^{-1}$  by the so-called “pseudo-inverse” operator  $(K^*K)^{-1}K^*$ , which leads to obtaining a pseudo-inverse matrix which guarantees a solution with a minimum mean-square error [16]. If the product  $K^*K$  is a linear operator, and if none of its singular values approximate zero, which is obtained by adequate introduction of the weights, so that dividing by elements close to zero does not impact the stability of the solution, the so-called Windowed SVD is obtained. The simplest selection of weights is to assume  $w_\nu = 1$  for small indexes  $\nu$  and  $w_\nu = 0$  for large  $\nu$ .

**Wavelet Decomposition** avoids the oscillations in SVD estimates, which are inherent to *sine/cosine* eigenfunctions of linear operators, by using other orthonormal function sets that guarantee better approximation with a smaller numbers of nonzero coefficients. Wavelets are dilations and translations of certain function, called mother wavelet [5]:

$$\psi_{j,k} = 2^{j/2}\psi(2^j t - k).$$

Wavelet expansion of  $Kf$  is obtained as [26]:

$$Kf = \sum_j \sum_k d_{j,k} \psi_{j,k} = \sum_j \sum_k [Kf, \psi_{j,k}] \psi_{j,k},$$

which leads to the estimate of the unknown function  $f$ :

$$\hat{f} = \sum_j \sum_k \delta_\lambda([z, \psi_{j,k}]) K^{-1} \psi_{j,k}$$

where the product  $[y, \psi_{j,k}]$  has a sense of estimates  $\hat{d}_{j,k}$  of wavelets coefficients  $d_{j,k}$ .

## 3. EXTENSION OF THE CONVENTIONAL TS-ESTIMATION METHODS

### 3.1. Characteristic Functions Ratio Method

**3.1.1. Logarithmic values domain (TS).** Characteristic function of random variable  $x$  represents the Fourier transform (with reversed sign) of its PDF  $p(x)$ :

$$\varphi_x(\omega) = E\{e^{j\omega x}\} = \int_{-\infty}^{+\infty} e^{j\omega x} p(x) dx. \quad (3)$$

The sum of two random variables  $z = x + y$  gives the product:

$$\varphi_z(t) = \varphi_x(t)\varphi_y(t). \quad (4)$$

Consequently, the unknown PDF of fish target strength can be expressed by the inverse Fourier transform of the ratio of characteristic functions of known PDF's in question:

$$p_{TS}(x - K) = \mathcal{F}^{-1} \left\{ \frac{\varphi_E(\cdot)}{\varphi_B(\cdot)} \right\}. \quad (5)$$

To avoid division by zero, the Fourier-Wiener [20] method can be used:

$$p_{TS}(x - K) = \mathbf{F}^{-1} \left\{ \frac{\Phi_E(\cdot)\Phi_B^*(\cdot)}{|\Phi(\cdot)|^2 + p} \right\}, \quad p \approx 10^{-5}. \quad (6)$$

Equation (6) can be also treated as a simple form of the regularization procedure, where  $p$  is the regularization parameter.

**3.1.2. Absolute values domain ( $\sigma_{bs}$ ).** Characteristic function of the product of two random variables  $z = xy$  can be expressed as:

$$\varphi_z(\omega) = \int_{-\infty}^{+\infty} e^{j\omega x} \left[ \int_{-\infty}^{+\infty} \frac{1}{\tau} p_x(\tau) p_y\left(\frac{t}{\tau}\right) d\tau \right] dx. \quad (7)$$

After changing the integration order and substituting the variable,  $u = t/\tau$  (7) can be rewritten as

$$\varphi_z(\omega) = \int_{-\infty}^{+\infty} \frac{1}{\tau} p_x(\tau) \left[ \int_{-\infty}^{+\infty} e^{j\omega\tau u} p_y(u) \tau du \right] d\tau \quad (8)$$

that can be further reduced to the form:

$$\varphi_z(\omega) = \int_{-\infty}^{+\infty} p_x(\tau) \varphi_y(\omega\tau) d\tau, \quad (9)$$

where  $p_x(\cdot)$  represents PDF of the unknown random variable ( $\sigma_{bs}$ ),  $\varphi_z$  and  $\varphi_y$  are characteristic functions of the known variables, beam pattern ( $b$ ) and echo ( $e$ ).

The discrete form of (9) can be written as:

$$\varphi_z(i) = \sum_n \varphi_y(ni) p_x(n), \quad (10)$$

which leads to the matrix equation:

$$\begin{bmatrix} \vdots \\ \varphi_z(-2) \\ \varphi_z(-1) \\ \varphi_z(0) \\ \varphi_z(1) \\ \varphi_z(2) \\ \vdots \end{bmatrix}$$

$$= \begin{bmatrix} \ddots & \vdots & \vdots & \vdots & \vdots & \vdots & \ddots \\ \dots & \ddots & \varphi_y(2) & \varphi_y(0) & \varphi_y(-2) & \ddots & \dots \\ \dots & \varphi_y(2) & \varphi_y(1) & \varphi_y(0) & \varphi_y(-1) & \varphi_y(-2) & \dots \\ \dots & \varphi_y(0) & \varphi_y(0) & \varphi_y(0) & \varphi_y(0) & \varphi_y(0) & \dots \\ \dots & \varphi_y(-2) & \varphi_y(-1) & \varphi_y(0) & \varphi_y(1) & \varphi_y(2) & \dots \\ \dots & \ddots & \varphi_y(-2) & \varphi_y(0) & \varphi_y(2) & \varphi_y(4) & \dots \\ \ddots & \vdots & \vdots & \vdots & \vdots & \vdots & \ddots \end{bmatrix} \times \begin{bmatrix} \vdots \\ p_x(-2) \\ p_x(-1) \\ p_x(0) \\ p_x(1) \\ p_x(2) \\ \vdots \end{bmatrix}. \quad (11)$$

Equation (11) can be reduced to following a form confined to the part of non-negative indices as the domain of actual PDF's of the echo and beam pattern variables is the non-negative numbers set.

$$\begin{bmatrix} \varphi_z(0) \\ \varphi_z(1) \\ \varphi_z(2) \\ \vdots \end{bmatrix} = \begin{bmatrix} \varphi_y(0) & \varphi_y(0) & \varphi_y(0) & \dots \\ \varphi_y(0) & \varphi_y(1) & \varphi_y(2) & \dots \\ \varphi_y(0) & \varphi_y(2) & \varphi_y(4) & \dots \\ \vdots & \vdots & \vdots & \ddots \end{bmatrix} \begin{bmatrix} p_x(0) \\ p_x(1) \\ p_x(2) \\ \vdots \end{bmatrix}. \quad (12)$$

The unknown PDF estimate can be obtained by the matrix  $\Phi_y$  inversion

$$\hat{p}_{\sqrt{\sigma_{BS}}} = \Phi_b^{-1} \varphi_e, \quad (13)$$

where the  $\Phi_b$  matrix is the characteristic function of beam pattern PDF, and the  $\varphi_e$  vector is the characteristic function of echo PDF.

$\Phi_b$  is the sparse matrix due to decreasing number of non-zero elements in successive rows. This fact implies singular features of the matrix and undesirable information reduction in the successive elements of the output vector ( $\varphi_e$ ). As a remedy the oversampling of data in characteristic function domain (by substantial zero padding in PDF domain) can be applied. Figure 3 shows characteristic functions of random variables in question ( $b$ ,  $\sigma_{bs}$ ,  $e$ ) - corresponding to their PDFs from Fig. 2.

### 3.2. Discrete Mellin Transform (DMT) Method

Estimation of the backscattering cross-section  $\sigma_{bs}$  from fish echoes requires solving a "single-beam" inte-

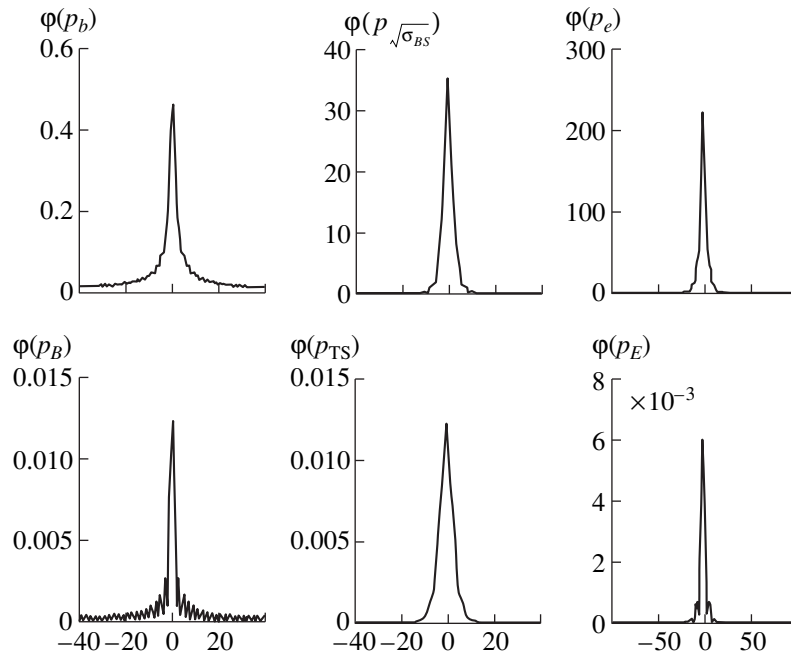


**Fig. 3.** Characteristic functions of random variables  $b$ ,  $\sigma_{BS}$ ,  $e$ , and their equivalents in decibels ( $B$ ,  $TS$ ,  $E$ ) as Fourier transforms of their PDF's from Fig. 2.

gral equation (2) which represents the PDF of echo expressed as the product of two random variables  $z = \underline{x} \underline{y}$ :

$$f_z(z) = \int_0^\infty f_z(z/x) f_y(x) dx/x. \quad (14)$$

Equation (14) rewritten for acoustic variable ( $e = b\sqrt{\sigma_{BS}}$ ) comes down to a pair of equations:

$$p_e(z) = \int_0^1 p_{\sqrt{\sigma_{BS}}}(z/x) p_b(x) dx \quad (15a)$$

or

$$p_e(z) = \int_0^\infty p_b(z/x) p_{\sqrt{\sigma_{BS}}}(x) dx/x, \quad (15b)$$

which can be solved with the use of the Mellin transform defined as [18]:

$$F(s) = \mathcal{M}\{f(t)\} = \int_0^\infty f(t) t^{s-1} dt, \quad s = \sigma + j\tau, \quad (16a)$$

$$f(t) = \mathcal{M}^{-1}\{F(s)\} = \frac{1}{2\pi j} \int_{\sigma - j\infty}^{\sigma + j\infty} F(s) t^{-s} ds. \quad (16b)$$

In the domain of the Mellin transform, (14) takes the form of a transforms product:

$$F_Z(s) = F_X(s) F_Y(s), \quad (17)$$

which leads to the solution of (14) in the form:

$$f_x(x) = \mathcal{M}^{-1}[\mathcal{M}\{f_z(z)\} / \mathcal{M}\{f_y(y)\}]. \quad (18)$$

Due to the analogy with the convolution integral, which for the Fourier transforms corresponds to the transforms product, the integral (14) was called the ‘‘Mellin convolution’’ which in the domain of the PDF's can be written as:

$$f_z(z) = f_x(x) *_M f_y(t) = \int_0^\infty f_x(x) f_y(z/y) dx/x, \quad (19)$$

where the asterisk symbol  $_M^*$  marks ‘‘Mellin convolution’’ as defined by (19).

Numerical computations of Mellin transform by FFT algorithms [18] leads to a non-uniform sampling of PDF's. The problem can be avoided if we notice that the direct Mellin transform resembles the formula for moments of PDF. Hence, if  $f(x)$  represents the PDF of a random variable taking positive values and the complex variable  $s$  belongs to the set of natural numbers  $s \in \{N\}$ ,

then the Mellin transform represents a series of moments: of the random variable  $x$ :

$$F(s) = \int_0^{\infty} x^{s-1} f(x) dx = m_{s-1}. \quad (20)$$

In the case of discrete random variables, the system of equations can be generalized by introducing a discrete Mellin transform (DMT), which on the real positive semi-axis represents a sampled continuous Mellin transform. Hence we have:

$$F(n) = \sum_{i=1}^N x_i^{n-1} f(x_i). \quad (21)$$

On the other hand, the same moments of the random variable  $x$  can be computed with the use of the mean value estimator for realizing the random variable:

$$m_n = \frac{1}{N} \sum_{i=1}^N x_i^n. \quad (22)$$

Considering the formula (18) and treating the moments as discrete Mellin transforms, we obtain the

relation, which links the moments of the three variables in question:

$$\mathbf{m}_x = \frac{\mathbf{m}_z}{\mathbf{m}_y}, \quad (23)$$

where  $\mathbf{m}_z$  represents a series of moments of the measured echo amplitude (“off-axis” voltage), which can be computed using the estimates given in (22). The series  $\mathbf{m}_y$  represents the moments of the beam pattern PDF, and can be obtained with the use of the DMT. The result of dividing the above moments gives the first solution stage, which is knowledge of moments  $\mathbf{m}_x$  of the unknown backscattering cross-section (“on-axis” voltage).

Figure 4 illustrates the described concept of using the Mellin Transform, along with statistical moments of random variable  $\sigma_{bs}$  as applied to the estimation of its PDF. The presented 2D plot of Mellin transform on a complex plane  $s = \alpha + j\beta$  refers to the Rayleigh PDF of the parameter  $\sigma = 0.5$ . Note that the zero- and first-order moments of the considered PDF are represented by samples of the Mellin Transform plot at  $\alpha = 1$  and  $\alpha = 2$ , respectively.

In the second (inverse transform) stage, the unknown PDF estimate is reconstructed from moments. Consider-

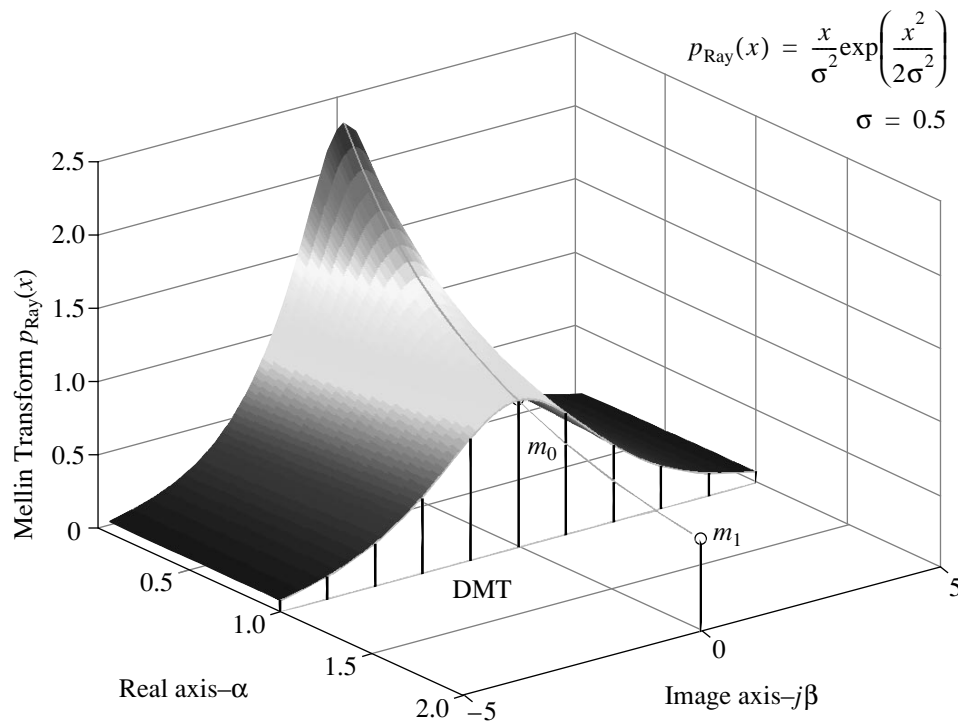


Fig. 4. Discrete Mellin Transform of Rayleigh PDF and interpretation of its moments.

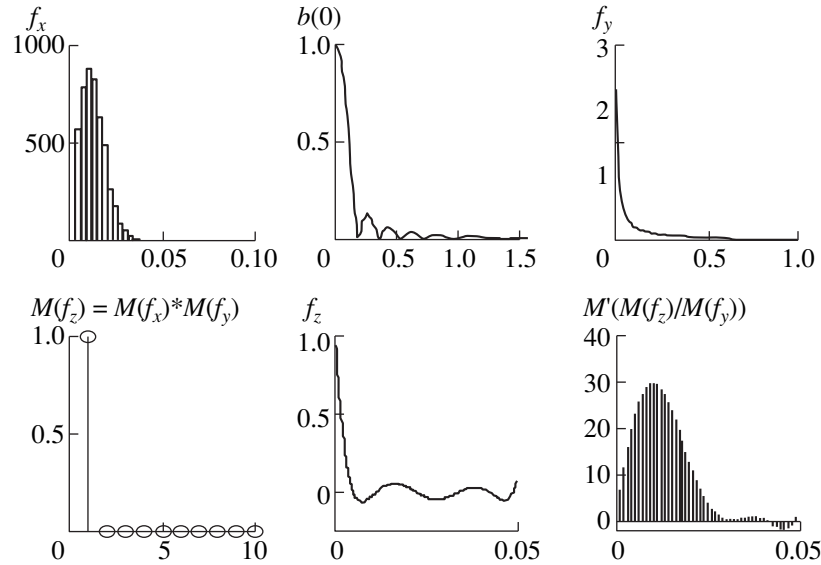


Fig. 5. Reconstruction of the Rayleigh PDF using Discrete Mellin Transform and SVD with a matrix pseudo-inversion.

ing the definition of moments of the discrete random variable:

$$m_v = \sum_{i=1}^N x_i^v P(x_i), \quad (24)$$

this problem requires solving Vandermonde's matrix equation:

$$\begin{bmatrix} 1 & 1 & 1 & \dots & 1 \\ x_1 & x_2 & x_3 & \dots & x_m \\ x_1^2 & x_2^2 & x_3^2 & \dots & x_m^2 \\ \dots & \dots & \dots & \dots & \dots \\ x_1^n & x_2^n & x_3^n & \dots & x_m^n \end{bmatrix} \begin{bmatrix} P_x(x_1) \\ P_x(x_2) \\ P_x(x_3) \\ \dots \\ P_x(x_m) \end{bmatrix} = \begin{bmatrix} m_{0,x} \\ m_{1,x} \\ m_{2,x} \\ \dots \\ m_{n,x} \end{bmatrix}, \quad (25)$$

in which  $\mathbf{m}_x$  is the moment estimates of unknown PDF,  $x_j$  are the predicted centers of the histogram bins,  $P_x(x_i)$  – estimates of unknown PDF. The matrix (25) is ill conditioned because the matrix on the left side of the equation generally does not have to be a square matrix and both the Gaussian elimination method and the LU decomposition give incorrect solutions [18]. One method of solving this problem is application of the singular value decomposition SVD that leads to obtaining a pseudo-inverse matrix that guarantees a solution with a minimum mean-square error. By writing (25) in the general matrix form:

$$\mathbf{Xp} = \mathbf{m} \quad (26)$$

we can get the solution

$$\mathbf{p} = \mathbf{X}^\# \mathbf{m}, \quad (27)$$

where matrix  $\mathbf{X}^\#$  is a pseudo-inverse matrix computed numerically using the SVD algorithm:

$$\begin{aligned} \mathbf{X} &= \mathbf{USV}^T = [\mathbf{U}]\text{diag}(s_i)[\mathbf{V}^T] \\ \mathbf{X}^\# &= \mathbf{US}^{-1}\mathbf{V}^T = [\mathbf{U}]\text{diag}(1/s_i)[\mathbf{V}^T], \end{aligned} \quad (28)$$

in which the matrices  $\mathbf{U}$ ,  $\mathbf{V}$  are orthonormal, and the diagonal matrix  $\mathbf{S}$  represents the singular values of matrix  $\mathbf{X}$ . Equation (27) simultaneously represents the matrix form of an inverse discrete Mellin transform, optimal in the sense of minimizing the mean-square error.

#### 4. RESULTS

Due to the singular features of the beam pattern characteristic function matrix (sparse matrix, see Section 3.1.2), the estimates of target strength PDF obtained from the Characteristic Function Ratio method can be unreliable and inaccurate [18]. Due to these reasons the following results are confined only to the second of the considered methods, viz., the Discrete Mellin Transform along with SVD.

Figure 5 shows the simulation results of testing the performance of the DMT as applied to estimation of  $\sigma_{bs}$  PDF. In the experiment, the Rayleigh pseudo-random generated histogram was used as an estimate of  $\sigma_{bs}$  PDF. Function  $f_z$  obtained as the result of ‘‘Mellin convolution’’ contains visible effects of an inverse Mellin transform calculated with the use of a pseudo-inverse matrix. On the other hand, the last plot in Fig. 5, showing a reconstruction of the original PDF, demonstrates slight artefactual modes or oscillations, which appeared for a larger estimate values region, but it also demonstrates the smoothing character of the operation [18],

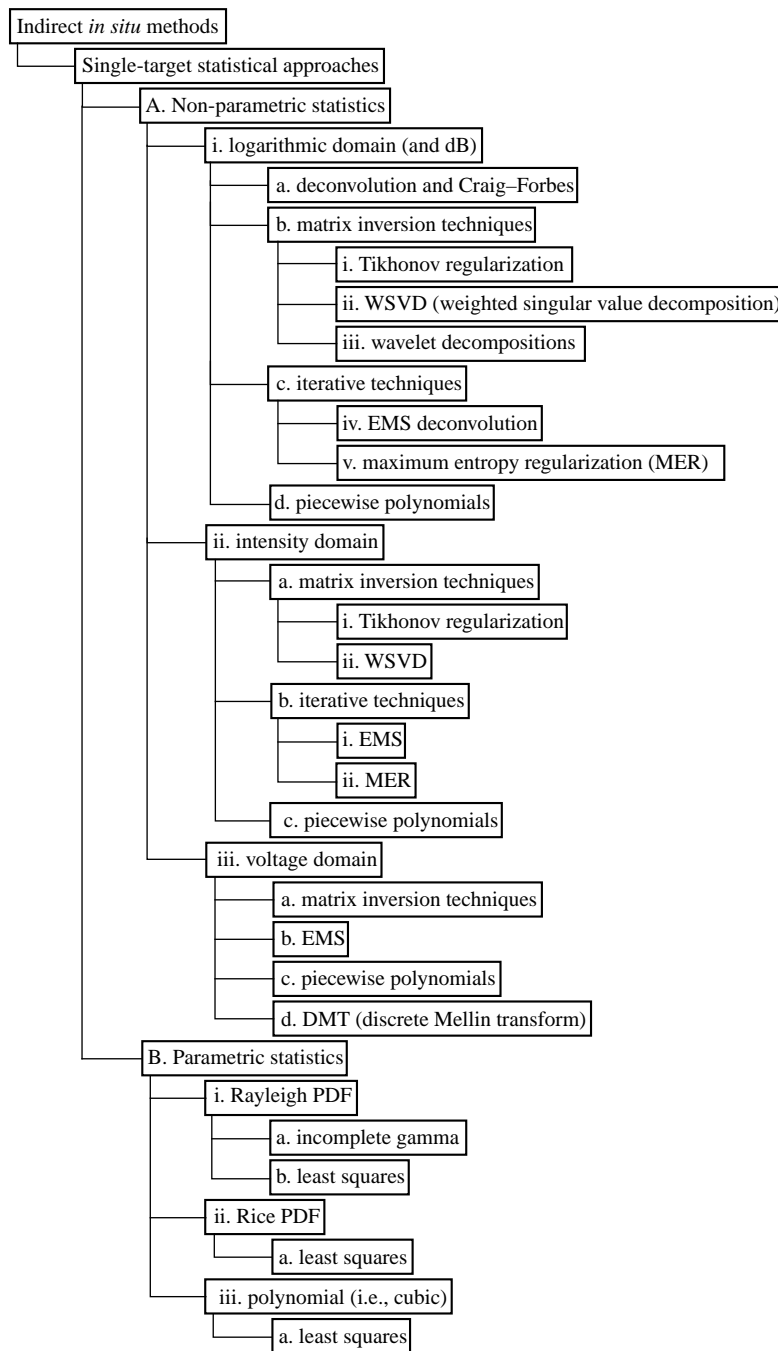


Fig. 6. Revised classification scheme of indirect *in situ* target strength estimation methods.

and correct location of the main modal value of the estimated PDF's.

In the simulation, the approximation of the main-lobe beam pattern was used as presented in [19]:

$$b(\theta) = \left( 1 - (1 - 2^{-\gamma}) \frac{(1 - \cos \theta)}{1 - \cos \theta_{3dB}} \right)^{\frac{1}{\gamma}}. \quad (29)$$

The exponential coefficient  $\gamma$  was fitted to be equal  $-0.1$ , which allows one to derive from (29) the following approximation of beam pattern PDF:

$$p_b(b) = \frac{k}{b^{1-\gamma}}, \quad (30)$$

where  $k$  is the normalization constant.

Equation (30) allows for the construction of the beam pattern PDF matrix to be a kernel of linear equation (19) in question.

## 5. CONCLUSIONS

The analysis of the performance of the recently developed state-of-the-art inverse techniques for fish target strength estimation as compared to the conventional methods was carried out by the author of this paper in [25] and [26], using the TS-PDF's estimates obtained as well from the experimental data (acoustic surveys) as from simulations. This comparison shows the apparent improvement achieved by introducing the novel methods, which come, however, at the cost of using much more sophisticated and complex computational techniques.

On the other hand, as it was shown in this paper, some improvements in extending the conventional indirect methods of fish TS-estimation, such as the application of the Discrete Mellin Transform with SVD or characteristic function ratio method are still possible. These, and other potential methods, may result in relatively easy obtaining reliable TS-estimates quite easily, without having to introduce demanding and elaborated inverse techniques.

To conclude this paper, some revisions of the target strength estimation methods classification scheme, as introduced by Foote [9], is proposed in order to include the two methods introduced in the paper, along with the discussed newly developed inverse techniques. The primary changes included in refer to:

(1) addition of the DMT (Discrete Mellin Transform) method to the voltage domain,

(2) placement of MER (maximum entropy regularization) along with the EMS method, labeled by the author as *iterative methods* in a logarithmic domain,

(3) addition of the WSVD (windowed singular value decomposition) method to matrix inversion as a subclass,

(4) addition of the Wavelet Decomposition method to the same class of matrix inversion. Other changes generally follow Hedgepeth's [12] suggestions and include the addition of the voltage domain, the inclusion of Craig-Forbes and deconvolution in the same sub-section, and the possibility of fitting the Rice PDF in parametric estimation (as opposed to *a posteriori*).

## ACKNOWLEDGMENTS

The author wishes to express his thanks to Dr. Marek Moszynski for his assistance and simulations, without which this paper would not have been possible.

## REFERENCES

1. C. S. Clay, *J. Acoust. Soc. Am.* **73**, 1989 (1983).
2. C. S. Clay and B. G. Heist, *J. Acoust. Soc. Am.* **75**, 1077 (1984).
3. R. E. Craig and S. T. Forbes, *Fiskeridir. Skr., Ser. Havunders.* **15**, 210 (1969).
4. P. H. Dahl and O. A. Mathisen, *J. Acoust. Soc. Am.* **73**, 1205 (1983).
5. D. L. Donoho, I. M. Johnstone, G. Kerkycharian, *et al.*, *Ann. Stat.* **24** (2), 508 (1996).
6. J. E. Ehrenberg, in *Proceedings of ICES/FAO Symposium on Fisheries Acoustics, Bergen, 1982*, Art. no. 104.
7. J. E. Ehrenberg, *FAO Fisheries Reports* **300**, 91 (1982).
8. K. G. Foote, *J. Acoust. Soc. Am.* **82**, 981 (1987).
9. K. G. Foote, *ICES J. Mar. Sci.* **48**, 211 (1991).
10. G. L. Goddard and V. G. Welsby, *Rapp. P.-V. Reun. Cons. Int.: Explor. Mer. (CIEM)* **170**, 70 (1977).
11. P. C. Hansen, *Inverse Problems* **8**, 849 (1992).
12. J. B. Hedgepeth, PhD Dissertation (University of Washington, Seattle, WA, 1994).
13. R. Kieser and J. E. Ehrenberg, *Rep. at Procees Verbaux des Reun. Du Cons. Int. Pour l'Explor. de la Mer.* **189**, 65 (1990).
14. T. Lindem, *FAO Fish. Report* **300**, 104 (1983).
15. D. N. MacLennan and E. J. Simmonds, *Fisheries Acoustics* (Chapman and Hall, London, 1992).
16. S. L. Marple, *Digital Spectral Analysis* (Prentice-Hall, New York, 1987).
17. O. H. J. Miinalainen and T. Eronen, *Rapp. P.-V. Reun. Cons. Int. Explor. Mer.* **189**, 312 (1990).
18. M. Moszynski, PhD Dissertation (in Polish) (Technical University of Gdansk, 1997).
19. M. Moszynski and A. Stepnowski, in *Proceedings of the International EAA/FASE Symposium on Hydroacoustics, Gdansk-Jurata, 1997*, pp. 31–36.
20. S. J. Orfanidis, *Optimum Signal Processing* (Macmillan, New York, 1985).
21. B. J. Robinson, *FAO Fish. Rep.* **300**, 99 (1983).
22. L. G. Rudstam, C. S. Clay, and J. J. Magnuson, *Can. J. Fish. Aquat. Sci.* **44**, 811 (1987).
23. A. Stepnowski and R. S. Mitchell, *Ultrasonics* **28**, 256 (1990).
24. A. Stepnowski, A. C. Gucu, and F. Bingel, *Arch. Acoust.* **18**, 83 (1993).
25. A. Stepnowski, in *Proceedings of the International EAA/FASE Symposium on Hydroacoustics, Gdańsk-Jurata, 1997*, pp. 15–26.
26. A. Stepnowski, in *Proceedings of the Fourth European Conference on Underwater Acoustics, Rome, 1998*, pp. 187–192.
27. O. N. Strand, *SIAM J. Num. Anal.* **5** (1973).
28. A. N. Tichonov, *Soviet Math. Doklady* **4** (1963).

# Calculation of the Eigenfunctions and Eigenvalues of Acoustic Modes in a Layered Medium with a Horizontal Current

M. Yu. Trofimov

*Pacific Institute of Oceanology, Far East Division, Russian Academy of Sciences,  
ul. Baltiĭskaya 43, Vladivostok, 690041 Russia*

*e-mail: pacific@online.marine.ru*

Received September 2, 1998

**Abstract**—From perturbation theory methods, eigenfunctions of acoustic modes in a layered medium with a horizontal current are calculated correct to the first order in the Mach number. Formulas are given for the wave number and for the coefficients of the expansion of the eigenfunctions of a moving medium in the eigenfunctions of a stationary medium. On the basis of these formulas, an expression for the wave number is obtained correct to the second order in the Mach number. An example illustrating the resulting formulas is presented. © 2000 MAIK “Nauka/Interperiodica”.

The calculation of the eigenfunctions and eigenvalues of acoustic modes in a moving, vertically stratified medium is reduced to a not self-adjoint spectral problem [1]. In the general case, the solution of such a problem by the known methods requires the use of cumbersome algorithms (see, e.g., [2]) and high-performance computers. Meanwhile, in ocean acoustics, the ratio of the typical current speed to the sound velocity (the Mach number) is small, which allows one to use the perturbation theory. However, in spite of the large amount of results obtained in the approximation of a small Mach number (see, e.g., reviews in [2, 3]), the perturbation theory for the above spectral problem was not constructed. However, it is worth noting Godin’s paper [4], where the formula for the wave number perturbation was obtained in connection with the calculation of the mode group velocity.

As is shown below, in the first approximation of the perturbation theory, the initial problem consists only of solving the spectral problem for a stationary medium and to numerical integration. Formulas obtained for the wave number and the vertical eigenfunctions of a moving medium allow one to derive the formula for the wave number correct to the second order in the Mach number. The accuracy reached with this method is quite sufficient for many specific applications in ocean acoustics, since it is consistent with the accuracy and the volume of the usual experimental data for the medium parameters. As a specific area of application of our results, we keep in mind the mode tomography [5]. For illustrating the formulas derived, we present a simple example, where the approximations obtained for the wave number are compared to the approximation for the effective sound velocity [6].

We will solve the spectral problem for acoustic modes in a layer  $-H \leq z \leq 0$  of a stratified medium with a horizontal current [1]

$$\rho\beta^2 \frac{d}{dz} \left( \frac{1}{\rho\beta^2} \frac{d\phi}{dz} \right) + n^2 \beta^2 \phi = k^2 \phi, \quad (1)$$
$$\phi|_{z=0} = 0, \quad \left. \frac{1}{\rho\beta^2} \frac{d\phi}{dz} \right|_{z=-H} = 0,$$

where  $\rho = \rho(z)$  is the density,  $n(z) = 1/c(z)$  is the refractive index,  $c = c(z)$  is the sound velocity,  $k$  is the wave number,  $\beta = 1 - kv$ , and  $v = v(z)$  is the current speed. All variables were made dimensionless with the use of the scales of length  $\bar{h} = \bar{c}/\omega$ , time  $\omega^{-1}$  ( $\omega$  is the circular frequency and  $\bar{c}$  is the typical sound velocity), and density  $\bar{\rho}$  (the typical value of the density). We assume that the parameters  $\rho$ ,  $n$ , and  $v$  are piecewise, continuous functions of  $z$  with discontinuities at  $z = -h_j$ ,  $j = 1, \dots, N$ , and at these points the internal boundary conditions must be fulfilled:

$$\phi_+ = \phi_-, \quad \left( \frac{1}{\rho\beta^2} \frac{d\phi}{dz} \right)_+ = \left( \frac{1}{\rho\beta^2} \frac{d\phi}{dz} \right)_-. \quad (2)$$

Here, the plus sign marks the values of variables at the point  $z = z_0$ , from above, i.e., at  $z > z_0$ , and the minus sign marks the corresponding values from below with respect to the boundary under study.

Let us denote the discrete spectrum of problem (1), (2) by  $\{k; j = 0, 1, \dots\}$  and the corresponding eigenfunctions by  $\{\phi; j = 0, 1, \dots\}$ . We will consider only the eigenvalues  $k$  of multiplicity 1, and, for the corre-

sponding eigenfunctions, we will adopt the normalization condition

$$\int_{-H}^0 \frac{1}{\rho \beta^3} \left( \frac{1-\beta}{k^2} \left( \frac{d_l \phi}{dz} \right)^2 + {}_l \phi^2 \right) dz = 1. \quad (3)$$

This formula is derived from two requirements (see [7]): the insolvability of the boundary value problem for associated functions [8] and the coincidence of expression (3) with the conventional normalization condition for a stationary medium at  $\beta = 1$ . We note that, in spite of the inclusion of internal boundary conditions (2) in our case in contrast to [1, 9], the normalization condition obtained above coincides with that presented in [9].

Let us introduce a small parameter  $M$  (the Mach number) and assume that the following expansions take place

$$w = Mu;$$

$${}_j \phi = {}_j \phi_0 + M {}_j \phi_1 + M^2 {}_j \phi_2 + \dots; \quad (4)$$

$${}_j k = {}_j k_0 + M {}_j k_1 + M^2 {}_j k_2 + \dots$$

Substituting these expansions in (1) and (2) and separating the terms according to the order of  $M$ , in the order  $O(1)$ , we obtain the spectral problem for the modes of a stationary medium

$$\rho \frac{d}{dz} \left( \frac{1}{\rho} \frac{d_j \phi_0}{dz} \right) + n^2 {}_j \phi_0 = k_{0j}^2 \phi_0, \quad (5)$$

$${}_j \phi_0|_{z=0} = 0, \quad \left. \frac{d_j \phi_0}{dz} \right|_{z=-H} = 0$$

with the internal boundary conditions at  $z = -h_j, j = 1, \dots, N$

$${}_j \phi_{0+} = {}_j \phi_{0-}, \quad \left( \frac{1}{\rho} \frac{d_j \phi_0}{dz} \right)_+ = \left( \frac{1}{\rho} \frac{d_j \phi_0}{dz} \right)_-. \quad (6)$$

As is known, in the Gilbert space  $L_{1/\rho}^2(-H, 0)$ , the functions  $\{{}_j \phi_0; j = 0, 1, \dots\}$  form a complete orthogonal system of functions square-integrable with the weighting function  $1/\rho$  within the interval  $[-H, 0]$ , which is also assumed to be normalized:

$$\int_{-H}^0 \frac{1}{\rho} {}_i \phi_{0j} \phi_0 dz = \delta_{ij}, \quad (7)$$

where  $\delta_{ij}$  is the Kronecker delta.

Let us fix the number  $l$  and assume that  ${}_l k$  is the eigenvalue of multiplicity 1. In the order  $O(M)$ , we obtain

$$\rho \frac{d}{dz} \left( \frac{1}{\rho} \frac{d_l \phi_1}{dz} \right) + n^2 {}_l \phi_1 - k_{0l}^2 \phi_1 = 2\rho {}_l k_0 u \frac{d}{dz} \left( \frac{1}{\rho} \frac{d_l \phi_0}{dz} \right) \quad (8)$$

$$- 2\rho {}_l k_0 \frac{d}{dz} \left( \frac{1}{\rho} u \frac{d_l \phi_0}{dz} \right) + 2{}_l k_0 n^2 u \phi_0 + 2{}_l k_0 {}_l k_1 \phi_0$$

with the boundary conditions

$${}_l \phi_1|_{z=0} = 0, \quad \left. \frac{d_l \phi_1}{dz} \right|_{z=-H} = 0 \quad (9)$$

and the internal boundary conditions

$${}_l \phi_{1+} = {}_l \phi_{1-},$$

$$\left( \frac{1}{\rho} \frac{d_l \phi_1}{dz} \right)_+ - \left( \frac{1}{\rho} \frac{d_l \phi_1}{dz} \right)_- = -2{}_l k_0 \left( \frac{1}{\rho} \frac{d_l \phi_0}{dz} \right) (u_+ - u_-) \quad (10)$$

at  $z = -h_j, j = 1, \dots, N$ .

We solve problem (8)–(10) for  ${}_l \phi_1$ . Using the completeness of the system  $\{{}_j \phi_0; j = 0, 1, \dots\}$ , we seek the solution as

$${}_l \phi_1(z) = \sum_{j=0}^{\infty} {}_l a_j \phi_0(z). \quad (11)$$

In this case, as usual, we have

$${}_l a_j = \int_{-H}^0 \frac{1}{\rho} {}_l \phi_1 \phi_0 dz.$$

In order to determine  ${}_l a_j$ , we multiply (8) by  ${}_l \phi_0/\rho$  and integrate from  $-H$  to 0. Twice integrating by parts the left-hand side of the equation obtained and transforming its right-hand side with the use of (5) and the integration by parts, with allowance for (10), we obtain

$${}_l a_j ({}_l k_0^2 - k_{0j}^2) = 2{}_l k_0 \int_{-H}^0 u \frac{1}{\rho} \times \left( k_{0j}^2 {}_l \phi_0 \phi_0 + \frac{d_l \phi_0}{dz} \frac{d_j \phi_0}{dz} \right) dz + 2{}_l k_0 {}_l k_1 \delta_{lj}. \quad (12)$$

Equation (12) allows us to determine  ${}_l a_j$  at  $j \neq l$ . In the case  $j = l$ , this equation is the condition of solvability of problem (8)–(10) (Chapter XI in [10]) and gives the expression for  ${}_l k_1$ .

To determine  ${}_l a_l$ , we expand (3) in powers of  $M$ . In the order  $O(1)$ , we obtain the normalization condition from relationships (7), and, in the order  $O(M)$ , we obtain the equation

$$\int_{-H}^0 \frac{u}{\rho {}_l k_0} \left( \frac{d_l \phi_0}{dz} \right)^2 dz + 2 \int_{-H}^0 \frac{1}{\rho} {}_l \phi_0 \phi_1 dz + 3{}_l k_0 \int_{-H}^0 \frac{u}{\rho} \phi_0^2 dz = 0.$$

Substituting the expression for  ${}_l \phi_1$  from (11) in this equation, we obtain the equation for  ${}_l a_l$ :

$$2{}_l a_l + \frac{1}{{}_l k_0} \int_{-H}^0 \frac{u}{\rho} \left( \frac{d_l \phi_0}{dz} \right)^2 dz + 3{}_l k_0 \int_{-H}^0 \frac{u}{\rho} \phi_0^2 dz = 0. \quad (13)$$

In addition to normalization condition (3), the solutions to problem (1), (2) also satisfy the orthogonality

Results of calculations for the illustrative example

$M$	$l$	${}_l k_0$	${}_l k$	${}_l k(M)$	${}_l k(M^2)$	${}_l k_{\text{pade}}$	${}_l k_{\text{eff}}$
0.005	0	9.29296	8.96806	8.93737	8.96855	8.96604	8.96478
0.005	1	8.16210	7.95971	7.96359	7.96074	7.96070	7.95689
0.001	0	9.29296	9.22308	9.22184	9.22309	9.22307	9.22082
0.001	1	8.16210	8.12227	8.12240	8.12228	8.12228	8.12171

condition in the form considered in [1], although our case differs from that considered in [1] by the presence of the internal boundary conditions. Note that the approximate expressions for  ${}_l \phi_0 + M {}_l \phi_1$  satisfy this condition correct to  $O(M^2)$ .

Let us present some results for higher order approximations. The solvability condition for the boundary value problem in the order  $O(M^2)$  yields the formula for  ${}_l k_2$ :

$$\begin{aligned}
 {}_l k_2 = & -\frac{3}{2} {}_l k_0 \int_{-H}^0 u^2 \frac{1}{\rho} \left( {}_l k_0 {}_l \phi_0^2 + \left( \frac{d {}_l \phi_0}{dz} \right)^2 \right) dz \\
 & - \frac{1}{2 {}_l k_0} \sum_{j \neq l} {}_l a_j^2 ({}_j k_0^2 - {}_l k_0^2) + 2 {}_l k_1 {}_l a_l - \frac{{}_j k_1^2}{2 {}_l k_0}.
 \end{aligned} \tag{14}$$

Solving the problem in the order  $O(M^2)$  in just the same way as for the first approximation, we can obtain the formulas for the second-order corrections to the eigenfunctions, but these formulas are too complicated for practical use.

The second-order approximation in  $M$  for  ${}_l k$  allows one to construct the Pade approximation  $P_1^2$  (Chapter 8 in [11]):

$${}_l k_{\text{pade}} = \frac{{}_l k_1 {}_l k_0 + M ({}_l k_1^2 - {}_l k_0 {}_l k_2)}{{}_l k_1 - M {}_l k_2}. \tag{15}$$

On the basis of formulas (12)–(14), the calculations are easily performed without any cumbersome computations. In this case, most eigenfunctions of problem (5), (6) can be calculated after applying the Godin transformation [1, 12] in the WKB approximation [13].

Now, we present an example illustrating the formulas obtained above. Let  $H = 1$ ,  $\rho(z) = 1$ , and  $n(z) = N\pi$ , where  $N$  is a constant,

$$u(z) = \begin{cases} 1 & \text{at } -1 \leq z < -0.5 \\ 0 & \text{at } z \geq -0.5. \end{cases}$$

Then,  ${}_j k_0 = (\pi/2) \sqrt{4N^2 - (2j + 1)^2}$ ,  ${}_j \phi_0(z) = \sqrt{2} \sin((\pi/2)(2j + 1)z)$ ,

$${}_l \phi(z) = \begin{cases} a \cos(\alpha(2z + 1)) + b \sin(\alpha(2z + 1)) & \text{at } -1 \leq z < -0.5 \\ A \sin(\sqrt{N^2 \pi^2 - {}_l k^2} z) & \text{at } z \geq -0.5, \end{cases}$$

where

$$\begin{aligned}
 a &= -A \sin(0.5 \sqrt{N^2 \pi^2 - {}_l k^2}), \\
 b &= A(1 - M {}_l k u)^2 \sqrt{\frac{N^2 \pi^2 - {}_l k^2}{N^2 \pi^2 (1 - M {}_l k u)^2 - {}_l k^2}} \\
 &\quad \times \cos(0.5 \sqrt{N^2 \pi^2 - {}_l k^2}), \\
 \alpha &= 0.5 \sqrt{N^2 \pi^2 (1 - M {}_l k u)^2 - {}_l k^2},
 \end{aligned}$$

and the constant  $A$  is found from the normalization condition (3).

The eigenvalue  ${}_l k$  is found as a root of the transcendental equation

$$a \sin(\alpha) + b \cos(\alpha) = 0. \tag{16}$$

We compare the approximation for  ${}_l k$  with the approximation of the effective sound velocity  ${}_l k_{\text{eff}}$  [6], which is calculated as the wave number for a stationary medium whose refractive index  $n$  is replaced by  $n_{\text{eff}} = n/(1 + Mun)$ . For this example,  ${}_l k_{\text{eff}}$  is the root of the transcendental equation

$$\tan c \tan d = d/c, \tag{17}$$

where  $c = 0.5 \sqrt{n_{\text{eff}}^2 - {}_l k_{\text{eff}}^2}$  and  $d = 0.5 \sqrt{n^2 - {}_l k_{\text{eff}}^2}$ . Figure 1 and the table exhibit the calculation results for the first and second modes for  $N = 3$ . In the table, the following notations are used:  ${}_l k(M) = {}_l k_0 + M {}_l k_1$  and  ${}_l k(M^2) = {}_l k_0 + M {}_l k_1 + M^2 {}_l k_2$ .

Figure 2 presents the relative errors of various approximations for the wave number versus the Mach number. The errors were calculated from the formulas  $\delta_1 = |{}_l k(M) - {}_l k|/{}_l k$ ,  $\delta_2 = |{}_l k(M^2) - {}_l k|/{}_l k$ ,  $\delta_{\text{pade}} = |{}_l k_{\text{pade}} - {}_l k|/{}_l k$ , and  $\delta_{\text{eff}} = |{}_l k_{\text{eff}} - {}_l k|/{}_l k$ . It is pertinent to call attention to the behavior of the relative errors of the Pade

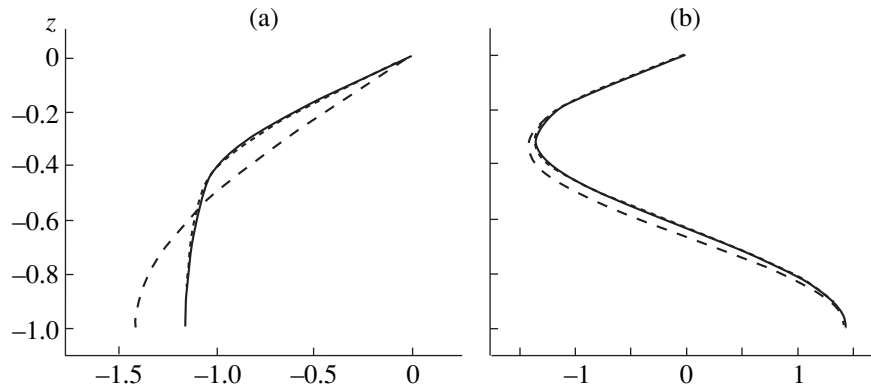


**Fig. 1.** Results of calculations for the illustrative example. (a) The first mode:  ${}_0\phi_0$  (dashed line),  ${}_0\phi$  (solid line), and  ${}_0\phi_0 + M_0\phi_1$  (dotted line). (b) The second mode:  ${}_1\phi_0$  (dashed line),  ${}_1\phi$  (solid line), and  ${}_1\phi_0 + M_1\phi_1$  (dotted line).

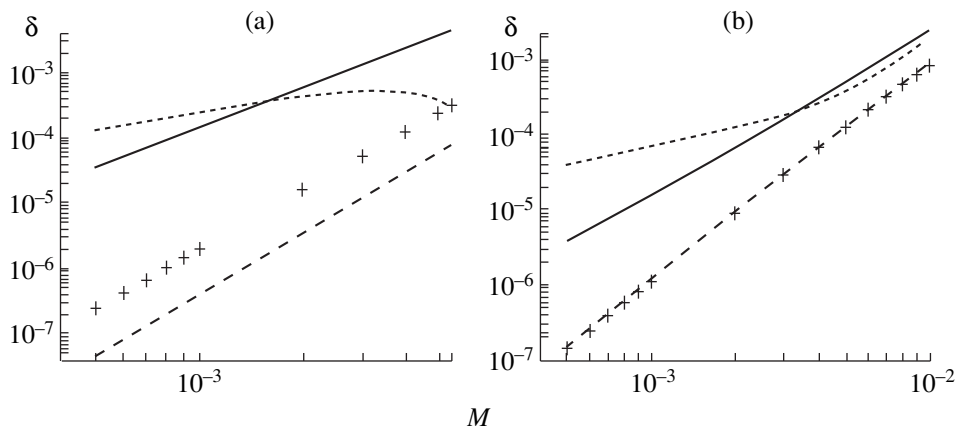


**Fig. 2.** Relative errors versus the Mach number  $M$  for the illustrative example. (a) The first mode:  $\delta_1$  (solid line),  $\delta_2$  (dash line), and  $\delta_{\text{eff}}, '+' - \delta_{\text{pade}}$  (dotted line). (b) The second mode: notations are the same as in (a).

approximation, which points to a poor convergence of the asymptotic series in this interval of the Mach numbers. Therefore, we can assume that higher approximations will provide no significant improvement in accuracy. It is of interest and somewhat unexpected that even the first approximation of the perturbation theory for the example under study is more correct than this approximation in the interval of small but significant values of the Mach numbers. Equations (16) and (17) were solved with the use of the MAPLE software package.

In closing, we briefly summarize the contents of the paper. By the methods of the perturbation theory, the eigenfunctions of acoustic modes are calculated in a layered medium with a horizontal current. Formulas (12) and (13) are derived; these formulas determine the wave number and the coefficients of the expansion of the eigenfunctions of a moving medium in the eigenfunctions of a stationary medium correct to the first order in the Mach number. On the basis of these results,

expression (14) is obtained for the determination of the wave number correct to the second order in the Mach number. For a simple example, the exact and approximate values (correct to the first and second orders) of the wave numbers were obtained for two values of the Mach number  $M = 0.001$  and  $M = 0.005$  (table), as well as the eigenfunctions (exact and approximate ones) for  $M = 0.005$  and the relative errors of various approximations in the interval  $0.0005 \leq M \leq 0.01$  of the Mach numbers (Fig. 2). The results of calculations testify to a fair accuracy of the proposed method.

ACKNOWLEDGMENTS

I am grateful to the reviewer for drawing my attention to the publication [6], which resulted in the study of the second-order approximation and the calculation of the errors presented in Fig. 2. This work was supported by the Russian Foundation for Basic Research (project nos. 96-05-64848 and 96-05-64086).

## REFERENCES

1. L. M. Brekhovskikh and O. A. Godin, *Acoustics of Layered Media* (Nauka, Moscow, 1989; Springer, Berlin, 1990).
2. N. S. Grigor'eva, *Asymptotic Methods in Problems of Sound Propagation in an Inhomogeneous Moving Medium* (Leningrad Univ., Leningrad, 1991).
3. V. E. Ostashev, *Sound Propagation in Moving Media* (Nauka, Moscow, 1992).
4. O. A. Godin, Dokl. Akad. Nauk SSSR **310**, 1084 (1990).
5. E. C. Shang, J. Acoust. Soc. Am. **85**, 1531 (1989).
6. O. A. Godin, D. Yu. Mikhin, and S. Ya. Molchanov, Izv. Akad. Nauk, Fiz. Atmos. Okeana **29**, 194 (1993).
7. M. V. Keldysh, Usp. Matem. Nauk **26** (4), 15 (1971).
8. M. A. Naïmark, *Linear Differential Operators* (Nauka, Moscow, 1969).
9. O. A. Godin, in *Ocean Acoustics*, Ed. by L. M. Brekhovskikh and Yu. P. Lysanov (Nauka, Moscow, 1993), pp. 3–8.
10. E. A. Coddington and H. Levinson, *Theory of Ordinary Differential Equations* (McGraw-Hill, New York, 1955).
11. C. M. Bender and S. A. Orszag, *Advanced Mathematical Methods for Scientists and Engineers* (McGraw-Hill, New York, 1978).
12. O. A. Godin, Dokl. Akad. Nauk **276**, 579 (1984).
13. M. A. Ainslie, M. N. Packman, and C. H. Harrison, J. Acoust. Soc. Am. **103**, 1804 (1998).

*Translated by Yu. P. Lysanov*

SHORT  
COMMUNICATIONS

## Axisymmetric Normal Sound Waves in an Infinite Cylindrical Three-Layer Waveguide with a Thin Intermediate Layer

L. A. Bulavin, Yu. F. Zabashta, and S. P. Senchurov

*Shevchenko University, pr. Glushkova 6, Kiev, 252022 Ukraine*

*e-mail: sergsenc@yahoo.com*

Received September 2, 1998

The interest taken by researchers in this problem is connected with the studies of the acoustic properties of optical fibers. Acoustics of multilayer fibers (in particular, optical fibers) is still a topical subject, as it follows from the works by Tchepe *et al.* and Noyfeh and Nagy [1, 2]. It is well known that an optical fiber consists of a glass core and a polymer protective coating. The radius of the glass core  $R$  is usually about 50–150  $\mu\text{m}$ , and the coating thickness  $H$  is about 50–500  $\mu\text{m}$ .

Two of the most important functional properties of optical fibers are their reliability and service life. These properties are determined by the mechanical state of the fiber core. The polymer coating performs a protective function increasing the compliance of the whole design and preventing the formation of cracks in the core.

According to Lipatov [3], an intermediate layer is formed at the polymer–glass boundary. The properties of this layer differ from the bulk properties of the polymer material. The mechanical protection of the core by the coating must depend on the quality of the contact between polymer and glass and, hence, on the properties of the intermediate layer. According to the estimates given in the literature [3], the thickness of such a layer is about 1–5  $\mu\text{m}$ . The possibility of the existence of such a boundary layer has not been taken into account in the previous studies [4]. The purpose of this paper is to study the effect of the boundary layer on the acoustic properties of optical fibers.

Our area of interest is the low-frequency range, namely, the frequencies at which the wavelength of sound propagating in the fiber far exceeds the transverse dimensions of the fiber. To describe the fiber dynamics in the low-frequency range, we can use simplified engineering equations. In the case of longitudi-

nal sound waves propagating along the fiber axis, these equations have the form

$$\rho'' \frac{\partial^2 U_z''}{\partial t^2} - E'' \frac{\partial^2 U_z''}{\partial z^2} = \frac{F_{conn}}{S''}, \quad (1)$$

$$\rho' \frac{\partial^2 U_z'}{\partial t^2} - E' \frac{\partial^2 U_z'}{\partial z^2} = \frac{F_{conn}}{S'}, \quad (2)$$

where  $\rho'$  and  $\rho''$  are the densities of materials of the core and the coating;  $E'$  and  $E''$  are the Young's moduli of the core and coating materials; and  $U_z'$  and  $U_z''$  are the particle displacements in the core and the coating along the fiber axis; the  $z$  axis coincides with the fiber axis;

$$S' = \pi R^2,$$

$$S'' = \pi(R + H)^2 - S',$$

$F_{conn}$  is the tangential force acting in the intermediate layer. The value of  $F_{conn}$  can be calculated approximately as

$$F_{conn} = -\frac{2\pi R \mu'''}{h} (U_z'' - U_z'), \quad (3)$$

where  $\frac{\mu'''}{h}$  is the average value of the ratio of the shear modulus of the intermediate layer of the fiber to its thickness.

We seek the solution of equations (1) and (2) in the form of waves propagating along the fiber axis, i.e., in the form

$$U_z(z, t) = U_z \exp(i\omega t - ikz), \quad (4)$$

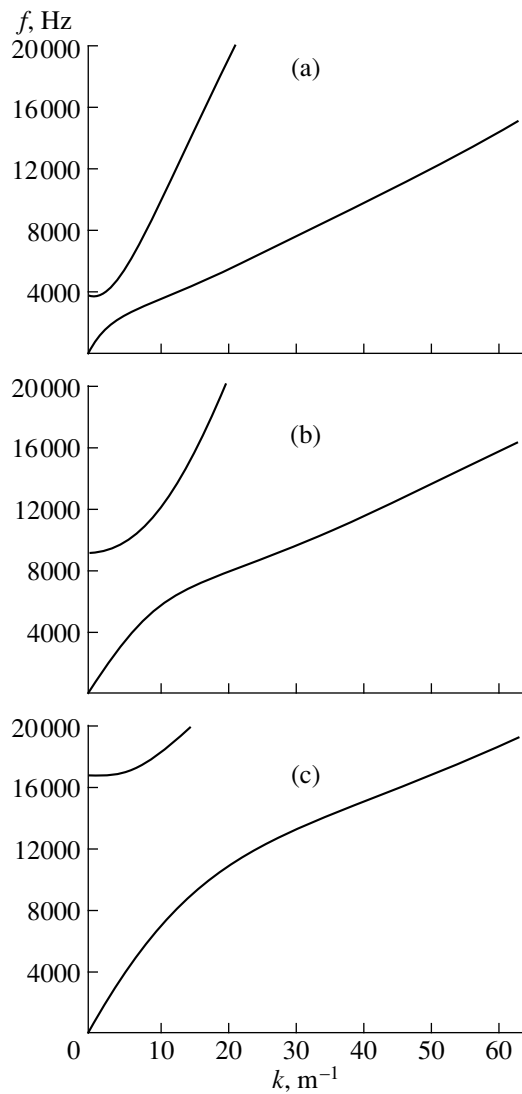


**Fig. 1.** Dispersion curves for three-layer waveguides with intermediate layers of different elasticity.

in both the core and the coating of the fiber. Here,  $\omega$  is the oscillation frequency,  $k = \frac{2\pi}{\lambda}$  is the wave number, and  $\lambda$  is the wavelength.

Substituting expressions (3) and (4) into equations (1) and (2), we obtain

$$2\pi R\mu''' \frac{U_z'' - U_z'}{h} - k^2 E' U_z' S' = -\rho' \omega^2 U_z' S', \quad (5)$$

$$-2\pi R\mu''' \frac{U_z'' - U_z'}{h} - k^2 E'' U_z'' S'' = -\rho'' \omega^2 U_z'' S''. \quad (6)$$

These equations represent a system of homogeneous equations for  $U_z'$  and  $U_z''$ . The condition of non-

triviality of the solutions of this system has the form

$$\omega^4 - \omega^2 [(c_1^2 + c_2^2)k^2 + \omega_0^2] + k^2 \frac{2\pi R\mu'''}{h} \left( \frac{c_2^2}{\rho' S'} + \frac{c_1^2}{\rho'' S''} \right) + k_4 c_1^2 c_2^2 = 0, \quad (7)$$

where  $c_1^2 = \frac{E'}{\rho'}$ ,  $c_2^2 = \frac{E''}{\rho''}$ , and  $\omega_0^2 = \frac{2\pi R\mu'''}{h} \left( \frac{1}{\rho' S'} + \frac{1}{\rho'' S''} \right)$ .

Let us use the following notation:

$$\eta = \omega^2,$$

$$2m = (c_1^2 + c_2^2)k^2 + \omega_0^2,$$

$$q = k^2 \frac{2\pi R\mu'''}{h} \left( \frac{c_2^2}{\rho' S'} + \frac{c_1^2}{\rho'' S''} \right) + k_4 c_1^2 c_2^2.$$

Then, we obtain

$$\eta^2 - 2m\eta + q = 0, \quad (8)$$

$$\eta_{1,2} = m \pm \sqrt{m^2 - q}. \quad (9)$$

Substituting expression (9) into expressions (5) and (6), we obtain:

$$\frac{U_z'(1, 2)}{U_z''(1, 2)} = \frac{\rho'' S'' (c_2^2 - c_1^2) k^2 + \frac{\omega_0^2}{2} \pm SQR}{\rho' S' (c_1^2 - c_2^2) k^2 + \frac{\omega_0^2}{2} \pm SQR}, \quad (10)$$

where

$$SQR = \sqrt{(c_1^2 - c_2^2) \frac{2k^4}{4} + \frac{\omega_0^4}{4} + (c_2^2 - c_1^2) k^2 \frac{2\pi R\mu'''}{h} \left( \frac{1}{\rho' S'} - \frac{1}{\rho'' S''} \right)}.$$

The results of solving equations (5) and (6) are presented in Fig. 1 in the form of dispersion curves. The calculations were conducted for the values  $\rho' = 2520 \frac{\text{kg}}{\text{m}^3}$ ,

$\rho'' = 1150 \frac{\text{kg}}{\text{m}^3}$ ,  $E' = 75 \text{ GPa}$ , and  $E'' = 2.5 \text{ GPa}$  taken

from handbooks and the values  $\frac{\mu'''}{h} = 0.02, 0.11,$  and

$0.36 \frac{\text{GPa}}{\text{m}}$  (Figs. 1a, 1b, and 1c, respectively).

As one can see from the figure, the frequency spectrum of a three-layer waveguide in the considered frequency range has two branches corresponding to two waves, which can propagate in such a waveguide.

We can also obtain a solution for a two-layer waveguide within the framework of the proposed model by performing the passage  $h \rightarrow 0$ , i.e.,  $\frac{\mu'''}{h} \rightarrow \infty$ , in equation (3), and, as the constraint force cannot acquire infinitely large values, we have to assume that  $U_z' = U_z''$ . Such a model was studied earlier by Dowell and Tauchert [5].

The dispersion curve obtained as the result of solving the equations of motion of a two-layer waveguide is given in Fig. 2 in the same frequency interval and for the same values of mechanical and elastic parameters of the waveguide. As one can see from this figure, the dispersion curve has one branch in this case.

The main result of this paper is the conclusion about the existence of two types of axisymmetric waves propagating in a three-layer waveguide. This conclusion seems to be quite logical, because it is well known that a set of normal waves must exist in an optical waveguide. In fact, two waves of this set are considered in this paper.

The first of them is a “zero” wave with a critical frequency equal to zero and a uniform distribution of the displacements  $U_z'$  and  $U_z''$  over the cross-section.

The second wave is the normal wave closest to the zero one with the critical frequency other than zero. The square of the latter is proportional to the quantity  $\frac{\mu'''}{h}$ . Therefore, an increase in this quantity can shift the frequency branch of the second wave beyond the ultrasonic range. This fact must be kept in mind when conducting experiments aimed at testing the theoretical conclusions of this paper.

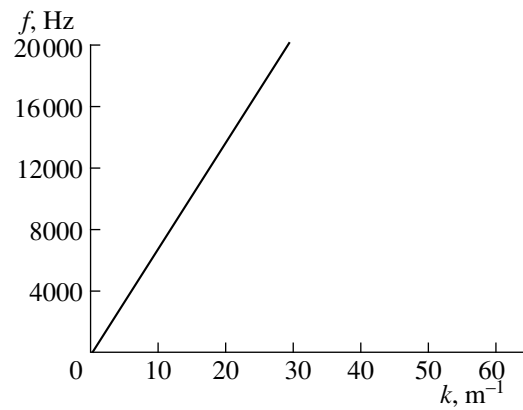


Fig. 2. Dispersion curve for a two-layer waveguide.

Thus, the calculations described above show that a single axisymmetric ultrasonic wave propagates in an optical fiber, while two waves propagate in a fiber with a boundary layer. This fact may be used for the detection and investigation of boundary layers in optical fibers.

REFERENCES

1. J. Tchepe, K. Desinger, G. Müller, *et al.*, in *Proceedings of Ultrasonics World Congress* (Berlin–Duisburg, Germany, 1995), Part 2, p. 1083.
2. A. H. Noyfeh and P. B. Nagy, *J. Acoust. Soc. Am.* **99**, 931 (1996).
3. Yu. S. Lipatov, *Polymer Reinforcement* (Chem. Tech., Canada, 1995).
4. N. Thurston, *J. Sound Vibr.* **159**, 441 (1992).
5. E. H. Dowell and T. R. Tauchert, *J. Acoust. Soc. Am.* **49** 220 (1971).

*Translated by M.L. Lyamshev*

**SHORT  
COMMUNICATIONS**

## Acoustic Waves in a Rotating Elastic Medium

**V. I. Grigor'evskii, Yu. V. Gulyaev, and A. I. Kozlov**

*Institute of Radio Engineering and Electronics, Russian Academy of Sciences,  
pl. Vvedenskogo 1, Fryazino, Moscow oblast, 141120 Russia*

*e-mail: pbsoy@cityline.ru*

Received December 22, 1998

Currently, a variety of devices based on Rayleigh surface acoustic waves (SAW), such as bandpass and dispersion filters, resonators, transducers, and delay lines, are widely used in engineering [1, 2]. A wide range of environmental conditions in which these devices are used stimulate researchers to study the effect of these conditions on the properties of SAW. This paper studies the propagation of the Rayleigh SAW, as well as bulk acoustic waves, along the surface of a rotating sound-transmitting medium from the viewpoint of an observer moving with the medium. A solution to this, at a first glance, academic problem could seemingly be of interest only for developing rotation gauges. However, Hall *et al.* [3] propose a new method for evaluating the quality of the paper pulp in the process of its production on the basis of the sound velocity measurements in different directions in the paper pulp rotating on special drums.

In a uniformly rotating elastic medium, the equations of motion acquire two additional terms, as compared to the inertial coordinate system:

$$\rho \frac{\partial^2 \mathbf{u}}{\partial t^2} = 2\rho(\mathbf{v} \times \boldsymbol{\Omega}) + \rho(\boldsymbol{\Omega} \times (\boldsymbol{\Omega} \times \mathbf{r})) + (\lambda + \mu)\text{grad div } \mathbf{u} + \mu\Delta \mathbf{u}, \quad (1)$$

where  $\rho$  is the density of the sound-transmitting medium,  $\mathbf{u}$  is the displacement vector,  $\mathbf{v} = \partial \mathbf{u} / \partial t$  is the particle velocity,  $\boldsymbol{\Omega}$  is the rotation speed of the medium,  $\mathbf{r}$  is the position vector of an elementary volume of the medium in a rotating coordinate system, and  $\lambda$  and  $\mu$  are the Lamé elastic constants.

The first term on the right-hand side of equation (1) describes the Coriolis force, and the second term describes the centrifugal force. In the following calculations, the centrifugal force will be neglected. This approximation is valid in two independent and sufficiently important particular cases:

(1) when the rotation speed is much less than the cyclic frequency of the elastic wave:  $\Omega/\omega \ll 1$ ;

(2) when the region of the acoustic medium in which the acoustic wave propagates is located sufficiently far from the rotation axis, so that the position vectors of all points that take part in the wave motion can approximately be considered as equal.

We limit our consideration to acoustic waves polarized in the  $XY$  plane of the coordinate system rotating about the  $OZ$  axis (Fig. 1).

Since, in this problem, the form of the equations of motion is significant and not quite conventional [4], we briefly explain how they are derived. Expand the displacement vector into the potential and solenoidal parts:

$$\mathbf{u} = \mathbf{u}_l + \mathbf{u}_r, \quad \text{where } \text{rot } \mathbf{u}_l = 0, \quad \text{div } \mathbf{u}_r = 0.$$

Apply the rotor and divergence operations to both sides of equation (1) to obtain

$$\left. \begin{aligned} \text{div} \left\{ \rho \frac{\partial^2 \mathbf{u}_l}{\partial t^2} + 2\rho \left( \frac{\partial \mathbf{u}_l}{\partial t} \times \boldsymbol{\Omega} \right) \right. \\ \left. + (\lambda + 2\mu)\text{grad div } \mathbf{u}_l \right\} = 0; \end{aligned} \quad (1a)$$

$$\left. \begin{aligned} \text{rot} \left\{ \rho \frac{\partial^2 \mathbf{u}_l}{\partial t^2} + 2\rho \left( \frac{\partial \mathbf{u}_l}{\partial t} \times \boldsymbol{\Omega} \right) \right. \\ \left. + (\lambda + 2\mu)\text{grad div } \mathbf{u}_l \right\} = 0. \end{aligned} \quad (1b)$$

Then, the first equation of motion follows from expressions (1a) and (1b), because, if rotor and divergence of a vector are zero in some space region, the vector itself is also zero [5]:

$$\rho \frac{\partial^2 \mathbf{u}_l}{\partial t^2} = 2\rho \left( \frac{\partial \mathbf{u}_l}{\partial t} \times \boldsymbol{\Omega} \right) + (\lambda + 2\mu)\text{grad div } \mathbf{u}_l. \quad (2a)$$

Note that equations (1a) and (1b) were derived using the following conditions:

$$\left. \begin{aligned} \text{div} \left( \frac{\partial \mathbf{u}_l}{\partial t} \times \boldsymbol{\Omega} \right) = \boldsymbol{\Omega} \cdot \frac{\partial}{\partial t} \text{rot } \mathbf{u}_l = 0, \\ \text{rot} \left( \frac{\partial \mathbf{u}_l}{\partial t} \times \boldsymbol{\Omega} \right) = (\boldsymbol{\Omega} \cdot \vec{\nabla}) \cdot \frac{\partial \mathbf{u}_l}{\partial t} = 0. \end{aligned} \quad (3)$$

The first of conditions (3) is always satisfied, while the second one essentially uses the fact that the elastic displacement vector lies in the plane perpendicular to the rotation axis:  $\mathbf{u} = \{u_x, u_y, 0\}$ ,  $\boldsymbol{\Omega} = \{0, 0, \Omega_z\}$ .

The second equation of motion can also be easily obtained in the same manner:

$$\rho \frac{\partial^2 \mathbf{u}_t}{\partial t^2} = 2\rho \left( \frac{\partial \mathbf{u}_t}{\partial t} \times \boldsymbol{\Omega} \right) + (\lambda + 2\mu) \text{gradiv} \mathbf{u}_t. \quad (2b)$$

As compared to the equations given in [4], the first terms on the right-hand side of equations (2) interchanged their positions, which made these equations interdependent. Therefore, we first consider the propagation of bulk acoustic waves in a rotating sound-transmitting medium. We seek a solution for the elastic displacements in the form of homogeneous shear  $u_t$  and longitudinal  $u_l$  bulk waves:

$$\mathbf{u}_t = \mathbf{f} \exp[i(qx - \omega t)]$$

$$\mathbf{u}_l = \mathbf{g} \exp[i(qx - \omega t)],$$

where  $\mathbf{f} \parallel OY$  and  $\mathbf{g} \parallel OX$ . We determine the wave numbers of the bulk waves by substituting these solutions into equations of motion (2):

$$\begin{aligned} q_t &\equiv \sqrt{\frac{k_t^2 + k_l^2}{2} + \sqrt{\frac{(k_t^2 - k_l^2)^2}{4} + 4\frac{\Omega^2}{\omega^2} k_t^2 k_l^2}}; \\ q_l &\equiv \sqrt{\frac{k_t^2 + k_l^2}{2} - \sqrt{\frac{(k_t^2 - k_l^2)^2}{4} + 4\frac{\Omega^2}{\omega^2} k_t^2 k_l^2}} \end{aligned} \quad (4)$$

for  $\Omega/\omega \rightarrow 0$ ,  $q_l \rightarrow k_l \equiv \sqrt{\rho\omega^2/(\lambda + 2\mu)}$ , and  $q_t \rightarrow k_t \equiv \sqrt{\rho\omega^2/\mu}$ .

Thus, the longitudinal and transverse acoustic waves in a rotating medium have the form of coupled modes:

$$\mathbf{u}_t = (\mathbf{f}_t + \mathbf{g}_t) \exp[i(q_t x - \omega t)],$$

$$g_t = -f_t(q_t^2 - k_t^2)/(2ik_t^2\Omega/\omega);$$

$$\mathbf{u}_l = (\mathbf{g}_l + \mathbf{f}_l) \exp[i(q_l x - \omega t)],$$

$$f_l = g_l(q_l^2 - k_l^2)/(2ik_l^2\Omega/\omega).$$

Consider expressions (4) in more detail. At  $\Omega = \omega/2$ , one can see that  $q_l = 0$  and  $f_l = ig_l$ , i.e., an attempt to excite a longitudinal wave under these conditions will cause harmonic oscillations of the sound-transmitting medium as a whole. As the rotation speed increases, the wave number  $q_l$  becomes an imaginary quantity. From the viewpoint of an observer connected with the inertial coordinate system, an imaginary value of the wave number indicates that it is impossible to excite a longi-

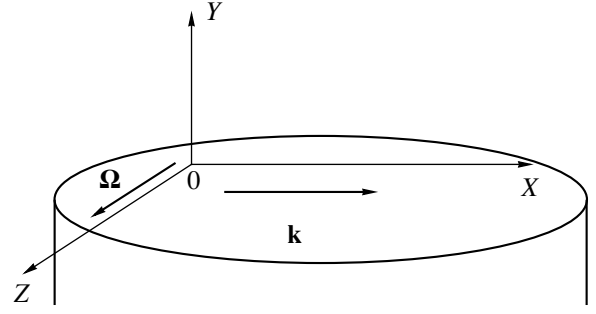


Fig. 1. Problem geometry.

tudinal elastic wave in a rapidly rotating medium, because a small element of the elastic medium changes its location due to the rotation faster than due to the oscillatory motion. With increasing rotation speed, the transverse wave velocity decreases as  $(\Omega/\omega)^{-1/2}$ .

We seek a solution for the Rayleigh SAW in the form of a usual two-component wave, which exponentially decays in the medium with depth:

$$\mathbf{u}_t = \mathbf{f} \exp[i(kx - \omega t) + ry];$$

$$\mathbf{u}_l = \mathbf{g} \exp[i(kx - \omega t) + ry].$$

Using the standard procedure [5], determine the SAW components from equations of motion (2):

$$\begin{cases} u_x = \{r_1 a \exp(r_1 y) + i k b \exp(r_1 y)\} \\ \quad \times \exp[i(kx - \omega t)] \\ u_y = \{-i k a \exp(r_1 y) + r_1 b \exp(r_1 y)\} \\ \quad \times \exp[i(kx - \omega t)], \end{cases} \quad (5)$$

where  $a$  and  $b$  are arbitrary constants,

$$r_1^2 = h_1^2 + k^2; \quad r_2^2 = h_2^2 + k^2,$$

$$h_1^2 = -\frac{k_t^2 + k_l^2}{2} + \sqrt{\frac{(k_t^2 + k_l^2)^2}{4} + 4\frac{\Omega^2}{\omega^2} k_t^2 k_l^2};$$

$$h_2^2 = -\frac{k_t^2 + k_l^2}{2} - \sqrt{\frac{(k_t^2 + k_l^2)^2}{4} + 4\frac{\Omega^2}{\omega^2} k_t^2 k_l^2}.$$

By inserting solution (5) into the boundary conditions that require that the elastic stress on a free surface of a solid be zero, we obtain the relationship that is somewhat different from the standard form of the Rayleigh determinant:

$$(r_t^2 + k^2)(k_t^2 h_1^2 + 2k^2 k_l^2) - 4k^2 r_1 r_2 k_l^2 = 0. \quad (6)$$

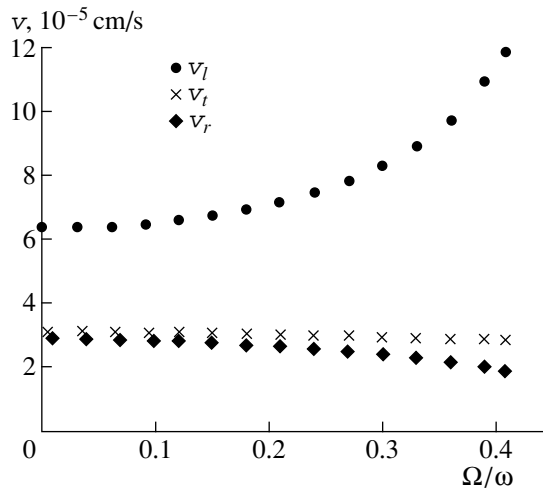


**Fig. 2.** Acoustic wave velocity as a function of the rotation speed of the medium: ( $v_l$ ) longitudinal wave, ( $v_t$ ) transverse wave, and ( $v_r$ ) Rayleigh SAW.

This equation can be written in a different form using the notation  $\xi = k_t/k$ :

$$\begin{aligned} & \xi^6 + 4\xi^4 \frac{(k_t^2 h_t^2 + k_t^2 h_l^2)}{h_t^2 h_l^2} \\ & + 4\xi^2 \frac{(k_t^4 h_l^4 + k_l^4 h_t^4) + 4k_t^2 h_t^2 h_l^2 (k_t^2 - k_l^2)}{h_t^4 h_l^2} \\ & + 16 \frac{k_t^2 k_l^2}{h_t^2 h_l^4} \left( 1 - \frac{k_t^2}{k_l^2} \right) = 0. \end{aligned} \quad (6a)$$

Familiar expressions for the Rayleigh determinant can easily be obtained from equations (6) and (6a) for  $\Omega/\omega \rightarrow 0$ . Equations (6) and (4) were solved numerically for aluminum (the Poisson ratio  $\sigma = 0.345$ , Young's modulus  $E = 7.03 \times 10^{11}$  dyn/cm<sup>2</sup>, and density  $\rho = 2.7$  g/cm<sup>3</sup>). The velocities of the bulk and surface waves as functions of frequency are plotted in Fig. 2.

No solutions to equation (6) in the form of an undamped Rayleigh SAW were found for  $\Omega \geq \omega/2$ . In fact, since the longitudinal elastic wave cannot be excited in a sound-transmitting medium rotating at a sufficiently high speed, the SAW, whose displacement vector has a longitudinal component, also cannot be generated. The unlimited increase in the longitudinal wave velocity (note that it occurs in a noninertial coordinate system) with increasing speed of rotation is a formal mathematical consequence of the above-mentioned degeneration of this wave into longitudinal oscillations of the whole sound-transmitting medium at  $\Omega = \omega/2$ .

Thus, in this paper, we studied the properties of the longitudinal and transverse elastic waves and a Rayleigh surface acoustic wave in a rotating elastic medium for the case of the polarization of these waves being perpendicular to the rotation axis. It is established that the longitudinal bulk wave and the surface wave cannot propagate in such a sound-transmitting medium when the rotation speed is more than twice as high as the wave frequency.

#### ACKNOWLEDGMENTS

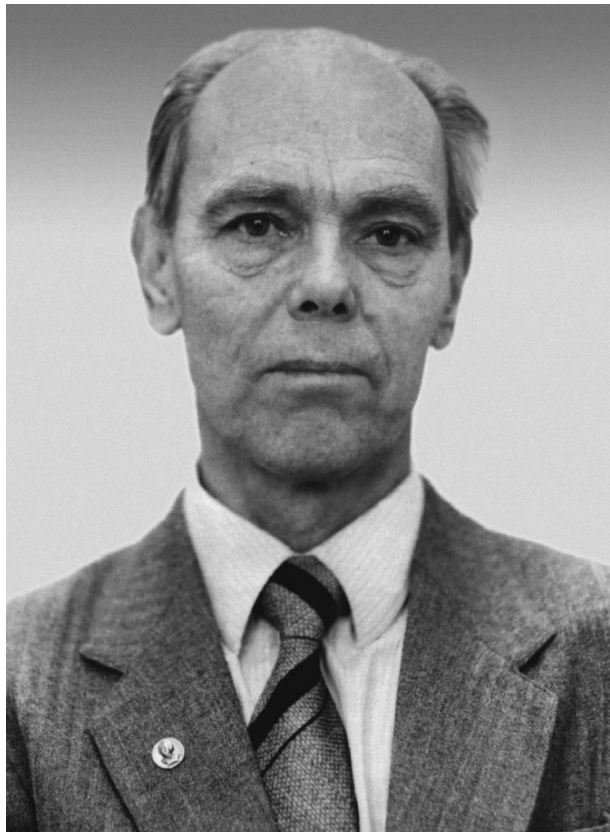
This work was supported by the INTAS, project no. INTAS-96-441.

#### REFERENCES

1. D. Morgan, *Surface-Wave Devices for Signal Processing* (Elsevier, New York, 1985; Radio i Svyaz', Moscow, 1990).
2. P. W. Zoveday and C. A. Rogers, *IEEE Trans. Ultrason. Ferroelect. Freq. Contr.* **45**, 1211 (1998).
3. M. S. Hall *et al.*, *J. Acoust. Soc. Am.* **100**, 686 (1996) (U.S. Patent No. 5,493,911).
4. H. Hamish, *Acustica* **72** (4), 275 (1990).
5. L. D. Landau and E. M. Lifshits, *Theory of Elasticity* (4th ed., Nauka, Moscow, 1987; 2nd ed., Pergamon, Oxford, 1970).

*Translated by A.D. Khzmalyan*

## Vitaliĭ Anatol'evich Zverev (On His 75th Birthday)



November 3, 1999, marked the 75th birthday of Corresponding Member of the Russian Academy of Sciences, Doctor of Physics and Mathematics, Professor Vitaliĭ Anatol'evich Zverev.

Zverev is a prominent specialist in radiophysics and acoustics. He is the author of more than 150 scientific works, including three monographs and 30 inventions. He made a substantial contribution to the development of acoustics; he was one of the first to lay the foundations of nonlinear acoustics, which later became a rapidly developing area of research.

Zverev's youth fell within the period of the Second World War. From 1942 to the Day of Victory, he served in the army, in the air-defense forces. Being a young soldier, Zverev demonstrated his talent for research and invention: he successfully fixed and tuned new complicated radar systems that appeared at that time in air defenses. Zverev's occupation in the army determined his civilian profession. In 1945, he left the army and became a student of the Radiophysical Faculty at Gor'kiĭ State University. In 1950, Zverev graduated

from the university and became a postgraduate student of Professor G.S. Gorelik.

Zverev's first research project was based on the idea put forward by M.A. Isakovich on the dispersion of acoustic waves in emulsions. To implement this idea, Zverev studied the specific features of the propagation of modulated waves in dispersive media. He found that the propagation of a modulated wave in a dispersive medium can be described by a single parameter—the phase invariant. Zverev developed a method for measuring this parameter and designed the corresponding equipment. This work resulted in his candidate dissertation, which he defended in 1953. The further development of these studies offered the possibility of using the same approach and equipment for studying spatial spectra of random inhomogeneities. This possibility was realized in acoustics.

In the following years, Zverev's scientific activity was related to the formation of images by wave fields. All three monographs written by Zverev are devoted to this subject. The last monograph entitled *Physical Foundations of the Formation of Images by Wave Fields* appeared in 1998, and the first monograph published in co-authorship with E.F. Orlov in 1971 was concerned with the optical processing of information. Zverev was one of the first to propose and develop the optical methods of spectral and correlation analysis. Based on these methods, unique instruments for spectral and correlation analysis were designed under his supervision. The instruments have found applications in radar, acoustics, and medicine.

The book *Radio-optics*, published by Zverev in 1975, and his monograph published in 1998 are unique editions that contain a unified description of all known specific features of image formation. To consider all possible cases, it was necessary to combine optics, acoustics, and radiophysics, because no single area covers the whole variety of conditions of the image formation.

The simplest and most illustrative example of the image formation by wave fields is our vision. Waves arriving at the pupil of the eye are processed so as to allow us to reconstruct (to see) their sources. In order to see objects, we do not need to understand the mechanism of the phenomenon. However, to “see” objects with some other waves, e.g., acoustic ones that cannot be perceived with our eyes or ears, a corresponding scientific description of the phenomenon is necessary, with allowances made for the specific conditions of the image formation. The variety of the conditions of

image formation can be illustrated by hearing and sight. We "see" with our ears in a completely different way than with our eyes. Zverev proposed a mathematical model describing how we "see" with our ears. The proposed procedure was close to the aperture synthesis widely used in radio astronomy. The determination of this procedure allowed Zverev to explain the specific features of the perception of monophonic and stereophonic sound and to propose an original method of volume sound reproduction; this method is now successfully used in industry.

Zverev's studies in nonlinear acoustics were also related to the problems of acoustic vision. Zverev proposed and implemented the parametric reception and transmission of sound. Parametric antennas possess some specific features of the image formation. A parametric acoustic array has a directional pattern close to an ideal one without any distortions due to technical factors. Similar systems were proposed by Westervelt two years later, and his publications marked the beginning of nonlinear acoustics in the western countries. For the studies in nonlinear acoustics, Zverev and his colleagues received a USSR State Award in 1985.

Currently, Zverev is involved in both scientific and tutorial activities. In the past five years, he has submitted for publication 19 scientific works, including one monograph; eleven papers were published in the *Akusticheskiĭ Zhurnal (Acoustical Physics)*. Zverev continues working on the problems of vision in acoustic fields. Many media that are opaque to other types of waves prove to be transparent to acoustic waves. However, conventional ways of image formation are not always appropriate in acoustics. The factors that hinder image formation and ways to overcome these difficulties are currently studied by Zverev. In his recent publications, he proposed the so-called acoustic dark-field method, which allows one to select the objects of interest against intense scattered and direct radiation.

Zverev developed original lecture courses on statistical radiophysics, acoustics, and physical foundations of the image formation by wave fields (radio-optics). For years, these lectures were delivered to the students

of Nizhni Novgorod University. Over a period of seven years, Zverev chaired the department of General Physics at the Radiophysical faculty of the Nizhni Novgorod University. Starting in 1956, he headed the department of Statistical Radiophysics and Acoustics of the Radiophysical Research Institute, and in 1977, he became head of the department of Physical Acoustics at the newly established Institute of Applied Physics of the Russian Academy of Sciences.

In 1964, Zverev defended his doctoral dissertation, which included the results of his studies of modulated waves, optical signal processing, nonlinear acoustics, and some applications. In 1979, he was elected corresponding member of the Russian Academy of Sciences for the Division of General Physics and Astronomy. For his achievements in science, Zverev was awarded an Order of the Red Banner of Labor and several medals.

While celebrating his 75th birthday, Zverev is deeply involved in his creative endeavors. He spends most of his time working with his personal computer verifying new ideas and algorithms of signal selection against background noise. In the aforementioned monograph published in 1998, Zverev considered some specific features of programming for different wave problems, described a method of taking into account the *a priori* data on the image formation in computer calculations, and included more than 20 specific computer codes for the image formation in different conditions. He shares his enthusiasm for work with his students and colleagues.

Zverev's hobby is classical music, which he has loved since childhood. At the age of 23, he started playing piano, and today, he can easily play his favorite pieces by Liszt, Beethoven, Rachmaninov, Schubert, and other composers.

The friends, students, and colleagues of Vitalii Anatol'evich Zverev wish him good health and further success in his creative endeavors.

*Translated by E.M. Golyamina*

---

---

**INFORMATION**

---

---

## **Information from the Division of General Physics and Astronomy of the Russian Academy of Sciences**

The Division of General Physics and Astronomy of the Russian Academy of Sciences approved the following membership of the Scientific Council on Acoustics of the Russian Academy of Sciences:

### **SCIENTIFIC COUNCIL ON ACOUSTICS OF THE RUSSIAN ACADEMY OF SCIENCES**

Chairman:

Leonid Mikhaĭlovich Lyamshev, Doctor of Physics and Mathematics, Head of Department, Andreev Acoustics Institute, Russian Academy of Sciences

Vice-Chairman:

Georgii Dmitrievich Mansfel'd, Doctor of Physics and Mathematics, Professor, Principal Researcher, Institute of Radio Engineering and Electronics, Russian Academy of Sciences

Scientist-secretary:

Andreĭ Viktorovich Fokin, Candidate of Physics and Mathematics, Senior Researcher, Andreev Acoustics Institute, Russian Academy of Sciences

Members:

Oleg Vladimirovich Abramov, Doctor of Physics and Mathematics, Professor, Head of Laboratory, Kurnakov Institute of General and Inorganic Chemistry, Russian Academy of Sciences

Irina Arkad'evna Aldoshina, Doctor of Engineering, Deputy Director, All-Russian Research Institute of Radio Reception and Acoustics

Viktor Anatol'evich Akulichev, Corresponding Member of the Russian Academy of Sciences, Director, Pacific Institute of Oceanology, Far East Division, Russian Academy of Sciences

Yuriĭ Ivanovich Bobrovnikskii, Doctor of Physics and Mathematics, Head of Laboratory, Blagonravov Institute of Machine Science, Russian Academy of Sciences

Sergeĭ Vasil'evich Bogdanov, Corresponding Member of the Russian Academy of Sciences, Principal Researcher, Institute of Semiconductor Physics, Siberian Division, Russian Academy of Sciences

Leonid Maksimovich Brekhovskikh, Member of the Russian Academy of Sciences, Shirshov Oceanology Institute, Russian Academy of Sciences

Fedor Vasil'evich Bunkin, Member of the Russian Academy of Sciences, Director, General Physics Institute, Russian Academy of Sciences

Valentin Andreevich Burov, Doctor of Physics and Mathematics, Professor, Moscow State University

Andreĭ Viktorovich Gaponov-Grekhov, Member of the Russian Academy of Sciences, Director, Institute of Applied Physics, Russian Academy of Sciences

Irina Petrovna Golyamina, Candidate of Physics and Mathematics, Leading Researcher, Andreev Acoustics Institute, Russian Academy of Sciences

Éduard Petrovich Gulin, Doctor of Physics and Mathematics, Head of Department, Andreev Acoustics Institute, Russian Academy of Sciences

Yuriĭ Vasil'evich Gulyaev, Member of the Russian Academy of Sciences, Director, Institute of Radio Engineering and Electronics, Russian Academy of Sciences

Sergeĭ Nikolaevich Gurbatov, Doctor of Physics and Mathematics, Professor, Chair of Department, Nizhni Novgorod State University

Nikolaĭ Andreevich Dubrovskii, Doctor of Physics and Mathematics, Professor, Director, Andreev Acoustics Institute, Russian Academy of Sciences

Sergeĭ Viktorovich Egerev, Doctor of Physics and Mathematics, Deputy Director, Andreev Acoustics Institute, Russian Academy of Sciences

Vladimir Ivanovich Erofeev, Doctor of Physics and Mathematics, Deputy Director, Blagonravov Institute of Machine Science, Nizhni Novgorod Branch, Russian Academy of Sciences

Igor' Borisovich Esipov, Doctor of Physics and Mathematics, Leading Researcher, Andreev Acoustics Institute, Russian Academy of Sciences

Boris Maksimovich Efimtsov, Doctor of Engineering, Head of Department, Zhukovskii Central Institute of Aerohydrodynamics

Vitalii Anatol'evich Zverev, Corresponding Member of the Russian Academy of Sciences, Head of Department, Institute of Applied Physics, Russian Academy of Sciences

Viktor Vasil'evich Zosimov, Doctor of Physics and Mathematics, Deputy Director, Institute of Applied Acoustics

Nikolaĭ Igorevich Ivanov, Doctor of Engineering, Professor, Chair of Department, Baltic State University, St. Petersburg

Sergeĭ Nikolaevich Ivanov, Doctor of Physics and Mathematics, Professor, Deputy Director, Institute of

Radio Engineering and Electronics, Russian Academy of Sciences

Vsevolod Feodos'evich Kazantsev, Doctor of Physics and Mathematics, Professor, Moscow Automobile and Transport Institute (State University)

Margarita Aleksandrovna Kallistratova, Doctor of Physics and Mathematics, Head of Laboratory, Obukhov Institute of Atmospheric Physics, Russian Academy of Sciences

Valerii Kirillovich Kedrinskiĭ, Doctor of Physics and Mathematics, Professor, Deputy Director, Lavrent'ev Institute of Hydrodynamics, Siberian Division, Russian Academy of Sciences

Aleksandr Ivanovich Korobov, Doctor of Physics and Mathematics, Professor, Moscow State University

Yurii Aleksandrovich Kravtsov, Doctor of Physics and Mathematics, Professor, Head of Department, Institute of Space Exploration, Russian Academy of Sciences

Vladimir Aleksandrovich Krasil'nikov, Doctor of Physics and Mathematics, Professor, Moscow State University

Sergei Nikolaevich Kulichkov, Doctor of Physics and Mathematics, Leading Researcher, Obukhov Institute of Atmospheric Physics, Russian Academy of Sciences

Boris Fedorovich Kur'yanov, Doctor of Physics and Mathematics, Head of Laboratory, Shirshov Oceanology Institute, Russian Academy of Sciences

Leonid Olegovich Makarov, Candidate of Engineering, Associate Professor, Moscow Automobile and Transport Institute (State University)

Vladislav Georgievich Mikhalevich, Doctor of Physics and Mathematics, Professor, Deputy Director, General Physics Institute, Russian Academy of Sciences

Aleksei Sergeevich Nikiforov, Doctor of Engineering, Principal Researcher, Krylov Central Research Institute

Vladislav Ivanovich Pustovoit, Corresponding Member of the Russian Academy of Sciences, Institute of Radio Engineering and Electronics, Russian Academy of Sciences

Oleg Vladimirovich Rudenko, Corresponding Member of the Russian Academy of Sciences, Chair of Department, Moscow State University

Samuil Akivovich Rybak, Doctor of Physics and Mathematics, Professor, Head of Laboratory, Andreev Acoustics Institute, Russian Academy of Sciences

Vladimir Ivanovich Timoshenko, Doctor of Engineering, Professor, Chair of Department, Taganrog Radio-Engineering University

Igor' Alekseevich Urusovskii, Doctor of Physics and Mathematics, Leading Researcher, Andreev Acoustics Institute, Russian Academy of Sciences

Aleksandr Aleksandrovich Chaban, Doctor of Physics and Mathematics, Leading Researcher, Andreev Acoustics Institute, Russian Academy of Sciences

Émmanuil Lazarevich Fabelinskiĭ, Corresponding Member of the Russian Academy of Sciences, Principal Researcher, Lebedev Physical Institute, Russian Academy of Sciences

Vladimir Grigor'evich Shavrov, Doctor of Physics and Mathematics, Head of Laboratory, Institute of Radio Engineering and Electronics, Russian Academy of Sciences

Evgenii L'vovich Shenderov, Doctor of Engineering, Head of Laboratory, Morfizpribor Central Research Institute

Georgii Iosifovich Étkin, Doctor of Engineering, Professor, Head of Laboratory, All-Russian Institute of Light Alloys

**Address:** ul. Shvernika 4, Moscow,  
117036 Russia Tel.: (095) 1269014,  
1269810 (scientist-secretary),  
1269845 (Irina Petrovna Smirnova, secretary)  
Fax: (095) 1268411